Rydberg–ground state interaction in ultracold quantum gases

Dissertation

Thomas Niederprüm

Vom Fachbereich Physik der Technischen Universität Kaiserslautern zur Verleihung des akademischen Grades „Doktor der Naturwissenschaften“ genehmigte Dissertation

Betreuer: Prof. Dr. Herwig Ott
Zweitgutachter: Prof. Dr. Artur Widera

Datum der wissenschaftlichen Aussprache: 29. August 2016

D 386

Zusammenfassung

Die Kombination ultrakalter Gase mit den außergewöhnlichen Eigenschaften hochangeregter Rydbergatome hat in den letzten Jahren große Aufmerksamkeit von theoretischer und experimenteller Seite erhalten. In dieser Kombination kommt es innerhalb eines ultrakalten Gases zur Wechselwirkung zwischen dem Rydbergatom und den umgebenden Grundzustandsatomen, welche bedingt ist durch die Streuung des Rydbergelektrons an dem in die Wellenfunktion eindringenden Grundzustandsatom. Im Rahmen dieser Doktorarbeit wird diese außergewöhnliche Wechselwirkung im Detail für Rydberg P-Zustände in Rubidium untersucht.

Bedingt durch ihre lange Lebensdauer sind Atome in Rydbergzuständen in ultrakalten Gasen Stößen mit den umgebenden Grundzustandsatomen ausgesetzt. Durch die Bestimmung ihrer Lebensdauer als Funktion des Flusses von Grundzustandsatomen durch ihre Oberfläche sind wir in der Lage, sowohl den totalen inelastischen Streuquerschnitt als auch den Streuquerschnitt für assoziative Ionisation zu bestimmen. Aufgrund der Tatsache, dass letzterer mehr als drei Größenordnungen größer ist als der geometrische Querschnitt des erzeugten Rb_2^+-Molekülions, schließen wir auf die Existenz eines effizienten Massentransports, der durch die Rydberg-Grundzustandswechselwirkung entsteht. Die daraus resultierende enorme Beschleunigung des Kollisionsprozesses weist starke Ähnlichkeiten zur Katalyse auf. Die beobachtete Vergrößerung des Streuquerschnitts macht assoziative Ionisation zu einem relevanten Zerfallsprozess, der in Experimenten an dichten ultrakalten Gasen berücksichtigt werden muss.

Die untersuchte Wechselwirkung des Rydbergatoms mit den umgebenden Grundzustandsatomen erzeugt ein stark oszillierendes Potential, in dem gebundene Zustände existieren können. Diese sogenannten *ultralong-range Rydbergmoleküle* werden in dieser Arbeit mittels einer hochaufgelösten Flugzeitspektroskopie untersucht, die es ermöglicht, die Bindungsenergien und die Lebenszeiten der Molekülzustände rund um die beiden Feinstrukturzustände des $25P$-Zustands zu untersuchen. In einem elektrischen Feld beobachten wir eine Verbreiterung der Moleküllinien, was auf ein permanentes elektrisches Dipolmoment der Moleküle hinweist, das durch die Zustandsmischung mit hohen Drehimpulszuständen entsteht. Das Mischen der Hyperfeinzustände des Grundzustandsatoms durch die molekulare Wechselwirkung sorgt dafür, dass wir während der Molekülanregung einen Spinflip im Grundzustandsatom beobachten können. Zudem führt eine Beinahe-Entartung im zugrundeliegenden Niveauschema des $25P$-Zustands dazu, dass Zustände entstehen, welche die Feinstruktur des Rydbergatoms mit der Hyperfeinstruktur des Grundzustandsatoms stark verschränken. Diese Effekte könnten eingesetzt werden, um den Quantenzustand von Teilchen zu manipulieren, die sehr viel weiter voneinander entfernt sind als die typische Kontaktwechselwirkungsdistanz.

Abgesehen von ultralong-range Rydbergmolekülen, die hauptsächlich aus nur einem Zustand geringen Drehimpulses bestehen, ist eine weitere Klasse an Rydbergmolekülen theoretisch vorhergesagt, welche die hohen Drehimpulszustände der entarteten wasserstoffähnlichen Mannigfaltigkeiten mischt. Diese sogenannten *trilobite-* und *butterfly-Rydbergmoleküle* weisen einzigartige Eigenschaften auf, die bei konventionellen Molekülen

unmöglich sind. Im Rahmen dieser Arbeit erbringen wir den ersten klaren experimentellen Nachweis für die Existenz von butterfly-Rydbergmolekülen. Zusätzlich zu einer detaillierten Spektroskopie, aus der wir die Bindungsenergie der Zustände bestimmen können, sind wir zum ersten Mal in der Lage, die Rotationsstruktur von Rydbergmolekülen experimentell zu beobachten. In einem externen elektrischen Feld nehmen die butterfly-Moleküle sogenannte *pendular states* ein. Der Vergleich der Spektroskopie dieser Zustände mit dem Modell eines dipolaren, starren Rotors erlaubt es uns, die Bindungslänge und das Dipolmoment dieser zu bestimmen. Mit den so gewonnenen Informationen ist es möglich, butterfly-Rydbergmoleküle mit wählbarer Bindungslänge, Vibrationszustand, Rotationszustand und Ausrichtung in einem elektrischen Feld anzuregen.

Durch das Aufzeigen verschiedener zuvor unbeobachteter Facetten der Rydberg-Grundzustandswechselwirkung trägt die vorliegende Arbeit entscheidend dazu bei, das Wissen über diese außergewöhnliche Wechselwirkung und die aus ihr entstehenden Effekte zu vergrößern. Die gewonnenen spektroskopischen Ergebnissen zu Rydbergmolekülen und der geänderten Reaktionsdynamik bei der Bildung von Rb_2^+ sind sicher wertvolle Grundlagen für quantenchemische Simulationen sowie für die Planung zukünftiger Experimente. Darüber hinaus zeigt die vorliegende Studie, dass die Hyperfeinwechselwirkung in Rydbergmolekülen und die außergewöhnlichen Eigenschaften von butterfly-Rydbergmolekülen ein großes Potential bergen, um die kurz- und langreichweitigen Wechselwirkungen in ultrakalten Vielteilchensystemen zu beeinflussen. In diesem Sinn liegt die untersuchte Rydberg-Grundzustandswechselwirkung nicht nur in der Schnittmenge zwischen Quantenchemie, Vielteilchenquantensystemen und Rydbergphysik, sondern bereichert jedes dieser Felder durch die faszinierende Physik, die durch ihre Kombination entsteht.

Abstract

Combining ultracold atomic gases with the peculiar properties of Rydberg excited atoms gained a lot of theoretical and experimental attention in recent years. Embedded in the ultracold gas, an interaction between the Rydberg atom and the surrounding ground state atoms arises through the scattering of the Rydberg electron from an intruding perturber atom. This peculiar interaction gives rise to a plenitude of previously unobserved effects. Within the framework of the present thesis, this interaction is studied in detail for Rydberg P-states in rubidium.

Due to their long lifetime, atoms in Rydberg states are subject to scattering with the surrounding ground state atoms in the ultracold cloud. By measuring their lifetime as a function of the ground state atom flux, we are able to obtain the total inelastic scattering cross section as well as the partial cross section for associative ionisation. The fact that the latter is three orders of magnitude larger than the size of the formed molecular ion indicates the presence of an efficient mass transport mechanism that is mediated by the Rydberg–ground state interaction. The immense acceleration of the collisional process shows a close analogy to a catalytic process. The increase of the scattering cross section renders associative ionisation an important process that has to be considered for experiments in dense ultracold systems.

The interaction of the Rydberg atom with a ground state perturber gives rise to a highly oscillatory potential that supports molecular bound states. These so-called *ultralong-range Rydberg molecules* are studied with high resolution time-of-flight spectroscopy, where we are able to determine the binding energies and lifetimes of the molecular states between the two fine structure split $25P$-states. Inside an electric field, we observe a broadening of the molecular lines that indicates the presence of a permanent electric dipole moment, induced by the mixing with high angular momentum states. Due to the mixing of the ground state atom's hyperfine states by the molecular interaction, we are able to observe a spin-flip of the perturber upon creation of a Rydberg molecule. Furthermore, an incidental near-degeneracy in the underlying level scheme of the $25P$-state gives rise to highly entangled states between the Rydberg fine structure state and the perturber's hyperfine structure. These mechanisms can be used to manipulate the quantum state of a remote particle over distances that exceed by far the typical contact interaction range.

Apart from the ultralong-range Rydberg molecules that predominantly consist of only one low angular momentum state, a class of Rydberg molecules is predicted to exist that strongly mixes the high angular momentum states of the degenerate hydrogenic manifolds. These states, the so-called trilobite- and butterfly Rydberg molecules, show very peculiar properties that cannot be observed for conventional molecules. Here we present the first experimental observation of butterfly Rydberg molecules. In addition to an extensive spectroscopy that reveals the binding energy, we are also able to observe the rotational structure of these exotic molecules. The arising pendular states inside an electric field allow us, in comparison to the model of a dipolar rotor, to extract the precise bond length and dipole moment of the molecule. With the information obtained in the present study, it is possible to photoassociate butterfly molecules with a selectable bond length,

vibrational state, rotational state, and orientation inside an electric field.

By shedding light on various previously unrevealed aspects, the experiments presented in this thesis significantly deepen our knowledge on the Rydberg–ground state interaction and the peculiar effects arising from it. The obtained spectroscopic information on Rydberg molecules and the changed reaction dynamics for molecular ion creation will surely provide valuable data for quantum chemical simulations and provide necessary data to plan future experiments. Beyond that, our study reveals that the hyperfine interaction in Rydberg molecules and the peculiar properties of butterfly states provide very promising new ways to alter the short- and long-range interactions in ultracold many-body systems. In this sense the investigated Rydberg–ground state interaction not only lies right at the interface between quantum chemistry, quantum many-body systems, and Rydberg physics, but also creates many new and fascinating possibilities by combining these fields.

Contents

1. Introduction **9**
Publications . . . 13

2. Theory **15**
2.1. Atom–light interaction . . . 15
2.1.1. The Jaynes–Cummings model for a two-level system . . . 15
2.1.2. Bare states and dressed states . . . 16
2.1.3. Semiclassical approximation . . . 17
2.2. Scattering theory . . . 18
2.2.1. Resolvent and Green's function . . . 19
2.2.2. Partial wave decomposition . . . 21
2.3. Rydberg atoms . . . 24
2.3.1. Numerical calculation of Rydberg wave functions . . . 26
2.3.2. Rydberg atoms in external fields . . . 28
2.3.3. Ionisation of Rydberg atoms . . . 30
2.4. Rydberg–ground state interaction . . . 36
2.4.1. The pseudopotential approach . . . 40
2.4.2. Partial wave expansion of the interaction operator . . . 42
2.4.3. Angular momentum couplings . . . 43
2.4.4. Scattering phase shifts . . . 48
2.4.5. Adiabatic potentials . . . 50
2.4.6. Ultralong-range potentials . . . 55
2.4.7. Trilobite and butterfly potentials . . . 56
2.4.8. Molecular bound states . . . 59
2.4.9. Determination of the dipole moment . . . 63
2.5. Rydberg–Rydberg interaction . . . 64
2.5.1. Rydberg blockade . . . 67
2.6. Pendular states of dipolar molecules . . . 68
2.6.1. Coupling strength and polarisation dependence . . . 70

3. Experimental setup **73**
3.1. The magneto-optical trap . . . 73
3.2. The dipole trap . . . 76
3.3. Absorption imaging . . . 81
3.4. Microwave state transfer . . . 82
3.5. Rydberg excitation laser . . . 82
3.5.1. Polarisation and coupling . . . 85
3.6. Ion detection system . . . 86

4. Rydberg–ground state collisions: An electron mediated mass transport **89**
4.1. Time-of-flight measurements . . . 89

4.2. Microscopical model 91
  4.2.1. Peak ratio 93
  4.2.2. Initial decay rate of the molecular ion signal 94
  4.2.3. Average collision velocity 94
4.3. Cross section measurement 96
  4.3.1. Partial cross section for associative ionisation 96
  4.3.2. Total inelastic scattering cross section 98
4.4. Directed mass transport 99
4.5. The electron as a catalyst 101
4.6. Summary 102

5. Ultralong-range Rydberg molecules 105
5.1. Spectroscopy of P-state Rydberg molecules 105
  5.1.1. Lifetimes 106
  5.1.2. Dipole moments 107
5.2. Spin-flips in Rydberg molecules 110
  5.2.1. The spin-flip regime 112
  5.2.2. The entanglement regime 114
5.3. Summary 116

6. Butterfly Rydberg molecules 117
6.1. Coupling to butterfly Rydberg molecules 117
6.2. Spectroscopy of butterfly Rydberg molecules 119
6.3. Butterfly molecules in electric fields 121
  6.3.1. Determination of dipole moment and bond length 123
  6.3.2. Polarisation dependence 125
6.4. Dipole moments 125
6.5. Comparison to theory 128
6.6. Summary 128

7. Conclusions and outlook 131

A. Appendix 137
A.1. Spherical Bessel functions 137
A.2. Angular momentum coupling with ladder operators 137
A.3. Clebsch–Gordan coefficients 138
A.4. Gradients of single particle wave functions 138
A.5. Decoupling of states and angular dependence in the diagonalisation 141
A.6. Regularised pseudopotentials 143
A.7. Calculation of the electronic density 144
A.8. Numerical calculation of bound states by the shooting method 145
A.9. Harmonic approximation to the r-butterfly potential 147
A.10.Butterfly spectra in electric fields 147
A.11.Photoionisation cross sections 149
A.12.Long-range Entanglement of ground state atoms 151

Bibliography 164

Curriculum Vitae 167

1. Introduction

All throughout human history, it was always the urge to understand the basic principles of our world that provided the driving force for science and technology. Up to the present day, this basic human property gives rise to constantly increasing knowledge, understanding, and control of our environment. Once in a while, this steady process undergoes giant leaps that might even have the potential to change our whole concept of reality. Surely, one such leap was taken by the advance into the microcosm of atomic particles and the arising need to break classical physical paradigms in favour of the newly developed quantum mechanics.

A fundamental corner stone for the development of modern quantum mechanics was set by the discovery and proper understanding of atomic spectra in the late 19th century. A systematic study of the spectral lines in hydrogen by Johann Balmer revealed the n^{-2} energy scaling [1] that was later on generalised by Johannes Rydberg in the well-known Rydberg formula [2, 3]. The significance of this empirical result became clear when Nils Bohr extended the Rutherford model by assuming quantisation of the electron's angular momentum [4] and, with this model, could successfully explain the observed spectra. Already the first experiments were able to see spectroscopical evidence for highly excited states with $n \gg 1$ and their peculiar properties were discussed in the context of the Bohr model [4]. Up to the present day, such states are usually called *Rydberg states* to honour the pioneering work of Johannes Rydberg.

Ever since, the atomic spectra and the properties of Rydberg states have attracted the attention of many researchers. In a pioneering work, Amaldi and Segrè studied the interaction of Rydberg states with a buffer gas in thermal vapour cells [5]. The observed pressure shift was successfully explained by Enrico Fermi through a contact interaction pseudopotential [6]. As the experimental techniques were refined, the interactions of Rydberg states with their environment could be studied in increasing detail. In the 1980s, the high degree of control on the collision parameters in atomic beam experiments [7, 8] allowed for the detailed study of the collisional properties of Rydberg atoms [9–13] and their interaction with the electro-magnetic field [14, 15]. The insights into the fundamental processes of Rydberg atoms gave valuable input to various fields of physics, including plasma physics [16, 17] and astronomy [18, 19].

A new chapter in the study of Rydberg atoms began with the advent of sophisticated cooling methods [20, 21] that in turn enabled cooling atomic gases down to quantum degeneracy [22–25]. By almost completely eliminating the thermal motion, such systems allow for an unprecedented degree of control on ensembles of atoms, or even single atoms, in the quantum regime. In combination with the ability to create arbitrary potential landscapes through off-resonant laser beams [17], ultracold gases have rapidly turned into a very versatile quantum playground. In combination with optical lattices [26] as well as in bulk systems, ultracold gases are a promising toy system to study effects also present in solid state systems [27–29]. However, usual ultracold systems only show contact interaction. In lattice and bulk systems, much richer many-body dynamics can be induced by adding long-range interactions to the system. Apart from employing atomic species with high magnetic dipole moments [30, 31], heteronuclear molecules with high electric dipole moments [32], or second order tunnelling [33], a very promising route to achieve this consists in using the strong long-range interaction between Rydberg atoms. In such systems, the Rydberg–Rydberg interaction gives rise to many-body phenomena like blockade [34–38] and anti-blockade [39, 40] that in turn allow for the emergence of superatoms [41–43] and strongly correlated excitation clusters [44, 45]. Up to now, the combination of ultracold quantum gases with Rydberg excitations is still a very vivid and increasing field of research.

The new possibility to study Rydberg atoms in the environment of an ultracold system puts also the observable Rydberg–ground state interactions in a completely new regime. Due to the high particle densities and the low collisional energies, hitherto unknown interactions can be observed. In particular, it could be shown that the scattering between the Rydberg electron and a ground state atom perturbing the Rydberg wave function gives rise to a peculiar new interaction. Due to the highly oscillatory shape of the corresponding interaction potential, wells are formed which support molecular bound states [46, 47]. The bond of these so-called *Rydberg molecules* cannot be attributed to any of the three well-known types of chemical bond and therefore comprises a completely new type of bond. Depending on the exact scattering mechanism and the involved angular momentum states, Rydberg molecules are further subdivided into ultralong-range molecules [48], trilobite molecules [49], and butterfly molecules [47, 50]. Due to the strong localisation of the perturber's valence electron, the exchange energy of these molecules is vanishingly small and the smallest fields suffice to break parity symmetry [51]. Thus, Rydberg molecules, despite of being homonuclear, show permanent electric dipole moments that can, due to their immense size, reach up to the kilo-Debye range [49]. In the recent years, great theoretical and experimental effort has been pushed forward to study these exotic molecules and to get a full understanding of the rich molecular spectra observed in dense cold clouds [52–54]. The results presented within this thesis not only contribute significantly to this ongoing process but also show possible new directions.

The aim of this thesis is to give a detailed overview of the interaction between Rydberg and ground state atoms in ultracold gases. Consequently, chapter 2 gives a concise summary of the theoretical foundations of Rydberg atoms and the arising Rydberg–ground state interaction in ultracold systems. In this context, we explicitly include the hyperfine interaction of the ground state atom in the theoretical description [55] and analyse the nature of the resulting states. We furthermore consider the nuclear degree of freedom for the emerging molecules and discuss how the interaction of a permanent electric dipole moment with an external electric field leads to the emergence of so-called pendular states. Subsequently, chapter 3 describes the experimental apparatus that is used to cool ^{87}Rb into a Bose–Einstein condensate (BEC) and to perform controlled excitation of the atoms into Rydberg states.

Focusing on the dynamic properties of the Rydberg–ground state interaction, we point out the effect of the molecular potential on the scattering properties [56, 57] in chapter 4. From a giant increase in the cross section for associative ionisation, we are able to deduce an efficient mass transport mechanism that is mediated by the Rydberg electron. This process shows a close resemblance of a catalysis where the Rydberg electron acts as the catalyst. Turning from the dynamic scattering picture to static bound states in the molecular potential, chapter 5 presents an extensive spectroscopy of P-state Rydberg molecules and discusses the possibility to induce spin-flips and highly entangled states in the ground state atom through the back-action of the molecular bond. In chapter 6, we extend the discussion to the shape-resonance-induced butterfly states which show the strongest interaction of all known Rydberg molecules. We present the first experimental evidence for the existence of these exotic molecules and demonstrate how their peculiar properties enable us to obtain full control on their internal and external degrees of freedom.

Finally, we discuss several implications of the obtained results and future research perspectives in chapter 7. In this context, we will emphasise that the strong decay arising from the studied mass transport mechanism might impede coherent many-body experiments in high-density clouds, such as Rydberg dressing [58–60], and is relevant for studies of dissipative quantum phases of Rydberg gases beyond the frozen gas approximation [61]. Furthermore, the studied spin-flip process in ultralong-range Rydberg molecules allows to employ the Rydberg interaction to manipulate the internal states of remote ground state atoms which are often used as qubits in the context of quantum information processing [62]. The peculiar properties of butterfly Rydberg molecules and the high degree of control on their internal and external degrees of freedom render them interesting objects to study ultracold chemical reactions and to induce controlled dipole–dipole interaction in many-body systems. We thus think that apart from being interesting in their own right, the presented results are likely to have direct impact on the fields of ultracold Rydberg physics and quantum chemistry and we envision the studied Rydberg molecules and the occurring spin-flip process to find application in many-body quantum systems as well as quantum information processing.

Publications in the context of this work

- **Rydberg molecule-induced remote spin flips**
  T. Niederprüm, O. Thomas, T. Eichert, and H. Ott
  arXiv:1604.06742 (2016) - In press at *Phys. Rev. Lett.*

- **Observation of pendular butterfly Rydberg molecules**
  T. Niederprüm, O. Thomas, T. Eichert, C. Lippe, J. Pérez-Ríos, C. H. Greene, and H. Ott
  Nat. Commun. 7:12820 (2016)

- **Giant cross section for molecular ion formation in ultracold Rydberg gases**
  T. Niederprüm, O. Thomas, T. Manthey, T. M. Weber, and H. Ott
  Phys. Rev. Lett. **115**, 013003 (2015)

The author also contributed to

- **Dynamically probing ultracold lattice gases via Rydberg molecules**
  T. Manthey, T. Niederprüm, O. Thomas, and H. Ott
  N. J. Phys. **17**, 103024 (2015)

- **Mesoscopic Rydberg-blockaded ensembles in the superatom regime and beyond**
  T. M. Weber, M. Höning, T. Niederprüm, T. Manthey, O. Thomas, V. Guarrera, M. Fleischhauer, G. Barontini, and H. Ott
  Nat. Phys. **11**, 157 (2014)

- **Scanning electron microscopy of Rydberg-excited Bose–Einstein condensates**
  T. Manthey, T.M. Weber, T. Niederprüm, P. Langer, V. Guarrera, G. Barontini, and H. Ott
  N. J. Phys. **16**, 083034 (2014)

- **Continuous coupling of ultracold atoms to an ionic plasma via Rydberg excitation**
  T. M. Weber, T. Niederprüm, T. Manthey, P. Langer, V. Guarrera, G. Barontini, and H. Ott
  Phys. Rev. A **86**, 020702(R) (2012)

2. Theory

This chapter introduces the basic theoretical concepts required to understand the experiments on Rydberg–ground state interaction presented within this thesis (secs. 4, 5, and 6). Since the experimental realisation of Rydberg atoms is usually based on laser excitation, we will give a brief review on the atom–light interaction in the Jaynes–Cummings model. Subsequently, we present the concepts of scattering theory that are needed to understand the following treatment of Rydberg–ground state interaction. With this foundation we start to study Rydberg atoms and their strong interactions. As it is required for the following numerics, we will briefly present how to calculate Rydberg wave functions and how to derive the dipole matrix elements and the Rabi frequency from this. We then give a concise summary of the interaction of Rydberg atoms with external fields before we turn to the interaction with other particles. As it is fundamental for the presented experiments, the discussion is focussed on the interaction with ground state atoms. To describe this interaction, we derive a pseudopotential from first principles and obtain the eigenenergies of the interacting system by diagonalisation of the derived Hamiltonian. The arising ultralong-range molecular states as well as the so-called trilobite and butterfly states are studied in detail and the underlying angular momentum coupling is discussed. Finally, the model of a dipolar rigid rotor is discussed because of its importance for the presented experiments on butterfly Rydberg molecules (sec. 6).

2.1. Atom–light interaction

The interaction of atoms with the electromagnetic field lies at the heart of atomic physics. The high level of control on the quantum level gained in recent years allows for the observation of single photons as well as single atoms. A firm understanding of the basic principles of atom–light interaction at the quantum level is therefore necessary. Based on refs. [63,64], this section gives a brief introduction in the necessary concepts of atom–light interaction for quantised fields as well as in the semiclassical limit.

2.1.1. Jaynes–Cummings model for a two-level system

Considering a system comprised of two energy levels $|1\rangle$ (at energy $E_1 \equiv 0$) and $|2\rangle$ (at energy $E_2 = \hbar\omega_0$) that interacts with a single mode light field with the wavevector $\vec{k}$ and the corresponding frequency $\omega = c|\vec{k}|$, it is useful to define the spin operators

$$\hat{\sigma} = |1\rangle\langle 2| \tag{2.1.1}$$

$$\hat{\sigma}^\dagger = |2\rangle\langle 1|. \tag{2.1.2}$$

The projection operator to either one of the two levels can be expressed in terms of those operators in the following way:

$$\hat{\sigma}^\dagger\hat{\sigma} = |2\rangle\langle 2| \tag{2.1.3}$$

$$\hat{\sigma}\hat{\sigma}^\dagger = |1\rangle\langle 1|. \tag{2.1.4}$$

The energy of the combined atom–light system is not only given by their individual energy contributions E_{atom}, E_{light} but also by the contribution of the interaction energy between the atom and the light field E_{int}. Accordingly, the Hamiliton operator for this system consists of three parts [64]

$$\hat{H}_{\text{atom}} = \hbar\omega_0 \hat{\sigma}^\dagger \hat{\sigma} \ , \tag{2.1.5}$$

$$\hat{H}_{\text{light}} = \hbar\omega(\hat{a}^\dagger \hat{a} + \frac{1}{2}) \ , \tag{2.1.6}$$

$$\hat{H}_{\text{int}} = \sqrt{\frac{\hbar\omega}{2\epsilon_0 V}} \vec{\epsilon} \cdot \vec{d}_{12} \left[\hat{a}^\dagger + \hat{a}\right] (\hat{\sigma}^\dagger + \hat{\sigma}). \tag{2.1.7}$$

Here the operators $\hat{a}$ and $\hat{a}^\dagger$ denote the bosonic field operators for the creation and annihilation of a photon, V is the mode volume of the quantised light field, $\vec{\epsilon}$ is the polarisation vector of the electric field, and $\vec{d}_{12}$ is the electric dipole moment. Carrying out the multiplication of the operators in $\hat{H}_{\text{int}}$ yields four terms, two of which violate energy conservation. In rotating wave approximation [63, 64], those terms are neglected and the interaction term is given by

$$\hat{H}_{\text{int}} = \frac{\hbar\Omega_0}{2} (\hat{a}\hat{\sigma}^\dagger + \hat{a}^\dagger \hat{\sigma}) \ , \tag{2.1.8}$$

where $\Omega_0 = \sqrt{\frac{2\omega}{\hbar\epsilon_0 V}} \vec{\epsilon} \cdot \vec{d}_{12}$ is the Rabi frequency, which is a measure for the coupling strength between the atom and the light field.

Combining the three parts of the system's Hamiltonian yields

$$\hat{H}_{\text{JC}} = \hbar\omega_0 \hat{\sigma}^\dagger \hat{\sigma} + \hbar\omega(\hat{a}^\dagger \hat{a} + \frac{1}{2}) + \frac{\hbar\Omega_0}{2} (\hat{a}\hat{\sigma}^\dagger + \hat{a}^\dagger \hat{\sigma}), \tag{2.1.9}$$

which is denoted *Jaynes–Cummings Hamiltonian.* This simple model for the atom light interaction can be solved analytically and shows some important consequences which are discussed in the following.

2.1.2. Bare states and dressed states

Neglecting the atom–light interaction, the system is described by $\hat{H}_{\text{bare}} = \hat{H}_{\text{atom}} + \hat{H}_{\text{light}}$. Since those Hamiltonians act on separate Hilbert spaces, the eigenstates are given by the tensor product $|n+1, 1\rangle = |n+1\rangle_{\text{light}} \otimes |1\rangle_{\text{atom}}$ and $|n, 2\rangle = |n\rangle_{\text{light}} \otimes |2\rangle_{\text{atom}}$. These eigenstates are called *bare states.* Due to the linearity of the Hamilton operator, the eigenenergies corresponding to the bare states are given by the sum of the eigenenergies of the comprising Hamiltonians

$$E_{n+1,1} = \hbar\omega(n + 1 + \frac{1}{2}) \ , \tag{2.1.10}$$

$$E_{n,2} = \hbar\omega_0 + \hbar\omega(n + \frac{1}{2}). \tag{2.1.11}$$

The energy difference between the states $|n+1, 1\rangle$ and $|n, 2\rangle$ is then given by

$$\begin{aligned} \Delta E &= E_{n+1,1} - E_{n,2} \\ &= \hbar(\omega - \omega_0) = \hbar\delta, \end{aligned} \tag{2.1.12}$$

where we introduced the laser detuning $\delta := \omega - \omega_0$. The case $\delta > 0$ is often called blue detuning, the case $\delta < 0$ red detuning. The two states are degenerate if the frequency of the laser mode coincides with the transition frequency of the two level system and thus $\delta = 0$.

Taking the atom light interaction into account, only the pairs of bare states $|n+1, 1\rangle$ and $|n, 2\rangle$ get coupled. For finding the eigenvalues of the complete Jaynes–Cummings Hamiltonian, it is therefore sufficient to diagonalise the Hamiltonian on the subspace created by these two bare states. The Hamiltonian then reads

$$\hat{H}_{\mathrm{JC}} = \hbar \begin{pmatrix} \omega(n+\frac{3}{2}) & \frac{\Omega_0}{2}\sqrt{n+1} \\ \frac{\Omega_0}{2}\sqrt{n+1} & \omega_0 + \omega(n+\frac{1}{2}) \end{pmatrix}, \tag{2.1.13}$$

with the eigenvalues

$$E_{+/-} = \frac{\hbar\omega_0}{2} + \hbar\omega(n+\frac{1}{2}) \pm \frac{1}{2}\hbar\Omega. \tag{2.1.14}$$

Here $\Omega = \sqrt{\Omega_0^2(n+1)+\delta^2}$ is the generalised Rabi frequency. The corresponding eigenstates $|n, +\rangle$ and $|n, -\rangle$ are called *dressed states* and are given by

$$\begin{pmatrix} |n,+\rangle \\ |n,-\rangle \end{pmatrix} = \begin{pmatrix} \cos\frac{\alpha}{2} & \sin\frac{\alpha}{2} \\ -\sin\frac{\alpha}{2} & \cos\frac{\alpha}{2} \end{pmatrix} \begin{pmatrix} |n,2\rangle \\ |n+1,1\rangle \end{pmatrix}. \tag{2.1.15}$$

The mixing angle α is defined to be $\alpha = \arctan\frac{\Omega\sqrt{n+1}}{\delta}$. As an example, one can consider a two level atom inside of a light field that is detuned by 10 MHz from the atomic resonance. If this system is driven with a Rabi frequency of 500 kHz, the resulting new eigenstates of the coupled atom light system are comprised of 99% atomic ground state and 1% excited state and vice versa. The splitting of the bare states into the dressed states is depicted in fig. 2.1a. The energy reduction in the $|n, -\rangle$ state is the foundation of optical traps (see sec. 3.2). The interaction Hamiltonian turns level crossings in the coupled system into avoided crossings (fig. 2.1b). In the vicinity of an avoided crossing it is possible to adiabatically transfer population from one state to another by sweeping one of the system parameters, i.e Ω or δ, across the avoided crossing. This is the basic principle behind the Landau–Zener sweep that will be discussed in sec. 3.4.

2.1.3. Semiclassical approximation

If the number of quanta in the light field is much bigger than unity $n \gg 1$, the absorption of one photon by the two level system has negligible influence on the light field. In this case, the quantum character of the electromagnetic field can be neglected and the system can be described in a semiclassical approximation. The light field is then described by an electromagnetic wave incident on the two level system. If, furthermore, the extent of the two level system is much smaller than the wavelength of the light field, the effect of the light field can be described in the dipole approximation as a locally oscillating electric field at the position of the two level system $\vec{E}(t) = \vec{E}_0\cos(\omega t)$. The corresponding interaction Hamiltonian reads

$$\hat{H}_{\mathrm{WW}} = -\vec{d}_{12}\cdot\vec{E}_0\cos(\omega t), \tag{2.1.16}$$

where $\vec{d}_{12}$ is the dipole matrix element of the two level system. The system Hamiltonian in the rotating wave approximation becomes

$$\hat{H} = \hbar \begin{pmatrix} 0 & \frac{\Omega_0}{2}\cos(\omega t) \\ \frac{\Omega_0}{2}\cos(\omega t) & \omega_0 \end{pmatrix}, \tag{2.1.17}$$

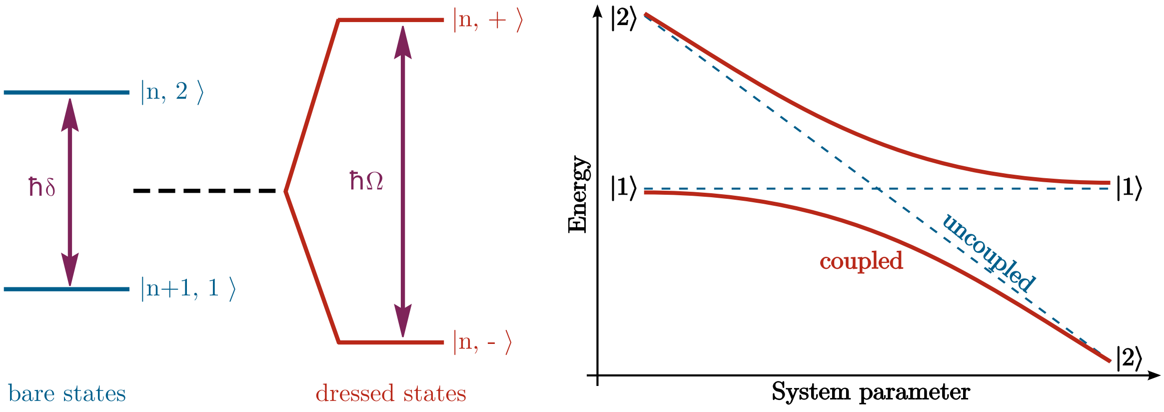

(a) (b)

Figure 2.1: (a) The bare states (left) of the non-interacting system turn to the dressed states (right side) due to the atom–light interaction. Here, the case $\delta < 0$ is depicted. (b) Where the bare states (blue) cross, an avoided crossing appears in the dressed states (red) due to the atom–light interaction term. This enables to adiabatically transfer a system from one state to another by sweeping a suited system parameter, i.e. the Rabi frequency Ω_0 or the detuning δ, across the crossing.

where the Rabi frequency Ω_0 is given by

$$\Omega_0 = \frac{E_0 e \langle 2 | \hat{\vec{\epsilon}} \cdot \hat{\vec{d}}_{12} | 1 \rangle}{\hbar} \equiv \frac{E_0 d_{12}}{\hbar} . \tag{2.1.18}$$

Here, the electric field vector $\vec{E}_0 = E_0 \vec{\epsilon}$ was decomposed into its length and direction (polarisation). Transforming the Hamiltonian into the interaction picture [65] that rotates with the frequency ω of the light field, the resulting Hamiltonian reads

$$\hat{H} = \hbar \begin{pmatrix} 0 & \frac{\Omega_0}{2} \\ \frac{\Omega_0}{2} & \delta \end{pmatrix} . \tag{2.1.19}$$

Calculating the eigenvalues yields the eigenenergies of the two level system in semiclassical approximation

$$E_{+/-} = \frac{\hbar}{2} \left(\delta \pm \Omega \right) , \tag{2.1.20}$$

with $\Omega = \sqrt{\Omega_0^2 + \delta^2}$ being the generalised Rabi frequency. Through the transformation into the interaction picture, the zero of the energy scale is shifted with respect to the eigenenergies from eq. (2.1.14) and is located in the middle between the two bare states, as depicted in fig. 2.1a.

The eigenstates of the system resemble those of the full quantum mechanical calculation from eq. (2.1.15) with the only difference that the factor $\sqrt{n+1}$ does not appear in the mixing angle of the states.

2.2. Scattering theory

Over the past century, a huge amount of successful theoretical models was gathered under the general framework of scattering theory. Based on refs. [9, 65, 66], this paragraph summarises the basic concepts and the most common methods used in scattering theory, as they are relevant for the physics of Rydberg–ground state interaction.

In the framework of this theory, it is convenient to describe the scattering between two particles in their centre of mass frame, giving rise to the reduced mass $\mu = \frac{m_1 m_2}{m_1+m_2}$ and their relative wave-vector $\vec{k}$. The problem is then fully described by the collision energy $E = \frac{\hbar^2 \vec{k}^2}{2\mu}$ and the mutual interaction $V(\vec{r})$ between the particles. The problem can thus be interpreted as a particle with the reduced mass μ scattering at an interaction potential $V(\vec{r})$ fixed at the origin. Such system is readily described by the time-independent Schrödinger equation. In space representation this reads

$$\left[-\frac{\hbar^2}{2\mu}\Delta + \hat{V}(\vec{r})\right]\Psi(\vec{r}) = E\Psi(\vec{r}), \tag{2.2.1}$$

where $\Psi(\vec{r})$ is the stationary scattering wave function. While this equation, of course, also describes the scattering of a single particle, which can be described as a superposition of many plane waves, it is more instructive to rather consider a permanent flux of particles that only involves a single plane wave. Before the scattering event, the incoming particle flux is in a state of directed motion towards the origin, which is described by the ingoing plane wave e^{ikz}. After the scattering event, it can move away from the scattering centre in the full solid angle, which is described by an outgoing spherical wave e^{ikr}/r with an angular-modulated amplitude. Therefore, the scattering wave function has to fulfil the boundary condition

$$\lim_{r\to\infty}\Psi(\vec{r}) = e^{ikz} + f(\theta,\phi)\frac{e^{ikr}}{r}, \tag{2.2.2}$$

where $f(\theta,\phi)$ is the *scattering amplitude*. The rather undefined terms "before the scattering" and "after the scattering" were replaced by $\lim_{r\to\infty}$. This is only valid if the effect of the interaction potential vanishes at infinity, meaning the potential vanishes faster than r^{-2}, so that $\lim_{r\to\infty} r^2 V(\vec{r}) = 0$. Such a potential is called a *finite-range potential.*

2.2.1. Resolvent and Green's function

In order to solve the scattering problem described in the previous section, a solution to the Schrödinger equation (2.2.1) that fulfils the boundary condition (2.2.2) has to be found. This can, of course, be done by numerically solving the differential equation given by the Schrödinger equation and matching the boundaries. Since this is a non-trivial task, several methods have been proposed in the past decades to simplify the solution. One of those methods is the resolvent-based Lippmann–Schwinger equation that turns the Schrödinger equation into an integral equation that inherently fulfils the boundary condition.

In order to understand this approach, we need to define the *resolvent* of the Hamilton operator $\hat{H}$ to be

$$\hat{G}(z) \equiv \frac{1}{z-\hat{H}}, \tag{2.2.3}$$

where z is a complex number and the notation $1/\hat{O}$ means taking the inverse of the operator $\hat{O}$. Multiplying both sides of the definition with $(z-\hat{H})$ and with $|\mathit{\Phi}_i\rangle\langle\mathit{\Phi}_i|$ being the projector of the eigenstates $|\mathit{\Phi}_i\rangle$ of $\hat{H}$ we obtain

$$\hat{G}(z)\,|\mathit{\Phi}_i\rangle\langle\mathit{\Phi}_i| = \frac{|\mathit{\Phi}_i\rangle\langle\mathit{\Phi}_i|}{z-E_i}. \tag{2.2.4}$$

Taking the sum over all projectors and identifying the unity operator $\sum_i |\Phi_i\rangle \langle\Phi_i| = 1$, we obtain the spectral decomposition of the resolvent

$$\hat{G}(z) = \sum_{i=0}^{\infty} \frac{|\Phi_i\rangle \langle\Phi_i|}{z - E_i}. \tag{2.2.5}$$

Hence, the poles of the resolvent obviously span the spectrum of the operator $\hat{H}$. This operator is thus highly singular on the real axis and one has to be careful when dealing with it. Applying this operator to a state from the Hilbert space might lead to a state outside of the Hilbert space. Strictly speaking the resolvent is therefore no operator on the Hilbert space. To circumvent this problem, it is customary to set $z = E \pm i\epsilon$ and to redefine the resolvent in the limit of approaching the diverging real axis as

$$\hat{G}^{(\pm)} = \lim_{\epsilon\to 0} \frac{1}{E \pm i\epsilon - \hat{H}}. \tag{2.2.6}$$

As shown in ref. [65, sec. 19.1.9] the resolvent of the free-particle Hamiltonian $\hat{H}_0 = \hbar^2 k^2/(2\mu)$ is the operator matrix for the free-particle (retarded) Green's function

$$\langle\vec{r}|\hat{G}_0^{\pm}(k)|\vec{r'}\rangle = \mathscr{G}^{\pm}(\vec{r}, \vec{r'}, k) = -\frac{m}{2\pi\hbar^2} \frac{e^{\pm ik|\vec{r}-\vec{r'}|}}{|\vec{r} - \vec{r'}|}. \tag{2.2.7}$$

Perturbation of the resolvent

Let us now consider a Hamiltonian $\hat{H}_0$ for which we know the resolvent $\hat{G}_0 = [z - \hat{H}_0]^{-1}$ and a perturbed Hamiltonian $\hat{H} = \hat{H}_0 + \hat{V}$. The resolvent of the latter Hamiltonian is given by

$$\hat{G}^{(\pm)}(E) = \frac{1}{E \pm i\epsilon - \hat{H}_0 - \hat{V}}. \tag{2.2.8}$$

It is possible to relate the resolvent $\hat{G}$ of the perturbed system to the resolvent of the unperturbed system $\hat{G}_0$ by multiplying eq. (2.2.8) with $1 = \hat{G}_0^{(\pm)}[E \pm i\epsilon - \hat{H}_0 - \hat{V} + \hat{V}]$:

$$\hat{G}^{(\pm)} = \hat{G}_0^{(\pm)} \left[(E \pm i\epsilon - \hat{H}_0 - \hat{V}) + \hat{V}\right] \frac{1}{E \pm i\epsilon - \hat{H}_0 - \hat{V}} \tag{2.2.9}$$

$$\Rightarrow \hat{G}^{(\pm)} = \hat{G}_0^{(\pm)} + \hat{G}_0^{(\pm)} \hat{V} \hat{G}^{(\pm)}. \tag{2.2.10}$$

It is easy to see that this recursive equation is equivalent to

$$\hat{G}^{(\pm)} = \sum_{n=0}^{\infty} (\hat{G}_0^{(\pm)} \hat{V})^n \; \hat{G}_0^{(\pm)}. \tag{2.2.11}$$

This equation is called *Hilbert identity* or *second resolvent equation* and gives an exact relation between the perturbed and the unperturbed resolvent. Of course, the perturbation can be described approximately by stopping the power series at a finite n. This corresponds to describing the problem in perturbation theory of n-th order.

Lippmann–Schwinger equation and Born series

We can now use the knowledge of the resolvent to derive an integral equation that describes the scattering problem. Our starting point is a free particle described by $\hat{H}_0 \left|\Phi\right\rangle = E \left|\Phi\right\rangle$. Since we only consider elastic scattering, we are interested in the eigenstates of this particle with the very same energy E inside the potential $\hat{V}(\vec{r})$. This is well described by the Schrödinger equation

$$\left(\hat{H}_0 + \hat{V}\right) \left|\Psi\right\rangle = E \left|\Psi\right\rangle . \tag{2.2.12}$$

Adding zero in terms of the free particle Schrödinger equation $\left(E - \hat{H}_0\right) \left|\Phi\right\rangle = 0$ we obtain

$$\left(E - \hat{H}_0\right) \left|\Psi\right\rangle = \left(E - \hat{H}_0\right) \left|\Phi\right\rangle + \hat{V} \left|\Psi\right\rangle . \tag{2.2.13}$$

By applying the resolvent of the free particle $\hat{G}_0^{(\pm)}$ from the left, we finally arrive at

$$\left|\Psi^{(\pm)}\right\rangle = \left|\Phi\right\rangle + \hat{G}_0^{(\pm)} \hat{V} \left|\Psi^{(\pm)}\right\rangle , \tag{2.2.14}$$

which is called the *Lippmann–Schwinger equation.* This is an integral equation that is equivalent to the stationary Schrödinger equation (2.2.1). Due to the insertion of the free particle state $\left|\Phi\right\rangle$, the integration offset is fixed and the equation inherently fulfils the boundary condition in eq. (2.2.2), which is also revealed by the structure of the Lippmann–Schwinger equation. Turning the recursion into a sum, we obtain

$$\left|\Psi^{(\pm)}\right\rangle = \sum_{n=0}^{\infty} (\hat{G}_0^{(\pm)} \hat{V})^n \left|\Phi\right\rangle , \tag{2.2.15}$$

which is called the *Born series.* As each propagator $\hat{G}_0^{(\pm)} \hat{V}$ introduces an intermediate state that scattered once from the potential, the n-th order of this series can be interpreted as the contribution of n-time scattering in the potential. Considering only 0-th order means the incoming plane wave does not interact with the potential at all. Expanding to first order means that the plane wave can only scatter from the potential once and multiple scattering is neglected. This case is called the *Born approximation.*

It is interesting to note the similarity in the structure of the Lippmann–Schwinger equation (2.2.15) and the perturbation series of the resolvent in eq. (2.2.11). It is therefore justified to also identify the perturbation expansion of the resolvent with the Born series and call the expansion to first order Born approximation.

2.2.2. Partial wave decomposition

If the scattering potential is not angular dependent $\hat{V}(\vec{r}) = \hat{V}(r)$, the Schrödinger equation (2.2.1) becomes rotationally invariant. Due to this symmetry, it is useful to represent the problem in spherical coordinates. The Schrödinger equation then reads

$$\left[-\frac{\hbar^2}{2\mu} \left(\frac{\partial^2}{\partial r^2} + \frac{2}{r} \frac{\partial}{\partial r} \right) + \frac{\hat{L}^2}{2\mu r^2} + \hat{V}(r) \right] \Psi(r, \theta, \phi) = E \Psi(r, \theta, \phi). \tag{2.2.16}$$

Since only the angular momentum operator $\hat{L}$ acts on the angular coordinates of the wave function, it might be tempting at that point to separate the problem in a radial and an angular part, in analogy to the Hydrogen problem. However, in contrast to the negative energy solutions of the Hydrogen problem the positive energy solutions of the scattering problem have to obey the boundary condition from eq. (2.2.2) that breaks the rotational symmetry. Due to the symmetry of the Hamiltonian itself, it is nevertheless useful to expand the scattered wave function in the eigenbasis of the angular momentum operator, which is given by the spherical harmonics. If we assume that the incident plane wave $e^{i\vec{k}\cdot\vec{r}} = e^{ikz}$ is directed along the z-axis, we can restrict the spherical harmonics to $m = 0$, in which case they are simply given by the l-th order Legendre polynomial $Y_l^{m=0}(\theta, \phi) \propto P_l(\cos\theta)$. The expansion then has the form

$$\Psi(r, \theta) = \sum_{l=0}^{\infty} \frac{u_l(r)}{r} P_l(\cos\theta), \tag{2.2.17}$$

where $u_l(r)$ is the radial wave function for the l-th partial wave. Putting this ansatz into the Schrödinger equation we obtain

$$\sum_{l=0}^{\infty} \left[E + \frac{\hbar^2}{2\mu} \frac{\partial^2}{\partial r^2} - \frac{\hbar^2 l(l+1)}{2\mu r^2} - \hat{V}(r) \right] u_l(r) P_l(\cos\theta) = 0, \tag{2.2.18}$$

which can only be fulfilled for all angles θ if every term of the sum vanishes on its own. Therefore, we obtain a set of differential equations for the radial wave function of the individual partial waves

$$\left[E + \frac{\hbar^2}{2\mu} \frac{\partial^2}{\partial r^2} - \frac{\hbar^2 l(l+1)}{2\mu r^2} - \hat{V}(r) \right] u_l = 0, \tag{2.2.19}$$

which has the form of a one-dimensional Schrödinger equation for a free particle with mass μ inside the effective potential $V_{\text{eff}}(r) = V(r) + \hbar^2 l(l+1)/(2\mu r^2)$. The full scattering process can therefore be decomposed into a set of one-dimensional scattering problems in terms of partial waves.

Since we assumed that $V(r)$ vanishes faster than r^{-2}, the centrifugal term will dominate at high r. In the asymptotic limit $r \to \infty$, eq. (2.2.19) the problem transforms to that of a free particle. In this limiting ($V(r) = 0$), the solution is given by a superposition of the regular modified spherical Bessel function $u_l^{(s)}(r) = krj_l(kr)$ and the irregular modified spherical Bessel function $u_l^{(c)}(r) = -kry_l(kr)$, where j_l and y_l are the spherical Bessel functions. The solution then reads

$$u_l(r) = a_l u_l^{(s)}(r) + b_l u_l^{(c)}(r) = a_l \left(u_l^{(s)}(r) + \tan(\delta_l) u_l^{(c)}(r) \right). \tag{2.2.20}$$

Here we introduced $\tan(\delta_l) = b_l/a_l$. In this form, the asymptotic scattering state is fully described by the coefficients a_l and δ_l, which gets even more obvious by replacing the spherical Bessel functions with their asymptotic expressions (see sec. A.1). Eq. (2.2.20) then resembles the asymptotic behaviour of the Bessel functions and has the form [66, eq. 2.42]

$$u_l(r) \underset{r\to\infty}{\to} a_l \sin\left(kr - \frac{1}{2} l\pi + \delta_l(k) \right). \tag{2.2.21}$$

As the previously introduced coefficient δ_l appears here as a phase shift in the sine, it is usually called *scattering phase shift*. Far from the scattering centre, the whole effect of the scattering process can thus be described by a changed amplitude and phase of the outgoing wave with respect to the ingoing wave for each partial wave.

In analogy to the expansion of the wave function in eq. (2.2.17), the scattering amplitude $f(\theta)$ can be expanded in partial waves by

$$f(\theta) = \sum_{l=0}^{\infty} f_l P_l(\cos\theta), \tag{2.2.22}$$

where f_l is the *partial wave scattering amplitude.* An expression for f_l in terms of the phase shifts δ_l can be obtained by inserting eq. (2.2.22) and the expansion of a plane wave in Legendre polynomials $e^{ikz} \equiv e^{ikr\cos\theta} = \sum_{l=0}^{\infty} = (2l+1)i^l j_l(kr)P_l(\cos\theta)$ into eq. (2.2.2). The partial wave decomposition of the wave function then reads

$$\Psi(r,\theta) = \sum_{l=0}^{\infty} \left((2l+1)i^l j_l(kr) + f_l \frac{e^{ikr}}{r} \right) P_l(\cos\theta). \tag{2.2.23}$$

Far from the scattering centre, we can replace the spherical Bessel function $j_l(kr)$ with its asymptotic expression (see sec. A.1) and we can write

$$r\Psi(r,\theta) \approx \sum_{l=0}^{\infty} \left(\frac{(2l+1)(-1)^{l+1}}{2ik} e^{-ikr} + \left[f_l + \frac{(2l+1)}{2ik} \right] e^{ikr} \right) P_l(\cos\theta). \tag{2.2.24}$$

Since the expression in parenthesis must be equal to the asymptotic expression for $u_l(r)$ from eq. (2.2.21), we can deduce the following relations

$$a_l = i^l \frac{2l+1}{k} e^{i\delta_l}, \tag{2.2.25a}$$

$$f_l = \frac{2l+1}{2ik} \left(e^{2i\delta_l} - 1 \right). \tag{2.2.25b}$$

Threshold behaviour

Due to the low energies involved in cold gas collisions, we are mainly interested in low energy collisions. It is therefore instructive to take a closer look at the scaling behaviour of the scattering amplitude for $k \to 0$. Even if we choose r sufficiently large to be outside the range of the scattering potential, the product kr still tends to zero as we approach the threshold, i.e. $k \to 0$. In this case, we can insert the approximations from eq. (A.1.2a) and eq. (A.1.2b) up to first order into the asymptotic radial wave function in eq. (2.2.20) and we obtain

$$u_l(kr) \underset{kr\to 0}{\approx} \frac{(ik)^l e^{i\delta_l} r^{l+1}}{(2l-1)!!} \left[1 + \tan(\delta_l) \frac{(2l+1)!!(2l-1)!!}{(kr)^{2l+1}} \right]. \tag{2.2.26}$$

Since the shape of the scattering wave function must not depend on k any more at the threshold, the tangent has to compensate the k-dependence in the second term of the sum. Therefore, we see that $\tan(\delta_l) \propto k^{2l+1}$. More rigorously one can show that [65, 66]

$$\tan(\delta_l) \underset{k\to 0}{\to} -\frac{1}{(2l+1)!!(2l-1)!!} (ka_l)^{2l+1}, \tag{2.2.27}$$

where a_l is the *scattering length* of the l-th partial wave. Inserting this into the approximation for the radial wave function eq. (2.2.26), we see that a_l denotes the point at which the radial wave function passes zero.

From the expansion of the tangent $\tan(\delta_l) \approx \delta_l$, we can see that for small k also $\delta_l \propto k^{2l+1}$. This particular scaling behaviour is called the *Wigner threshold law* and is connected to the centrifugal barrier imposed by the $l(l+1)/(2\mu r^2)$-term in the effective scattering potential. A striking consequence of this scaling becomes clear if we expand the exponential function in eq. (2.2.25b) to $e^{2i\delta_l} \approx 1 + 2i\delta_l$ and apply the scaling of δ_l. We obtain

$$f_l \underset{k\to 0}{\rightarrow} (2l+1)k^{2l}. \tag{2.2.28}$$

This shows that higher partial waves vanish rapidly as the collision energy approaches the threshold. A physical interpretation of this behaviour is that for high partial waves the decreasing collision energy is not sufficient to overcome the centrifugal barrier any more and thus the inner scattering potential is not probed. Since only the s-wave ($l = 0$) and thus f_0 stays finite, while all other scattering amplitudes tend to zero, only s-wave scattering has to be considered for sufficiently small collision energies. In this case, the whole physics of the scattering process is reduced to one scalar quantity, the s-wave scattering length $a_0 \equiv a$. This simplification is often the reason to do a partial wave analysis in the first place.

2.3. Rydberg atoms

High-lying electronic states of atoms and molecules are called Rydberg states after their namesake Johannes Rydberg, who was the first to phenomenologically describe the correct scaling of the transition frequencies between two excited states n_1, n_2 in hydrogen to be $1/n_2^2 - 1/n_1^2$ [1,2]. Later on, this experimental observation gained a theoretical basis in the Bohr model, which is able to explain the discrete energy levels and their $1/n^2$ - scaling by assuming a quantisation of the angular momentum $L = n\hbar$ of the electron. This model predicts the classical electron orbital radius r_n and the energy levels E_n of a hydrogen atom to be

$$r_n = a_0 n^2 \tag{2.3.1}$$

$$E_n = -\frac{Ry}{n^2}, \tag{2.3.2}$$

where $a_0 = \frac{4\pi\epsilon_0\hbar^2}{e^2 m_e} \approx 0.05\,\mathrm{nm}$ is the Bohr radius and $Ry = \frac{e^2 m_e}{16\pi^2\epsilon_0^2\hbar^2} \approx 13.6\,\mathrm{eV}$ is the Rydberg constant [4]. Due to the similarity to the hydrogen atom, this simple model can be extended to the valence electron of alkali atoms by introducing the so-called quantum defect δ_{nl} and the effective principal quantum number $n^* = n - \delta_{nl}$. Within this model, the interaction of the valence electron with the inner electrons is completely governed by the quantum defect and eq. (2.3.2) accurately describes the levels of alkali atoms if n is replaced by n^*. In the following, we can thus discuss the properties of Rydberg states of alkali atoms and still refer to the hydrogen model.

Already the simple Bohr model shows important consequences for Rydberg states, i.e. states with high principal quantum numbers $n \gg 1$. Since those states have sufficient kinetic energy, they can probe remote parts of the Coulomb potential. Thus, as shown by eq. (2.3.1), the size of the atom grows quadratically with the principal quantum number, making Rydberg atoms very large objects compared to their ground state counter parts. This increase in size has a direct effect on the properties of Rydberg states. As the size of the atom increases, also its geometric cross section for scattering events with other particles increases. Furthermore, it decreases the probability for a dipole transition from the ground state to the Rydberg state and vice versa due to the poor spatial overlap of the huge Rydberg wave function with the small ground state wave function. This leads to a decreasing coupling strength for laser excitation and to an increasing lifetime of the Rydberg state. Despite the high charge separation, Rydberg atoms do not possess a permanent electric dipole moment due to the symmetry of their electron orbitals. Nevertheless, the charge separation has a tremendous effect on the electric properties of Rydberg atoms. Since the Coulomb potential becomes flatter for increasing distance to the origin, small external fields suffice to induce a significant change to the outer parts of the potential and thus to shift the energy of the Rydberg state that probes these outer parts. This renders Rydberg atoms very sensitive to electric fields and gives rise to the enormous scaling of the polarisability

$$\alpha \propto n^7 \tag{2.3.3}$$

with the principal quantum number n [76]. This high sensibility to electric fields leads to a strong interaction between two approaching Rydberg atoms since the separated charges in one Rydberg atom can easily break the symmetry and induce a dipole in the second atom and vice versa. Hence, even though there is no direct dipole–dipole interaction between two Rydberg atoms due to their symmetry, there is a second-order van-der-Waals interaction, that gives rise to an energy shift

$$\Delta E = -\frac{C_6}{r^6} \tag{2.3.4}$$

with the van-der-Waals constant $C_6 \propto n^{11}$ (see also sec. 2.5). It is this enormous scaling that makes Rydberg atoms the object of many studies. Especially since the advent of ultracold atomic and molecular gases, there has been a steadily increasing interest in the strong long-range interactions of Rydberg atoms because they complement the pure contact interaction usually found in such systems. Therefore, over the last decade Rydberg atoms became a steadily growing field of research in the areas of interacting many-body systems [42, 67, 68], ultracold chemistry [69], ultracold plasmas [70–72], and quantum computation/simulation [73, 74].

The application of Rydberg atoms in those fields also poses some challenges since the high sensitivity also implies that Rydberg states are very fragile. As the energy gap to adjacent states $\Delta E \propto 1/n^3$ becomes smaller, transitions to other Rydberg states can easily be induced by collisions or low energy photons. Therefore, a limit on the lifetime of a certain Rydberg state at room temperature is imposed by the transition to neighbouring states induced by black-body radiation [75, 76]. As the energy gap to the continuum also lies in the spectral range of the black-body radiation, Rydberg atoms are always subject to black-body induced ionisation, if not in a cryogenic environment. Also the presence of laser light, e.g. for trapping atoms as shown in sec. 3.2, usually implies additional coupling to continuum states. These decay mechanisms need to be properly understood in order to make use of the beneficial properties of Rydberg atoms.

To put these arguments on a more quantitative basis, we will show in the following how electronic wave functions for alkali atoms can be obtained numerically. Since the wave function fully describes the atom, we can calculate any single particle property, such as transition rates, lifetimes and polarisabilities, as well as many-body properties like the Van-der-Waals coefficient.

2.3.1. Numerical calculation of Rydberg wave functions

In close analogy to the hydrogen atom, the Hamiltonian for an alkali atom is described by

$$\hat{H}_0 = -\frac{\hbar^2}{2\mu}\Delta + V_{\text{eff}}(r), \tag{2.3.5}$$

with the reduced mass $\mu \approx m_e$ and the effective potential

$$V_{\text{eff}}(r) = -\frac{e}{4\pi\epsilon_0|\hat{\vec{r}}|} + \hat{V}_{\text{qd}}(|\vec{r}|), \tag{2.3.6}$$

which is composed of the usual $1/r$-Coulomb potential of the core's residual charge and the polarisation potential $\hat{V}_{\text{qd}}(|\vec{r}|)$ that takes into account the interaction of the valence electron with the core. In order to find a rough estimate for the polarisation potential $\hat{V}_{\text{qd}}(|\vec{r}|)$, one can just consider the second-order DC-Stark shift $\Delta E_{\text{Stark}} = -\frac{1}{2}\alpha E^2$ that is induced in the core by the electric field $E = e^2/(4\pi\epsilon_0 r^2)$ of the electron, leading to

$$\hat{V}_{\text{qd}}(|\vec{r}|) \equiv \Delta E_{\text{Stark}} = -\frac{C_4}{r^4}, \tag{2.3.7}$$

with $C_4 = \frac{\alpha e^4}{32\pi^2\epsilon_0^2}$ that relies on the polarisability α of the Rb^+ ion. If we transform eq. (2.3.5) and eq. (2.3.6) to atomic units ($\frac{1}{4\pi\epsilon_0} = \hbar = e = m_e \equiv 1$) and divide by $-\frac{1}{2}$, we obtain the Schrödinger equation

$$\left[\Delta + \left(\frac{2}{r} + \frac{\alpha}{r^4} + 2E_{nl}\right)\right]\Psi_{nl}(r,\theta,\phi) = 0, \tag{2.3.8}$$

with the eigenenergies E_{nl} and the spatial wave function $\Psi_{nl}(r,\theta,\phi)$ in spherical coordinates. The Laplace operator can be expressed in terms of the squared angular momentum operator $\hat{\vec{L}}^2$ and a radial derivative and we obtain

$$\left[\frac{1}{r}\frac{\partial^2}{\partial r^2}r + \left(-\frac{\hat{\vec{L}}^2}{r^2} + \frac{2}{r} + \frac{\alpha}{r^4} + 2E_{nl}\right)\right]\Psi_{nl}(r,\theta,\phi) = 0. \tag{2.3.9}$$

From the structure of this differential equation, it is reasonable to assume that the wave function $\Psi_{nl}(r,\theta,\phi) = R_{nl}(r)Y_l^m(\theta,\phi)$ is separable in a radial and an angular part. As known from the hydrogen problem the angular part is solved by the spherical harmonics, which are the eigenfunctions of the angular momentum operator and thus fulfil $\left[\hat{\vec{L}}^2 - l(l+1)\right]Y_l^m(\theta,\phi) = 0$ [77]. Inserting the above ansatz for the wave function in eq. (2.3.9), dividing by $Y_l^m(\theta,\phi)$, and multiplying by r from the left, yields the one-dimensional differential equation for the reduced radial wave function $u_{nl}(r) = rR_{nl}(r)$

$$\left[\frac{\partial^2}{\partial r^2} + \left(-\frac{l(l+1)}{r^2} + \frac{2}{r} + \frac{\alpha}{r^4} + 2E_{nl}\right)\right]u_{nl}(r) = 0. \tag{2.3.10}$$

While the angular part of the problem can be covered analytically, the radial wave function must be integrated numerically due to the deviation from the Coulomb potential imposed by the polarisation potential. A problem arises at this point since a priori the eigenenergies E_{nl} are not known and thus it is not clear for which energy the differential equation has to be integrated to obtain the radial wave function. Within the quantum defect theory, the energies $E_{nl} = -1/(n-\delta_{nl})^2$ can be obtained if the quantum defects δ_{nl} are known. Those can be calculated by the Rydberg–Ritz formula

$$\delta(n,l,j) = \delta_0(l,j) + \sum_i \frac{\delta_{2i}(l,j)}{(n-\delta_0(l,j))^{2k}}, \tag{2.3.11}$$

where the $\delta_i(l,j)$ are empirical parameters, that are obtained by fitting the level energies obtained from experimental spectra. As implied by the parameter j, the quantum defect can also include the energy correction due to the spin–orbit coupling and thus depends on the total angular momentum quantum number j. Values for $\delta_i(l,j)$ can be found in refs. [78, 79] in the case of rubidium and in refs. [80, 81] in the case of caesium. With the known eigenenergies E_{nlj}, the differential equation can be integrated numerically by the Numerov algorithm, which is concisely summarised in ref. [82]. From the integrated radial wave function $R_{nlj}(r)$ and the spherical harmonics we can obtain the full spin–orbit coupled wave function

$$\Psi_{nljm_j}(r,\theta,\phi) = R_{nlj}(r) \sum_{m_s=-1/2}^{1/2} \langle l, m_l, s, m_s | j, m_j \rangle \, Y_l^{m_j - m_s}(\theta,\phi) \otimes \chi_{m_s}, \tag{2.3.12}$$

where χ_{m_s} is the spin wave function and $\langle l, m_l, s, m_s | j, m_j\rangle$ is the Clebsch–Gordan coefficient as explained in sec. A.3.

Dipole coupling strength

As pointed out in sec. 2.1.3, the matrix elements of the dipole operator $\hat{\vec{d}}$ are required in order to calculate the Rabi frequency as a measure of the coupling strength between two states. In spherical coordinates, the dipole operator $\hat{d}_q = e\hat{r}\hat{Y}_1^q(\theta,\phi)$ can be expressed in terms of the spherical harmonics for $l = 1$, where q determines the helicity of the transition[1]. We are therefore interested in the matrix element

$$\langle nljm_j | \hat{d}_q | n'l'j'm_j' \rangle = e \, \langle nlj | \hat{r} | n'l'j' \rangle_R \times \langle ljm_j | \hat{Y}_1^q | l'j'm_j' \rangle_Y \,, \tag{2.3.13}$$

where the index R (Y) indicates that only the radial (angular) part of the state is considered for the matrix element. While the radial matrix element is frequently denoted *reduced dipole matrix element* and is calculated as

$$\langle nlj | \hat{r} | n'l'j' \rangle = \int_0^\infty r |R_{nlj}(r)|^2 r^2 \, \mathrm{d}r, \tag{2.3.14}$$

the angular matrix element of the spherical harmonic function can be obtained analytically by the Wigner–Eckart theorem. In the spin–orbit coupled basis, the matrix element is thus given by [83]

$$\begin{aligned} \langle ljm_j | \hat{Y}_1^q | l'j'm_j' \rangle = (-1)^{m_j - l' - l - \frac{3}{2}} & \sqrt{(2j'+1)(2j+1)(2l'+1)(2l+1)} \\ \times & \begin{pmatrix} j & j' & 1 \\ -m_j & m_j' & q \end{pmatrix} \begin{Bmatrix} l & l' & 1 \\ j' & j & \frac{1}{2} \end{Bmatrix} \begin{pmatrix} l & 1 & l' \\ 0 & 0 & 0 \end{pmatrix} \end{aligned}, \tag{2.3.15}$$

---

[1] A value of $q = 0$ represents a π-transition and $q = \pm 1$ corresponds to a $\sigma^\pm$-transition.

where the expression in parenthesis is the Wigner-3j symbol and the expression in braces is the Wigner-6j symbol. The dipole matrix element is directly connected to the rate of spontaneous decay from one state to the other with a transition wavelength λ, as described by the Einstein A-coefficient

$$A = \frac{2}{3}\left(\frac{2\pi}{\lambda}\right)^3 \frac{1}{\epsilon_0 h} |\left\langle nljm_j|\hat{d}_q|n'l'j'm_j'\right\rangle|^2. \tag{2.3.16}$$

From this rate coefficient, it is straight forward to obtain the natural lifetime of a certain state by summing over all possible final states. The lifetime τ_k of the state k can thus be expressed as

$$\tau_k = \frac{1}{\sum_i A_{ik}}, \tag{2.3.17}$$

where i runs over all possible final states, i.e. $E_i < E_k$. A quantitative comparison of the lifetimes we obtain with the ones from refs. [76, 82] is given in ref. [84]. In the coherent atom–light model furthermore the Rabi frequency can be calculated from the known dipole matrix element according to eq. (2.1.18). With $I = \frac{1}{2}c\epsilon_0 E_0^2$, we can express the Rabi frequency in terms of the light intensity as

$$\Omega_0^{(q)} = \sqrt{\frac{2I}{c\epsilon_0\hbar^2}}\left\langle nljm_j|\hat{d}_q|n'l'j'm_j'\right\rangle. \tag{2.3.18}$$

2.3.2. Rydberg atoms in external fields

Rydberg atoms in external magnetic fields

The interaction of an atom in the Rydberg state with an external magnetic field is solely determined by the spin and the angular momentum of the valence electron. Since these properties do not change with the principal quantum number n, the magnetic properties of Rydberg atoms do not differ significantly from that of ground state atoms. Accordingly, the magnetic field $\vec{B} = B\hat{e}_z$ induces a fine structure Zeeman-splitting of the otherwise degenerate m_j states, that is described by

$$\Delta E = g_j m_j \mu_\mathrm{B} B, \tag{2.3.19}$$

where $g_j = 1 + \frac{j(j+1)+s(s+1)-l(l+1)}{2j(j+1)}$ is the Landé factor for the spin–orbit coupled electron.

Rydberg atoms in external electric fields

The Hamiltonian describing the interaction of the dipole moment $\vec{d}$ with an electric field aligned on the z-axis is

$$\hat{H}_\mathrm{E} = \hat{d}_z E = qE\hat{z}. \tag{2.3.20}$$

Since in spherical coordinates $z = r\cos\theta$, the matrix element becomes

$$\langle n,l,j,m_j|z|n',l',j',m_j'\rangle = \langle n,l,j|r|n',l',j'\rangle_R \left\langle j,m_j|\cos\theta|j',m_j'\right\rangle_Y, \tag{2.3.21}$$

where the first term is the reduced dipole matrix element and the second term imposes the dipole selection rules. The latter term is identical to the renormalised spherical harmonic

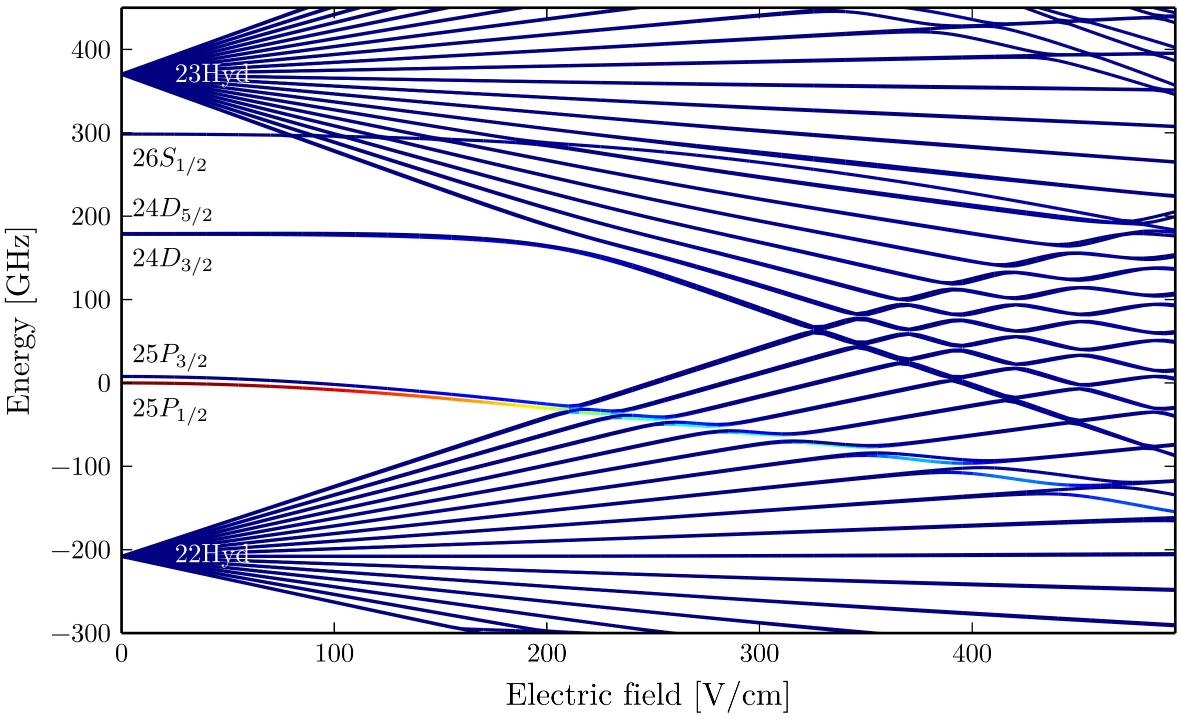

Figure 2.2: Stark map of a rubidium Rydberg atom as a function of an applied external electric field. Only states with $|m_j| = 1/2$ are plotted. Zero energy is set to the $25P_{1/2}$-state. The colour denotes the relative admixture of the $25P_{1/2}$-state to the diagonalised eigenstates (dark blue is no admixture, dark red is maximal admixture). S-, P-, and D-states show the quadratic Stark effect, while the degenerate states in the hydrogenic manifolds show the linear Stark effect.

$C_{1,0}(\theta, \varphi) = \cos\theta$ and its matrix elements can thus be obtained through the Wigner–Eckart theorem [85, eq. 12.213] that for a generic angular momentum with quantum numbers l and m_l is given by

$$\langle l, m| \cos\theta |l', m'\rangle = \delta_{m,m'} \left[\sqrt{\frac{(l+1)^2 - m^2}{4(l+1)^2 - 1}} \delta_{l,l'+1} + \sqrt{\frac{l^2 - m^2}{4l^2 - 1}} \delta_{l,l'-1} \right] . \qquad (2.3.22)$$

Thus, the interaction with the electric field couples states with $\Delta m = 0$ and $\Delta l = \pm 1$. If no other m-coupling terms are present in the Hamiltonian, the Hilbert space can be separated into subspaces in terms of m. As a consequence, m stays a good quantum number even in the presence of the field, while the l-states are mixed. The physical reason is that the presence of the electric field breaks the spherical symmetry of the system and consequently the total angular momentum is no conserved quantity any more. However, there is still a rotational symmetry around the electric field axis (aligned to the z-axis) that keeps the z-projection of the angular momentum a conserved quantity. From this argument, it is clear that the matrix element in eq. (2.3.21) must hold for any angular momentum eigenstates. In particular, this means that also in the spin–orbit coupled basis this expression is valid and l and m are simply replaced by j and m_j.

In order to see the effect of an electric field on a Rydberg atom, we consider $\hat{H}_\mathrm{E}$ as a perturbation of the Rydberg Hamiltonian in eq. (2.3.5). From eq. (2.3.21), one can directly see that in first order perturbation theory the effect of the electric field vanishes for non-degenerate l-states since $l = l'$. In this case, we proceed to second order perturbation theory and obtain the quadratic Stark effect

$$(\Delta E)^{(2)} = -\frac{1}{2}\alpha_m E^2, \tag{2.3.23}$$

where α_m is the static polarisability of the particular $|l, m\rangle$-state and E is the electric field strength. The polarisability depends on the strength of the dipole matrix element between all states in the energetic vicinity. Since the coupling to adjacent states increases rapidly for higher principal quantum number n, the polarisability scales as $\alpha \propto n^7$. Semicassically, this can also be explained by the notion that for higher n the electron gets more and more probability to be far away from the core, where the Coulomb interaction is weak. Therefore, only little field is sufficient to distort the trajectory of the electron and to move the centre of mass of the electron wave function away from the nucleus.

If, on the other hand, all $|l, m\rangle$-states are degenerate, like in the hydrogen atom[2], we still retain an energy shift in first order perturbation theory. In this case, one has to diagonalise $\hat{H}_\mathrm{E}$ in the degenerate subspace and obtains l_max linearly split states for each m. The splitting of the new eigenstates is often referred to as the *Stark splitting.* In alkali atoms, due to the finite quantum defect, the low angular momentum states (mainly S-, P-, D-, and F-states) are energetically separated from the otherwise degenerate manifold of l-states. Therefore, both, the linear and the quadratic Stark effect, can be observed in alkali atoms. By diagonalisation of the Hamiltonian $\hat{H} = \hat{H}_0 + \hat{H}_\mathrm{E}$, the eigenenergies of a Rydberg atom in an external electric field can be obtained. Due to the separation of the Hilbert space, this Hamiltonian can be diagonalised independently for the different m_j states. The Stark map of the $m_j = 1/2$ states for the case of a rubidium Rydberg state is depicted in fig. 2.2. One can clearly see that the non-degenerate S-, P-, and D- states exhibit the quadratic Stark effect, while the degenerate high-l states show the first-order linear Stark splitting. Additionally fig. 2.2 demonstrates the mixing of the l-states. It becomes obvious that, even though the adiabatic $25P_{1/2}$-state undergoes an avoided crossing at $202\,{}^{\mathrm{V}}\!/\mathrm{cm}$ and does not follow the quadratic scaling any more, the $25P_{1/2}$ character jumps from one state to the other and continues following the quadratic behaviour, as it is common for avoided crossings. In the course of crossing the manifold, the $25P_{1/2}$ character distributes more and more to the hydrogenic states and ultimately, for very high fields, the $25P_{1/2}$-state will be equally distributed over all Stark states.

2.3.3. Ionisation of Rydberg atoms

Since Rydberg states are close to the continuum, only little energy is required to ionise them. This renders ionisation an ubiquitous process when dealing with Rydberg atoms. In typical ultracold gas experiments, the most relevant ionisation processes for Rydberg atoms are photoionisation by black-body radiation and lasers, non-elastic collisions with other Rydberg atoms, and associative ionisation in the course of a collision with a ground state atom (fig. 2.3). In the following, we will discuss these processes individually and demonstrate under which conditions they appear.

---

[2] The l-degeneracy is a unique feature of an electron in the Coulomb potential. In general, there is no degeneracy of angular momentum states even in rotationally symmetric potentials.

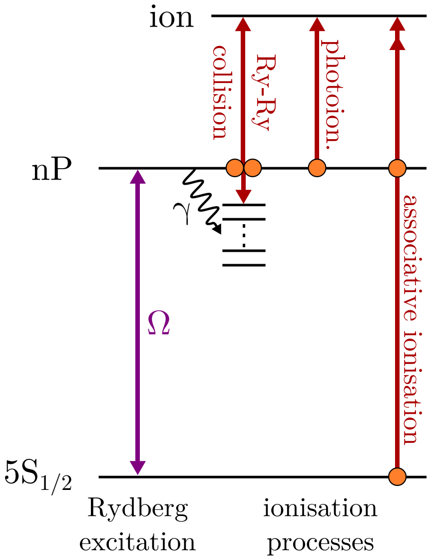

Figure 2.3: Relevant ionisation processes for Rydberg atoms in ultracold gases. As a single particle process, photoionisation by the trapping lasers or black-body radiation only depends on the Rydberg density (orange circle in the Rydberg level) and is ubiquitous in Rydberg systems. If the Rydberg excitation is embedded in a high density of ground state atoms, associative ionisation occurs in the collision between a ground state and a Rydberg atom. This process depends, both, on the ground state and the Rydberg density (orange circle in the Rydberg and the $5S_{1/2}$ level). In the case of a high Rydberg density, also collisions between two Rydberg atoms can ionise either of them. This process depends quadratically on the Rydberg density (two orange circles in the Rydberg level). In addition to these ionisation processes, radiative decay γ into lower-lying states is possible.

Photoionisation

Photoionisation describes the excitation of the bound electron e^- in the Rydberg atom A^* into a continuum state by the photon γ with the energy $h\nu$

$$A^* + \gamma \rightarrow A^+ + e^-. \tag{2.3.24}$$

The excess energy of the photon is converted to kinetic energy of the A^+–e^- system. Since the mass of the ion is much bigger than that of the electron, most of the energy is carried away by the electron. The rate γ_{PI}, at which a Rydberg atom is photoionised by the incident photon, is given by

$$\gamma_{\mathrm{PI}} = \sigma_{\mathrm{PI}} \frac{N_{\mathrm{ph}}}{At} = \sigma_{\mathrm{PI}} \frac{I}{h\nu}, \tag{2.3.25}$$

where $\frac{N_{\mathrm{ph}}}{At}$ is the number of incident photons per time and unit area and I is the corresponding intensity. The photoionisation cross section σ_{PI} depends on the exact Rydberg state and the energy of the photon. In general, the ionisation is most efficient if the photon excites continuum states close to the threshold. Therefore, for a fixed photon energy, higher Rydberg states have a lower photoionisation cross section. P- and D-states also show a much higher photoionisation cross section compared to S-states, due to the $\pi/2$ phase shift between the radial wave functions of the S- and P-states [76, 86].

The main source of photons in our setup are the trap lasers that operate at a wavelength of 1064 nm. Due to the simple relation between the laser intensity and the photoionisation rate in eq. (2.3.24), we can measure the photoionisation cross section for this particular wavelength. A summary of the results is given in sec. A.11. Since the ionisation rate depends on the intensity of the trapping laser, it varies depending on the specific experimental setting. Since the YAG laser's photon energy of 281 THz already reaches far into the continuum for all relevant Rydberg states, an energy difference in the initial state does not significantly change the cross section and consequently we do not see a strong variation in the ionisation rate with the principal quantum number. For all principal quantum numbers studied in this thesis the photoionisation cross section for Rydberg P-states in rubidium is on the order of $10\,\mathrm{kb} = 10^{-6}\,\mathrm{nm}^2$. Compared with the geometric cross section $\sigma_{\mathrm{geo},60P} = 3 \times 10^5\,\mathrm{nm}^2$ of a Rydberg atom in the $60P_{3/2}$-state, this is eleven orders of magnitude smaller. This illustrates that the vast majority of the trapping laser photons just passes the Rydberg atom without ionising it and the fact that we nevertheless see photoionisation by the trapping light is caused by the immense number of photons incident to the Rydberg atom.

A second source of photoionisation arises because our experimental apparatus is not cooled to cryogenic temperatures and thus the atoms are always subject to the black-body spectrum emitted at 300 K. For this temperature, according to Wien's displacement law, the black-body spectrum peaks at 17.6 THz, which is close to the typical energy gap between the studied Rydberg states and the continuum. In combination with the n-dependence of the photoionisation cross section, this leads to a maximum in the ionisation rate at $n = 27$, which is roughly 300 Hz [87].

Rydberg–Rydberg collisions

As will be shown in sec. 2.5, there is a strong interaction between Rydberg atoms. Depending on the chosen Rydberg state, these interactions can be repulsive as well as attractive. An attractive interaction will eventually lead to a collision of the two Rydberg atoms A^{**} during which energy can be exchanged among them. This gives rise to the process

$$A^{**} + A^{**} \to A^{*} + A^{+} + e^{-}, \tag{2.3.26}$$

where one Rydberg atom is ionised and the other one is transferred into a lower-lying excited state A^{*}. This process is a special case of the so-called Penning-ionisation [76], where both atoms are in a Rydberg state. Since this process depends quadratically on the number of Rydberg atoms present in the system, it becomes important in the regime of high excitation densities. This quadratic dependency on the excitation density, and in turn on the driving strength, allows to identify this process experimentally. However, for the experiments discussed in this thesis, the excitation densities were usually low and Rydberg–Rydberg collisions play no major role. We refer to refs. [88, 89] for a detailed discussion on this process.

Associative ionisation

Since the collisional energy in ultracold clouds is on the order of 10 kHz, Rydberg atoms with a binding energy of several THz cannot be ionised by impact ionisation. A ground state atom also does not carry any internal energy and consequently one would not expect any ionisation channel in a Rydberg–ground state collision. However, associative ionisation constitutes a collisional process where a Rydberg atom A^{*} collides with a ground state atom A to form a molecular ion and a free electron

$$A^{*} + A \to A_2^{+} + e^{-}. \tag{2.3.27}$$

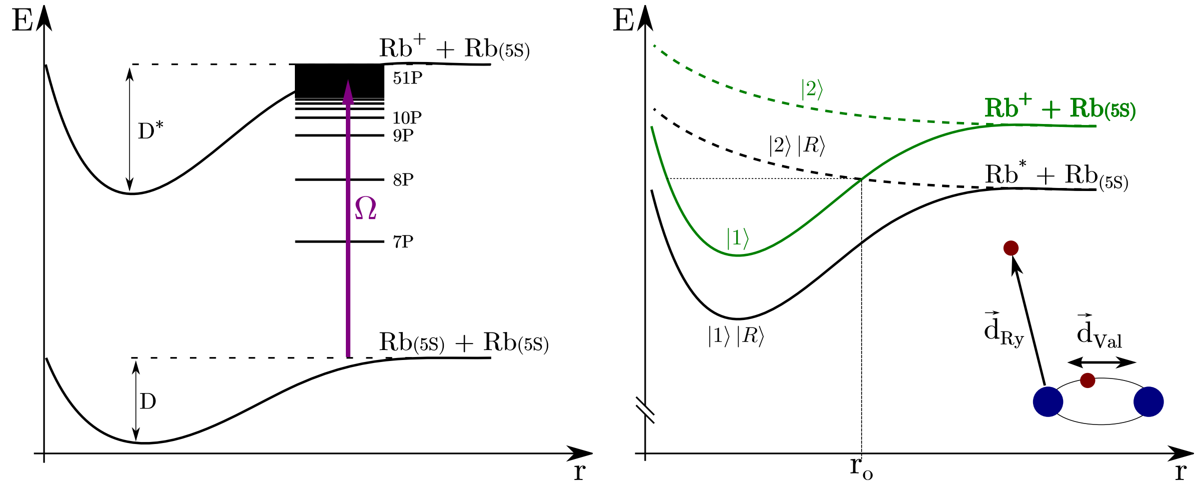

(a) **(b)**

Figure 2.4: Associative Ionisation. (a) In ^{87}Rb, associative ionisation is energetically possible for all Rydberg states with $n \geq 8$. (b) Potential energy curves of the ground state $|1\rangle$ (solid green line) and the first electronically excited state $|2\rangle$ (dashed green line) of the ground state atom–Rydberg core system $\mathrm{Rb}^+ + \mathrm{Rb}_{(5\mathrm{S})} = \mathrm{Rb}_2^+$. When the Rydberg electron is still bound to the Rb^+ ion in the Rydberg state $|R\rangle$, the same molecular potential structure arises for the ground state atom–Rydberg core system (black). Through the dipole resonant mechanism (inset), the binding energy of the formed molecule is transferred to the Rydberg electron by the coupling of the two dipoles. The highest probability for this process is found at r_o where the binding energy of the molecule equals that of the Rydberg electron. This point equals the classical outer turning point of the formed molecule.

This process is sometimes also referred to as Hornbeck–Molnar ionisation and differs significantly from impact ionisation since the energy required to excite the electron into the continuum state is taken from the bond energy of the formed Rb_2^+ ion rather than from the kinetic energy of the collision partners. ”Ignoring the translational kinetic energy of the collision partners, associative ionization is in fact the only way in which a collision with a ground state atom can ionize a Rydberg atom” [76]. Since energy must be conserved, this process can only occur as long as the energy of the $A^* + A$ state is higher than the lowest energy state of the formed A_2^+ dimer. As depicted in fig. 2.4a, in rubidium all Rydberg states above and including $n = 8$ can undergo associative ionisation since the molecular potential of Rb_2^+ has a well depth of 174.1 THz (0.72 eV) [11]. For low-lying Rydberg states, associative ionisation has been studied extensively in vapour cell experiments in the 1980s [11–13] but due to the high thermal energies in these experiments, impact ionisation imposed restrictions on the highest achievable Rydberg state. In sec. 4, we extend the study of associative ionisation to the ultracold regime, where we overcome these restrictions and discover a giant increase in the associative ionisation cross section due to a directed mass transport mechanism mediated by the Rydberg electron.

The associative ionisation process can be understood in terms of the *dipole resonance mechanism* (DRM) [90, 91]. In this model, we consider the electronic potentials of the molecule formed by the Rydberg core and the ground state atom $\mathrm{Rb}^+ + \mathrm{Rb}_{(5\mathrm{S})} = \mathrm{Rb}_2^+$, as they are depicted in fig. 2.4b. This molecule can either be in the electronic ground state $|1\rangle$ or in the first excited state $|2\rangle$. Also in the case of a Rydberg atom in the Rydberg state $|R\rangle$, an approaching ground state atom and the Rydberg core will form a Rb_2^+ molecular system. Since the Rydberg electron is highly delocalised, it will only

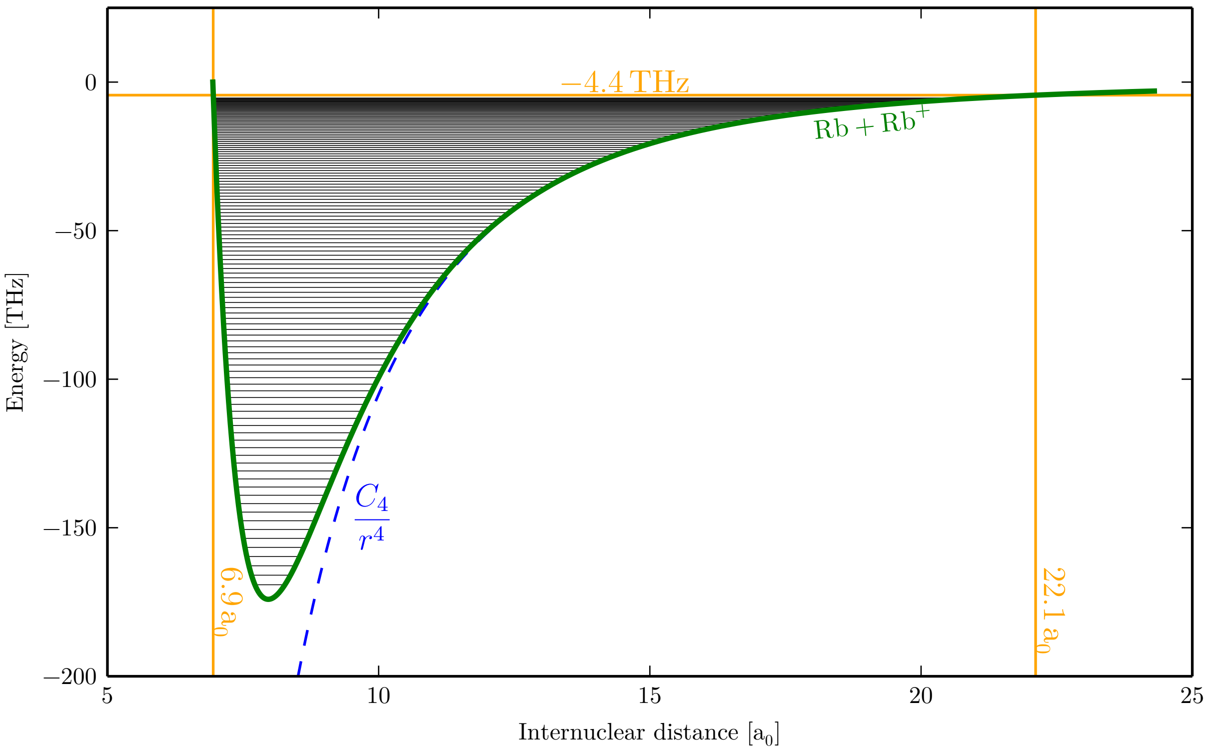

Figure 2.5: Lennard-Jones type potential to model the molecular potential of Rb_2^+ (solid green) with vibrational bound state energies (black lines) determined by the shooting method (see sec. A.8). For large internuclear separations, the potential tends to the C_4/r^4 polarisation potential (dashed blue). When the molecule is formed in the associative ionisation process the bond energy equals the bond energy of the former Rydberg atom. For the bond energy of $E_{\mathrm{bond}} = 4.4\,\mathrm{THz}$ imposed by the $30P$-state (horizontal orange line), highly excited vibrational states with classical inner and outer turning points of $r_i = 6.9\,\mathrm{a}_0$ and $r_o = 22.1\,\mathrm{a}_0$ (vertical orange lines) are most likely to be populated.

slightly change the molecular potentials compared to the ionised case. In this case the state of the Rydberg electron and the molecular state of the atom–Rydberg core system have to be taken into account. The state of the system is thus described by $|1\rangle\,|R\rangle$ for the molecular ground state and by $|2\rangle\,|R\rangle$ for the molecular excited state.

The DRM model further relies on the fact that for small internuclear separation r the ground state atom's valence electron can tunnel to the Rydberg core and can thus not be solely attributed to the ground state atom. Indeed, the electron starts to tunnel back and forth between the two cores and, due to its charge, creates the oscillating dipole $\vec{d}_{\mathrm{Val}}$ (inset fig. 2.4b). The oscillation frequency depends on the height of the tunnel barrier and thus on the internuclear separation. Of course, the dipole moment created by the Rydberg electron $\vec{d}_{\mathrm{Ry}}$ interacts with the oscillating dipole of the shared valence electron. At the internuclear distance r_0 (fig. 2.4b) the oscillation frequency of the valence electron becomes equal to the transition frequency of the Rydberg electron into the lowest continuum states and through the dipole–dipole coupling the energy is transferred to the Rydberg electron. In the potential picture of fig. 2.4b, this implies that, due to the dipole–dipole coupling, the crossing between the $|2\rangle\,|R\rangle$ potential and the $|1\rangle$ potential becomes an avoided crossing and a particle entering on the former can adiabatically cross into a bound state of the Rb_2^+ molecule. While the transition can also occur beyond the crossing point due to the infinite amount of continuum states for higher energies, it seems likely that in analogy to

Table 2.1: Binding energies $E - E_{\mathrm{thr}}$ for some exemplary nP Rydberg states and the classical inner (outer) turning point r_{i} (r_{o}) for the respective energy inside the modelled Rb_2^+ molecular potential. From the outer turning point, the geometric cross section $\sigma_{\mathrm{geo}} = \pi r_o^2$ is calculated.

n	$E - E_{\mathrm{thr}}$ [meV]	r_{i} [$\mathrm{a_0}$]	r_{o} [$\mathrm{a_0}$]	σ_{geo} [$10^{-18}\,\mathrm{m}^2$]
30	-18.18	6.94	22.09	4.3
51	-5.82	6.94	29.38	7.6
99	-1.47	6.94	41.45	15.1

photoionisation the coupling to the continuum is the strongest close to the threshold and thus the DRM is most effective at the crossing point.

In order to get an estimate on the size of the formed Rb_2^+ dimers and thus on the geometrical cross section of the ionisation process, we need to model the dimer's molecular potential. A good starting point is a Lennard-Jones potential that is modified to take into account that the dominant binding force between the Rb^+ ion and the neutral Rb ground state atom is a $1/r^4$ interaction rather than the $1/r^6$ van-der-Waals interaction of two neutral atoms. Nevertheless, the $1/r^{12}$ term in the Lennard-Jones potential should still adequately model the Pauli repulsion. Thus, a reasonable model potential has the form

$$V(r) = \frac{D^*}{2}\left(\left(\frac{r_{\mathrm{m}}}{r}\right)^{12} - 3\left(\frac{r_{\mathrm{m}}}{r}\right)^{4}\right), \tag{2.3.28}$$

where $D^* = 174.1\,\mathrm{THz}$ [11] is the well depth and r_{m} is the internuclear distance of minimal energy. For large separations of the nuclei, the potential has to recover the C_4/r^4 behaviour that arises from the neutral ground state atom being polarised by the electric field of the Rb^+ ion. How the C_4 coefficient can be obtained from the polarisability α_0 is explained in sec. 2.3.1 in a slightly different context. For the neutral atom the polarisability is $\alpha_0 = 0.0794\,\mathrm{Hz}/(\mathrm{V/cm})^2$ [92]. In the limit $r \to \infty$, the $1/r^{12}$ term in the potential vanishes and we can therefore identify the following relation between r_{m} and C_4:

$$V(r \to \infty) = -\frac{3D^* r_{\mathrm{m}}^4}{2r^4} = -\frac{C_4}{r^4} \Rightarrow r_{\mathrm{m}} = \sqrt[4]{\frac{2C_4}{3D^*}}. \tag{2.3.29}$$

With the values for D^* and r_{m} the molecular potential is fully determined and can be plotted, as shown in fig. 2.5.

When exciting Rydberg states with $n = 30$, the system is 4.4 THz below the dissociation threshold, which is also the energy at which the Rb_2^+ molecule is most likely created through the DRM. The molecule is thus created in high-lying vibrational states, as indicated by the bound state energies in fig. 2.5. Since a model potential is at hand, we can deduce the classical turning points of the vibrational state to get an estimate on the size of the formed molecule. The energy, at which the molecule is created, and the corresponding turning points are indicated in fig. 2.5. A summary of the turning points obtained this way and the corresponding geometrical cross sections for different initial Rydberg states is given in tab. 2.1.

The cross sections obtained from these simple theoretical considerations are in agreement with the ones observed in experiments with Na beams [93]. Here, the rate constant [94]

$$k = \langle \sigma(v) \cdot v \rangle_{v_{\mathrm{th}}} \tag{2.3.30}$$

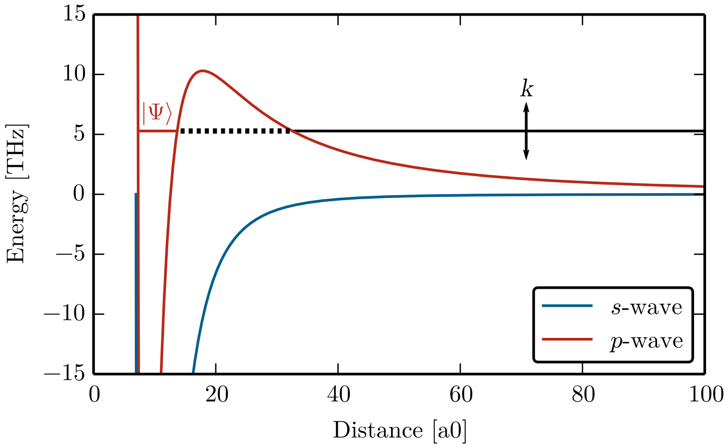

Figure 2.6: Shape resonance in the p-wave scattering for the C_4 potential shown in fig. 2.5. In contrast to the s-wave potential (blue), the p-wave potential (red) has a centrifugal barrier that allows for meta-stable bound states. If the incident wave of wave vector k is resonant to the bound state $|\Psi\rangle$, the scattering is resonantly enhanced and the cross section increases. In a classical picture the particle gets trapped in the potential for a short time and eventually leaves it again.

was determined rather than the cross section. While the involved averaging over the different thermal velocities in the atom beam in general does not allow to extract the cross section alone, an estimate for its order of magnitude can be found by assuming the beam to be monoenergetic with the most probable thermal velocity. For the studied Na beam at a temperature of $600\,\mathrm{K} \equiv 50\,\mathrm{meV} \equiv 12\,\mathrm{THz}$, this amounts to $v_\mathrm{prob} = \sqrt{\frac{2k_BT}{m}} = 658.6\,{}^\mathrm{m}/_\mathrm{s}$. The observed maximum rate constant for associative ionisation of $k = 3 \cdot 10^{-9}\,{}^{\mathrm{cm}^3}/_\mathrm{s}$ can thus be used to calculate a cross section of $\sigma = \frac{k}{v_\mathrm{prob}} = 4.6 \times 10^{-18}\,\mathrm{m}^2$, which matches the order of magnitude of the geometric cross section of the molecules, as shown in tab. 2.1.

2.4. Rydberg–ground state interaction

Rydberg atoms excited from an atomic ensemble are always subject to interaction with surrounding ground state atoms (perturbers). In this section, we discuss the Rydberg–ground state interaction, after separating the nuclear degrees of freedom, in terms of scattering of the quasi free electron with the perturber. Since the Rydberg electron carries a small momentum in the shallow outer parts of the Coulomb potential and since the thermal velocities in ultracold gases are small, we are exclusively concerned with low energy scattering of the electron from the perturber. It is therefore useful to restrict the discussion only to the lowest partial wave of the interaction.

However, a peculiar situation can arise due to the centrifugal barrier present for higher partial waves. As depicted in fig. 2.6, there can be meta-stable states at positive energy that are bound by the centrifugal barrier. If the incident particle energy is identical to the energy of the bound state, the corresponding matter wave couples resonantly to the bound state and consequently acquires a strong phase shift. Such situation is usually called a *shape resonance* since it is characterised by a resonance in the scattering cross section as a function of the incident particle's energy.

Also the scattering between a rubidium atom and an electron shows a shape resonance

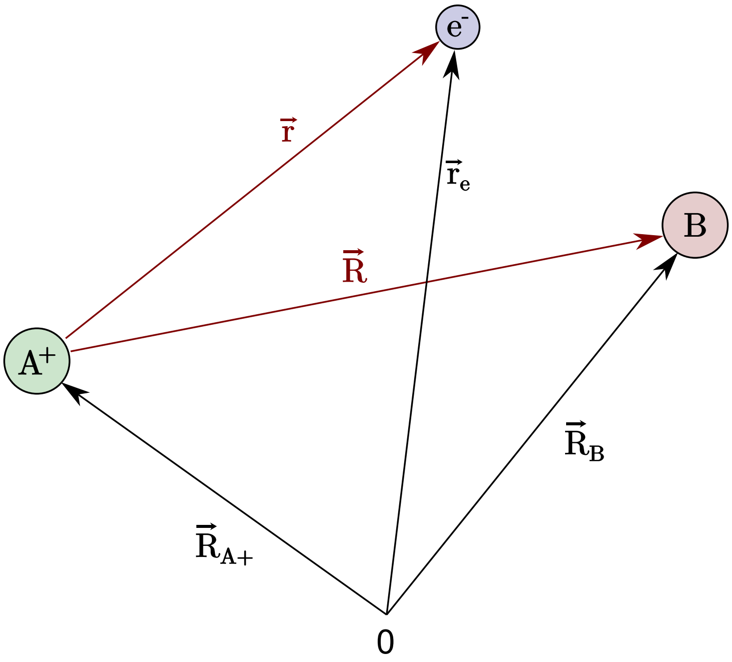

Figure 2.7: Definition of the position vectors to the Rydberg core A^+, the perturber atom B, and the Rydberg electron e^- for an arbitrary position of the origin (black) and for the origin centred on the Rydberg core (red).

in the p-wave at an incident k-vector of $k = 0.058\,\text{a.u.}$ [95]. In order not to miss important parts of the scattering physics, we thus have to take into account the p-wave scattering in the modelling of the Rydberg–ground state interaction [47]. Hence, we follow the derivation of Omont [96] to obtain a generalised expression for the interaction that also includes higher partial waves. The new eigenenergies resulting from a diagonalisation of the interaction operator show a rich potential landscape that not only strongly influences the scattering properties of Rydberg–ground state collisions, but also gives rise to vibrational bound states of the nuclei, which are called *Rydberg molecules*. Depending on the mixing states and the dominant scattering channel, these molecules can be further subdivided into ultralong-range Rydberg molecules, butterfly molecules, and trilobite molecules. Due to the interaction with the ground state atom, these molecules show a rich angular momentum coupling that inculdes the nuclear spin of the perturber. Ultimately, we are able to calculate vibrational bound states in the diagonalised potentials and thus to predict their energies and wave functions.

Description of the system

Obviously, the low-energy scattering between two atoms can be considered a two-body problem. However, if one of the atoms is in a Rydberg state the electron cloud is orders of magnitude bigger than the size of the second ground state atom. When the ground state atom enters the electron cloud, the two-body description breaks down and one has to consider it as a three-body problem. We are therefore interested in an electron e at position $\vec{r}_e$ interacting with the charge distributions of the Rydberg core A^+ at position

$\vec{R}_{A^+}$ and the ground state atom B[3] at position $\vec{R}_B$ (fig. 2.7). In general, the inner electrons of the A^+ ion and the atom B lead to higher order multipole moments in the electrostatic interaction. To simplify the problem, the following discussion is restricted to the first two orders of the multipole expansion of the charge distributions. Since neither of the three considered particles possesses a permanent dipole moment, the Rydberg core and the ground state atom are described as polarisable monopoles and the electron as an unpolarisable point charge. In this approximation the system Hamiltonian reads

$$\begin{aligned}\hat{H} = &-\frac{\hbar^2}{2m_{\mathrm{A}^+}}\Delta_{\mathrm{A}^+} - \frac{\hbar^2}{2m_{\mathrm{B}}}\Delta_{\mathrm{B}} - \frac{\hbar^2}{2m_{\mathrm{e}}}\Delta_{\mathrm{e}} \\ &+ \hat{V}_{\mathrm{A}^+}(\vec{r}_e - \vec{R}_{A^+}) + \hat{V}_B(\vec{r}_e - \vec{R}_B) + \hat{V}_{\mathrm{pol}}(\vec{r}_e, \vec{R}_{A^+}, \vec{R}_B),\end{aligned} \tag{2.4.1}$$

where the first three terms correspond to the kinetic energy of the three particles. Furthermore, $\hat{V}_{\mathrm{A}^+}(\vec{r}_e - \vec{R}_{A^+})$ describes the interaction of the electron with the ionic core. This includes the usual Coulomb interaction and additionally the polarisation of the core by the electron, which leads to the quantum defects. Additionally, $\hat{V}_{\mathrm{B}}(\vec{r}_e - \vec{R}_B)$ denotes the interaction of the electron with the ground state perturber B. The term $\hat{V}_{\mathrm{pol}}(\vec{r}_e, \vec{R}_{A^+}, \vec{R}_B)$ describes the direct and indirect polarisation interactions arising through the Coulomb field of A^+ and the electron and is later discussed in more detail. If we assume that the internuclear motion is slow compared to the electronic motion, the electron cloud will instantaneously adapt to a changed nuclear position. In this so-called Born–Oppenheimer approximation the full wave function Ψ_{M} is separable into a nuclear part $\Phi(\vec{R}_{A^+}, \vec{R}_B)$ that only depends on the nuclear positions and an electronic part $\Psi_{\vec{R}_{A^+},\vec{R}_B}(\vec{r}_e)$ that depends on the electron's position and parametrically on the nuclear positions

$$\Psi_{\mathrm{M}} = \Phi(\vec{R}_{A^+}, \vec{R}_B)\Psi_{\vec{R}_{A^+},\vec{R}_B}(\vec{r}_e). \tag{2.4.2}$$

Inserting the ansatz (2.4.2) into the time independent Schrödinger equation with the Hamiltonian (2.4.1) leads to two coupled Schrödinger equations, one for the electron and one for the nuclei:

$$\left[-\frac{\hbar^2}{2m_{\mathrm{e}}}\Delta_{\mathrm{e}} + \hat{V}_{\mathrm{A}^+}(\vec{r}_e - \vec{R}_{A^+}) + \hat{V}_B(\vec{r}_e - \vec{R}_B) + \hat{V}_{\mathrm{pol}}(\vec{r}_e, \vec{R}_{A^+}, \vec{R}_B) - E_{\mathrm{pot}}\right]\Psi_{\vec{R}_{A^+},\vec{R}_B}(\vec{r}_e) = 0, \tag{2.4.3}$$

$$\left[-\frac{\hbar^2}{2m_{\mathrm{A}^+}}\Delta_{A^+} - \frac{\hbar}{2m_B}\Delta_B - (E - E_{\mathrm{pot}})\right]\Phi(\vec{R}_{A^+}, \vec{R}_B) = 0. \tag{2.4.4}$$

Here, E is the total energy of the state and the separation constant E_{pot} is the energy of the electronic configuration. As the electronic wave function parametrically depends on the nuclear positions, the energy $E_{\mathrm{pot}} \equiv E_{\mathrm{pot}}(\vec{R}_{A^+}, \vec{R}_B)$ also depends on their position. Since the physics does not depend on the choice of the coordinate system, we can transform the electronic Schrödinger equation in a coordinate system fixed at the position of A^+

---

[3] It may be noted that already at this point we introduced an asymmetry in our system since we describe the system as one electron with a neutral particle and an ionic core rather than two electrons with two ionic cores.

(fig. 2.7) and the nuclear equation to the centre of mass frame with $M = \frac{m_{A^+} m_B}{m_{A^+} + m_B}$. With $\vec{R} = \vec{R}_B - \vec{R}_{A^+}$ and $\vec{r} = \vec{r}_e - \vec{R}_{A^+}$, we obtain

$$\left[-\frac{\hbar^2}{2m_\mathrm{e}} \Delta_\mathrm{e} + \hat{V}_{\mathrm{A}^+}(\vec{r}) + \hat{V}_\mathrm{B}(\vec{r} - \vec{R}) + \hat{V}_\mathrm{pol}(\hat{\vec{r}}, \vec{R}) - E_\mathrm{pot}(R) \right] \Psi_{\vec{R}}(\vec{r}) = 0, \tag{2.4.5}$$

$$\left[-\frac{\hbar^2}{2M} \Delta - (E - E_\mathrm{pot}(R)) \right] \Phi(\vec{R}) = 0. \tag{2.4.6}$$

The structure of these equations is identical to the ones obtained for conventional molecules, as can be found in most textbooks on molecular physics [77]. In particular, the equation for the nuclear degree of freedom (2.4.6) does not differ from that of conventional molecules. This implies that the known concepts of rotation and vibration of diatomic molecules can also be applied to Rydberg molecules. If the electronic adiabatic potential $E_\mathrm{pot}(R)$ supports bound states, the corresponding overall state $|\Psi_M\rangle$ is called a *Rydberg molecule*. Significant differences compared to conventional molecules arise in the electronic Schrödinger equation (2.4.5) due to the negligible exchange energy of the electrons in the Rydberg system. Since the typical nuclear separation in a Rydberg molecule is on the order of $1000\,\mathrm{a}_0$, the valence electron of the ground state atom B is highly unlikely to tunnel to the Rydberg core A^+. Unlike in conventional homonuclear molecules it is thus possible to distinguish both electrons [51]. In essence, this is the major difference between a Rydberg molecule and a conventional molecule.

From eq. (2.4.6) we can see that the nuclear motion is restricted by the potential arising from the R-dependent eigenenergies $E_\mathrm{pot}(R)$ of the electronic wave function. We are therefore especially interested in potential wells that can support bound states, as those correspond to vibrational states of Rydberg molecules. In the following, we will thus solve the electronic problem to determine $E_\mathrm{pot}(R)$ and then insert it into the nuclear problem to obtain the vibrational bound states of the Rydberg molecule (sec. 2.4.8).

The electronic Hamiltonian

After separating the nuclear motion, we can now focus on the solution of the electronic Schrödinger equation for a fixed nuclear position. From eq. (2.4.5) we can see that the electronic Hamiltonian $\hat{H}$ is given by

$$\hat{H}(\vec{R}) = \hat{H}_0 + \hat{V}_\mathrm{B}(\hat{\vec{r}} - \vec{R}) + \hat{V}_\mathrm{pol}(\hat{\vec{r}}, \vec{R}), \tag{2.4.7}$$

where $\hat{H}_0 = -\frac{\hbar^2}{2m_\mathrm{e}} \Delta_\mathrm{e} + \hat{V}_{\mathrm{A}^+}(\vec{r})$ is the Hamiltonian of the unperturbed Rydberg atom from eq. (2.3.5). This expression is identical to the one given in ref. [97] and describes an electron in the combined potential of the neutral atom B and the Rydberg core A^+. In addition to the direct e^--B interaction $\hat{V}_B$, also induced interactions appear because we describe the system up to the second order of the multipole expansion. These interactions are summarised in the polarisation potential V_pol, which is defined by

$$\hat{V}_\mathrm{pol}(\vec{r}, \vec{R}) = -\frac{\alpha_d}{|\hat{\vec{r}} - \vec{R}|^2 R^2} \left[\frac{(\hat{\vec{r}} - \vec{R})}{|\hat{\vec{r}} - \vec{R}|} \cdot \frac{\vec{R}}{R} \right] - \frac{\alpha_d}{2R^4}. \tag{2.4.8}$$

The first term describes the interaction of the electron with the perturber B due to the polarisation through A^+ as well as the interaction of A^+ with the perturber due to polarisation through the electron. Furthermore, the interaction due to the polarisation of the perturber B through the Coulomb field of A^+ is taken into account by the second term[4]. As the latter interaction only depends on the internuclear distance R and not on the electron's position, it adds as a scalar to the Hamiltonian and is thus a simple offset for the eigenenergies. Since the polarisation interaction vanishes for $R \to \infty$ but the scattering potential $V_\mathrm{B}(\hat{\vec{r}} - \vec{R})$ only depends on the relative electron–perturber distance and not on the internuclear distance, the polarisation interaction dominates the energy of the system only for very small internuclear distances. As this discussion is targeted towards the behaviour of the system far from the Rydberg core, we will neglect the polarisation terms in the following but refer to ref. [97] for a full treatment including the polarisation interaction. Without the polarisation terms, the Hamiltonian of the system reads

$$\hat{H}(\vec{R}) = \hat{H}_0 + \hat{V}_\mathrm{B}(\hat{\vec{r}} - \vec{R}) \tag{2.4.9}$$

and, according to eq. (2.2.3), the resolvent of the system is defined by

$$\hat{G}(\vec{R}) = \frac{1}{E - \hat{H}(\vec{R})} = \frac{1}{E - \hat{H}_0 - \hat{V}_\mathrm{B}(\hat{\vec{r}} - \vec{R})}. \tag{2.4.10}$$

2.4.1. Pseudopotential approach

Since the explicit form of the scattering potential $V_\mathrm{B}(\hat{\vec{r}} - \vec{R})$ is not trivial, our goal is to replace the actual potential by a δ-type pseudopotential $V_\mathrm{sc}(\vec{R})$ that reproduces the phase shift of the wave function outside of the potential $V_\mathrm{B}(\hat{\vec{r}} - \vec{R})$. This approach can be made only if "outside of the potential" is meaningful, i.e. if the potential $V_\mathrm{B}(\hat{\vec{r}} - \vec{R})$ is of finite range[5]. This assumption is well justified for a perturber atom in the atomic ground state. Due to its almost point-like dimension compared with the size of the Rydberg atom, the Rydberg electron only sees the vanishing monopole moment of the perturber's nucleus shielded by its electrons. Only upon close approach, the Rydberg electron probes the higher order multipole moments of the perturbers charge distribution and the electron–perturber interaction becomes important. On the one hand, this local interaction is strong at the position of the perturber but, on the other hand, it leaves the electron unperturbed in most of the volume it occupies. Thus, the perturbation is weak and strong at the same time, which renders a classical perturbation approach useless. Instead, as pointed out by Omont [96], it is useful to expand the problem in terms of the reaction matrix K. Following Omont's derivation, we consider the electron in a Rydberg state with energy E that can also be seen as a quasi-free electron, whose kinetic energy is given by

$$\hat{T}_e = E - \hat{V}_{\mathrm{A}^+}. \tag{2.4.11}$$

The scattering of such a (quasi)-free electron with the potential V_B is described by the K-matrix[6], which is defined by the integral equation

$$\hat{K}_{\vec{R}} = \hat{V}_\mathrm{B}(1 + \hat{G}^0_{0,\vec{R}} \hat{K}_{\vec{R}}) = \sum_{n=0}^{\infty} \hat{V}_\mathrm{B}(\hat{G}^0_{0,\vec{R}} \hat{V}_\mathrm{B})^n. \tag{2.4.12}$$

---

[4] The polarisation interaction between a charged and a neutral particle leads to a $1/r^4$-interaction, as shown in eq. (2.3.7).

[5] Any potential tending faster to zero than r^{-2} is considered finite range.

[6] In order to point out that the reference frame for the K-matrix is centred at $\vec{R}$, we denote it $\hat{K}_{\vec{R}}$

Here, $\hat{G}^0_{0,\vec{R}} = (E - \hat{T}_e)^{-1}$ is the resolvent for the quasi-free electron, which carries only the kinetic energy $\hat{T}_e$. Note that in order to describe the strong but localised interaction with the perturber, we changed the perspective here: Rather than describing a strong interaction localised at $\vec{R}$, we changed to a description where an electron with an $\vec{R}$-dependent energy is scattered from a potential that is fixed in space. The connection between both descriptions is drawn by the expansion of the system resolvent $\hat{G}$ from eq. (2.4.10) in terms of the K-matrix [96] by

$$\hat{G}(\vec{R}) = \hat{G}_0 + \hat{G}_0 \hat{K}_{\vec{R}} \sum_{n=0}^{\infty} \left\{ (\hat{G}_0 - \hat{G}^0_{0,\vec{R}}) \hat{K}_{\vec{R}} \right\}^n \hat{G}_0, \tag{2.4.13}$$

where $\hat{G}_0 = (E - \hat{H}_0)^{-1}$ is the resolvent of the unperturbed Rydberg atom. If one considers only a small range of energy $\Delta E \ll E_{\mathrm{Ry}}$ around the Rydberg state with energy E_{Ry} and, furthermore, assumes that in this small energy range the kinetic energy of the Rydberg electron $T_e(R)$ is approximately the same for all states, the terms containing $\hat{G}^0_{0,\vec{R}}$ can be neglected and we obtain[7]

$$\hat{G}(\vec{R}) = \sum_{n=0}^{\infty} \left\{ \hat{G}_0 \hat{K}_{\vec{R}} \right\}^n \hat{G}_0 = \frac{1}{E - \hat{H}_0 - \hat{K}_{\vec{R}}}, \tag{2.4.14}$$

where in the last step we identified the expansion of $\hat{G}_0$ for a perturbation given by the K-matrix (see sec. 2.2.1). By comparing eq. (2.4.10) and eq. (2.4.14), we obtain

$$\hat{H}(\vec{R}) = \hat{H}_0 + \hat{V}_{\mathrm{sc}}(\vec{R}), \tag{2.4.15}$$

where we used the notation $\hat{V}_{\mathrm{sc}}(\vec{R}) \equiv \hat{K}_{\vec{R}}$ for the K-matrix to emphasise that it takes the role of a *pseudopotential* that describes the scattering between the Rydberg electron and the perturber.

In order to calculate the eigenenergies of the system, it is useful to know the matrix elements of the K-matrix in the eigenbasis of $\hat{H}_0$. Care must be taken at this point since the frame of reference for the K-matrix $\hat{K}_{\vec{R}}$ is centred at $\vec{R}$ while the spatial wave functions $\Psi_i(\vec{r})$ are centred at the origin. This can be taken into account by translating the K-matrix through the unitary translation operator $\hat{U}(\vec{R})$ [98] with $\hat{U}(\vec{R}) \left|\vec{r}\right\rangle = \left|\vec{r} + \vec{R}\right\rangle$, which leads to $\hat{V}_{\mathrm{sc}}(\vec{R}) \equiv \hat{K}_{\vec{R}} = \hat{U}(\vec{R}) \hat{K} \hat{U}^\dagger(\vec{R})$. Applying the translation operator, inserting unity in terms of the momentum eigenstates before and after the K-matrix, and implying atomic units, one can see that

$$\begin{aligned} \left\langle \Psi_j \right| \hat{V}_{\mathrm{sc}}(\vec{R}) \left| \Psi_i \right\rangle &= \left\langle \Psi_j \right| \hat{U}(\vec{R}) \hat{K} \hat{U}^\dagger(\vec{R}) \left| \Psi_i \right\rangle & (2.4.16) \\ &= \int \mathrm{d}\vec{k}\mathrm{d}\vec{k'} \left\langle \Psi_j | \hat{U}(\vec{R}) | \vec{k'} \right\rangle \left\langle \vec{k'} \right| \hat{K} \left| \vec{k} \right\rangle \left\langle \vec{k} | \hat{U}^\dagger(\vec{R}) | \Psi_i \right\rangle. & (2.4.17) \end{aligned}$$

The appearing projections of the translated wave functions $\langle \Psi_j | \hat{U}(\vec{R}) | \vec{k'} \rangle$ and $\langle \vec{k} | \hat{U}^\dagger(\vec{R}) | \Psi_i \rangle$ on the wave vector basis are obtained by inserting unity in terms of the position projector $\left|\vec{r}\right\rangle \left\langle \vec{r}\right|$

$$\begin{aligned} \langle \vec{k} | \hat{U}^\dagger(\vec{R}) | \Psi \rangle &= \int \mathrm{d}\vec{r'} \langle \vec{k} | \vec{r'} \rangle \langle \vec{r'} | \hat{U}^\dagger(\vec{R}) | \Psi \rangle = \int \mathrm{d}\vec{r'} \langle \vec{k} | \vec{r'} \rangle \langle \vec{r'} + \vec{R} | \Psi \rangle \\ &= \frac{1}{(\sqrt{2\pi})^3} \int \mathrm{d}\vec{r} \, e^{-i\vec{k} \cdot \vec{r'}} \Psi(\vec{r'} + \vec{R}). \end{aligned} \tag{2.4.18}$$

---

[7] The constant term $\hat{G}_0$ seams to disappear because the index n of the sum is shifted by one and thus the constant term is absorbed into the sum.

In the second step we applied the translation operator to the left and in the last step we inserted the projection of the position eigenstate on the momentum basis $\langle \vec{k}|\vec{r'}\rangle = \frac{1}{(\sqrt{2\pi})^3} e^{-i\vec{k}\cdot\vec{r'}}$ [99] and switched to the space representation of the state $|\Psi\rangle$. Since the appearing integral runs over the whole space, we can apply the coordinate shift $\vec{r} = \vec{r'} + \vec{R}$ and obtain

$$\langle \vec{k}|\hat{U}^\dagger(\vec{R})|\Psi\rangle = \frac{1}{(\sqrt{2\pi})^3} \int \mathrm{d}\vec{r}\; e^{-i\vec{k}\cdot(\vec{r}-\vec{R})}\Psi(\vec{r}). \tag{2.4.19}$$

Thus the K-matrix element becomes

$$\langle \Psi_j|\, \hat{V}_{\mathrm{sc}}(\vec{R})\, |\Psi_i\rangle = \frac{1}{(2\pi)^3} \int \mathrm{d}\vec{k}\mathrm{d}\vec{k'}\mathrm{d}\vec{r}\mathrm{d}\vec{r'}\; \langle \vec{k'}|\, \hat{K}\, |\vec{k}\rangle\, e^{-i\vec{k}\cdot(\vec{r}-\vec{R})+i\vec{k'}\cdot(\vec{r'}-\vec{R})}\Psi_j^*(\vec{r'})\Psi_i(\vec{r}). \tag{2.4.20}$$

Since the scattering potential is of finite range, only values of $\vec{r}$ and $\vec{r'}$ close to $\vec{R}$ will contribute to the integral. Furthermore, the wave vector of the electron is almost constant in the vicinity of $\vec{R}$ and its magnitude is given by $k_R = \sqrt{2(E - V_{\mathrm{A}^+})}$. The K-matrix element can therefore be considered constant and can be drawn out of the k-integrals. Identifying the definition of the three-dimensional Dirac delta function $\delta^{(3)}(\vec{r} - \vec{R}) = \frac{1}{(2\pi)^3}\int \mathrm{d}\vec{k}\; e^{-i\vec{k}(\vec{r}-\vec{R})}$, we can write in *zero-range approximation*

$$\begin{aligned}\langle \Psi_j|\, \hat{V}_{\mathrm{sc}}(\vec{R})\, |\Psi_i\rangle &= \int \mathrm{d}\vec{r}\mathrm{d}\vec{r'}\; \langle \vec{k'}_{\mathrm{R}}|\, \hat{K}\, |\vec{k}_{\mathrm{R}}\rangle\, \delta^{(3)}(\vec{r}-\vec{R})\delta^{(3)}(\vec{r'}-\vec{R})\Psi_j^*(\vec{r'})\Psi_i(\vec{r}) &(2.4.21)\\ &= \Big[\langle \vec{k'}_{\mathrm{R}}|\, \hat{K}\, |\vec{k}_{\mathrm{R}}\rangle\, \Psi_j^*(\vec{r'})\Psi_i(\vec{r})\Big]_{\vec{r'}=\vec{r}=\vec{R}}. &(2.4.22)\end{aligned}$$

$\vec{k_R}$ and $\vec{k'_R}$ now denote two k-vectors of the same magnitude but different direction, which implies that an elastic scattering process is described. A more explicit expression for the remaining K-matrix element $\langle \vec{k'_R}|\, \hat{K}\, |\vec{k_R}\rangle$ can be obtained when expanding the K-matrix in terms of partial waves, as shown in the following section.

2.4.2. Partial wave expansion of the interaction operator

Due to the low thermal energies involved in cold gases and due to the fact that the kinetic energy of the Rydberg electron is rather low far from the core, we are mainly interested in low energy scattering of the Rydberg electron from the perturber. Therefore, it is useful to expand the scattering process in partial waves as only the lowest partial waves will contribute to the scattering process (see section 2.2.2). If we consider elastic scattering ($|\vec{k'}| = |\vec{k}| \equiv k$) in a central potential, the expansion of the K-matrix elements in partial waves is given by [65, eq. 19.51]

$$\langle \vec{k'}|\, \hat{K}\, |\vec{k}\rangle = 2\pi \sum_{l=0}^{\infty}(2l+1)A_l(k)P_l\left(\frac{\vec{k'}\cdot\vec{k}}{k^2}\right), \tag{2.4.23}$$

where $A_l(k) = -\frac{\tan\delta_l(k)}{k}$ is the scattering length of the l-th partial wave and $P_l(x)$ denotes the Legendre polynomial of l-th order. If we apply this to eq. (2.4.22), we obtain

$$\langle\Psi_j|\,\hat{V}_{\mathrm{sc}}(\vec{R})\,|\Psi_i\rangle = 2\pi\sum_{l=0}^{\infty}(2l+1)A_l(k_R)P_l\left(\frac{\vec{k}'_R\cdot\vec{k}_R}{k_R^2}\right)\Psi_j^*(\vec{R})\Psi_i(\vec{R}) \tag{2.4.24}$$

$$= 2\pi\sum_{l=0}^{\infty}(2l+1)A_l(k_R)\Psi_j^*(\vec{R})P_l\left(\frac{\overleftarrow{\nabla}\cdot\vec{\nabla}}{k_R^2}\right)\Psi_i(\vec{R}), \tag{2.4.25}$$

where in the last step we used the representation of the k-vector in position space $\vec{k} = \vec{\nabla}\Psi(\vec{r})$ and $\overleftarrow{\nabla}$ denotes a gradient that acts on the bra wave function. Based on the matrix element above, we can finally express the interaction operator for the pseudopotential as

$$\hat{V}_{\mathrm{sc}} = \sum_{l=0}^{\infty}2\pi(2l+1)A_l(k_R)P_l\left(\frac{\overleftarrow{\nabla}\cdot\vec{\nabla}}{k_R^2}\right)\delta^{(3)}(\vec{r}-\vec{R}). \tag{2.4.26}$$

Here, $k_R = \sqrt{\frac{2}{R}-\frac{1}{n_{\mathrm{eff}}^2}}$ is the classical momentum of the Rydberg electron impinging on the perturber atom B[8]. Inserting the Legendre polynomials $P_0(x) = 1$ and $P_1(x) = x$, we finally obtain the two leading terms of the potential in the partial wave expansion

$$\hat{V}_s = 2\pi A_0(k_R)\delta^{(3)}(\vec{r}-\vec{R}), \tag{2.4.27}$$

$$\hat{V}_p = 6\pi A_1(k_R)\delta^{(3)}(\vec{r}-\vec{R})\frac{1}{k_R^2}\overleftarrow{\nabla}\cdot\vec{\nabla}, \tag{2.4.28}$$

where

$$A_l(k_R) = -\frac{\tan(\delta_l(k_R))}{k_R} \tag{2.4.29}$$

is the scattering length of the l-th partial wave. Eq. (2.4.27) (s-wave interaction) and eq. (2.4.28) (p-wave interaction) are the expressions for the pseudopotential we were looking for and are of fundamental importance for modelling the Rydberg–ground state interaction. Note that due to the scalar product of the gradients, the p-wave interaction in eq. (2.4.28) consists of three individual terms, corresponding to the three spatial directions of the gradient. In spherical coordinates, we can therefore identify one radial and two angular parts (θ and ϕ-direction) of the p-wave interaction, leading, respectively, to Σ and Π symmetries, as will be discussed in sec. 2.4.7.

2.4.3. Angular momentum couplings

So far, we did not take into account any internal degree of freedom of the Rydberg electron or the perturber atom. However, due to angular momentum coupling between the spin of the collision partners, the K-matrix, and therefore the scattering phase shifts, will differ for singlet- and triplet-scattering, as will be discussed in sec. 2.4.4. Since the derivation of the pseudopotentials (sec. 2.4.1 and 2.4.2) holds for either of the two scattering channels, the resulting pseudopotential is given by the sum over singlet(S) and triplet(T) scattering.

---

[8] In the classically forbidden region ($\frac{2}{R} < \frac{1}{n_{\mathrm{eff}}^2}$), the classical electron momentum becomes imaginary. To circumvent this problem, we take the absolute value of the momentum to determine the scattering length.

To this end, the interaction operator from eq. (2.4.26) can be generalised to include the angular momentum coupling. It then reads

$$\hat{V}_{\text{sc}} = 2\pi \sum_{l=0}^{\infty} (2l+1) \left[\hat{\mathbb{I}}^S A_l^S(k_R) + \hat{\mathbb{I}}^T A_l^T(k_R)\right] P_l \left(\frac{\overleftarrow{\nabla} \cdot \overrightarrow{\nabla}}{k_R^2}\right) \delta^{(3)}(\vec{r} - \vec{R}). \tag{2.4.30}$$

Here, $\hat{\mathbb{I}}^S$ and $\hat{\mathbb{I}}^P$ denote the projection operators onto the singlet and the triplet state, respectively. The scattering length $A_l^{S,T}(k_R) = -\frac{\tan \delta_l^{S,T}(k_R)}{k_R}$ now also depends on the spin state through the spin dependency of the scattering phase shift. If we define $\hat{\vec{S}}_1$ to measure the spin of the Rydberg electron and $\hat{\vec{S}}_2$ to measure the total electronic angular momentum of the perturber, the appearing spin projectors can be written as

$$\hat{\mathbb{I}}^S = -\hat{\vec{S}}_1 \cdot \hat{\vec{S}}_2 - \frac{1}{4}, \tag{2.4.31}$$

$$\hat{\mathbb{I}}^T = \hat{\vec{S}}_1 \cdot \hat{\vec{S}}_2 + \frac{3}{4}. \tag{2.4.32}$$

The scalar product of the angular momentum operators $\hat{\vec{S}}_1 \cdot \hat{\vec{S}}_2$ can be expressed in terms of the angular momentum ladder operators, as shown in sec. A.2. Even though eq. 2.4.30 is valid for any choice of basis, it is instructive to settle for one particular basis at this point. In accordance with what is done in ref. [55], we employ a basis set of the form $|n_1, l_1, j_1, m_{j1}\rangle \otimes |m_{s2}, m_{I2}\rangle$. The first part of this basis describes the Rydberg atom (index 1) and consists of the usual n_1, l_1, j_1, m_{j1} quantum numbers of the spin–orbit coupled Rydberg state. The second part describes the perturber (index 2), whose electron is assumed to be in an S-state and whose total angular momentum projection m_{j2} is thus equal to the spin projection m_{s2}. Furthermore, the perturber possesses a nuclear spin I, whose projection quantum number is m_{I2}. For the Rydberg atom, the choice of the spin–orbit coupled basis is reasonable because the numerical calculation of the Rydberg wave functions in sec. 2.3.1 is also carried out in this basis. For the ground state, it is useful to keep the hyperfine states uncoupled since in the uncoupled basis the electronic spin projection m_{s2} is readily available, which facilitates the calculation of the spin projectors. For the Rydberg state on the other hand, the electron spin is not so easily available due to the spin–orbit coupling. In order to obtain the different spin contributions of any particular fine structure state, one can in general decouple the spin and the orbital angular momentum of a state $|n, l, j, m_j\rangle$ by

$$|n, l, j, m_j\rangle = \sum_{m_s=-1/2}^{1/2} \langle n, l, m_l; s, m_s | n, l, j, m_j\rangle \, |n, l, m_l; s, m_s\rangle \,. \tag{2.4.33}$$

The appearing scalar product $\langle n, l, m_l; s, m_s | n, l, m, m_j\rangle$ is the Clebsch–Gordan coefficient, as discussed in sec. A.3. This choice of basis also implies that the hyperfine coupling of the perturber atom is not yet included. Therefore, the term $\hat{H}_{\text{HFS}} = A\hat{\vec{S}}_2 \cdot \hat{\vec{I}}_2$, which couples the electronic and the nuclear spin in the perturber, has to be added to the system Hamiltonian[9]. If we restrict the partial wave expansion of the interaction operator in eq. (2.4.30) to the s- and p-wave, we finally obtain the angular momentum coupled system Hamiltonian

---

[9] A denotes the hyperfine structure constant. For the $5S$-state in rubidium, it is $A = h \times 3.4\,\text{GHz}$.

$$\begin{aligned}\hat{H} = {} & \hat{H}_0 \\ & + 2\pi \left[A_s^S(k_R)\hat{\mathbb{I}}^S + A_s^T(k_R)\hat{\mathbb{I}}^T\right] \delta^{(3)}(\vec{r} - \vec{R}) \\ & + 6\pi \left[A_p^S(k_R)\hat{\mathbb{I}}^S + A_p^T(k_R)\hat{\mathbb{I}}^T\right] \delta^{(3)}(\vec{r} - \vec{R}) \frac{\overleftarrow{\nabla} \cdot \overrightarrow{\nabla}}{k_R^2} \\ & + A\hat{\vec{S}}_2 \cdot \hat{\vec{I}}_2, \end{aligned} \tag{2.4.34}$$

which will be the basis for all further considerations.

In order to understand the states arising from this Hamiltonian, we want to analyse the coupling of the four involved angular momenta $\vec{L}_1$, $\vec{S}_1$, $\vec{S}_2$, and $\vec{I}_2$. Since it is easier to understand the underlying mechanisms, we will discuss the problem in the completely uncoupled basis and assume the internuclear axis to be oriented along the z-axis. In a simplified picture, the system at hand is represented by a toy Hamiltonian that includes three angular momentum couplings of the form

$$\hat{H}_{\text{toy}} \propto a_{\text{LS}} \hat{\vec{L}}_1 \cdot \hat{\vec{S}}_1 + a_{\text{SS}}(m_{l1}) \hat{\vec{S}}_1 \cdot \hat{\vec{S}}_2 + a_{\text{HFS}} \hat{\vec{S}}_2 \cdot \hat{\vec{I}}_2, \tag{2.4.35}$$

where the LS term originates from the spin–orbit coupled unperturbed Hamiltonian $\hat{H}_0$ and the spin–spin term (SS) stems from the singlet and triplet projectors. From the structure of these coupling terms, it is clear that only the spin–spin interaction couples the Rydberg spin–orbit term with the hyperfine term of the perturber. For vanishing spin–spin interaction, the Hilbert space is thus separable and the states are product states of the form $|n_1, l_1, j_1, m_{j1}\rangle \otimes |F_2, m_{F2}\rangle$. This is relevant for large internuclear separations, where the perturber is not inside the Rydberg wave function any more and there is thus no spin–spin interaction. Whenever the magnetic substates are not of interest for our discussion, we will therefore label our infinitely separated two-particle states in the following by the notation, i.e. $25P_{1/2}; F = 1$, denoting the Rydberg atom in the $25P_{1/2}$-state and the ground state in the $F = 1$ hyperfine state. If the omission of the magnetic substates creates ambiguities, we will explicitly give the full quantum state of both particles.

If, on the other hand, the spin–spin interaction is present, it is not clear what are good quantum numbers for the system. Ignoring the nuclear motion, the Hamiltonian from eq. (2.4.35) in principle gives rise to the total hyperfine coupled angular momentum[10]

$$\vec{\tilde{F}} = \vec{L}_1 + \vec{S}_1 + \vec{S}_2 + \vec{I}_2 \tag{2.4.36}$$

and its projection on the z-axis

$$\tilde{m}_F = m_{l1} + m_{s1} + m_{s2} + m_{I2}. \tag{2.4.37}$$

Due to the peculiar nature of the spin–spin interaction, its prefactor a_{SS} implicitly depends on the orbital angular momentum projection m_{l1} in a way that it vanishes if $m_{l1} \neq 0$ (s-wave and radial p-wave interaction) or $m_{l1} \neq \pm 1$ (angular p-wave interaction), as will be discussed in sec. 2.4.5. If these conditions are not fulfilled, the spin–spin interaction does not mediate between the Rydberg atom and the ground state atom and consequently we

---

[10] The hyperfine quantum number is named $\tilde{F}$ to distinguish it from the hyperfine states F of the isolated perturber atom.

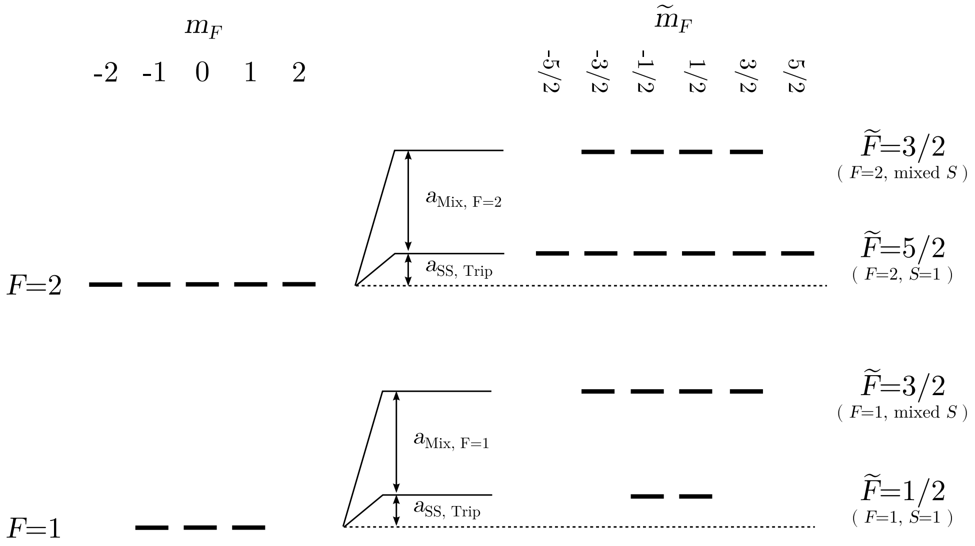

Figure 2.8: Angular momentum coupling scheme and the arising states for dominant hyperfine interaction. Without the spin–spin interaction (left side) the ground state perturber's spin S_2 and its nuclear spin I_2 form three degenerate $F = 1$ states and five degenerate $F = 2$ states. Each of the depicted m_F states is two times degenerate due to the uncoupled spin S_1. The spin–spin interaction couples the Rydberg spin S_1 to the system (right side) and splits each of the two hyperfine levels in a pure triplet (S=1) and a mixed singlet–triplet (mixed S) state. The total angular momentum $\tilde{F}$ ranges from $|F - S_1|$ to $F + S_1$. In this regime, the system is well-described by the quantum numbers F, $\tilde{F}$ and $\tilde{m}_F$.

again expect to obtain a product state of the form $|n_1, l_1, j_1, m_{j1}\rangle \otimes |F_2, m_{F2}\rangle$, independent of the internuclear separation. If, in contrast, the conditions are fulfilled, we are restricted to a certain subspace of the Hilbert space with fixed m_{l1}. When the $\vec{L}_1 \cdot \vec{S}_1$ term is represented in terms of the ladder operators, as described in sec. A.2, we obtain

$$\hat{\vec{L}}_1 \cdot \hat{\vec{S}}_1 = \frac{1}{2}(\hat{L}_{1,+}\hat{S}_{1,-} + \hat{L}_{1,-}\hat{S}_{1,+} + 2\hat{L}_{1,z}\hat{S}_{1,z}). \tag{2.4.38}$$

It becomes obvious that through the ladder operators the LS term couples states with the same $L_1' = L_1$ but different $m_{l1}' = m_{l1} \pm 1$. Within the restricted subspaces of fixed m_{l1}, there is no $m_{l1} \pm 1$ state available, such that the terms including the ladder operators vanish and only the $\hat{L}_{1,z}\hat{S}_{1,z}$ term persists. In the case of $m_{l1} = 0$, the projection term also vanishes and there is thus no spin–orbit coupling in this subspace. This implies that the s-wave interaction and the radial part of the p-wave interaction do not show any influence of the Rydberg atom's spin–orbit interaction. Only the angular part of the p-wave interaction will thus show a line splitting due to the spin–orbit coupling. To get a qualitative understanding of the states arising in the coupled system and still keep the discussion as simple as possible, we will restrict ourself to the case $m_{l1} = 0$. Under this assumption, we can replace eq. (2.4.36) by

$$\vec{\tilde{F}} = \vec{S}_1 + \vec{S}_2 + \vec{I}_2 \tag{2.4.39}$$

and its projection on the z-axis (2.4.37) by

$$\tilde{m}_F = m_{s1} + m_{s2} + m_{I2}. \tag{2.4.40}$$

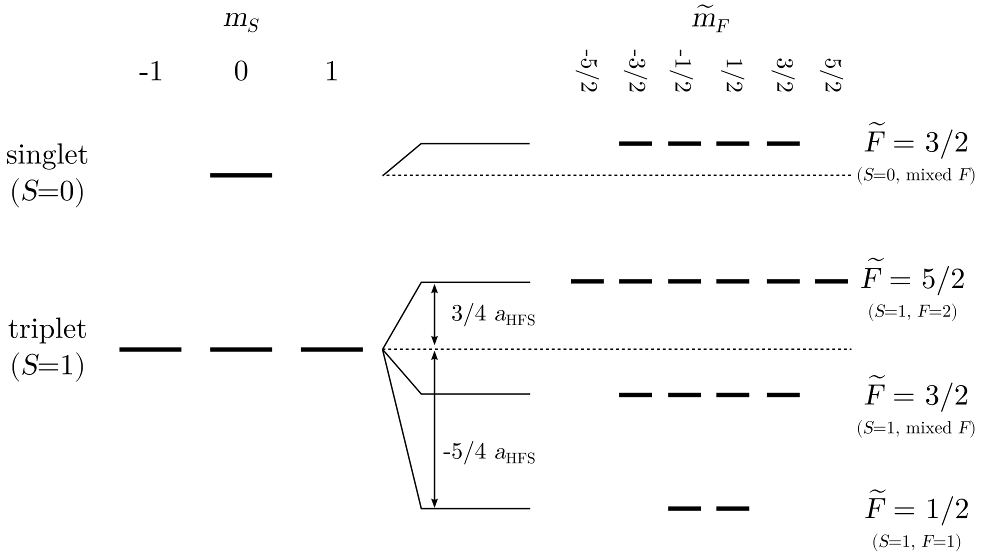

Figure 2.9: Angular momentum coupling scheme and the arising states for dominant spin–spin coupling. Without the hyperfine interaction (left side) the Rydberg spin S_1 and the ground state spin S_2 form one singlet state ($S = 0$) and three degenerate triplet states ($S = 1$). Due to the uncoupled nuclear spin, each of the depicted levels is four times degenerate. The hyperfine interaction lifts the degeneracy of the triplet states (right side) and gives rise to the molecular hyperfine states $\tilde{F}$ running from $|I - S|$ to $I + S$. In this regime, the system is well-described by the quantum numbers S, $\tilde{F}$ and $\tilde{m}_F$.

Even for infinitesimal interaction between the Rydberg electron and the perturber, a molecular axis is defined that breaks the isotropy of the system and, consequently, the orbital angular momentum is not a good quantum number any more. However, in the case discussed above we only include the spins in the total angular momentum $\tilde{F}$. Therefore, $\tilde{F}$ and its projection on the z-axis $\tilde{m}_F$ remain good quantum numbers as long as the molecule is oriented along the quantisation axis. Thus, a labelling of the quantum states in terms of $\tilde{F}$ in combination with either F or S is very instructive and provides a unique label for each state. Which combination of quantum numbers gives an adequate description of the state depends on the relative strength of the two involved angular momentum couplings. In the following, we will therefore consider two cases where either the spin–spin coupling or the hyperfine coupling is the dominant interaction.

Dominant hyperfine interaction

In the case of a dominant hyperfine interaction ($a_{\mathrm{SS}} \ll a_{\mathrm{HFS}}$), the electronic spin of the perturber $\vec{S}_2$ and its nuclear spin are coupled to the hyperfine states characterised by the quantum numbers F and m_F. In the case of ^{87}Rb, we obtain three degenerate $F = 1$ states and five degenerate $F = 2$ states as shown on the left side of fig. 2.8. Due to the spin–spin interaction, these states are coupled to the spin $\vec{S}_1$ of the Rydberg electron, giving rise to hyperfine states with the quantum numbers

$$\tilde{F} = |F - S_1|, ..., F + S_1. \tag{2.4.41}$$

Consequently, the $F = 1$ state splits up into $\tilde{F} = 1/2$ and $\tilde{F} = 3/2$ and the $F = 2$ state splits up into $\tilde{F} = 3/2$ and $\tilde{F} = 5/2$, as shown on the right side of fig. 2.8. While the energetic ordering of the $\tilde{F}$ states is as expected for the $F = 1$ state, it is inverted in the $F = 2$ case, which is due to the opposite sign of the Landé factors g_I of the two F states [92]. Analysing the contribution of singlet and triplet states of the spin–spin system $\vec{S} = \vec{S}_1 + \vec{S}_2$, we see that the $\tilde{F} = 1/2$ state and the $\tilde{F} = 5/2$ are of pure triplet character and both $\tilde{F} = 3/2$ states are of mixed singlet–triplet character, as described in ref. [55, 100]. For increasing strength of the spin–spin interaction also the hyperfine subspaces get mixed and the $F = 1$ mixed state gets an increasing contribution of the $F = 2$ state and vice versa. This small admixture of opposite ground state character enables spin-flip processes in the perturber upon excitation of Rydberg molecules, as will be shown in sec. 5.2.

Dominant spin–spin interaction

When the spin–spin interaction is dominant ($a_{\mathrm{SS}} \gg a_{\mathrm{HFS}}$), the Rydberg spin $\vec{S}_1$ and the ground state spin $\vec{S}_2$ form a singlet–triplet system $\vec{S} = \vec{S}_1 + \vec{S}_2$ that consists of one singlet state ($|\vec{S}| = 0$) and three degenerate triplet states ($|\vec{S}| = 1$), as depicted on the left side of fig. 2.9. Since the full Hamiltonian in eq. (2.4.34) contains explicit terms for the singlet and the triplet states of the spin–spin system, their energy is individually determined by the respective term. In analogy to the hyperfine splitting of the J-states in the hydrogen atom, here the hyperfine interaction gives rise to the states with the quantum numbers

$$\tilde{F} = |S - I|, ..., S + I. \tag{2.4.42}$$

In the case of the triplet states ($S = 1$) and for the nuclear spin $I = 3/2$ in ^{87}Rb, we obtain the quantum numbers $\tilde{F} = 1/2$, $\tilde{F} = 3/2$ and $\tilde{F} = 5/2$, as shown on the right side of fig. 2.9. Thus, the hyperfine interaction thus lifts the degeneracy of the three triplet states. The resulting states, however, cannot be attributed to a certain triplet state but consist of different mixtures of them. It is interesting to note that the $\tilde{F} = 1/2$ state contains only $F = 1$ states and the $\tilde{F} = 5/2$ contains only $F = 2$ states and, consequently, these two states energetically differ by the hyperfine splitting $2a_{\mathrm{HFS}} = 6.8\,\mathrm{GHz}$ of the perturber. The triplet $\tilde{F} = 3/2$ state is composed of a mixture of $F = 1$ and $F = 2$ states and its energetic position depends on the exact mixing that is determined by the relative strength of the spin–spin and the hyperfine interaction. Since the resulting spin of the singlet state is zero ($S = 0$), only the $\tilde{F} = 3/2$ state appears in this case. Due to the vanishing magnetic moment of the singlet state, there is no interaction with the nuclear spin and the resulting state is a product state of the form $|\tilde{m}_F\rangle = |S = 0\rangle\,|m_I\rangle$. The $\tilde{m}_F$ states thus reflect the projection of the nuclear spin m_{I2}.

Comparing the coupled energy levels (right side) in fig. 2.8 and fig. 2.9, we realise that both show the same structure and just differ in the energy gaps between the $\tilde{F}$ levels. Indeed,we find that in both pictures the $\tilde{F} = 1/2$ state and the $\tilde{F} = 5/2$ states are pure triplet states and pure $F = 1$ and $F = 2$ states, respectively. It is therefore possible to describe these states solely by their $\tilde{F}$ quantum number and $S = 1$. The $\tilde{F} = 3/2$ states on the other hand have the property that they are always mixed singlet–triplet and mixed $F = 1$–$F = 2$ states. Even though both subspaces will always be mixed for those states, the states corresponding to the weaker interaction will experience the stronger mixing. For a dominant hyperfine interaction, they are thus strongly mixed singlet–triplet states with a small mixing of the hyperfine states and we can describe the state as either "$F = 1, \tilde{F} = 3/2$" or "$F = 2, \tilde{F} = 3/2$". For a dominant spin–spin coupling on the other hand, they are a strong mixture of $F = 1$ and $F = 2$ and show only a small mixing of the singlet and triplet subspace and we can therefore describe them as "singlet $\tilde{F} = 3/2$" or "triplet $\tilde{F} = 3/2$".

2.4.4. Scattering phase shifts

As pointed out in sec. 2.2.2, for small collision energies, the whole scattering process between the Rydberg electron and the rubidium ground state atom can be described by a single scalar quantity in terms of the scattering phase shift. Due to the approximations made, the expressions for the interaction potentials $\hat{V}_s$ from eq. (2.4.27) and $\hat{V}_p$ from eq. (2.4.28) also depend on the energy dependent scattering length $A_l^{S,T}$ and, therefore, on the scattering phase shift as indicated by eq. (2.4.29).

Since an ab-initio calculation of the scattering phase shifts is beyond the scope of this work, calculated values for the non-relativistic scattering phase shifts generously provided by Ilya Fabrikant were used. In order to obtain a continuous function for $\delta(k)$ also between the provided data points, a high order polynomial was fitted to the phase shift data. Even though this method works satisfactory within the range of the provided data, it shows problems at the edges, as high order polynomials tend to diverge outside the fitting range. This problem becomes especially evident for $k \to 0$ since the fit function has to meet the right scaling behaviour (see sec. 2.2.2) in order to obtain the right zero energy scattering length $a_l = -\lim_{k\to 0} A_l(k)$. For small k the fit function is thus replaced by the right asymptotic function $\delta(k) \propto k^{2l+1}$, which is scaled in order to match the value of the fit function at the crossover point.

The data provided by Fabrikant, along with the fitted polynomials for singlet and triplet scattering of the s- and p-wave channels, are shown in fig. 2.10. Two interesting features of the scattering process can be seen in this plot. First of all the ^3S phase shift crosses zero at $k = 0.058\,\text{a.u.}$. This effect is called *Ramsauer-Townsend effect* and can be understood in terms of constructive interference of multiply scattered waves within the potential that leads to full transmission of the incident wave [101]. In the context of the pseudopotentials derived above, this means that for $k = 0.058\,\text{a.u.}$ the triplet potential $\hat{V}_s^T$ vanishes since $A_s^T(k = 0.058\,\text{a.u.}) = 0$. This Ramsauer-Townsend minimum, however, only occurs in the triplet but not in the singlet s-wave channel. The second important feature is the $\pi/2$-crossings of the scattering phase shifts. As can be seen in fig. 2.10, there are multiple such $\pi/2$-crossings for the different scattering channels. This discussion should however be limited to the one at $k = 0.048\,\text{a.u.}$ for the ^3P channel since higher k-vectors are only reached very close to the Rydberg core where the derived pseudopotentials are likely to fail anyway. The interesting feature of this point is that here the scattering length diverges due to the tangent in eq. (2.4.29). This rise of the scattering length is caused by a *shape resonance* in rubidium [95]. This means that for an incident wave vector $k = 0.048\,\text{a.u.}$ the triplet p-wave scattering channel can form a meta-stable Rb$^-$ bound state. Due to this binding, the outgoing wave gets increasingly delayed as the exact shape resonance is approached, which reflects in the diverging scattering length in the stationary Schrödinger picture. Of course, an infinite scattering length is unphysical since it should be at least limited by the de-Broglie wavelength of the incident particle. Usually, this is covered by a complex scattering phase shift in the T-Matrix formalism. Since we derived the Fermi pseudopotentials using the real K-Matrix, we also obtained real phase shifts. While this is indeed a problem for first-order perturbation treatments of the p-wave pseudopotentials, it does not affect the results of an exact diagonalisation of the Hamiltonian if a sufficient number of states above and below the state of interest is included in the basis. Due to

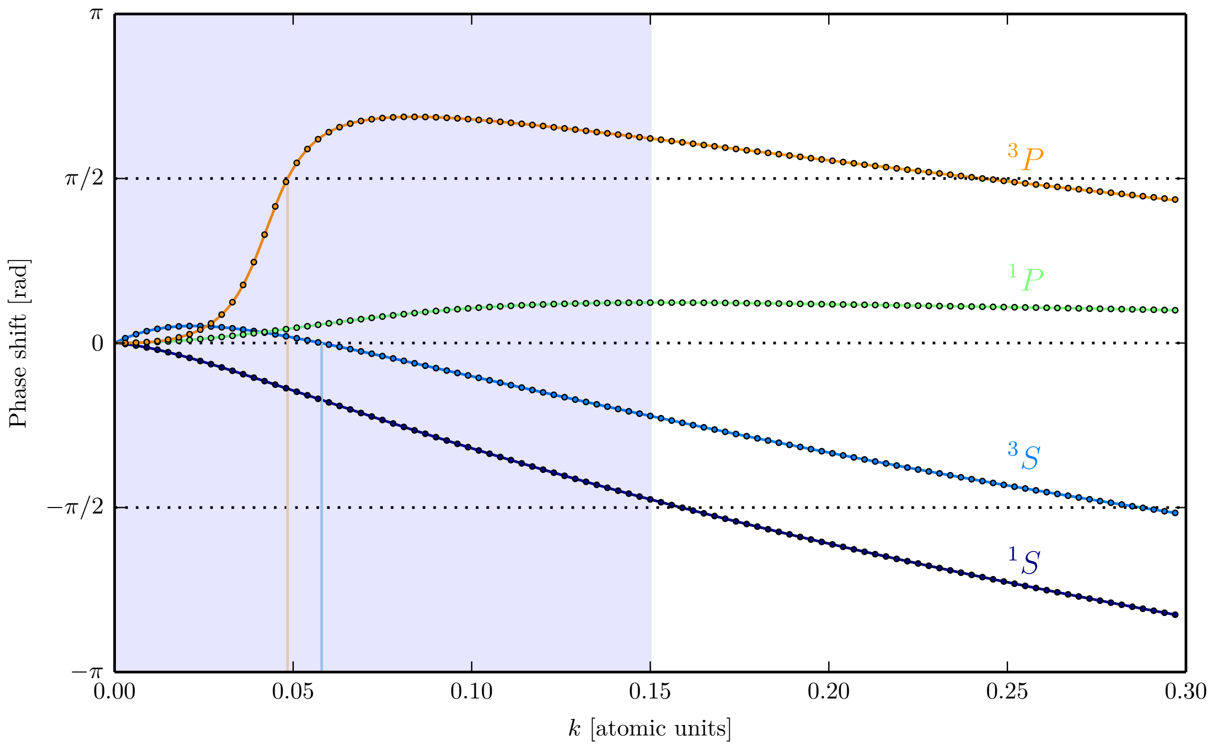

Figure 2.10: Non-relativistic scattering phase shift as a function of the relative wave vector k for singlet s-wave (dark blue), triplet s-wave (light blue), singlet p-wave (green), and triplet p-wave (orange) scattering between a rubidium atom and an electron. The dots indicate the data provided by I. Fabrikant, the lines are polyonimal fits to the data (see text). The blue shaded area indicates the relevant region for the pseudopotential calculations down to an internuclear distance of $R = 80\,\mathrm{a}_0$. The $\pi/2$-crossing (shape resonance) for the ^3P phase shift at $k = 0.048$ is indicated by the light orange line. The zero crossing (Ramsauer-Townsend effect) of the ^3S phase shift at $k = 0.058$ is indicated by the light blue line.

level repulsion, the effect of the diverging scattering length is then only visible for the energetically highest/lowest states of the basis [102].

Since the scattering phase shifts used are non-relativistic, they do not include the spin–orbit splitting of the scattering phase shifts that arises due to the coupling of the atom's spin with the electrons orbital angular momentum. Including the spin–orbit interaction leads to a triplet splitting of the ^3P state into $^3P_{0,1,2}$. A discussion of this effect in the context of Rydberg molecules is given in refs. [95, 97].

2.4.5. Adiabatic potentials

We have now all necessary ingredients to calculate the potential energy $E_{\mathrm{pot}}(R)$ of the electronic problem. Before discussing the results of the full diagonalisation of the electronic Hamiltonian (2.4.34), we will shortly treat a simplified problem in perturbation theory to gain some qualitative insight into the nature of this interaction.

Adiabatic potentials in perturbation theory

In order to learn more about the interaction potential, it is instructive to calculate the energy correction in first order perturbation theory. This approach should yield valid results for the non-degenerate S-, P-, and D-states in rubidium as long as the interaction

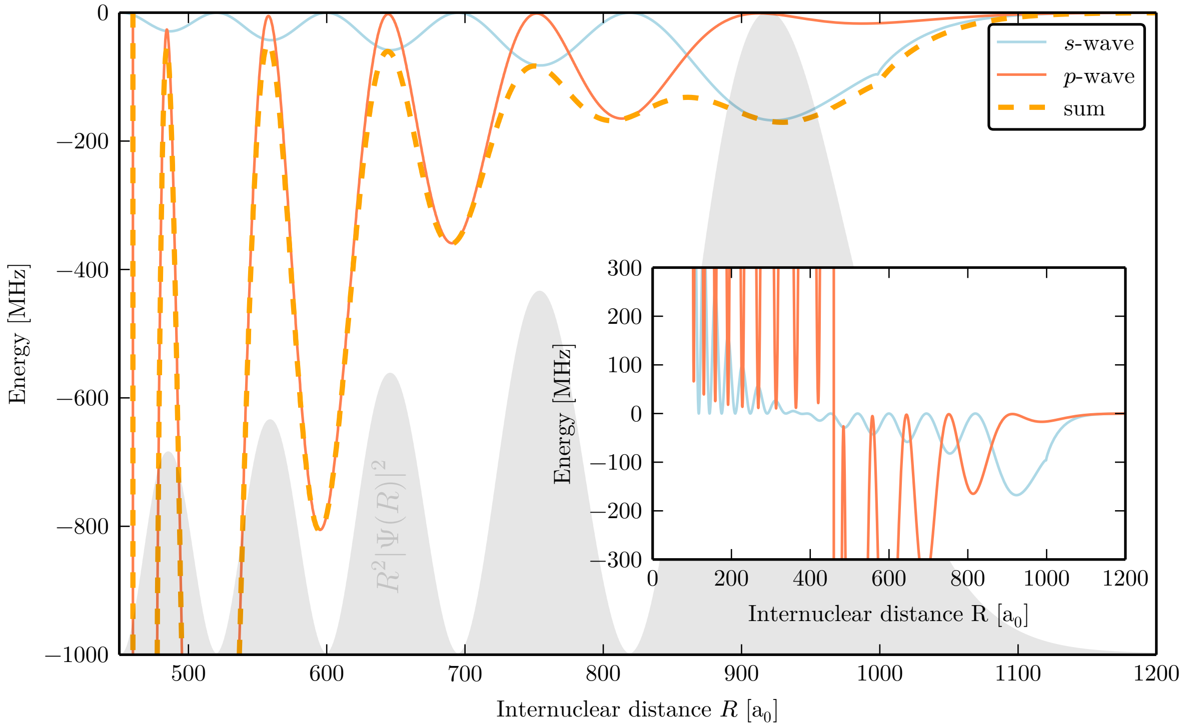

Figure 2.11: Adiabatic energy curves for the $25P_{1/2}$ state obtained in first order perturbation theory for triplet scattering only and the perturber located on the z-axis. The s-wave contribution (light blue) and the p-wave contribution (red) add to the combined potential (orange dashed). Since the s-wave interaction is proportional to $|\Psi(R)|^2$, it is strongest at the maxima of the radial electronic density $R^2|\Psi(R)|^2$ (gray shaded). Since it is proportional to the wave function's gradient, the p-wave interaction is strongest at the nodes of the wave function. The inset shows a zoomed-out view of the s- and the p-wave potential.

is smaller than the energy gap to the neighbouring states. Since we are only interested in qualitative statements at this point, and for the sake of simplicity, we will restrict the perturbative discussion to the case of triplet scattering, but, of course, the following reasoning applies to singlet scattering as well. Under these assumptions, the Rydberg–ground state interaction terms in the angular momentum coupled expression in eq. (2.4.34) reduce to the ones in eq. (2.4.27) and (2.4.28) for the s- and p-wave, respectively. For a state $|\Psi\rangle$ with the radial wave function $\Psi(r)$ the first order energy correction for s- and p-wave is given by

$$\Delta E_s(R) = \langle\Psi|\hat{V}_s(R)|\Psi\rangle = 2\pi A_s^T(k_R)|\Psi(R)|^2, \tag{2.4.43}$$

$$\Delta E_p(R) = \langle\Psi|\hat{V}_p(R)|\Psi\rangle = 6\pi A_p^T(k_R)|\nabla\Psi(R)|^2. \tag{2.4.44}$$

Obviously, the s-wave interaction is given by the electron density of the Rydberg state scaled with the scattering length, while the p-wave interaction is determined by the gradient of the wave function scaled with the respective scattering length. As shown in fig. 2.11, the s-wave interaction is extremal where the electron density is maximal. The p-wave interaction on the other hand maximises at the nodes of the wave function since there the radial gradient is maximised. The envelope of the oscillating potentials is determined by the scattering lengths. Due to the Ramsauer-Townsend effect (sec. 2.4.4), the s-wave potential changes its sign and vanishes at 373 a_0. The appearing shape resonance in the triplet channel thus causes the p-wave interaction to diverge at 460 a_0 and to change its sign, as shown in the inset of fig. 2.11. This unphysical divergence leads to unusable results in the vicinity of the divergence. For longer internuclear distances, where the k-vector of the Rydberg electron is well below the critical value, it is still possible to obtain a valid approximation, even in perturbation theory. The combined s- and p-wave potential in fig. 2.11 carries over the oscillatory behaviour of its constituents. Since the s-wave contribution is maximal when the p-wave contribution vanishes and vice versa, the combined potential does not oscillate back to zero. This effect changes the scattering characteristics between a Rydberg atom and a ground state atom, as will be shown in sec. 4. Furthermore, the oscillatory behaviour of the combined potential gives rise to bound molecular states. Such states in the outer wells of the potential are dubbed *ultralong-range Rydberg molecules* [46, 48, 103, 104]. A generic method for finding those bound states in the calculated adiabatic potentials is presented in section 2.4.8.

Diagonalisation of the interaction operator

In order to also take into account the mixing of states when the interaction becomes larger than the level spacing, we performed a full diagonalisation of the Hamiltonian eq. (2.4.34) using a basis representation, as described in sec. 2.4.3 with a truncated basis set. As the approximations made to derive the pseudopotential in sec. 2.4.1 restricts the problem to elastic scattering and thus requires all states to have the same electron momentum, we have to settle for one particular $k(R) = \sqrt{\frac{2}{R} - \frac{1}{n_{\text{eff}}^2}}$. We therefore choose a state of interest, i.e. $25P$, and approximate all other states in our truncated basis to have the same semi-classical momentum distribution $k(R)$. When truncating the basis, it must not be chosen too small in order to cover all major contributions of other states. However, due to the zero range approximation made in the derivation of the pseudopotential, it must also not be chosen too big in order to avoid divergence of the eigenenergies, as described in sec. A.6. Furthermore, the effect of divergences in the scattering length on the diagonalisation can be eliminated by including the adjacent hydrogenic manifolds above and below the state of interest. Since all included states have the same $k(R)$, the divergence will appear at the same point and the level repulsion in the diagonalisation will promote the divergence to the outermost states of the truncated basis while the divergence is lifted for the central states. It is thus possible to obtain valid eigenvalues also close[11] to the divergence of the triplet p-wave [102]. In the light of those arguments, we truncate our basis to include the state of interest and all states up to and including the next hydrogenic manifold above and below.

In order to reduce our basis set even further, we can make use of the symmetry of the system. Since we do not include any external fields that break the rotational symmetry of the system, the eigenvalues of the interaction Hamiltonian are not angular dependent, as demonstrated in sec. A.5. To simplify the calculation, we can therefore choose the internuclear axis to coincide with the z-axis, in which case we need to know the value and the gradient of the Rydberg wave function $\Psi(r, 0, \phi) = R_{n_1 l_1}(r) Y_{l_1}^{m_1}(0, \phi)$ along the z-axis in order to evaluate the pseudopotential terms of the Hamiltonian. Due to the behaviour of the associated Legendre polynomials, the spherical harmonics inside the Rydberg wave function

$$Y_l^m(\theta, \phi) \propto (1 - \cos^2(\theta))^{m_1/2} \tag{2.4.45}$$

---

[11] While mathematically possible, one cannot go arbitrarily close to the divergence, as the involved high numbers will cause numerical errors.

vanish on the z-axis ($\theta = 0$) except for $m_{l1} = 0$. Since the s-wave interaction is proportional to the value of the wave function, it consequently vanishes for higher m_{l1} states. As shown by eq. (A.4.12), the gradient of the wave function in the radial direction is still proportional to the spherical harmonics and thus the same argument applies for the radial part of the p-wave interaction. The gradient in θ direction includes terms of the form $Y_{l_1}^{m_{l1}+1}(\theta = 0, \phi)$ and $Y_{l_1}^{m_{l1}-1}(\theta = 0, \phi)$, which are only non-vanishing in the case $m_{l1} = \pm 1$. It is therefore only necessary to include states with $m_{l1} = 0, \pm 1$ in our basis set, as the interactions vanish for higher m_{l1} states. In the spin–orbit coupled basis the coupled angular momentum projection fulfils $m_{j1} = m_{l1} + m_{s1}$, which implies that for the s-wave interaction only states with $|m_{j1}| = 1/2$ and for the p-wave interaction only states with $|m_{j1}| \leq 3/2$ contribute. It should be stressed again that this simplification can only be made if the internuclear axis is aligned with the z-axis. If this is not the case, i.e. due to an external field breaking the symmetry, all m_{j1} states need to be included. If, on the other hand, all m_{j1} states are included, the internuclear axis can enclose an arbitrary angle θ with the z-axis and we will always recover the exact same eigenenergies in the field-free case, as expected from the symmetry of the system. In contrast to the eigenvalues, the eigenvectors do still depend on the angle θ. It is, however, not necessary to diagonalise the problem for every angle θ since a known set of eigenvectors for a certain angle can be transformed to a different angle by the Wigner d-matrix [105]. As a consequence of this angular dependence, the coupling strength for the excitation by a linear polarised laser beam also varies with θ. In an atomic cloud however, the positions of the atoms are randomly distributed and therefore many atom pairs with different orientations to the polarisation axis can be found at every time. Thus, in experiments involving atomic clouds, the angular dependence of the coupling strength averages out over the many angles realised in the ensemble.

Since our main interest is in the field-free eigenenergies, we can fix the internuclear axis to the z-axis and restrict our basis to $|m_{j1}| \leq 3/2$. The potential energy curves (PECs) obtained from the diagonalisation around the $25P$-state in rubidium in combination with the $1/r^4$ polarisation potential (sec. 2.4) is shown in fig. 2.12. In the resulting potential landscape, we observe a qualitatively different behaviour for the low-l states and the hydrogenic manifolds. In the following, we want to address both cases individually.

2.4.6. Ultralong-range potentials

At high internuclear separations, close to the outermost lobe of the electronic wave function, the potential curves connecting to the low-l states, in this case $25P$, $24D$, and $26S$, are called ultralong-range potentials and the molecular bound states in these potentials are called *ultralong-range Rydberg molecules*. Due to their high energetic separation from the hydrogenic manifold, higher l states are not significantly mixed in by the interaction. Consequently, we expect to recover the perturbative result of sec. 2.4.5 from the diagonalisation. Fig. 2.14a shows a zoomed view on the two $25P_{1/2}; F = 1$ PECs that are obtained from the diagonalisation and fig. 2.14b shows the two PECs obtained for the $25P_{1/2}; F = 2$ state. Since the spin–spin interaction strength is small compared to the hyperfine interaction, we obtain two distinct potential curves for each hyperfine state, as discussed in sec. 2.4.3. While the deeper of the two potentials ("triplet", $\tilde{F} = 1/2$ or $\tilde{F} = 5/2$) is of pure triplet type and is identical to the combined s- and p-wave triplet potential calculated in perturbation theory (fig. 2.11), the shallow potential ("mixed", $\tilde{F} = 3/2$) is of mixed singlet–triplet type [55], which is a direct consequence of the hy-

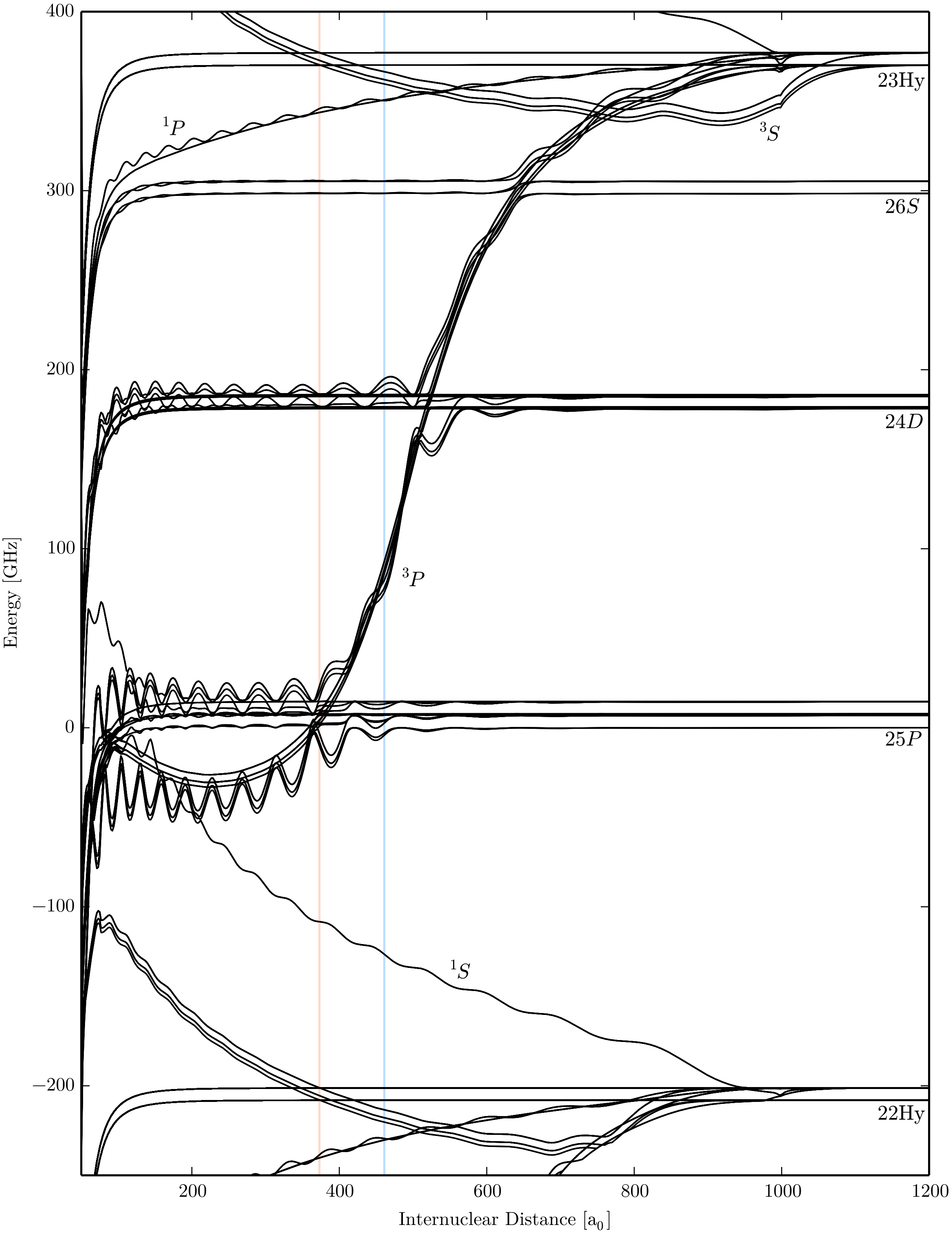

Figure 2.12: Adiabatic potential energy curves (PECs) obtained by a full diagonalisation of the Hamiltonian from eq. (2.4.34) around the $25P_{1/2}; F = 1$ state. The terms of the asymptotic free Rydberg states are noted beneath each group of states. From the hydrogenic manifolds (nHy) the trilobite states (^1S and ^3S) and butterfly states (^1P and ^3P) detach. The blue lines indicate where the divergence of the ^3P scattering length ($461\,\mathrm{a}_0$) appears. The red line indicates the position of the Ramsauer-Townsend minimum in the ^3S channel.

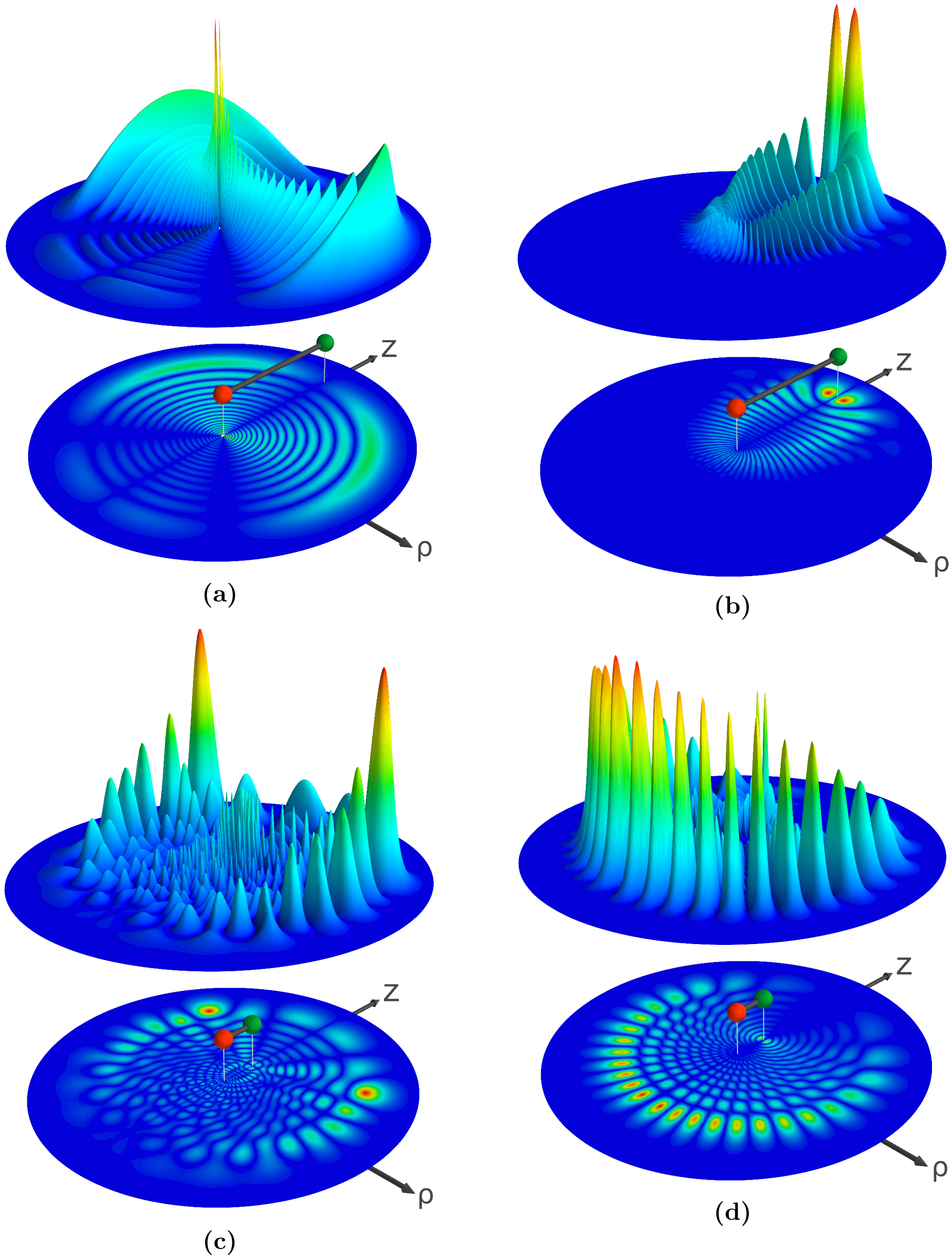

(a)

(b)

(c)

(d)

Figure 2.13: Radial electron density $\rho|\Psi(z,\rho)|^2$ in cylindrical coordinates, illustrating the shape of the electronic density distribution for the different classes of potentials. In each case a surface plot and a 2D projection is shown. A sketch of the molecule above the projection plane shows, where the Rb$^+$ ion (red) and the ground state perturber (green) are located. The vanishing electron density on the z-axis is caused by the volume element in cylindrical coordinates. (a) Ultralong-range triplet potential for the $25P_{1/2}; F = 1$ state ($R = 933\,\mathrm{a}_0$). (b) Trilobite potential ($\tilde{F} = 1/2$, $R = 920\,\mathrm{a}_0$). (c) r-butterfly potential ($\tilde{F} = 1/2$, $R = 245\,\mathrm{a}_0$). (d) θ-butterfly potential ($\tilde{F} = 1/2$, $R = 227\,\mathrm{a}_0$).

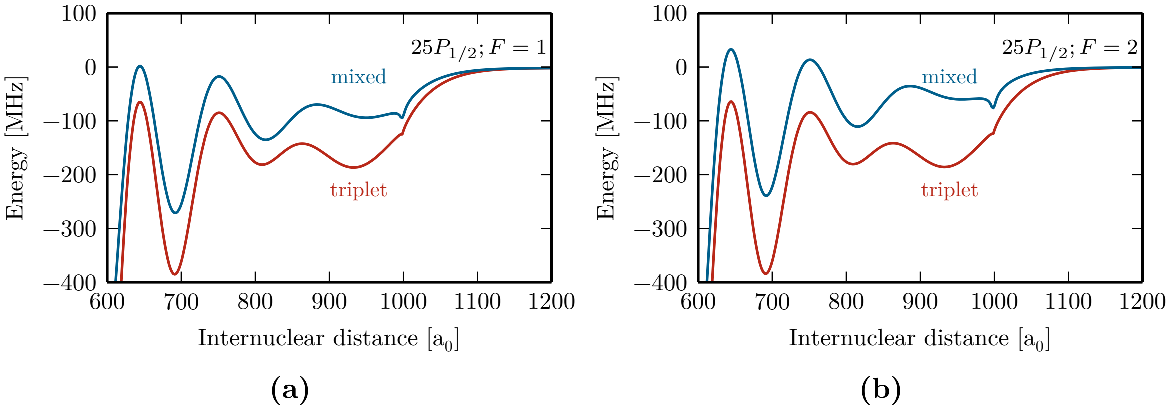

Figure 2.14: Ultralong-range potentials for the two hyperfine states (a) $F = 1$ and (b) $F = 2$ of the $25P_{1/2}$ state for large internuclear separations. Due to the hyperfine interaction in the perturber, two classes of potentials appear: a pure triplet potential (red) and a mixed singlet–triplet potential (blue). The triplet potential is identical for both F states while the mixed states differ from each other. Zero energy in (b) is 6.8 GHz higher than in (a).

perfine interaction term in the Hamiltonian from eq. (2.4.34). Without this term, the Hilbert space separates into a singlet and a triplet subspace and we obtain a pure triplet and a pure singlet potential, which are both identical to the respective perturbative result. However, the hyperfine interaction in the perturber mixes the subspaces and instead of the pure singlet and triplet potentials we obtain a mixed type potential and a pure triplet potential. The exact mixing of the two scattering channels depends on the hyperfine state of the perturber, which is the reason why the mixed potentials differ for the $25P_{1/2}; F = 1$ state and the $25P_{1/2}; F = 2$ state [55]. The difference in the mixed potentials can be seen from the comparison between the hyperfine states in fig. 2.14. While already the first observed Rydberg molecules in 2009 proved the existence of the triplet potential [48], only recently the existence of the mixed type potential was experimentally confirmed in rubidium [52] and caesium [53].

The subspace mixing through the hyperfine interaction has another important consequence since the argument also applies the other way around: The scattering interaction terms in the Hamiltonian mix the $F = 1$ and $F = 2$ subspaces of the Hilbert space and thus the mixed type potential consists of both hyperfine states. The admixture of the opposite hyperfine state is experimentally confirmed by showing spin-flips and the emergence of entangled states, as will be shown in sec. 5.2.

The diagonalisation of the Hamiltonian not only allows us to extract the eigenenergies of the system for an arbitrary internuclear distance R but also to obtain the eigenvector at this position. As described in sec. A.7, we can calculate the electronic density from the eigenvector. The obtained electronic density for the minimum of the outermost well ($R = 933\,\mathrm{a}_0$) in the triplet potential of fig. 2.14 is shown in fig. 2.13a. Since almost no other states are admixed in this low-l class potential, the overall shape is mainly given by the spin–orbit coupled $P_{1/2}$ state wave function.

2.4.7. Trilobite and butterfly potentials

The situation in the hydrogenic manifolds is very different to the low-l states since a high number of degenerate states are mixed by the pseudopotential terms in the Hamiltonian. This results in a set of states that mix to minimise the interaction energy while the residual

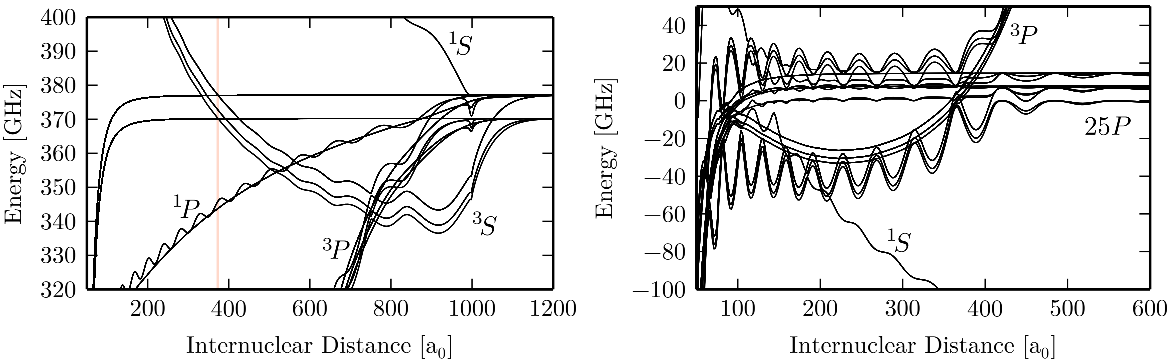

(a) **(b)**

Figure 2.15: High-l class of potential curves. (a) Zoom-in on the $n = 23$ hydrogenic manifold with the detaching trilobite (^3S and ^1S) and butterfly states (^3P and ^1P). The kinks in the potential at $\approx 1000\,\mathrm{a}_0$ appear at the transition into the classically forbidden region and originate from a wrong low-k scaling of the fitted scattering phases (sec. 2.4.4). The red line indicates the position of the Ramsauer-Townsend minimum (sec. 2.4.4). Due to a shape resonance in the triplet p-wave, the ^3P butterfly forms very deep potentials with the minimum slightly below the $25P$ state. (b) Zoom-in on the minimum of the smooth θ-butterfly and the oscillating r-butterfly potentials. For both plots, zero energy was set to the $25P_{1/2}; F = 1$ state.

states are uncoupled, as explained in sec. A.5. Fig. 2.15a shows that four different types of PECs (^1S, ^3S, ^1P, ^3P) detach from the hydrogenic manifolds (nHy), corresponding to the maximisation of the different scattering terms in the Hamiltonian. Depending on whether the s- or the p-wave interaction is maximised, we can further subdivide this class of states into trilobite states and butterfly states, which are discussed in the following.

Trilobite states

The two classes of states denoted with ^1S and ^3S are the so-called trilobite PECs. They are characterised by maximising the s-wave interaction. Since the s-wave interaction is proportional to the electron density at the position of the perturber, these states mix the hydrogenic states in a way that their superposition has the maximum possible electron density at the perturber's position. This means that for a given internuclear separation the state from the hydrogenic manifold with the highest electron density at this point will give the leading contribution. Since the contributions of many states from the hydrogenic manifold add up, we obtain a very strong overall energy shift compared to the ultralong-range states. The s-wave interaction mixes only states with $|m_{l1}| = 0$ ($m_{j1} = 1/2$), as higher m_{l1} states have a vanishing wave function on the z-axis (see above). The resulting state thus shows a Σ-symmetry ($\Lambda = 0$), known from conventional diatomic molecules. Since $m_{l1} = 0$ states have no angular dependence, the mixing in the trilobite state is solely determined by the radial wave functions of the involved states. Consequently, the trilobite potential curves inherit the oscillatory behaviour of the radial wave functions of the constituting hydrogenic states. Since the high number of radial wave function nodes limits the maximum electron density of low-l states, it is beneficial for the system to admix high-l states as those have few nodes and can thus provide a high, localised electron density. Even in the case of an avoided crossing with a low-l state, the trilobite state does not admix significant amounts of the low-l state. In rubidium, no crossings between the trilobite states and low-l states appear. In caesium, however, where due to the small non-integer part of the quantum defect the S-state lies close to the hydrogenic manifold, the small S-admixture at the crossing of the trilobite state with the S-state can be used to couple to hybrid states that are predominantly of trilobite character and thus prove the existence of this class of potentials [49].

Due to the added interaction of numerous degenerate hydrogenic states in the trilobite PECs, the spin–spin interaction dominates the hyperfine interaction and thus the degeneracy of the three triplet states is lifted, as discussed in sec. 2.4.3. Consequently, we observe one ^1S-trilobite PEC with the total angular momentum $\tilde{F} = 3/2$ and three ^3S-trilobite PECs with the total angular momenta $\tilde{F} = 1/2$, $\tilde{F} = 3/2$ and $\tilde{F} = 5/2$ (compare fig. 2.15a). Since the ^1S scattering phase shifts are negative for all k, the according scattering length is positive and thus the singlet trilobite state forms a repulsive potential curve. The small oscillations of its potential do not form wells and thus do not support bound states. In contrast, the three triplet trilobite potentials detach to the red side of the hydrogenic manifold and reach down almost 30 GHz before they bend up again to ultimately cross the manifold again at the Ramsauer-Townsend minimum of the ^3S scattering channel at $373\,\mathrm{a}_0$. The oscillations of the trilobite PECs around its minimum at $930\,\mathrm{a}_0$ form individual wells that support vibrational bound states, which are referred to as *trilobite states* or *trilobite molecules*. A summary of the properties of trilobite states is given in tab. 2.2.

As explained in sec. A.7, we can use the eigenvectors from the diagonalisation to obtain the probability density of the Rydberg electron in the trilobite potential for arbitrary internuclear separation R. For the outermost minimum ($R = 920\,\mathrm{a}_0$) of the $\tilde{F} = 1/2$ triplet trilobite potential fig. 2.13b, shows that the resulting electron density has a strong peak at the perturbers position and the overall shape of a trilobite, which gives the name to this class of states.

Butterfly states

The p-wave interaction gives rise to so-called butterfly states that maximise the wave function gradient at the position of the perturber. The nature of the gradient leads to an important qualitative difference compared to trilobite states. Since the gradient of the wave function is a vector, it can be maximised individually in three spatial dimensions, enabling, in principle, three independent butterfly states. However, due to the problem's rotational symmetry around the z-axis, the wave function may not change in ϕ direction and thus there cannot be a gradient in this direction. In the residual two directions, namely the radial and the θ-direction, however, the gradient can be maximised. Therefore, we obtain two qualitatively different butterfly states in the radial (”r-butterfly”) and the

Table 2.2: Properties of butterfly and trilobite states. The table summarises the dominant scattering channels, the symmetry of the electronic wave function, whether high- or low-l states create strong contributions, which $|m_{l1}|$ states are admixed, and which hyperfine states exist in ^{87}Rb.

State	Channel	Symmetry	Preferred l	m_{l1}	Hyperfine states $\tilde{F}$
Trilobite	s-wave	Σ	high-l	0	1/2, 3/2, 5/2
r-Butterfly	p-wave	Σ	low-l	0	1/2, 3/2, 5/2
θ-Butterfly	p-wave	Π	high-l	± 1	3/2, 5/2, 7/2

angular ("θ-butterfly") direction.

If the internuclear axis is aligned with the z-axis, only states with $m_{l1} = \pm 1$ have a non-vanishing gradient in θ direction. The θ-butterfly is thus restricted to this subspace of the Hilbert space and, consequently, possesses a Π-symmetry ($\Lambda = 1$). As high-l states with small m_{j1} have many nodes in θ-direction, they show strong gradients perpendicular to the internuclear axis and are therefore dominantly mixed into the θ-butterfly. Thus, even in the presence of an avoided crossing with a low-l state, we do not observe strong admixture of low-l states.

The r-butterfly state on the other hand maximises the gradient in the radial direction. For the internuclear axis aligned along the z-axis, the Rydberg wave function, and thus its radial gradient, is only non-vanishing at the perturber for $m_{l1} = 0$. Consequently, the r-butterfly is restricted to the $m_{l1} = 0$ subspace and thus possesses a Σ-symmetry ($\Lambda = 0$). Since the radial wave function has the maximum number of nodes for $l = 0$, we see the opposite behaviour compared to the θ-butterfly: It is beneficial for the system to admix low-l states in the r-butterfly states and in the vicinity of an avoided crossing with a low-l state, this will be the leading contribution to the r-butterfly state.

Just like in the case of the trilobite state, the difference in the singlet and triplet scattering length gives rise to two independent singlet (^1P) and triplet (^3P) butterfly states. In fig. 2.12 and fig. 2.15a we thus see one oscillatory ^1P r-butterfly PEC with the total angular momentum $\tilde{F} = 3/2$ and one non-oscillatory ^1P θ-butterfly PEC with the total angular momentum $\tilde{F} = 5/2$. Due to the added value of the maximised gradients, also the butterfly PECs are dominated by the spin–spin interaction and we see the lifting of the triplet states' degeneracy, as described in sec. 2.4.3. In fig. 2.12 we thus see three oscillatory ^3P r-butterfly PECs with the total angular momenta $\tilde{F} = 1/2$, $\tilde{F} = 3/2$, $\tilde{F} = 5/2$ and three non-oscillatory ^3P θ-butterfly PECs with the total angular momentum $\tilde{F} = 3/2$, $\tilde{F} = 5/2$, $\tilde{F} = 7/2$. Due to the increased scattering length in the vicinity of the ^3P shape resonance, these PECs form very deep potentials that cross all low-l states up to and including the $25P$ state. The butterfly PECs around their minimum in the vicinity of the $25P$ state are shown in fig. 2.15b. Since the r-butterfly preferably admixes low-l states, it is not surprising that the r-butterfly states, due to the nearby crossing with the P-state, consist of 15% $25P$ states in the vicinity of the potential minimum, as will be shown in sec. 6.1. The θ-butterfly states on the other hand show no significant admixture of the $25P$ state despite of the crossing. It is therefore possible to use a single photon transition to couple to bound states in the highly oscillatory r-butterfly potential, while the coupling to the θ-butterfly potential is very weak.

As already explained for the other classes of states, we can also visualise the electron density for the r-butterfly state (fig. 2.13c) and the θ-butterfly (fig. 2.13d). Because the shape of the r-butterfly electron density resembles the shape of a butterfly, the whole class of p-wave dominated states is dubbed butterfly states. A summary of the properties of the two classes of butterfly states in comparison to the trilobite state is given in tab. 2.2.

2.4.8. Molecular bound states

After we solved the electronic part of the full molecular problem described in sec. 2.4 and we know the adiabatic PECs $E_{\text{pot}}(R)$, we can now proceed to solving the Hamiltonian of the nuclear motion in eq. (2.4.6). Since the structure of the Hamiltonian is the same as for conventional molecules, the following discussion is valid for every diatomic molecule and can thus be found in standard text books on molecular physics [77, 106]. It should further be noticed that the structure of the Schrödinger equation arising from eq. (2.4.6) is identical to the hydrogen problem but includes a very different radial potential $E_{\mathrm{pot}}(R)$. Accordingly, we can apply the same formalism to solve the problem at hand. Since the potential term in eq. (2.4.6) does not depend on the angles θ and ϕ, it is useful to express the Laplace operator in terms of the squared angular momentum operator $\hat{\vec{L}}^2$ and the radial momentum $\hat{p}_R$ [65, eq. 9.13]. The resulting Schrödinger equation reads

$$\left[\frac{\hat{p}_R^2}{2M}+\frac{\hat{\vec{L}}^2}{2MR^2}-(E-E_{\mathrm{pot}}(R))\right]\mathit{\Phi}(\vec{R})=0. \tag{2.4.46}$$

Due to the structure of the differential equation, it is reasonable to assume that the solution has the structure

$$\mathit{\Phi}(R,\theta,\phi)=\mathit{\Phi}_{\mathrm{vib}}(R)Y_l^m(\theta,\phi). \tag{2.4.47}$$

With this ansatz we obtain the two coupled differential equations

$$\left[\hat{\vec{L}}^2-\hbar^2 l(l+1)\right]Y_l^m(\theta,\phi)=0, \tag{2.4.48}$$

$$\left[\frac{\hat{p}_R^2}{2M}+\frac{\hbar^2 l(l+1)}{2MR^2}-(E-E_{\mathrm{pot}}(R))\right]\mathit{\Phi}_{\mathrm{vib}}(R)=0. \tag{2.4.49}$$

While the former differential equation describes the angular motion of the internuclear axis, i.e. the rotation of the molecular system, and is solved by the spherical harmonics, the latter one describes the distance between the nuclei and thus the vibration of the molecule. In the following, we will briefly discuss the arising rotational and vibrational states and highlight some of their properties.

Rotational states

As already mentioned above, the differential equation for the angular degree of freedom given in eq. (2.4.48) is solved by the spherical harmonics $Y_l^m(\theta,\phi)$. This solution gives rise to discrete states of rotation that are characterised by the quantum numbers l and m. In the context of molecular rotation, the angular momentum operator is often denoted $\hat{\vec{N}}$ and the according quantum numbers are N and M_N, such that $|l,m\rangle \equiv |N,M_N\rangle$. Sticking to this notation the energy term connected to the rotation of the molecule in eq. (2.4.46) reads

$$E_{\mathrm{rot}}=\left\langle\frac{\hat{\vec{N}}^2}{2MR^2}\right\rangle=BN(N+1), \tag{2.4.50}$$

where $B=\hbar^2/(2I)$ is the rotational constant and $I=MR^2$ the moment of inertia of the molecule. When evaluating the expectation value, we assumed the molecule to be a *rigid rotor*, meaning that R is constant. Care has to be taken as this assumption is not always justified for highly excited vibrational states of Rydberg molecules that are delocalised over hundreds of Bohr radii. In this case, a proper calculation of the expectation value $\langle 1/R^2\rangle$ has to performed. For low-lying vibrational states that are well-localised, the rigid rotor model is, however, a good approximation. Even for molecules in the vibrational ground state, there is a small spread in the internuclear distance due to the vibration.

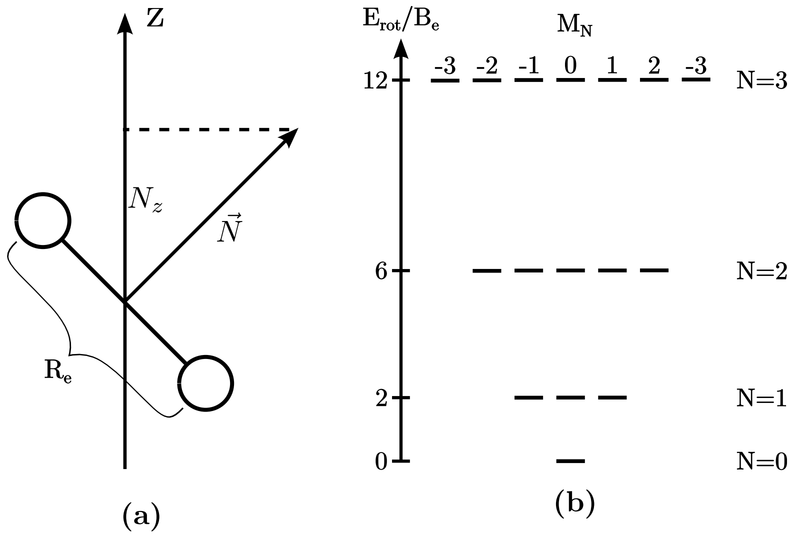

Figure 2.16: Geometry and level structure of a rigid rotor. (a) The rotational angular momentum $\vec{N}$ is perpendicular to the internuclear axis of length R_e. The projection of the angular momentum on the z-axis N_z can only have the discrete values $\hbar M_N$. (b) The energy levels of the first four N-states. The $N(N+1)$ scaling gives rise to increasing energy gaps between adjacent N-states. Each N-state consists of $2N+1$ degenerate M_N states.

To emphasise that the rotation of vibrating molecules with the equilibrium distance R_e is described, the (equilibrium) rotational constant is often denoted B_e.

As depicted in fig. 2.16a, the angular momentum $\vec{N}$ is perpendicular to the plane in which the internuclear axis rotates. The length of the angular momentum vector is given by $|\vec{N}| = \hbar\sqrt{N(N+1)}$ and its z-projection is $N_z = \hbar M_N$. For given quantum numbers N and M_N, the tip of $\vec{N}$ is thus fixed to a circle around the z-axis. The probability to find the internuclear axis oriented at an angle θ, ϕ with respect to the z-axis is given by the modulus square of the spherical harmonics $|Y_N^{M_N}(\theta,\phi)|^2$. An illustration of the spherical harmonics is given in fig. A.1. It should be noted here that without any external force all rotational states are symmetric with respect to reflection at the x-y-plane. This changes if the molecule possesses a permanent dipole moment that interacts with an external electric field along the z-axis, as will be discussed in sec. 2.6. In the field-free case the M_N states for a certain N are degenerate, as shown in fig. 2.16b.

Since the rotational constant and thus the energy splitting of the rotational states depend on $1/R_\mathrm{e}^2$, they are typically small for the high internuclear separations found in Rydberg molecules. For an internuclear separation of 933 a_0, where we find the outermost well of the ultralong-range PECs, the model predicts a rotational constant of 48 kHz. This splitting is comparable to the natural decay rate of the Rydberg states considered here[12] and thus it is hard to observe it experimentally if only the lowest N states are populated. In the other limit, the rotational constant is 3.1 MHz for the well of the triplet r-butterfly potential at 116 a_0. This splitting is not only well above the limit given by the natural decay but also within reach of the spectroscopic resolution of many experiments. In both cases, however, the rotational constant is negligible compared to the depth of the potential, which simplifies the calculation of the vibrational bound states, as shown in

---

[12] From the low-l states that support ultralong-range potentials, the P-state is the one with the smallest decay rate. In the case of the $25P$, it is 53 kHz.

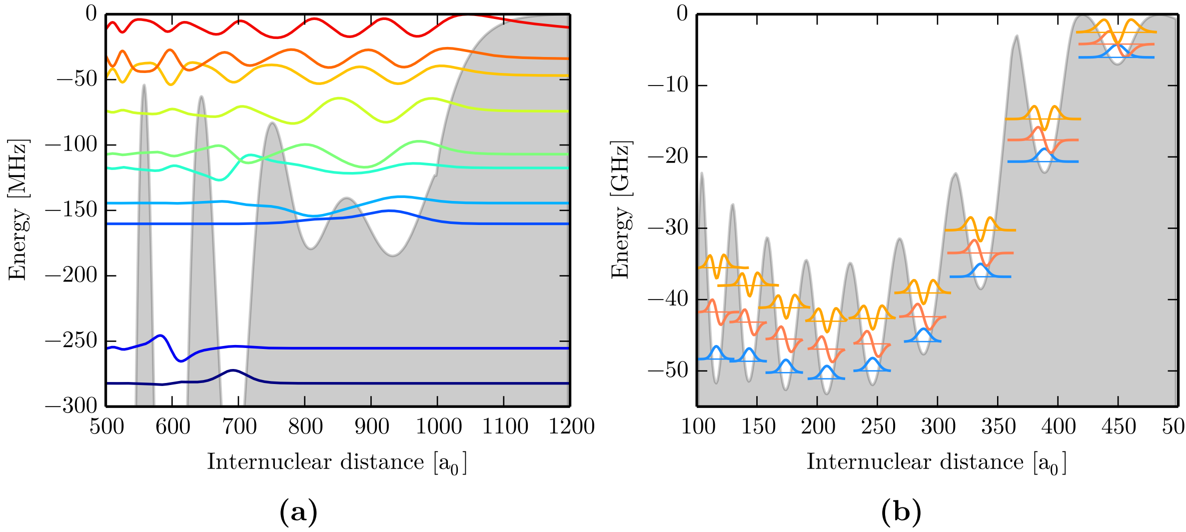

(a) **(b)**

Figure 2.17: Wave functions of the vibrational bound states obtained by the shooting method. Every wave function is shifted on the y-axis according to its binding energy. The vibrational wave functions are normalised to their respective maximum value rather than the enclosed area to visualise the structure of the excited states. (a) All appearing bound states in the $25P_{1/2}; F = 1$ triplet potential ($\tilde{F} = 1/2$) around the outermost potential minimum. The colour is a guide to the eye. (b) A subset of the vibrational bound states in the $\tilde{F} = 1/2$ r-butterfly potential. Only the states corresponding to the harmonic oscillator states in the individual wells are shown. The illustrated potential supports many more bound states, most of them highly oscillatory states bound by the envelope of the potential.

the following.

Numerical calculation of vibrational bound states

While the angular differential equation can be solved analytically, it is much harder to solve the radial equation to obtain the vibrational bound states. Due to their high bond length, the rotational energy of Rydberg molecules $BN(N+1)$ is small compared to the depth of the PECs $E_{\text{pot}}(R)$ and we can neglect the former. From eq. (2.4.49), we thus obtain

$$\left[\frac{\hat{p}_R^2}{2M} - (E - E_{\text{pot}}(R))\right] \Phi_{\text{vib}}(R) = 0. \tag{2.4.51}$$

This Schrödinger equation describes a particle of the effective mass M moving in the one-dimensional potential $E_{\text{pot}}(R)$. Due to the non-trivial behaviour of the electronic PECs (see fig. 2.12), it is in general not possible to find an analytic solution for the vibrational states and we have to resort to a numerical solution of the problem.

Here, we employ the shooting method described in sec. A.8 to determine the vibrational bound states in the PECs we obtained from the diagonalisation. Fig. 2.17a shows the bound states in the $25P_{1/2}; F = 1$ triplet potential ($\tilde{F} = 1/2$) around the outermost potential minimum, as it is shown in fig. 2.14. The leftmost plotted point is the analysis point R_1 of the shooting method (see sec. A.8). Even though this is not in the classically forbidden region, we still obtain reasonable results if the wave function passed a sufficiently high energy barrier that confines the bound state to the left. Looking at the bound states, we see that the double-well with minima at $808\,\mathrm{a}_0$ and $933\,\mathrm{a}_0$ formed by the potential give rise to non-trivial bound states. The bound state with an energy of $-160.2\,\mathrm{MHz}$ can be considered as the ground state in the double-well. Since the well at $933\,\mathrm{a}_0$ is slightly deeper, the wave function is more localised in this well and shows a shoulder at the position of the other well. For smaller binding energies, we find more vibrational wave functions that start to probe the potential at smaller internuclear separations as the potential barrier becomes smaller towards smaller internuclear separations. For example, the bound states with an energy of $-117\,\mathrm{MHz}$ and $-107\,\mathrm{MHz}$ already show a high wave function amplitude in the wells at $691\,\mathrm{a}_0$ and $597\,\mathrm{a}_0$. At even higher energies, the states are not confined by any potential barrier on the inside, which makes it counter-intuitive to see any bound states. These states are bound by the quantum reflection imposed by the sharp drop of the potential underneath them [107] that is caused by the increasing depth of the potential wells and ultimately by the crossing of the r-butterfly curves. Thus, the highly excited vibrational states are strongly oscillating and delocalised over a very long distance.

The very opposite situation is found in the increasingly deep wells that are formed by the potential for smaller internuclear separations. Already the well at $691\,\mathrm{a}_0$ is sufficiently deep that tunneling to the neighbouring wells is negligible for energies close to the minimum of the well. Such almost isolated wells can be approximated by the harmonic oscillator potential given in eq. (A.8.3). Indeed, the bound states found by the shooting method reveal the same structure of bound states as they are obtained in the harmonic oscillator model and the bound state at an energy of $-282\,\mathrm{MHz}$ can be identified with the harmonic ground state in the well. In the neighbouring well at $597\,\mathrm{a}_0$, we find a bound state at an energy of $-255\,\mathrm{MHz}$ that can be identified with the first excited state in this well.

The presence of the harmonic oscillator states gets even more obvious if we look at the highly oscillatory PEC of the $\tilde{F} = 1/2$ r-butterfly curve in fig. 2.17b. For this potential, the shooting method finds a plenitude bound states, most of which are bound by the envelope of the oscillating potential, giving rise to strongly oscillating wave functions. However, we also see the harmonic oscillator states in the individual wells. The corresponding subset of wave functions for the first three vibrational states in each well is plotted on top of the potential in fig. 2.17b. The parameters for a best fit of a harmonic potential to the individual wells of the potential for all r-butterfly PECs can be found in sec. A.9.

2.4.9. Determination of the dipole moment

In conventional diatomic homonuclear molecules, the two constituents approach each other so close that the extent of even the lowest lying electronic orbitals overlap. In such configuration, it is impossible to attribute a certain electron to a certain nucleus. Instead of the two possible localised states, the eigenstates of the system become the symmetric (gerade) and anti-symmetric (ungerade) superposition of these states, giving rise to the well-known binding and anti-binding orbitals. Since the state localised at the first nucleus overlaps the state localised at the second nucleus as much as the other way around, there can be no asymmetry in the resulting orbital. Consequently, such molecules cannot possess a permanent electric dipole moment. For Rydberg molecules, however, the situation is different. Due to the high bond length, there is no overlap of the perturber's ground state with the Rydberg core. It is therefore possible to excite the system in an asymmetric state, where one electron is in the ground state and the second electron is in the Rydberg state. Therefore, Rydberg molecules, despite of being homonuclear, possess a permanent electric dipole moment [51]. In particular, the dipole moment of the butterfly molecule arises because the maximisation of the wave function gradient at the position of the perturber requires an asymmetric distribution of the electron density along the z-axis (see fig. 2.13). In order to calculate this permanent dipole moment of the butterfly molecule, we need to know the dipole moment of the butterfly state for each internuclear separation in the region of the vibrational wave function. Let the butterfly state be

$$|\Psi_R\rangle = \sum_{i=0}^{N} c_{R,i} |i\rangle \, , \tag{2.4.52}$$

where $|i\rangle$ are the eigenstates of the unperturbed Rydberg atom. In order to get the z-component of the dipole moment of this state, we have to calculate the expectation value of the dipole operator $\hat{d}_z = q\hat{z}$ and we obtain

$$d_z(R) = q \langle \Psi_R|\hat{z}|\Psi_R\rangle = \sum_{i,j}^{N} c^*_{R,i} c_{R,j} \langle i|\hat{z}|j\rangle \, . \tag{2.4.53}$$

This means that the dipole moment of the butterfly state can be calculated from a sum of the dipole matrix elements $\langle i|q\hat{z}|j\rangle$ of the unperturbed Rydberg states. As described in sec. 2.3.1, the numerical calculation of these dipole matrix elements is readily available. The coefficients $c^*_{R,i}$ and $c_{R,j}$ are obtained from the eigenvectors of the diagonalisation described in sec. 2.4.5. As one can see from eq. (2.4.53), we only obtain a permanent electric dipole moment if states with a dipole-allowed transition are mixed. Since ultralong-range Rydberg molecules are predominantly in only one low-l state, they show negligible dipole moments. The high-l states on the other hand strongly mix the degenerate states from the hydrogenic manifold and thus many dipole-allowed combinations of states in eq. (2.4.53) lead to a high permanent electric dipole moment. For instance, the butterfly molecules studied in sec. 6.3 show dipole moments in excess of 500 D and in caesium molecular states with a high admixture of the trilobite state were reported to have a dipole moment in the kilo-Debye range [49]. The dipole moment of the butterfly states is almost identical for the three different $\tilde{F}$ quantum numbers and will be discussed in sec. 6.3.1.

In order to obtain the dipole moment of a certain molecular bound state, we also have to take into account the vibrational wave function of the molecule $\varPhi(R)$. The averaged dipole moment is then given by

$$\bar{d_z} = \int |\varPhi(R)|^2 d_z(R) \; \mathrm{d}R. \tag{2.4.54}$$

2.5. Rydberg–Rydberg interaction

After a detailed introduction to the interaction between a Rydberg atom and a ground state atom, we will now turn to the interaction between a pair of atoms which are both in Rydberg states. This interaction is of particular interest in the case of high excitation densities in atomic samples, where on average more than one atom is excited into Rydberg states. The discussion given here will be restricted to the fundamental principles and the consequences of the Rydberg–Rydberg interaction as far as they are of relevance for this work. A more detailed discussion of these interactions can be found in refs. [73, 76, 108].

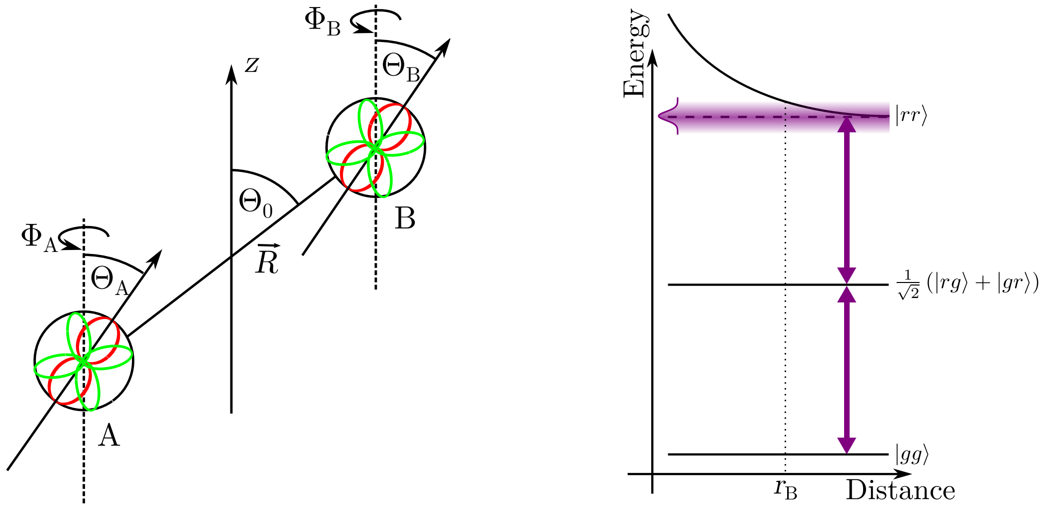

(a) **(b)**

Figure 2.18: Rydberg–Rydberg interaction and the blockade mechanism arising from it. (a) The Rydberg atoms A and B are separated by the vector $\vec{R}$ that encloses the angle Θ_0 with the quantisation axis. By the multipole expansion, the charge distribution of the atoms can be expandend in the monopole moment (black), the dipole moment (red), the quadrupole moment (green), and so on. The reference frame of the multipole of atom A (B) is tilted with respect to the quantisation axis by Θ_A (Θ_B). (b) Two-atom energy scheme for two atoms that are either in the ground state $|g\rangle$ or in the Rydberg states $|r\rangle$. The strong Rydberg–Rydberg interaction gives rise to a distance dependent energy level for the doubly excited state $|rr\rangle$. At the blockade radius r_B, the interaction shift becomes bigger than the linewidth of the excitation laser (purple shaded area). It is thus not possible to excite two Rydberg atoms at smaller separations than r_B.

To obtain the electro-magnetic interaction between the two Rydberg atoms A and B in its most general form, their charge distribution can be expanded in the respective multipole moments. In spherical coordinates and atomic units, the Coulomb interaction between the multipoles that are separated by the vector $\vec{R} = (R, \Theta_0, \Phi_0)$ reads [109]

$$\hat{V}_{AB} = \sum_{l=0}^{\infty} \sum_{l'=0}^{\infty} \frac{(-1)^{l'} \hat{r}_A^{l} \hat{r}_B^{l'}}{R^{l+l'+1}} \sum_{m=-l}^{l} \sum_{m'=-l'}^{l'} B_{ll'}^{mm'} C_{l+l'}^{-m-m'}(\Theta_0, 0) \hat{C}_l^m(\Theta_A, \Phi_A) \hat{C}_{l'}^{m'}(\Theta_B, \Phi_B), \tag{2.5.1}$$

where l and l' denote the order of the dipole expansion of the respective atom, the angles Θ_0, Θ_A, Θ_B, Φ_A, and Φ_B are defined as shown in fig. 2.18a,

$$B_{ll'}^{mm'} = (-1)^{m+m'} \sqrt{\frac{(l+l'+m+m')!(l+l'-m-m')!}{(l+m)!(l-m)!(l'+m')!(l'-m')!}}, \tag{2.5.2}$$

and

$$C_k^q(\Theta, \Phi) = \sqrt{\frac{4\pi}{2k+1}} Y_k^q(\Theta, \Phi) \tag{2.5.3}$$

are the renormalised spherical harmonics. As the interaction scales with $R^{l+l'+1}$, the higher orders of the multipole expansion quickly vanish if the atoms are separated further from each other. Since neutral atoms possess no monopole moment, the leading order for $R \to \infty$ is the dipole–dipole interaction ($l = l' = 1$). For large separations, the interaction operator in eq. (2.5.1) can thus be approximated by the dipole–dipole potential $\hat{V}_{\mathrm{dd}}$. By carrying out the sums in eq. (2.5.1) and realising that the dipole operator for atom $i \in \{\mathrm{A}, \mathrm{B}\}$ in spherical coordinates is given by $\hat{p}_i^q = \hat{r}_i \hat{C}_1^q$ one can show that the dipole–dipole interaction operator is given by [108]

$$\begin{aligned}\hat{V}_{\mathrm{dd}} = \frac{1}{R^3}\Bigg[& -\hat{p}_{\mathrm{A}}^{+}\hat{p}_{\mathrm{B}}^{-} - \hat{p}_{\mathrm{A}}^{-}\hat{p}_{\mathrm{B}}^{+} + \hat{p}_{\mathrm{A}}^{0}\hat{p}_{\mathrm{B}}^{0}(1 - 3\cos^2\Theta_0) \\ & - \frac{3}{2}\sin^2\Theta_0(\hat{p}_{\mathrm{A}}^{+}\hat{p}_{\mathrm{B}}^{+} - \hat{p}_{\mathrm{A}}^{+}\hat{p}_{\mathrm{B}}^{-} - \hat{p}_{\mathrm{A}}^{-}\hat{p}_{\mathrm{B}}^{+} + \hat{p}_{\mathrm{A}}^{-}\hat{p}_{\mathrm{B}}^{-}) \\ & - \frac{3}{\sqrt{2}}\sin\Theta_0\cos\Theta_0(-\hat{p}_{\mathrm{A}}^{+}\hat{p}_{\mathrm{B}}^{0} + \hat{p}_{\mathrm{A}}^{-}\hat{p}_{\mathrm{B}}^{0} - \hat{p}_{\mathrm{A}}^{0}\hat{p}_{\mathrm{B}}^{+} + \hat{p}_{\mathrm{A}}^{0}\hat{p}_{\mathrm{B}}^{-})\Bigg],\end{aligned} \tag{2.5.4}$$

where $q = \pm 1$ in the index of the dipole operators was abbreviated by ±. As pointed out in sec. 2.3, alkali atoms do not possess a permanent dipole moment due to the symmetry of the atomic orbitals. Therefore, the expectation value of V_{dd} will vanish and we obtain no interaction in first order perturbation theory.

In second order, however, we can take into account the interaction of the mutually induced dipole moments. If we consider a pair state of the form $|\mathrm{pair}\rangle = |n, l, j, m_j\rangle_{\mathrm{A}} \otimes |n', l', j', m_j'\rangle_{\mathrm{B}}$, the energy correction reads

$$\Delta E_{\mathrm{pair}} = \sum_{|\mathrm{pair}'\rangle} \frac{|\langle \mathrm{pair}'|\hat{V}_{\mathrm{dd}}|\mathrm{pair}\rangle|^2}{E_{\mathrm{pair}'} - E_{\mathrm{pair}}}, \tag{2.5.5}$$

where the sum runs over all possible pair states. Since there is an infinite number of pair states, the basis has to be truncated to be able to calculate the energy correction. Since the denominator of eq. (2.5.5) weights the individual terms with their energy difference to the considered pair state, it is reasonable to restrict the basis to those states that are close in energy. In most cases, there are only few neighbouring pair states that contribute the most to the overall energy shift. If we insert the expression for the dipole–dipole interaction from eq. (2.5.4) into eq. (2.5.5), we see that the R-dependence can be drawn out of the sum and the energy correction can be written as

$$\Delta E_{\mathrm{pair}} = \frac{C_6(\Theta_0)}{R^6}, \tag{2.5.6}$$

which is the well-known form of the van-der-Waals interaction. It should be stressed here that the angular dependence of the C_6 coefficient is only meaningful if the interaction that creates the quantisation axis is stronger than the van-der-Waals interaction. If, on the other hand, the van-der-Waals interaction is much stronger, the angle Θ_0 becomes meaningless and the dipoles will orient in the configuration of minimal energy, which is the anti-parallel alignment. Since the reference frame of our perturbation calculation still relies on the (weak) quantisation axis and the quantum numbers arising from it, we will only obtain the right result in the case where the dipoles orient along the quantisation axis. From fig. 2.18a, we can see that this situation is realised for $\Theta_0 = \pi/2$. In case of a weak quantisation axis, we therefore obtain

$$C_6 = -\sum_{|\mathrm{pair}'\rangle} \frac{|\langle \mathrm{pair}'|\hat{p}_{\mathrm{A}}^{+}\hat{p}_{\mathrm{B}}^{-} + \hat{p}_{\mathrm{A}}^{-}\hat{p}_{\mathrm{B}}^{+} + 2\hat{p}_{\mathrm{A}}^{0}\hat{p}_{\mathrm{B}}^{0}|\mathrm{pair}\rangle|^2}{E_{\mathrm{pair}'} - E_{\mathrm{pair}}}. \tag{2.5.7}$$

To evaluate the importance of this interaction for Rydberg atoms, it is instructive to look at the scaling behaviour of the C_6 coefficient with the principal quantum number n of the Rydberg state. If we consider two neighbouring pair states that give rise to the leading contribution of the sum in eq. (2.5.7) and realise that the dipole moment scales as $p \propto n^2$ and the energy difference of adjacent Rydberg states scales as $\Delta E \propto n^{-3}$, we see that C_6 scales as

$$C_6 \propto \frac{|n^2 n^2|^2}{n^{-3}} = n^{11}. \tag{2.5.8}$$

While for ground state atoms the van-der-Waals interaction is only relevant for very short atomic separations, i.e. in the molecular potential of Rb_2, the enormous scaling of the C_6 coefficient renders it an important process for Rydberg atoms over distances of several micrometre. For example, a pair of rubidium atoms in the $51P$-state that is separated by $1\,\mu\mathrm{m}$ experiences an energy shift on the order of $50\,\mathrm{GHz}$. This giant interaction over a length scale that is much bigger than the typical interatomic distance in dense cold gases gives rise to the unique many-body effect of interaction blockade, as explained in the following.

2.5.1. Rydberg blockade

The strong interaction between two Rydberg atoms has a tremendous effect on the excitation dynamics of the two-body system. If the excitation laser is set to resonantly drive the $|g\rangle \leftrightarrow |r\rangle$ transition, it can excite one of the two atoms into the Rydberg state. Whether the second atom can also be excited now depends on the distance between the two atoms since the Rydberg–Rydberg interaction shifts the doubly excited state $|rr\rangle$ out of resonance with the excitation laser. As shown in fig. 2.18b, one can define the so-called *blockade radius* at which the energy shift due to the interaction becomes bigger than the maximum of the linewidth of the excitation laser γ_L and the linewidth γ of the $|rr\rangle$ level. If the two Rydberg atoms are far enough apart such that we can neglect higher multipole moments, they undergo pure van-der-Waals interaction and the blockade radius is given by

$$r_B = \sqrt[6]{\frac{C_6}{\hbar \max(\gamma, \gamma_L)}}. \tag{2.5.9}$$

Inserting eq. (2.5.8) into eq. (2.5.9), we see that the blockade radius scales almost quadratically with the principal quantum number n. For experimentally achievable parameters, the blockade radius becomes significantly larger than the typical particle separations in cold clouds. It is therefore reasonable to extent the results from the simple two-atom model to a many-body picture. In this case, a single Rydberg atom is able to suppress the excitation of a second atom within a sphere of radius r_B, the so-called blockade sphere. In ultracold rubidium clouds, it has already been shown experimentally that the blockade radius is roughly $5\,\mu\mathrm{m}$ for the $43S$ state [110] and $2.5\,\mu\mathrm{m}$ for the $51P$-state [42], which gives rise to several hundred atoms per blockade sphere. Since all atoms within the blockade sphere can at maximum share one excitation, they act like a simple two-level system, that is often referred to as a *superatom* [41–43, 111, 112].

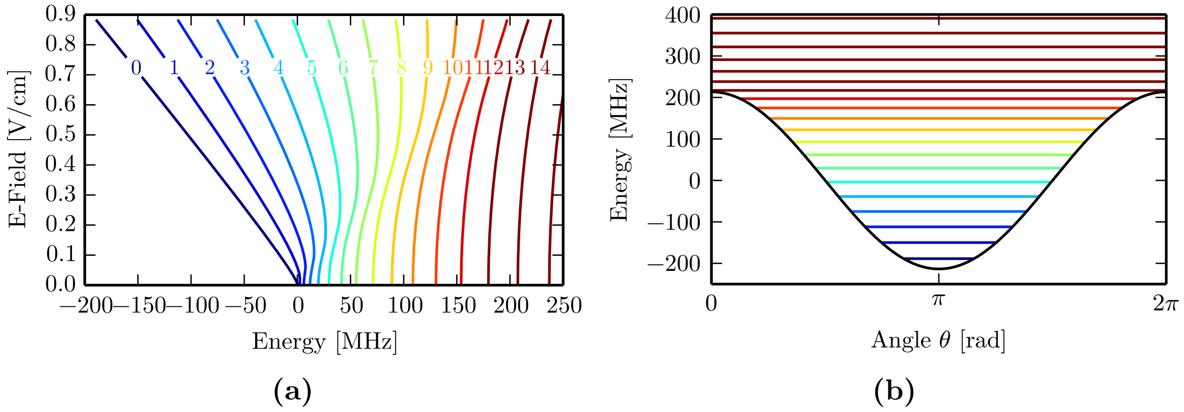

Figure 2.19: Eigenenergies of the $|M_N| = 0$ pendular states for a molecule with a dipole moment of $d = 482\,\mathrm{D}$ and a bond length of $R_\mathrm{e} = 205\,\mathrm{a}_0$. (a) Eigenenergies obtained from the diagonalisation of the Hamiltonian from eq. (2.6.1) for varied electric fields up to $0.88\,\mathrm{V/cm}$. For vanishing field, the resulting states show the expected $N(N+1)$ scaling. For high fields ($dE \gg B_\mathrm{e}$), the rotation is more and more restricted by the interaction with the field and the pendular states emerge. The quantum number ν of the pendular state is noted for every energy curve. The colour is a guide to the eye, all states with $\nu > 13$ have the same colour. (b) For the highest electric field of $0.88\,\mathrm{V/cm}$ the eigenenergies are shown in the effective $\cos(\theta)$ potential (black). The energy axis and the colour code are identical to (a).

2.6. Pendular states of dipolar molecules

Motivated by the large permanent electric dipole moment that trilobite and butterfly Rydberg molecules exhibit (see also secs. 2.4.9 and 6.4), we will now analyse the behaviour of a diatomic dipolar molecule inside an electric field. In a classical picture, the dipole moment of the molecule would simply align along the direction of the electric field to minimise its energy. However, we also have to take into account the rotation of the molecule (sec. 2.4.8) that counteracts the orientation. In the rigid rotor model[13], we can describe the rotation of the molecule with the reduced mass M in an electric field $\vec{E} = E\hat{z}$ in analogy to eq. (2.4.50) by

$$\hat{H}_\mathrm{rot} = B_\mathrm{e}\hat{\vec{N}}^2 - dE\cos\theta, \tag{2.6.1}$$

with the rotational constant $B_\mathrm{e} = \frac{\hbar^2}{2MR_\mathrm{e}^2}$ and the dipole moment d of the molecule. To diagonalise the Hamiltonian, it is convenient to use the eigenbasis of the squared angular momentum operator $\hat{\vec{N}}^2$ that is described by the rotational quantum number N and its projection M_N. In this basis, the matrix elements of the $\cos\theta$-term are expressed by eq. (2.3.21). Already from the form of the $\cos\theta$-operator, we see that the electric field interaction couples states of the same M_N but different N quantum number. This is the mathematical expression of the fact that the electric field breaks the isotropy of the problem and thus the angular momentum is not conserved. Consequently, N is not a good quantum number any more. Yet, the rotational invariance around the z-axis is not violated and the projection of the angular momentum is a conserved quantity. Accordingly, M_N remains a good quantum number even in the presence of the electric field.

Since the $\cos\theta$-operator couples only states of the same M_N, the Hilbert space can be separated in independent subspaces according to this quantum number. The diagonalisa-

---

[13] The assumption that the bond length is fixed is well justified for the tightly localised butterfly molecules.

tion of the Hamiltonian in eq.(2.6.1) can then be performed for the individual subspaces. Since, furthermore, the sign of the M_N quantum number has no physical relevance with respect to the electric field interaction, the two $\pm M_N$ states are degenerate and we can identify those two degenerate states by $|M_N|$. For the $|M_N| = 0$ subspace, the result of the diagonalisation for varied field strength E is shown in fig. 2.19a. Since for vanishing field the molecule can rotate freely, we recover the case discussed in sec. 2.4.8 where the eigenenergies scale as $N(N+1)$ and the eigenfunctions are the spherical harmonics (see fig. A.1). As the external field increases, the dipole tends to align along the electric field direction but the rotation counteracts the alignment. A figurative image of the situation can be obtained if the $\cos\theta$-term in eq. (2.6.1) is understood as an angular potential[14]. If the interaction with the field is much stronger than the rotational energy $dE \gg B_\mathrm{e}$, the motion in θ-direction is restricted by the $\cos(\theta)$ potential shown in fig. 2.19b [113]. If the potential is sufficiently deep, the cosine can be approximated by a harmonic potential and the eigenfunctions are given by the harmonic oscillator solution. Due to this analogy and due to the confinement in θ-direction that causes the classical dipole to oscillate like a pendulum, the solutions in the high field limit are often called *pendular states* [113,114] and labeled by the quantum number ν. For $dE/B_\mathrm{e} \to \infty$, the energies of the pendular states scale as

$$E_\nu \to -\frac{dE}{B_\mathrm{e}} + \frac{1}{\sqrt{2dE/B_\mathrm{e}}}\,(\nu + 1)\,. \qquad (2.6.2)$$

The expected linear scaling of the eigenenergies with respect to ν can be observed for the highest fields in the diagonalisation results in fig. 2.19a. While this holds for the lowest pendular states, it breaks down at around $\nu = 10$, where the rotational energy starts to dominate the electric field interaction and for even higher ν we will recover the $N(N+1)$ scaling.

In order to illustrate the angular orientation probability of the dipolar molecule, we analysed the eigenvectors from the diagonalisation for the highest field in fig. 2.19a and overlapped the spherical harmonics that form our basis accordingly. For the lowest four ν states in the lowest four $|M_N|$ subspaces, the result is shown in fig. 2.20a. In general, all depicted pendular states have a vanishing probability to orient in $-z$ direction due to the strong interaction with the field. Furthermore, we can see that the quantum number ν corresponds to the number of nodes in θ-direction, independent of $|M_N|$. Consequently, the states with $\nu = 0$ possess the highest alignment in the field, which is also reflected by the fact that the $\nu = 0$ state is the lowest in energy. The alignment strength of a pendular state $|\varPhi_\nu\rangle$ can be quantified by the expectation value $\langle\varPhi_\nu|\cos\theta|\varPhi_\nu\rangle$ of the $\cos\theta$-operator. Since the pendular states are a superposition of the angular momentum states $|N, M_N\rangle$, we can express the expectation value as

$$\langle\varPhi_\nu|\cos\theta|\varPhi_\nu\rangle = \sum_{N,N'} c^*_{\nu,N'} c_{\nu,N}\,\langle N', M_N|\cos\theta|N, M_N\rangle \qquad (2.6.3)$$

and the occurring expectation value of the angular momentum eigenstates with respect to the $\cos\theta = C^0_1(\theta,\phi)$ operator can be solved by applying the Wigner–Eckart theorem. For the case demonstrated in fig. 2.20a, the alignment of the $|M_N| = 0$, $\nu = 0$ state in a field of $0.88\,\mathrm{V/cm}$ is $\langle\cos\theta\rangle = 0.96$, which is already close to unity, meaning perfect

---

[14] Note that in terms of angular motion the squared angular momentum operator $\hat{\vec{N}}^2$ is equivalent to the squared momentum operator $\hat{\vec{p}}^2$ that appears in the kinetic energy of a linear motion.

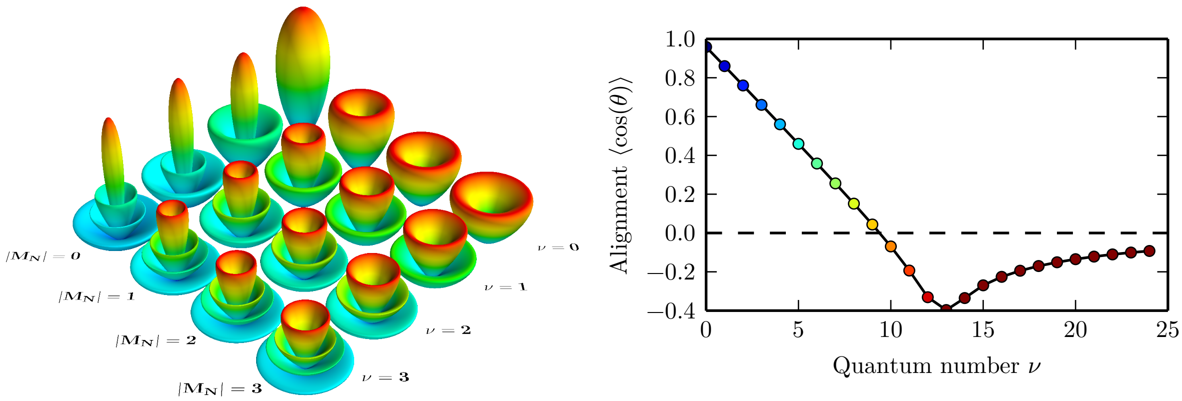

(a) **(b)**

Figure 2.20: Alignment of the pendular states. (a) Plot of the eigenfunctions in a field of 0.88 V/cm for the first four $|M_N|$ subspaces. For each ν and $|M_N|$, the distance from the respective origin gives the absolute value of the wave function $|\Phi(\theta, \phi)|$. The colour is a guide to the eye. (b) Alignment $\langle\cos(\theta)\rangle$ of the different $|M_N| = 0$ pendular states with the quantum number ν for a dipole moment of $d = 482\,\mathrm{D}$ and a bond length of $R_\mathrm{e} = 205\,\mathrm{a}_0$ in a field of 0.88 V/cm. While for low ν the rotor is highly aligned with the field, it is perpendicular to the field between $\nu = 9$ and $\nu = 10$. For $\nu = 13$, it becomes maximally anti-aligned to the field. For even higher quantum numbers, the rotation is not bound any more in the cos-potential (fig. 2.19b) and the alignment vanishes. The colour denotes the same ν states as in fig. 2.19.

alignment. For increasing ν, however, the orientation vanishes and the dipole can even become anti-aligned to the field [113], as depicted in fig. 2.20b. Here, we see that the $|M_N| = 0$, $\nu = 13$ state has an alignment of $\langle\cos\theta\rangle = -0.40$. In the cos-potential, shown in fig. 2.19b, this is the highest energy state that is still bound in the potential. All higher quantum numbers correspond to unbound states for which the interaction with the field can be seen as a perturbation of the free rotation. Hence, we approximately recover the spherical harmonics as eigenfunctions and the alignment vanishes as the quantum number ν increases.

2.6.1. Coupling strength and polarisation dependence

Upon photoassociation of a molecule, the angular momentum of the incident photon is transferred to the molecular system. If the photoassociation is performed from a BEC that possesses no angular momentum in the centre of mass motion, the initial rotational state is described by $|N = 0, M_N = 0\rangle$. Since the photons of the excitation laser carry one quantum of angular momentum, it is only possible to couple to the $|N = 1, M_N = 0, \pm 1\rangle$ state. Which of the three possible M_N states is coupled depends on the polarisation of the excitation laser. Motivated by the excitation beam setup described in sec. 3.5.1, we consider the case of a laser propagating in the horizontal plane while the electric field is applied in the vertical direction. For a linearly polarised laser, it is thus possible to realise pure π-coupling if the polarisation is aligned parallel to the electric field. On the other hand, a superposition of $\sigma^\pm$-coupling is realised if the polarisation is aligned perpendicular to the electric field axis. By rotating the polarisation of the excitation laser, it is thus possible to select whether to couple to the $|N = 1, M_N = 0\rangle$ or to the $|N = 1, |M_N| = 1\rangle$ state.

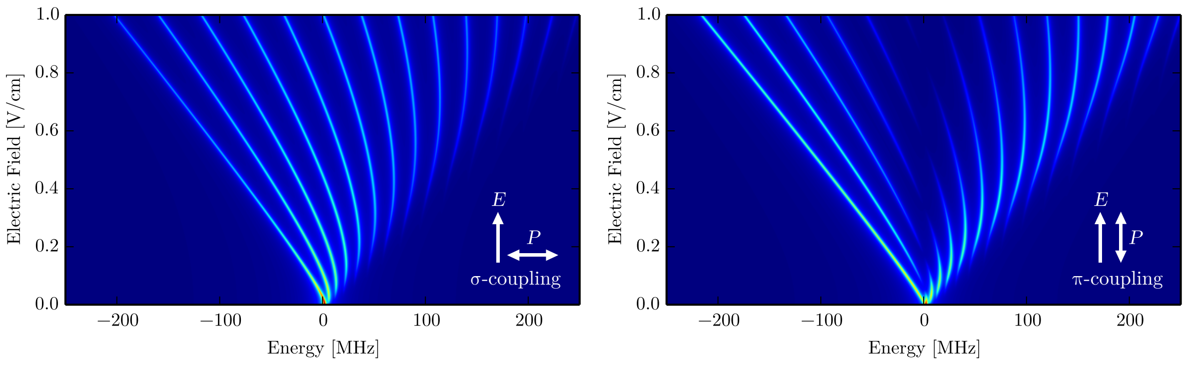

(a) **(b)**

Figure 2.21: Theoretical spectrum of pendular states in various electric field strengths (Stark map). The colour denotes the coupling strength. The calculation was performed for a dipole moment of $d = 482\,\mathrm{D}$ and a bond length of $R_\mathrm{e} = 205\,\mathrm{a}_0$. (a) Coupling to the $|N = 1, |M_N| = 1\rangle$ state as it is relevant for a $\sigma^\pm$-transition driven by linear laser polarisation perpendicular to the field axis. (b) Coupling to the $|N = 1, M_N = 0\rangle$ state as it is relevant for a π-transition driven by linear laser polarisation parallel to the field axis.

Due to the interaction with the electric field, the $|N = 1, M_N = 0, \pm 1\rangle$-character spreads over the emerging pendular states. In order to calculate the coupling strength to a certain pendular state $|\Phi_\nu\rangle$, we therefore have to analyse the eigenvectors from the diagonalisation described in sec. 2.6 to find the overlap with the $|N = 1, M_N = 0, \pm 1\rangle$ state. If for every pendular state ν we use the coupling strength as the amplitude of a Lorentzian profile that is displaced on the detuning axis by the corresponding eigenenergy E_ν (fig. 2.19a), we can model the spectrum for a certain electric field strength. Repeating this procedure for various electrical field strengths and combining the spectra to a Stark map, we obtain the results shown in fig. 2.21. Since these Stark maps are calculated for the same parameters, they can be directly compared to fig. 2.19a, which does not include the coupling strength. It is striking that for increasing field strength the $|N = 1, M_N = 0, \pm 1\rangle$ state spreads over more and more pendular states and we recover an envelope that is symmetric around the energy of the field-free $|N = 1, M_N = 0, \pm 1\rangle$ state.

The comparison between the $\sigma^\pm$-coupling in fig. 2.21a and the π-coupling in fig. 2.21b reveals a very intriguing difference. While in the $\sigma^\pm$-case the coupling is maximal in the centre of the fan, it shows a nodal line at the same place for π-coupling. This behaviour can be understood qualitatively by the orientation of the dipole in the electric field relative to the laser polarisation. As discussed in sec. 2.6, the orientation $\langle\cos\theta\rangle$ is maximal for $\nu = 0$ and we can imagine the dipole to be aligned parallel to the field. Since the coupling to the dipole is the strongest when the polarisation of the light is parallel to the orientation of the dipole, we see a strong coupling for the π-case, where the light polarisation is also aligned to the field axis. In the $\sigma^\pm$-case, however, the light polarisation is perpendicular to the field axis and thus to the alignment of the dipole. Consequently, we see a weak coupling to the $\nu = 0$ state in this case[15]. The situation changes when we consider pendular states of higher ν, where the orientation $\langle\cos\theta\rangle$ reduces and at some point vanishes. In this situation, the dipole moment has no z-component anymore and can thus be imagined to lie in the plane perpendicular to the field. In this case, we obviously cannot couple any more with the π-transition since the dipole is now perpendicular to the laser polarisation.

---

[15] The coupling does not vanish completely as the orientation of the dipole is not perfect and has a residual component in the horizontal plane.

We therefore see the nodal line in the coupling strength in fig. 2.21b. If the dipole is perpendicular to the field, the system does neither loose nor win energy compared to the field-free case. Therefore, the nodal line appears at the energy of the field free $|N = 1, M_N = 0\rangle$ state. The $\sigma^{\pm}$-transition on the other hand has the strongest coupling at this point since the dipole is now parallel to the laser polarisation. Going to even higher values of ν, the dipole starts to anti-align with the field and consequently recovers a better coupling by the π-light while the coupling in the $\sigma^{\pm}$-case starts to drop again. Ultimately, ν becomes so high that the rotational energy dominates over the field interaction and the wave function becomes symmetric again. Due to this symmetry, the dipole moment averages out and the coupling vanishes irrespective of the laser polarisation.

3. Experimental setup

The apparatus used for the presented study on Rydberg–ground state interactions in ultracold gases is a highly efficient state-of-the-art quantum gas experiment. Based on the experiences of an earlier design [115], the second-generation apparatus puts the focus on combining electron microscopy of ultracold gases with the peculiar properties of Rydberg states. The ability of the electron beam to image and tailor the ground state density distribution [116, 117] combined with a single photon transition into Rydberg states [118] and a 3D optical lattice [119] allows to study many facets of the rich phenomena arising through the strong Rydberg interactions. In the past, this unique combination could be used to successfully study electron-impact induced l-changing collisions [120] and collective many-body behaviour in a superatom [42] and to establish a new method to observe the superfluid to Mott insulator transition by monitoring the creation of Rydberg molecules [121].

This chapter will give a brief description of the parts of the apparatus that are relevant for the presented experiments. We will review the laser system for optical cooling in a 2D and a 3D magneto-optical trap (MOT) and the near-infrared laser system for evaporative cooling, which are used to prepare ultracold samples of ^{87}Rb. Furthermore we will present the UV laser system used to realise a single photon transition into Rydberg P-states and the ion detection system that allows to observe the Rydberg population by means of spontaneously created ions. A more detailed description of the experimental apparatus, including the electron beam and the optical lattice setup, can be found in refs. [112, 119, 120].

3.1. Magneto-optical trap

For the presented experiments, we need to cool an atomic cloud to temperatures in the nanokelvin range. Starting from room temperature, the majority of kinetic energy is removed from the atoms by laser cooling [122]. In this scheme, the Doppler effect shifts a closed atomic transition into resonance with the counter-propagating laser beam only. Consequently, the atom is slowed down by the momentum kick imposed by absorption of the counter-propagating photons. Since the result is a velocity dependent force, such configuration is called *optical molasses* in analogy to the situation in viscous media. Extending this scheme by means of a magnetic gradient field that shifts the Zeeman-levels of the atoms depending on their position, an additional spatial confinement can be added. Such combined system is called *magneto-optical trap* (MOT) and was first demonstrated in 1987 [21].

Since the momentum kick from a single photon is very small, hundred thousands of scattering events are required to stop a particle with a thermal velocity set by room temperature. It is therefore necessary to find a closed transition in the atom such that after the scattering the atom ends up in the same initial state as before the scattering. In this case, the atom can repeatedly undergo the scattering and can thus be cooled

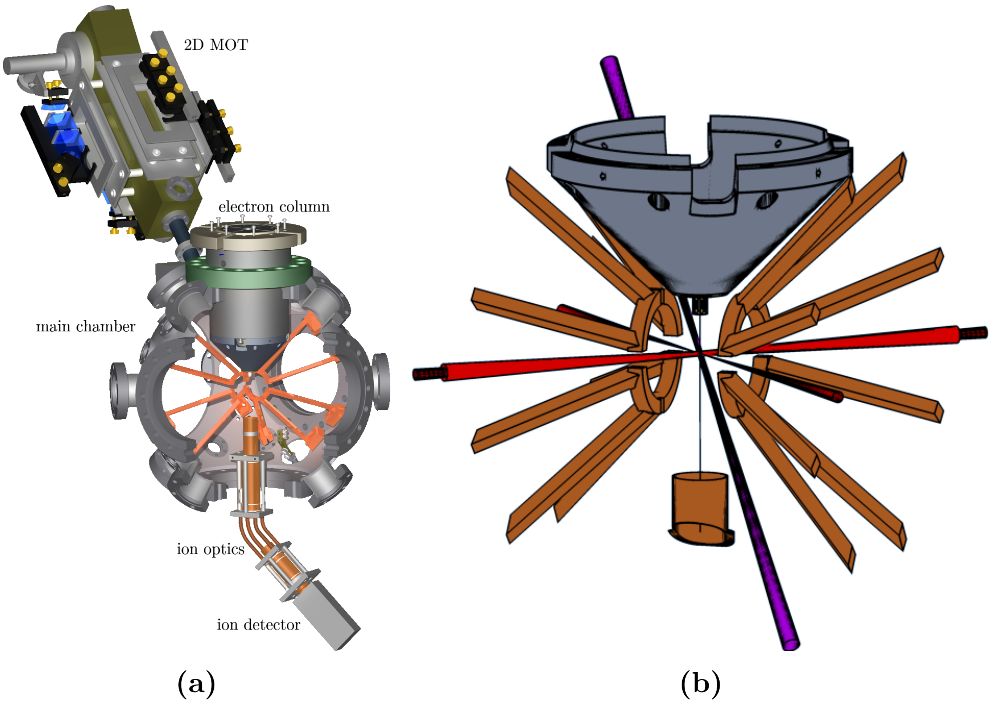

Figure 3.1: The experimental apparatus. (a) The body of the 2D MOT (olive, upper left) is surrounded by the mounting for the rectangular coils (grey) and the optomechanics (black) to insert and reflect the cooling light into the chamber. The resulting atomic beam enters the main chamber through the differential pumping tube. The main chamber (grey, centre) hosts eight copper electrodes whose tips form two opposing circles. On the top flange of the chamber, the electron column [112, 116] is connected, on the bottom flange an ion optics enters the chamber. (b) A magnified, schematic view of the main chamber. The beam axes for the dipole trap (red) and the UV laser (purple) are indicated. The figures were taken from ref. [111].

efficiently. In ^{87}Rb, the hyperfine transition

$$|5S_{1/2}, F = 2\rangle \leftrightarrow |5P_{3/2}, F' = 3\rangle \tag{3.1.1}$$

at a wavelength of $\lambda = 780\,\mathrm{nm}$ is commonly used as a cooling transition. This transition alone does not completely fulfil our requirements for a closed transition because off-resonant scattering to the $|5P_{3/2}, F' = 2\rangle$ and subsequent decay to the $|5S_{1/2}, F = 1\rangle$ can occur. While the probability for this transition is small for a single scattering event, the immense number of events will eventually pump all atoms into the $|5S_{1/2}, F = 1\rangle$ state and the cooling stops. In order to close the cooling cycle again, a further laser on the $|5S_{1/2}, F = 1\rangle \leftrightarrow |5P_{3/2}, F' = 2\rangle$ transition is added to depopulate the $|5S_{1/2}, F = 1\rangle$ state.

The limit of laser cooling is usually given by the Doppler-temperature that originates from the equilibrium between the laser cooling effect and the heating of the atoms due to photon scattering [122]. However, because of the typical beam configuration of counter-propagating counter-rotating σ-polarised laser beams, sub-Doppler cooling is usually achieved in MOT-setups by inherent polarisation gradient cooling [123].

To create the necessary laser light for cooling and repumping, we employ external cavity diode lasers (ECDL) in Littrow configuration [124, 125] that feature a typical linewidth below 1 MHz. A frequency reference is created by FM-locking [126] the so-called *master* *laser* to the $(1, 3)$-crossover peak in a Doppler-free absorption spectroscopy [127], which is 212 MHz red shifted with respect to the resonance. The laser for the cooling transition (*"cooler"*) is stabilised by a beating-lock [128] to the master laser. This allows to detune the cooler up to several hundred MHz relative to the master laser's frequency and thus overcome the frequency gap to the resonance. While running the MOT, the cooling laser is blue-detuned by 196 MHz from the master frequency, giving rise to 16 MHz red-detuning from the cooling transition's resonance. The laser for the repumping transition is FM-locked to the $(1, 2)$-crossover of the repumping transition, which is 76.5 MHz red-detuned with respect to the repumper line. The frequency of the laser is shifted back to resonance by a single pass through an acusto-optical modulator (AOM) [129]. A more detailed discussion of the stabilisation and the distribution of the lasers is given in refs. [42, 125].

The presented apparatus employs a two-step laser cooling scheme that consists of a 2D MOT [130, 131] and a 3D MOT in separated vacuum chambers that are connected by a differential pumping tube (fig. 3.1a). In the following, the two subsystems are discussed separately.

2D MOT

The 2D MOT vacuum system is evacuated to a residual gas pressure of $p_{\mathrm{2D},0} \approx 10^{-10}$ mbar. A piece of bulk rubidium is degassing inside the chamber such that the chamber is flooded with rubidium vapour. The resulting pressure in the chamber that is solely pumped by the pump in the main chamber through the differential pumping tube is $p_{\mathrm{2D}} = 10^{-6}$ mbar. Two orthogonal coil pairs in anti-Helmholtz configuration create a magnetic gradient field in two spatial dimensions, resulting in a line of vanishing magnetic field in the centre of the chamber. The cooling light for the 2D MOT is generated by amplification of the master laser through a tapered amplifier (TA) [132] and subsequent frequency shift by an AOM. The light is split into two separate beams, each aligned to propagate on one of the coil-pair axes and each being reflected back after passing the chamber. Such configuration gives rise to a cigar-shaped cooling volume that captures atoms from the rubidium-rich background gas and cools it radially. Since the third spatial dimension maintains its thermal velocity distribution and there is also no confinement in this direction, such setup creates a directed beam of atoms that spreads in both directions of the third dimension. An additional laser resonant to the cooling transition, the so-called *push-beam*, is aligned along the third axis. The radiation pressure of this laser forces the backwards moving atoms in the opposite direction and thus creates an atom beam that only expands in a single direction. The alignment of this configuration is such that the resulting atom beam is directed towards the differential pumping tube and can thus propagate into the main chamber where the 3D MOT is loaded from the atom beam.

3D MOT

Through the differential pumping tube, a pressure difference of four orders of magnitude between the 2D MOT chamber and the main chamber is achieved. Consequently, the background pressure in the main chamber is typically $p_{\mathrm{3D}} = 10^{-10}$ mbar. A magnetic quadrupole field for the 3D MOT is created by driving an electric current through the eight in-vacuum electrodes to create a circular current in the ring-shaped tips (fig. 3.1b). In anti-Helmholtz configuration and for a current of 100 A, we achieve a magnetic field gradient of 16.8(12) $^{\mathrm{G}}/_{\mathrm{cm}}$ along the coil axis and 8.2(7) $^{\mathrm{G}}/_{\mathrm{cm}}$ perpendicular to it [119].

The cooling laser is split into six individual two-inch σ-polarised beams with a power of roughly 15 mW each to realise two counter-propagating beams for each of the three spatial dimensions. The normal of the two coils formed by the electrodes defines the so-called strong axis to which one of the cooling axes is aligned. Due to the presence of the electron column, the vertical axis is blocked and the residual two MOT axes are aligned under 45° with respect to the vertical. The overlap of the three perpendicular cooling axes at the position of the magnetic field's zero crossing gives rise to the 3D MOT.

In a typical experimental cycle, the 2D MOT and the 3D MOT are operated simultaneously for 2.5 s during which the 3D MOT loading is saturated. Since the size of the MOT is on the order of centimetres and the radial size of the dipole trap is on the order of micrometres, we compress the atomic cloud in a subsequent dark MOT phase [133] to maximise the loading into the dipole trap. The dark MOT phase additionally transfers all atoms into the $5S_{1/2}; F = 1$ state, which is the absolute ground state of the system.

3.2. Dipole trap

If an atom is subject to a monochromatic light field with the spatial dependent intensity $I(r)$ that is detuned by δ from the atomic resonance frequency ω_0, the eigenstates of the coupled atom–light system in rotating wave approximation are given by the dressed states of energy

$$E_\pm = \frac{\hbar}{2}\left[\delta \pm \Omega(r)\right], \tag{3.2.1}$$

with the generalised Rabi frequency $\Omega = \sqrt{\Omega_0^2(r) + \delta^2}$ (see sec. 2.1.3). The spatial dependence in the Rabi frequency originates from the spatial dependence of the laser intensity. In the case of a large laser detuning $\delta \gg \Omega_0$, we can expand the square root in the generalised Rabi frequency according to $\sqrt{1+x} \approx 1 + \frac{1}{2}x$ and obtain

$$E_\pm \approx \frac{\hbar}{2}\left[\delta \pm |\delta|\left(1 + \frac{\Omega_0^2(r)}{2\delta^2}\right)\right]. \tag{3.2.2}$$

If we only consider the $|-\rangle$ state that adiabatically connects to the ground state and is thus at zero energy for no atom–light interaction, we obtain the energy shift

$$\Delta E_- \approx -\frac{\hbar}{4}\frac{\Omega_0^2(r)}{\delta}. \tag{3.2.3}$$

With the relation between the electric field strength E and the light intensity $I(r) = \frac{1}{2}c\epsilon_0 E^2(r)$ as well as the relation between the decay rate Γ of the upper level and the dipole matrix element $d^2 = \frac{3\Gamma\epsilon_0 hc^3}{2\omega_0^3}$ [134], the definition of the Rabi frequency from eq. (2.1.18) leads to

$$\Omega_0^2(r) = \frac{6\pi c^2\Gamma}{\omega_0^3\hbar} I(r). \tag{3.2.4}$$

Inserting this result into eq. (3.2.3) yields

$$U_{\text{dip}}(r) \equiv \Delta E_-(r) \approx -\frac{3\pi c^2}{2\omega_0^3}\frac{\Gamma}{\delta} I(r). \tag{3.2.5}$$

A red-detuned laser beam thus creates an attractive potential for atoms that are prepared in the adiabatic ground state of the two-level system[1]. As this potential arises from the interaction of the light field with the induced atomic dipole, a setup that uses this attractive potential to trap atoms is called *optical dipole trap.* Even though derived only for a simple two-level system, this effect also holds in the case of a multi-level atom but in principle all possible transitions have to be taken into account. Due to the inverse scaling with δ however, only the levels closest to the transition wavelength contribute significantly to the resulting potential. In the case of rubidium and a YAG laser at a wavelength of $\lambda = 1064\,\mathrm{nm}$, the D_1 line with a detuning of $\delta_{1,F}$ and the D_2 line with a detuning of $\delta_{2,F}$ have to be considered and the resulting potential is given by [26]

$$U_{\mathrm{dip}}(r) = -\frac{\pi c^2}{2\omega_0^3}\left(\frac{2 + P g_F m_F}{\delta_{2,F}} + \frac{1 - P g_F m_F}{\delta_{1,F}}\right) I(r), \tag{3.2.6}$$

where g_F is the well-known Landé factor, m_F is the magnetic quantum number and P specifies the polarisation of the light ($P = 0, \pm 1$ accounts for linear and circularly polarised $\sigma^{\pm}$ light).

A limit on the maximal trapping time is imposed by the off-resonant scattering of the trapping light and the resulting heating of the trapped atoms. For this situation, the scattering rate into the excited state is well described by the optical Bloch equation [64, 135] that for $\delta \gg \Delta$ and $\delta \gg \Gamma$ can be simplified to

$$\Gamma_{\mathrm{sc}}(r) = \frac{\Gamma}{4}\frac{\Omega_0^2(r)}{\delta^2}. \tag{3.2.7}$$

With eq. (3.2.4) this becomes

$$\Gamma_{\mathrm{sc}}(r) = \frac{3\pi c^2}{2\omega_0^3 \hbar}\left(\frac{\Gamma}{\delta}\right)^2 I(r). \tag{3.2.8}$$

Hence, in order to reduce heating of the trapped atomic ensemble it is beneficial to minimise the scattering rate as much as possible. As the scattering rate scales with δ^{-2} while the potential depth scales with δ^{-1}, it is useful to choose far detuned lasers with high intensities to obtain deep potentials at low scattering rates. In our experiment, we therefore use a YAG laser[2] at a wavelength of $\lambda_{\mathrm{YAG}} = 1064\,\mathrm{nm}$, which is detuned by 269 nm from the D_1 line.

From eq. (3.2.6) we see that the shape of the optical dipole potential is directly given by the spatial beam profile of the confining laser beam. While this in principle allows for arbitrary potential shapes, e.g. by shaping the spatial mode of a laser beam by spatial light modulators [136, 137], the most common case is a Gaussian potential shape. Around the minimum, such potential can be approximated by the second order Taylor term, resulting in the harmonic potential

$$U_{\mathrm{dip}}(r)\big|_{r\approx 0} \approx \frac{1}{2} m \omega^2 r^2, \tag{3.2.9}$$

---

[1] If we had considered the $|+\rangle$-state, we would have seen that this increases its energy for a red-detuned laser and thus the excited state sees a repulsive potential. For a blue-detuned laser the situation is inverted.

[2] We use a "Mephisto" solid-state YAG laser system from Innolight to seed a NUA-1064-PD-0050 fibre amplifier from Nufern that achieves a total output power of 50 W.

where m is the mass of the atom and $\omega = \sqrt{\partial_r^2 U_{\mathrm{dip}}(r)|_{r=0}/m}$ is the so-called *trapping frequency* that quantifies the spatial confinement. In a classical picture of moving point-like particles, the trapping frequency gives the average oscillation frequency of such particles in the formed trap and thus also determines the timescale on which an atomic ensemble can thermalise.

In order to cool trapped atoms by forced evaporation (see the following section) on a reasonable timescale, high trapping frequencies are required for the system to thermalise fast enough. While this requirement can be met in the radial direction by tightly focusing the trapping laser beam, the axial confinement is solely determined by the Rayleigh length [138] and thus depends on the laser's wavelength. For the used YAG lasers, the Rayleigh length is so large that in a single beam trap evaporation becomes inefficient before the desired temperatures are reached. It is thus necessary to add a perpendicular laser beam that, by its radial confinement, increases the confinement in the axial direction of the initial beam. As the additional beam only becomes important in the final state of the evaporation, its maximum intensity can be much lower than that of the HP beam. Our setup thus consists of a primary, high-power trapping beam (”HP”) that achieves a maximum intensity of $I_{\mathrm{HP}} = 9.4 \times 10^9\,\mathrm{W/m^2}$ by focusing $P_{\mathrm{HP}} = 12\,\mathrm{W}$ to a Gaussian beam waist of $w_{\mathrm{HP}} = 28.5\,\mu\mathrm{m}$ as well as a crossed, low-power trapping beam (”LP2”) that has a maximum intensity of $I_{\mathrm{LP2}} = 1.4 \times 10^8\,\mathrm{W/m^2}$ by focusing $P_{\mathrm{LP2}} = 1.5\,\mathrm{W}$ to a Gaussian beam waist of $w_{\mathrm{HP}} = 82\,\mu\mathrm{m}$. Both beams propagate in the horizontal plane and intersect at the position of the 3D MOT. Since the differing beam waists of the two trapping beams necessarily lead to different trapping frequencies in the three spatial dimensions, we optionally add another low-power trapping beam (”LP1”) that is identical to the LP2 beam but copropagates with the HP beam (fig. 3.2a). This enables us to replace the HP beam by the LP1 beam in the final stage of the evaporation and thus to realise an isotropic trap[3].

Evaporative cooling

Since the temperatures achieved in the MOT are not sufficiently small for many experiments, additional cooling can be provided by forced evaporation. This relies on the fact that in a thermalised sample those atoms with the highest kinetic energy can leave the trap if the trap depth is reduced. As those atoms carry more than the average kinetic energy of the gas and this portion of energy is removed from the ensemble when they leave the trap, the system looses energy and thermalises at a lower temperature. In other words, by reducing the trap depth the high energy wings of the thermal Boltzmann distribution are cut off. When the system equilibrates, the energy is redistributed to form a new Boltzmann distribution of lower total energy, meaning at a lower temperature. After the system is thermalised, it is possible to start the process again. However, it is crucial that the reduction of the trap depth is slower than the current trapping frequencies such that the system can always thermalise. An exponential decrease of the trap depth is therefore well-suited to drive forced evaporation.

To load the pre-cooled atoms from the 3D MOT, we keep the HP beam and the LP2 beam constantly on during the loading of the MOT. In the dark MOT phase, the cloud

---

[3] Due to the overlap of the two low-power beams, the atoms see twice the confinement in the vertical direction. This confinement is however reduced by the gravitational force. There is thus a specific power of the low-power beams where gravitation compensates the double confinement and we obtain equal trapping frequencies in all three dimensions.

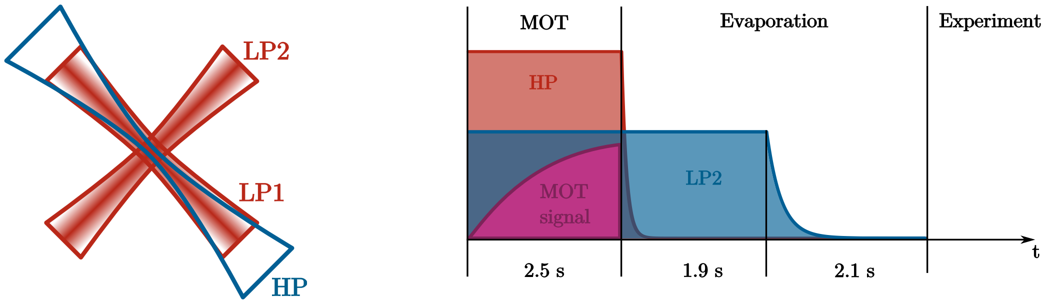

(a) (b)

Figure 3.2: Experimental configuration of the YAG dipole trap. (a) Geometry of the three trapping beams. The tightly focused high-power beam HP intersects with the less-focused low-power beam LP2 under 90°. In order to have equal trapping frequencies in all directions, the high-power beam can be replaced by a second low-power beam LP1 that is collinear with the high-power beam but has the same beam properties as the LP2 beam. (b) While the MOT (purple) is loaded for 2.5 s, the high-power YAG beam HP (red) and the crossed low-power beam LP2 (blue) are at maximum power. After the dark MOT phase, in which we transfer the atoms to the dipole trap, we hold the sample for 50 ms to let it evaporate freely. Subsequently, we drive forced evaporation by exponentially ramping down the high power beam. After 1.9 s we also ramp down the LP2 beam exponentially. The evaporation takes in 4 s. After the evaporation, the ultracold sample is ready for the specific experiment.

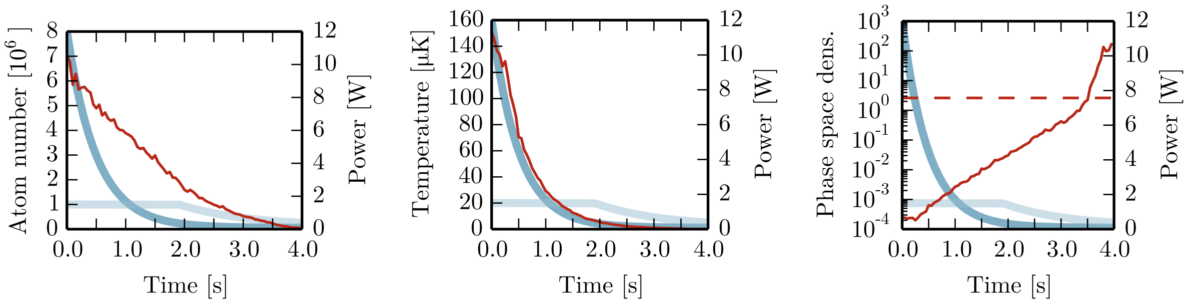

(a) (b) (c)

Figure 3.3: Experimental fingerprint of evaporative cooling. As a reference, each plot shows the exponential evaporation ramps in the high power beam HP (deep blue) and the low power beam LP2 (light blue). (a) In the course of the evaporation the atom number (red) drops almost linearly from 6×10^6 to 1×10^5. (b) The temperature in the sample (red) drops proportionally to the trap depth from 150 μK to below 100 nK. (c) For the first three seconds, the phase space density (red) increases exponentially to the critical point for $\zeta(3/2) \approx 2.61$ where the sample condenses into a Bose–Einstein condensate. From that point on, the determination of the cloud's temperature is not reliable any more, which leads to the stronger increase in the final phase of the evaporation.

is compressed and thus also the number of atoms transferred into the dipole trap is increased. After the MOT is switched off, we hold the sample for 50 ms during which it evaporates freely until the equilibrium energy distribution fits the depth of the trapping potential. Subsequently, we start to drive forced evaporation by ramping down the power of the trapping lasers. Starting from a maximum laser power of 12 W and a resulting trap depth of 1.2 mK, the HP beam is ramped down exponentially with a time constant of $\tau_{\mathrm{HP}} = 0.4\,\mathrm{s}$ to a final power of 90 mW within 4 s. The low-power beam LP2 is kept constant at 1.3 W until $t = 1.9\,\mathrm{s}$ where its potential becomes relevant compared to the decreasing potential of the HP beam. It is subsequently ramped down exponentially with a time constant of $\tau_{\mathrm{LP2}} = 1.2\,\mathrm{s}$ to a final laser power of 305 mW. The whole loading and evaporation sequence is depicted in fig. 3.2b. During the evaporation process, the number of atoms in the trap is reduced almost linearly (fig. 3.3a) while the temperature follows the functional behaviour of the trap depth (fig. 3.3b) as long as the ramps are slow enough for the system to thermalise. Ultimately, the forced evaporation reduces the number of atoms by one order of magnitude while the temperature is decreased by almost three orders of magnitude. By varying the final power of the evaporation ramps, we can set the temperature of the prepared sample. During the evaporation, the phase space density of the sample increases almost exponentially (fig. 3.3c). Once the phase space density passes the critical point of $\zeta(3/2) \approx 2.61$ [139], a Bose–Einstein condensate (BEC) is formed [22–24]. For the evaporation ramps explained above, we typically achieve an atom number of $N = 2.5 \times 10^5$ in the BEC inside the asymmetric trap formed by the high-power beam HP and the low-power beam LP2. The transfer into the low-power beam LP1 leads to an additional loss of atoms, resulting in a maximum atom number of $N = 1.5 \times 10^5$ atoms in the symmetric low-power trapping configuration. If we hold the BEC in the trap, we see a background-gas-collision-induced exponential decrease of the atom number with a characteristic decay time of 12.5 s. An overview of the two commonly used trapping configurations along with typical parameters is shown in tab. 3.1.

Due to a magnetic field gradient along the vertical direction, the effect of gravity is reduced for atoms in the $m_F = +1$ state and increased for atoms in the $m_F = -1$ state. The $m_F = -1$ component of the cloud thus evaporates faster and for decreasing trapping laser power gets pulled out of the trap before the other two components. It is thus possible, by simply setting the final power of the evaporation ramps low enough, to end up in a spin polarised sample in the $5S_{1/2}; F = 1, m_F = +1$ state. If for some specific experiments a spinor condensate with all three spin components is needed, external compensation coils can be used to compensate the magnetic field gradient.

Table 3.1: Typical parameters for the low-power and the high-power trapping configuration. The power in the high-power beam P_{HP} and the two low-power beams P_{LP1}, P_{LP2} is given along with the calculated trapping frequencies in the three spatial dimensions $\omega_x, \omega_y, \omega_z$ and the height of the potential barrier, i.e. the trap depth, $U_{\mathrm{dip}}^{\mathrm{max}}$.

name	P_{HP} [mW]	P_{LP1} [mW]	P_{LP2} [mW]	$\omega_x, \omega_y, \omega_z$ [$2\pi \times$ Hz]	$U_{\mathrm{dip}}^{\mathrm{max}}$ [nK]
high-power	95	-	380	179, 82, 180	1015
low-power	-	305	305	65, 65, 65	159

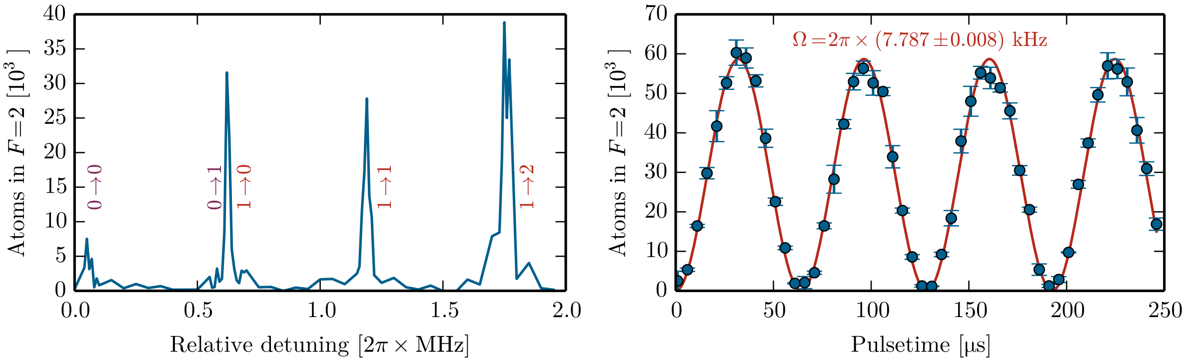

(a) **(b)**

Figure 3.4: Characterisation of the microwave setup. (a) Spectrum obtained by monitoring the population in the $F = 2$ hyperfine state after a 100 ms microwave pulse in a sample initially prepared in the $F = 1, m_F = +1$ state. The frequency is relative to 6.834682 GHz. For each appearing peak, the corresponding m_F transition is noted. All three possible transitions from the $F = 1, m_F = +1$ state (red) are observed. Due to a residual population of $F = 1, m_F = 0$ in the initial sample, also the transitions from this state into the $F = 2, m_F = 0$ and $F = 2, m_F = 1$ states can be seen (purple). (b) For a varied length of the microwave pulse, we can observe the Rabi flopping on the $F = 1, m_F = 0 \leftrightarrow F = 2, m_F = 0$ transition. The measured population in the $F = 2$ state (blue points) is fitted with a $\sin^2$ function to extract the oscillation frequency (red line).

3.3. Absorption imaging

Since it is crucial to control the preparation of the atomic sample, an imaging method that gives access to the atomic ground state density distribution, the total atom number, and the temperature of the sample is needed. A non-standard imaging technique is implemented in our setup by the image formation with an electron beam [117, 140] that gives access to the in-trap density distribution of the prepared sample. We further employ the widely used method of absorption imaging [139] to gain access to the total atom number and the temperature of the cloud. Here, the atoms are released from the dipole trap and, after an expansion time of typically 15 ms, illuminated by a homogeneous laser beam. The image of the laser beam behind the sample is magnified by a factor of 2.18 through a lens system and steered to a CCD camera[4]. Due to spontaneous scattering in the full solid angle, photons are removed from the laser mode and the resulting image shows the shadow of the cloud. By quantitatively analysing the amount of missing light intensity in the shadow, the number of atoms can be deduced. For a thermal ensemble, also the temperature of the cloud can be extracted from the width of the shadow since the cloud broadens according to the Boltzmann distribution during the free expansion time.

Usually, the cooling transition (sec. 3.1) is used as the resonant transition for absorption imaging. This however implies that only atoms in the $F = 2$ state will scatter photons and thus atoms in the $F = 1$ state remain invisible. If the atoms in the $F = 1$ state should be imaged as well, we apply a short pulse of the repumping laser to transfer them into the $F = 2$ state. By either shining in the repumper prior to imaging or not, we can decide whether we observe only the $F = 2$ population or all atoms.

---

[4] Theta Systems, SiS1-s285M

3.4. Microwave state transfer

While it is beneficial for many experiments that the sample is spin-polarised in the absolute ground state, it sometimes becomes necessary to prepare it in different hyperfine states. In this context, the fully stretched states $F = 2; m_F = \pm 2$ are of special importance since they consist of only one defined m_j state. This simplifies the coupling to Rydberg states, where usually the hyperfine structure is not resolved. To achieve a state transfer, we use a direct microwave transition between the $F = 1$ and $F = 2$ states at a frequency of $\nu = 6.834\,\mathrm{GHz}$. While this transition is not allowed for an electric dipole, it is possible to drive it through the magnetic dipole moment of the atom [141, 142]. The required microwave frequency is generated by a function generator[5] and is amplified up to 2 W by a C-band GaAs FET power amplifier[6]. Isolated by a microwave circulator the power is fed to a far-field microwave antenna[7] and radiated into the main experimental chamber. The exact transition frequency between the different Zeeman-sublevels depends on the strength of the magnetic field in the chamber. Therefore, the spectrum shown in fig. 3.4a reveals the energetic splitting of the individual Zeeman levels in the stray magnetic field of 0.7 G [111]. In the presence of the field, it is thus possible to address transitions between specific Zeeman states by setting the frequency of the microwave accordingly.

Since the microwave's wavelength of 4.4 cm is only a factor of ten smaller than the diameter of the vacuum chamber, the latter acts as an efficient resonator and the coupling of the microwave radiation is strongly influenced by the geometry of the chamber. While this makes it hard to estimate the coupling theoretically, it is easy to measure it by observing the Rabi flopping [64] between the coupled hyperfine states. We therefore set the frequency of the microwave to 6.834707 GHz to drive the transition $F = 1, m_F = 0 \leftrightarrow F = 2, m_F = 0$. Observing the population in the $F = 2$ state as a function of the pulse duration[8] in a sample of 6×10^4 atoms initially prepared in the $F = 1$ state, we see the Rabi flopping shown in fig. 3.4b. From a fit of a $\sin^2$ function to the data, we can extract the Rabi frequency and thus quantify the coupling strength. It should be noted here that due to fluctuations of the magnetic field in the experimental chamber, the Rabi flopping can be seen so nicely only between the two $m_F = 0$ states as they are not affected by the field.

To reliably transfer the atoms into the $F = 2$ state, we rely on an adiabatic passage through a Landau–Zener sweep [143]. We therefore sweep the frequency of the microwave ±300 kHz around the line centre of the desired transition within 30 ms. Due to the broad frequency scan range, small variations in the exact line position arising from magnetic field fluctuations do not affect the population transfer. This scheme is thus rather robust against external changes while providing a transfer efficiency of close to 100%.

3.5. Rydberg excitation laser

To excite high-lying Rydberg states from the rubidium ground state, an energy of $4.3\,\mathrm{eV} \equiv h \times 1010\,\mathrm{THz}$ is required. In the past, continuous wave (cw) laser systems with such photon energies were not available. The transition was thus often realised by a resonance-

---

[5] Rohde+Schwarz, SMB100A

[6] Kuhne electronic, KU PA 600770-2A

[7] Quasar Microwave, QRA14MZH014-A

[8] Strictly, the Rabi flopping depends on ΩT and thus the area under the pulse is relevant. In our case however, Ω is constant and we just vary the pulse time.

enhanced two-photon transition via the $5P$ intermediate state [84,144] and more recently via the $6P$ intermediate state [145,146]. Such excitation schemes however impose restrictions either on the timescale of the experiment through strong scattering on the intermediate level or on the maximal achievable effective coupling to the Rydberg state [59].

To overcome these limitations, our setup features a frequency-doubled cw UV laser system at a wavelength of $\lambda_{\mathrm{UV}} = 297\,\mathrm{nm}$ that enables direct transitions into Rydberg P-states. The laser system, which is depicted in fig. 3.5 and described in detail in refs. [42, 118,119], is based on a ring-cavity dye laser[9] that is pumped by a frequency doubled solid-state laser[10] with an output power of 15 W at a wavelength of 532 nm. Due to the broad operation range of the dye laser system, the wavelength can be largely tuned around the desired central wavelength of $\lambda_{\mathrm{Fund}} = 594\,\mathrm{nm}$. While the dye laser system provides a short time stabilisation down to 50 kHz linewidth by locking to a temperature stabilised low-expansion reference cavity, the frequency of the laser is not sufficiently stable on longer timescales. We therefore actively stabilise the optical length of the cavity by transmitting a second, otherwise stabilised laser (”reference laser”) through the cavity and keeping its transmission constant. In that way, we transform the passive cavity to a so-called *transfer-cavity* that transfers the absolute frequency stability of one laser onto another [147]. The reference laser operates at a wavelength of $\lambda_{\mathrm{ref}} = 780\,\mathrm{nm}$ and is stabilised on the beat note with a third laser that itself is locked to a rubidium spectroscopy. This scheme combines the absolute frequency stability of the atomic spectroscopy with the possibility to detune the reference laser by the beating-lock. By detuning the reference laser, we in turn also change the optical length of the transfer cavity and thus detune the frequency of the dye laser that is locked to it. The frequency of the dye laser is constantly monitored by a Fizeau-interferometer based wavemeter[11] that allows to read out the frequency with a precision of 1 MHz but is limited in its absolute precision by frequency drifts on the order of 10 MHz.

From the 2.2 W optical output power of the dye laser, roughly 1.6 W can be passed through an optical fibre and is inserted into a home-built resonator-enhanced frequency doubling. This in-vacuum bow-tie resonator based setup uses a caesium lithium borate (CLBO) crystal as non-linear medium for second harmonics generation. While the handling of these crystals is challenging due to their high hygroscopy, they feature a high nonlinearity at a much smaller walk-off angle compared to other materials available for the required wavelength. The crystal is type-I critically phase matched, which allows to tune the phase matching for a changed wavelength of the fundamental solely by changing the temperature of the crystal. This allows for a high flexibility in the addressed principal quantum number of the Rydberg state without the need of mechanical realignment of the resonator or the crystal. With this setup it is possible to reach a conversion efficiency of more than 50% and thus to obtain up to 700 mW of optical power at the harmonic wavelength $\lambda_{\mathrm{SHG}} = 297\,\mathrm{nm}$ [118]. After leaving the frequency doubling, the UV beam passes through an AOM[12] that is used to adjust the intensity of the beam in the experiments. The spatial mode of the first-order defracted beam is subsequently shaped by a lens system and passes a half-wave plate to set the orientation of the linear polarisation. Finally, the beam can enter one of two possible beam paths leading to the experimental chamber. Through the first path the beam enters the chamber under an angle of 48.4°

---

[9] Sirah GmbH, Matisse DS; The used dye is rhodamine 6G.

[10] Newport Spectra-Physics GmbH, Millenia Prime DPSS

[11] High-Finesse GmbH, WS7

[12] AA Opto Electronic, MQ200-A1,5-266.300

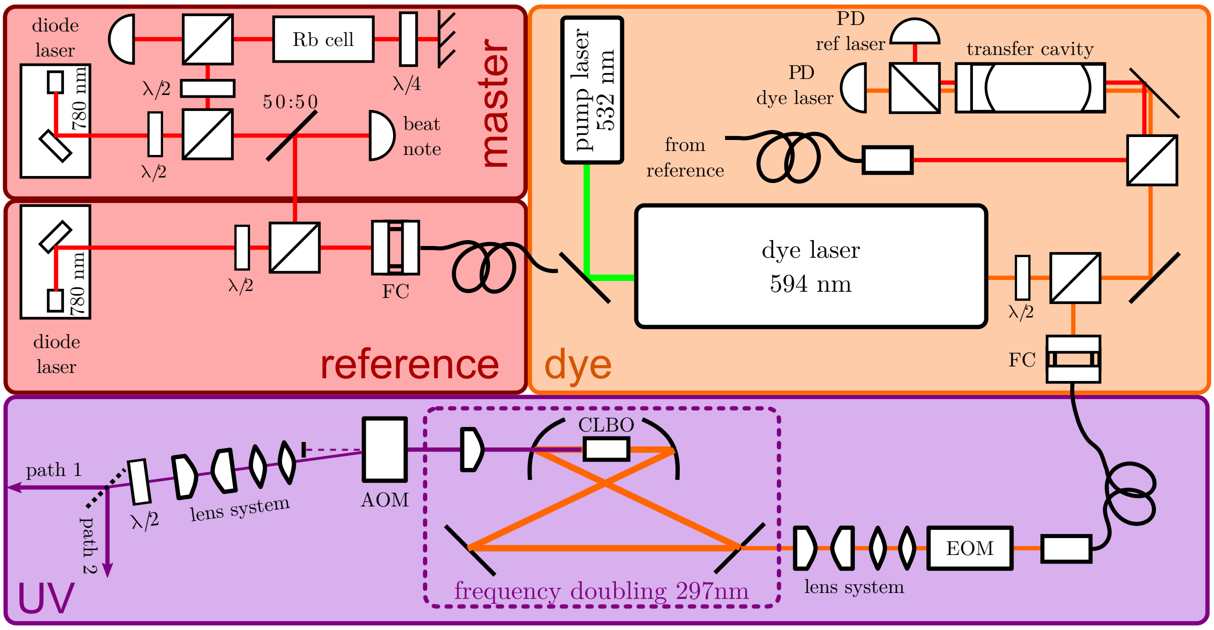

Figure 3.5: UV laser setup. The master laser system at 780 nm is FM-locked to a Doppler-free absorption spectroscopy in a rubidium vapour cell. A fraction of the reference laser's power is overlapped with the master on a high-bandwidth photodiode (PD) that is able to see the beat note of the two beams. The reference laser is locked to a constant beating frequency. A part of the reference laser is coupled to an optical fibre. The dye laser system is pumped by a 15 W laser at 532 nm. A fraction of the 2.2 W output power of the dye laser is overlapped with the reference laser and both are transmitted to the transfer cavity. The majority of the dye laser's output power is coupled to a fibre and transferred to the frequency doubling setup. The beam passes an EOM that is used to modulate sidebands to generate a Pound-Drever-Hall [148] signal for locking the doubling resonator. After a lens system for matching the spatial mode of the beam to the cavity, the light enters the in-vacuum doubling resonator with the CLBO crystal inside. Hereafter, the frequency-doubled beam passes an AOM, a beam-shaping lens system and a half-wave plate. Ultimately, the beam can alternatively be sent to the experiment on two different beam paths (see text).

with respect to the vertical and is focused to a Gaussian waist of $w_0 = 100\,\mu\mathrm{m}$ on the position of the atoms. The viewports on this axis are specifically coated for the UV wavelength and thus transmit more than 99% of the power. Via the second path, the beam enters the chamber in the horizontal plane and is thus perpendicular to the quantisation axis set by the electric and magnetic fields along the vertical direction. A lens in this beam path focuses the beam to a Gaussian waist of roughly $w_0 = 40\,\mu\mathrm{m}$ on the atoms. While this beam path provides controlled σ- and π-coupling through its geometry (see the following section), it has the disadvantage that the viewports on this axis transmit only 81% of the power due to their coating being optimised for NIR lasers. Depending on the experimental requirements, we thus choose either the one or the other beam path.

Due to the technically challenging wavelength, the linewidth of the UV laser system is hard to determine independently. Since homodyne beating methods are not possible due to the lack of optical fibres in the UV range and a heterodyne beating would require a second identical laser system, we could so far only estimate the linewidth. One possibility to find an upper bound is provided by the spectroscopy of Rydberg states performed on dilute ultracold gases. From the minimal observed width of atomic resonances in such samples, we can conclude that the linewidth of the UV laser is below 700 kHz. However,

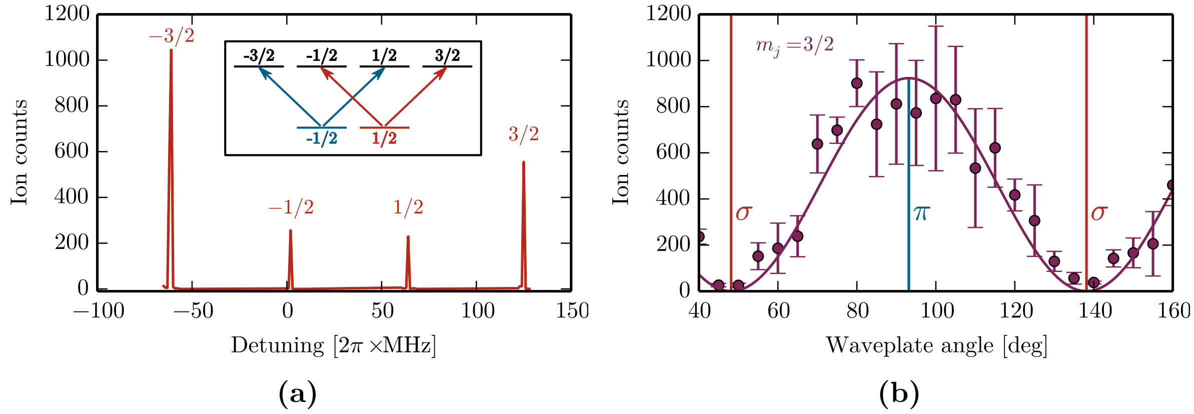

Figure 3.6: Coupling to the Zeeman sublevels of the $25P_{3/2}$ Rydberg state. (a) As witnessed by the ion signal, we can excite all four possible Zeeman sublevels if the linear laser polarisation is perpendicular to the quantisation axis and the sample is prepared in the $F = 1, m_F = 1$ ground state. The Zeeman-splitting of 64 MHz arises from the presence of a magnetic field of 35 G. The m_j quantum number of the excited final state is noted above each peak. The inset shows the $\sigma^{\pm}$-coupling from the two m_j components of the prepared initial hyperfine state (see text). (b) On resonance with the transition into the $m_j = 3/2$ state, we see that the signal (purple points) varies sinusoidally with the rotation of the half-wave plate. By fitting a $\sin^2$ function (purple line), we can extract the exact angular position for maximal π-coupling (blue) and maximal $\sigma^{\pm}$-coupling (red).

since the linewidth of the fundamental laser is on the order of 50 kHz, it is likely that the linewidth of the UV laser is far below this upper bound.

3.5.1. Polarisation and coupling

For many experiments, it is important to selectively address a single Zeeman level of the excited Rydberg state. By applying a magnetic field to the sample, it is possible to split the Zeeman states and resolve them spectroscopically. Fig. 3.6a shows a spectrum that was obtained by observing the spontaneous ions created from the excitation into the $25P_{3/2}$ Rydberg state. Due to the field, we can clearly see four distinct resonances belonging to the four possible m_j states. It is possible to see all four states in a single spectrum because the sample was prepared in the $F = 1, m_F = 1$ ground state which is a superposition of $m_j = 1/2$ and $m_j = -1/2$ states. Further, the linear polarisation of the laser was set perpendicular to the quantisation axis, leading to an equal superposition of σ^+- and σ^--coupling. The two possible transitions from the two different m_j ground state components give in total the four coupled lines (inset of fig. 3.6a).

To obtain control on the helicity of the transition, it is crucial to have a defined quantisation axis. Depending on which interaction is stronger, the quantisation axis is set by the magnetic or the electric field. Since their small electric polarisability leads to a weak interaction with the electric field, the quantisation axis for ground state atoms is usually set by the magnetic field. For Rydberg atoms however, the interaction even with small residual electric fields can dominate the magnetic interaction and in such case the quantisation axis is set by the electric field[13]. To reduce the complexity in our setup, the

---

[13] Moreover, in this case the Stark states become the eigenstates of the system rather than the Zeeman states.

electric and the magnetic fields are both aligned along the vertical axis. It is thus possible with the horizontal UV beam to drive pure π-transitions by orienting the linear laser polarisation vertically and thus parallel to the quantisation axis. On the other hand, we can create an equal superposition of $\sigma^{\pm}$, as described above, if the polarisation is aligned perpendicular to the quantisation axis.

This was confirmed experimentally by monitoring the Rydberg population in terms of created ions on the transition into the $25P_{3/2}$ state while the angle of the half-wave plate, and thus the polarisation angle, was changed (fig. 3.6b). As from the $m_j = \pm 1/2$ initial states the $m_j = 3/2$ Rydberg state can only be reached by a σ^{+}-transition, the signal is expected to vanish for pure π-coupling. Indeed, we find a sinusoidal behaviour of the measured ion signal on this peak that can be fitted by a $\sin^2$ function to extract the precise points for pure π- and pure $\sigma^{\pm}$-coupling.

With the additional possibility to transfer the sample into the fully stretched $F = 2, m_F = 2$ ground state (sec. 3.4) that consists only of the $m_j = 1/2$ component, we are able to drive a controlled transition to a single Zeeman sublevel of the Rydberg state.

3.6. Ion detection system

Our primary measurement signal is given by the ions that the Rydberg atoms evolve into. To accelerate these ions, we set each of the eight main electrodes (fig. 3.1a) on a controlled voltage level. By applying a positive voltage to the upper four electrodes and a negative voltage to the lower four electrodes, we create a downwards-pointing electric field vector at the position of the atoms. By measuring the quadratic Stark shift (sec. 2.3.2) for a Rydberg state of known polarisability, we can calibrate the relation between the applied voltage and the strength of the created field [112, 119]. This downward-pointing field is needed for the ions to move towards the ion optics that ultimately guide them to a discrete dynode ion detector[14]. To find the setting where the vertical component of the electric field vanishes, we slowly reduce the acceleration voltage until the ion signal drops. With this method, we are able to reduce the residual field in the vertical direction to less than $20\,\mathrm{mV/cm}$. To ensure a reliable acceleration of the ions, we add $80\,\mathrm{mV/cm}$ to that configuration so that in total a field of less then $100\,\mathrm{mV/cm}$ is applied to the atoms. While this method allows to precisely control the offset field in the vertical direction, the other two directions are harder to compensate exactly as a sensitive measurement signal is missing. We estimate the maximum offset field in this direction to be roughly $70\,\mathrm{mV/cm}$.

By the initial acceleration, the ions move towards the ion optics (lower part in fig. 3.1a). The ion optics consists of two cylindrical einzel lenses [149], one below the atoms and one in front of the ion detector. Since the ion detector cannot be placed on the vertical axis without interfering with the electron beam, the ion beam is bended by 45° between the two lenses through four additional rod electrodes and the detector can is placed off-axis. The ion detector is capable of detecting single ions with a specified detection efficiency of 81%. We measured the overall detection efficiency of our setup to be 43%, which implies that the ion optics on average guides every second ion to the detector. The voltage pulse emitted by the detector upon detection of an ion has a typical length of 50 ns, which imposes a fundamental upper limit of 20 MHz to the detection rate of our system. The detector signal is discriminated to generate logical signals that are subsequently registered by an edge detection circuit that saves the current value of a counter for each detected

---

[14] ETP Electron multipliers, ETP 14553

logical edge. Our primary measurement data is thus a list of timestamps at which ions were detected. This allows not only to determine the total number of detected ions but also enables time-of-flight detection (see sec. 4.1) and the analysis of temporal correlations in the signal [42].

4. Rydberg–ground state collisions: An electron mediated mass transport

Ultracold Rydberg systems are often studied in the so-called frozen gas regime, where the surrounding ground state atoms are assumed to be at rest within the relevant time scale of the experiment. In dense samples however, due to the long lifetime of Rydberg states, they can actually move by more than the average inter-particle distance before the excitations decay. Consequently, collisions between Rydberg atoms and surrounding ground state atoms can occur, as it is witnessed by the presence of associative ionisation for resonantly excited Rydberg atoms in dense ultracold samples [53, 150, 151].

In this chapter, we will present an experimental study on the scattering between an atom that was resonantly excited into a Rydberg state and surrounding ground state atoms. We will discuss the employed time-of-flight measurement technique that relies on the present ionisation processes and allows to selectively study associative ionisation. A simple model based on rate equations will be presented that allows us to extract the partial cross section for associative ionisation and the total inelastic scattering cross section from our measured data. A comparison of the obtained cross section reveals that associative ionisation in ultracold clouds is three orders of magnitude larger than for previous experiments in atomic beam experiments [11–13]. Furthermore, we see that the total inelastic scattering cross section agrees well with the geometric size of the excited Rydberg state and thus every Rydberg–ground state collision leads to a decay. In combination, both results indicate the presence of a directed mass transport that we attribute to an overall attractive potential created by the Rydberg electron. We will also point out that through the observed transport mechanism the Rydberg electron can be seen as a catalyst [152] that accelerates the formation of molecular ions.

4.1. Time-of-flight measurements

In order to detect the excitation of Rydberg atoms, we rely on the ions created from the excited atoms through the different ionisation channels presented in sec. 2.3.3. In our case, two channels are of particular importance. Photoionisation is ubiquitous in our system because the black-body radiation emitted from the environment has sufficient energy to promote the Rydberg electron into continuum states. Additionally, the photons of the trapping lasers can ionise the Rydberg atoms if they are kept in the trap. While the black-body induced ionisation cannot be tuned and happens at a fixed rate of less than 300 Hz, the ionisation due to the trapping lasers depends on the incident laser intensity and thus varies between 500 Hz and 50 kHz. In both cases, the ionisation is a single particle effect and thus acts on all atoms in the same way. If photoionisation is slow compared to the other decay channels, it does not significantly influence the dynamics but still produces a signal that is proportional to the Rydberg population. As the process is continuous in time, the created ions are a well-suited signal to observe the dynamics of the created Rydberg excitations.

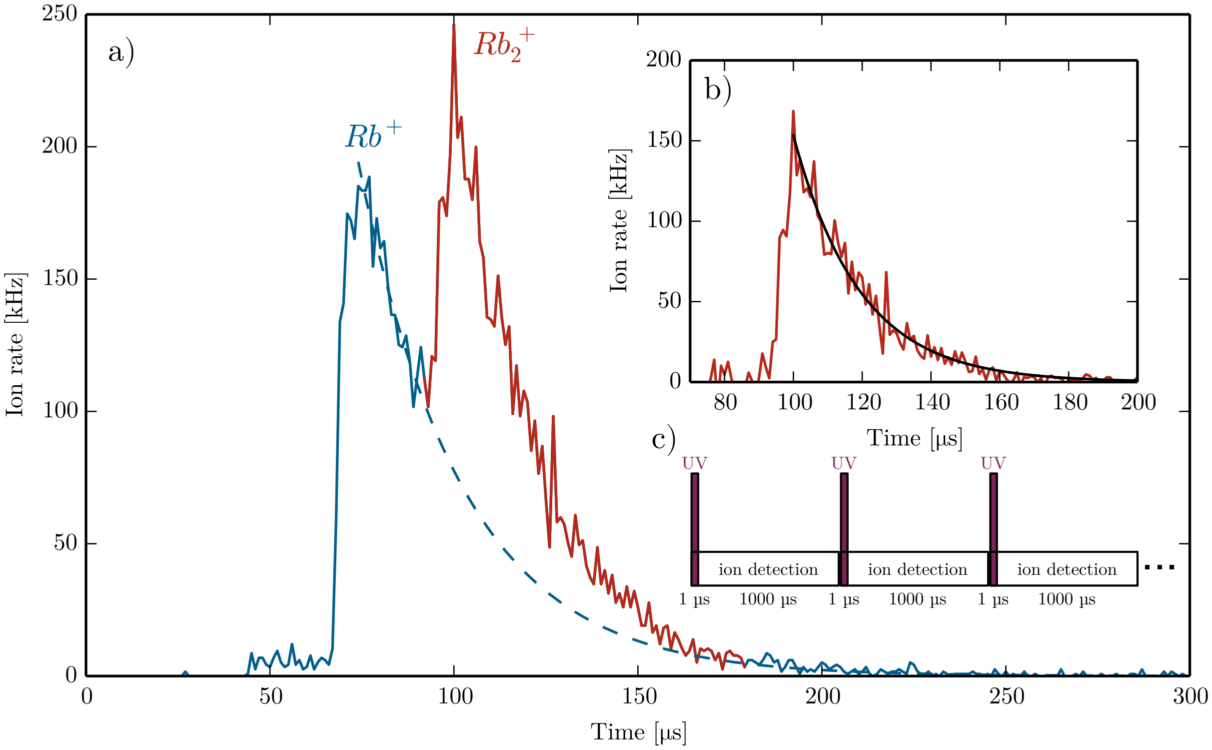

Figure 4.1: Ion signal obtained in a time-of-flight experiment for resonant excitation of the $30P_{3/2}$, $m_j = 3/2$ state from a thermal cloud with a peak density of $n_0 = 3 \times 10^{13}\,\mathrm{cm}^{-3}$. The peak generated by the Rb^+ ions (blue) is well separated from the peak generated by the Rb_2^+ ions (red) through their different flight time. After subtracting the fitted decay of the Rb^+ signal (dashed blue line), we obtain the pure signal from the Rb_2^+ ions shown in (b). (c) The sequence of a short excitation pulse with subsequent ion detection is repeated multiple times as long as the atom loss does not exceed 20% of the sample size.

In addition to photoionisation, we also observe associative ionisation, where a Rydberg atom collides with a ground state atom to form a Rb_2^+ molecular ion, as explained in sec. 2.3.3. Since this process depends on the presence of a ground state atom, the rate for associative ionisation $\gamma_{\mathrm{AI}}(r)$ linearly depends on the ground state density. Hence, this process becomes dominant in high-density samples, i.e. dense thermal clouds and BECs.

To detect the created ions, we apply a small electric field on the order of $80\,{}^{\mathrm{mV}}/_{\mathrm{cm}}$ to accelerate the ions towards the ion optics where they are guided to the ion detector. In order to calculate the time the ions need to arrive at the detector, we employ a simplified model involving a constant electric field. In such a model, the motion of the ions is determined by the electrostatic force $F_{\mathrm{e}} = qE$ and counteracted by inertia $F_{\mathrm{i}} = ma$. Since the acceleration is constant, we see that $s = \frac{1}{2}at^2$ and by setting $F_{\mathrm{e}} = F_{\mathrm{i}}$, we can express the time t that an ion of mass m and charge q needs to travel the distance s in a field E as

$$t = \sqrt{\frac{2sm}{Eq}}. \tag{4.1.1}$$

Evidently, this leads to a factor of $\sqrt{2}$ longer time of flight (TOF) for the double mass Rb_2^+ ions created by associative ionisation compared to the flight time of the single mass Rb^+ ions created by photoionisation. Even though it was derived under the assumption of a constant electric field, this result still holds for the complex potential landscape the ions pass in the ion optics. Hence, we see this differing TOF in the signal that is typically observed in the ion detector after a short excitation pulse of 1 µs and subsequent continuous ion detection (fig. 4.1a). After the excitation pulse is applied at $t = 0$, we observe no signal in the detector for the first 65 µs, which corresponds to the TOF of the Rb^+ ions[1]. After the steep rise of the signal, we see an exponential decay that reflects the temporal decay of the Rydberg population. After 92 µs the signal rises again, which is the time when the Rb_2^+ ions created at $t = 0$ arrive at the detector. Due to their different TOF, it is thus possible to distinguish between the two generated types of ions in the signal. Since the lifetime of the Rydberg atoms is often longer than the difference in the TOF of both ion types, the signals overlap. In order to correct for this overlap, we fit the decay of the Rb^+ peak and subtract the fit function from the signal. In this way we not only extract the amplitude and the decay constant of the Rb^+ peak through the fit but also obtain the pure signal generated by the Rb_2^+ ions (fig. 4.1b). For the resulting pure Rb_2^+ signal we could also perform an exponential fit of the decay to extract the amplitude and the decay constant. However, this decay is often non-exponential and therefore we rather fit the initial part of the decay with a linear function to obtain the amplitude and the initial decay rate.

Since the short excitation pulse often hardly affects the sample, it is reasonable to repeat the TOF experiment several times on the same sample to reduce the statistical error. In order to allow for all excitations, even for the highest studied Rydberg states where the lifetime can exceed 100 µs, to decay, we wait for 1 ms after each excitation pulse for the system to equilibrate again (fig. 4.1c). The number of subsequent repetitions of the TOF experiment is varied such that the loss of atoms by excitation and subsequent ionisation does not exceed 20% of the sample size. Depending on the excitation laser intensity and the addressed Rydberg state, we typically perform between 50 and 1000 repetitions on a single sample. The results of multiple samples prepared with identical parameters are averaged to obtain a TOF signal as shown in fig. 4.1a.

The possibility to distinguish the two different types of ions in the measurement and the fact that there is only one possible source of Rb_2^+ ions allows us to selectively study the associative ionisation process in dense ultracold samples. With the help of the simple rate-equation based model presented in the following, we see how it is possible to extract the cross section for associative ionisation σ_{AI} and the total inelastic scattering cross section σ_{inel} between Rydberg atoms and ground state atoms from the obtained TOF signals.

4.2. Microscopical model

In the following, we will employ rate equations to model the decay of Rydberg excitations in a cold dense thermal cloud. Motivated by the TOF measurement technique, we assume a short excitation pulse that creates a distribution of excitations $n^0_{\mathrm{Ry}}(\vec{r})$ in the sample. Once the excitations are present in the system, they can undergo natural decay with rate γ_{n}, photoionisation with rate γ_{PI}, collisions with ground state atoms with rate $\gamma_{\mathrm{coll}}(\vec{r}) = n(\vec{r})\sigma_{\mathrm{inel}}\bar{v}_{\mathrm{coll}}$ (with the collision velocity $\bar{v}_{\mathrm{coll}}$ and the ground state density distribution

---

[1] The origin of the small constant signal starting at 45 µs is unknown. It is highly unlikely that we see multiply ionised atoms since the binding of the second electron would require six UV photons to break it. Since furthermore the arrival time does not change with the applied electric field, we assume the signal to have technical reasons.

$n(\vec{r})$), or Rydberg–Rydberg[2] collisions with rate β. The time evolution of the Rydberg population can then be described by the differential equation

$$\dot{n}_{\mathrm{Ry}}(\vec{r},t) = -\left[\gamma_{\mathrm{n}} + \gamma_{\mathrm{PI}} + \gamma_{\mathrm{coll}}(\vec{r})\right] n_{\mathrm{Ry}}(\vec{r},t) - \beta n_{\mathrm{Ry}}(\vec{r},t)^2. \tag{4.2.1}$$

With the definition $\gamma(\vec{r}) = (\gamma_{\mathrm{n}} + \gamma_{\mathrm{PI}} + \gamma_{\mathrm{coll}}(\vec{r}))$ the solution of the differential equation reads

$$n_{\mathrm{Ry}}(\vec{r},t) = -\frac{\gamma(\vec{r})e^{\gamma(\vec{r})t_0}}{\beta e^{\gamma(\vec{r})t_0} - e^{\gamma(\vec{r})t}} \ . \tag{4.2.2}$$

As the integration constant t_0 has no intuitive physical meaning, we transform the boundary condition to fulfil $n_{\mathrm{Ry}}(\vec{r},0) = n^0_{\mathrm{Ry}}(\vec{r})$. The solution then becomes

$$n_{\mathrm{Ry}}(\vec{r},t) = \frac{\gamma(\vec{r})}{\left(\frac{\gamma(\vec{r})}{n^0_{\mathrm{Ry}}(\vec{r})} + \beta\right) e^{\gamma(\vec{r})t} - \beta} = \frac{\gamma(\vec{r})}{\frac{\gamma(\vec{r})}{n^0_{\mathrm{Ry}}(\vec{r})} + \beta\left(1 - e^{-\gamma(\vec{r})t}\right)} e^{-\gamma(\vec{r})t} \ . \tag{4.2.3}$$

In the experiment, we observe Rb^+ ions and molecular Rb_2^+ ions, which can, due to the differing mass, be distinguished by the TOF to the ion detector. The Rb^+ ions can originate from photoionisation at rate γ_{PI} and from ionising Rydberg–Rydberg collisions at rate $\beta n_{\mathrm{Ry}}(\vec{r},t)$. Due to the higher energy of the doubly excited system, Rydberg–Rydberg collisions are unlikely to create molecular Rb_2^+ ions. Hence, it is valid to assume that Rb_2^+ ions are solely created through collisions with ground state atoms at a rate $\gamma_{\mathrm{AI}}(\vec{r}) = n(\vec{r})\sigma_{\mathrm{AI}}\bar{v}_{\mathrm{coll}}$. By carrying out the spatial integration over the whole sample, we can thus obtain the rate at which the two types of ions are created in the experiment

$$R_{\mathrm{Rb}^+}(t) = \gamma_{\mathrm{PI}} \int n_{\mathrm{Ry}}(\vec{r},t)\,\mathrm{d}\vec{r} + \beta \int n^2_{\mathrm{Ry}}(\vec{r},t)\,\mathrm{d}\vec{r}, \tag{4.2.4}$$

$$R_{\mathrm{Rb}_2^+}(t) = \int \gamma_{\mathrm{AI}}(\vec{r}) n_{\mathrm{Ry}}(\vec{r},t)\,\mathrm{d}\vec{r}. \tag{4.2.5}$$

If we now assume the ground state and the Rydberg density to only depend on the distance from the origin $r = |\vec{r}|$ and insert expression (4.2.3) for the Rydberg density, we obtain

$$R_{\mathrm{Rb}^+}(t) = 4\pi \left[\gamma_{\mathrm{PI}} \int \frac{\gamma(r)e^{-\gamma(r)t}}{\frac{\gamma(r)}{n^0_{\mathrm{Ry}}(r)} + \beta\left(1 - e^{-\gamma(r)t}\right)} r^2 \mathrm{d}r + \beta \int \left(\frac{\gamma(r)e^{-\gamma(r)t}}{\frac{\gamma(r)}{n^0_{\mathrm{Ry}}(r)} + \beta\left(1 - e^{-\gamma(r)t}\right)}\right)^2 r^2 \mathrm{d}r\right] \tag{4.2.6}$$

$$R_{\mathrm{Rb}_2^+}(t) = 4\pi \int \frac{\gamma_{\mathrm{AI}}(r)\gamma(r)e^{-\gamma(r)t}}{\frac{\gamma(r)}{n^0_{\mathrm{Ry}}(r)} + \beta\left(1 - e^{-\gamma(r)t}\right)} r^2 \mathrm{d}r. \tag{4.2.7}$$

In principle, these equations describe the decay of the TOF spectra that we observe and a fit with these functions should allow to directly extract the appearing ionisation rates. However, due to the necessary time-dependent spatial integration, it is computationally challenging to perform the fit. We will therefore simplify the problem by restricting it to the beginning of the decay, i.e. $t = 0$. In the following, we therefore show how to extract relevant quantities like σ_{AI} and σ_{inel} from the relative peak heights at $t = 0$ and the initial decay rate.

---

[2] Even if one of the Rydberg atoms decays into an ion, we still recover the quadratic dependence on the Rydberg density. Thus, the Rydberg–Rydberg process implicitly includes also ion–Rydberg collisions.

4.2.1. Peak ratio

For the analysis, it is useful to consider the ratio of the peak heights for the Rb^+ and the Rb_2^+ peak rather than their absolute values as the number of excitations in the system and the ion detector efficiency cancels out in this quantity[3]. From eq. (4.2.4) and eq. (4.2.5), we see that this ratio can be expressed as

$$\left.\frac{R_{\mathrm{Rb}_2^+}}{R_{\mathrm{Rb}^+}}\right|_{t=0} = \frac{\int n_{\mathrm{Ry}}^0(r)\gamma_{\mathrm{AI}}(r)r^2\,\mathrm{d}r}{\gamma_{\mathrm{PI}}\int n_{\mathrm{Ry}}^0(r)r^2\,\mathrm{d}r + \beta\int n_{\mathrm{Ry}}^0(r)^2r^2\,\mathrm{d}r}. \tag{4.2.8}$$

To carry out the appearing integrals, we have to assume some explicit distribution of the Rydberg excitations $n_{\mathrm{Ry}}^0(r)$. As we are working in the limit of weak driving, i.e. small Rabi frequency Ω, we can neglect Rydberg blockade effects and the excitation distribution follows the distribution of ground state atoms. It is thus reasonable to assume the Rydberg density to be proportional to the ground state density $n_{\mathrm{Ry}}^0(r) = an_0e^{-r^2/2\sigma^2}$, where $n_0 = N(2\pi)^{-3/2}\sigma^{-3}$ is determined by the number of ground state atoms N and the Gaussian width σ. Note that the proportionality constant $a \equiv a(\Omega)$ carries an implicit dependency on the driving strength Ω. It is easy to see that the first integral in the denominator of eq. (4.2.8) is the norm of the density distribution, i.e. the number of Rydberg atoms in the system $N_{\mathrm{Ry}} \equiv aN$. The second integral in the denominator can, under the above assumptions, also be solved analytically as $N_{\mathrm{Ry}}\beta an_0 2^{-3/2}$. Similarly, the integral in the nominator can be solved and yields $N_{\mathrm{Ry}}\sigma_{\mathrm{AI}}\bar{v}_{\mathrm{th}}2^{-3/2}$. Inserting the solutions of the integrals and cancelling $N_{\mathrm{Ry}}2^{-3/2}$, we obtain

$$\left.\frac{R_{\mathrm{Rb}_2^+}}{R_{\mathrm{Rb}^+}}\right|_{t=0} = \frac{\sigma_{\mathrm{AI}}}{\sqrt{8}\gamma_{\mathrm{PI}} + \beta an_0}\Phi, \tag{4.2.9}$$

where $\Phi = n_0\bar{v}_{\mathrm{coll}}$ is the atom flux through the surface of the Rydberg atom. If Rydberg–Rydberg collisions are weak and the photoionisation rate γ_{PI} is known, it is thus possible to extract the cross section for associative ionisation σ_{AI} as the slope of a linear fit to the peak ratio for varying atom fluxes. If, on the other hand, Rydberg–Rydberg collisions dominate ($\beta an_0(r) \gg \gamma_{\mathrm{PI}}$), the peak ratio becomes $\frac{\sigma_{\mathrm{AI}}v_{\mathrm{th}}}{\beta a}$, which is independent of the ground state density. If both processes are of similar magnitude, the observed curve shape will be bended. It is thus easy to judge on the importance of Rydberg–Rydberg collisions just by looking at the scaling behaviour of the peak ratio.

It should be noted that the dependency on β results only from the fact that we also observe ions from Rydberg–Rydberg collisions. If Rydberg–Rydberg collisions did not create ions, the peak ratio would be independent of β. This is due to the fact that the considered peak ratio is a static quantity at $t = 0$ and thus concurrency in the decay channels does not play a role. In this case (or when $\beta \approx 0$), the peak ratio also becomes independent of the actual number of excitations in the system. Note also that the factor of $\sqrt{8}$ appears just due to the integration over the different densities in the cloud. For a fully blockaded system with a constant Rydberg density, however, this numerical factor strongly depends on the boundaries of the integration.

---

[3] The detector efficiency cancels only if it is equal for Rb^+ and Rb_2^+ ions. Due to the discrete dynode design and the dynode material used in the ion detector, we assume the detection efficiency to be rather insensitive to the ion mass. Consequently, we expect to have approximately the same detection efficiency for both detected ion types.

4.2.2. Initial decay rate of the molecular ion signal

In contrast to the peak ratio, the initial decay rate of the Rb_2^+ signal is a dynamic quantity that involves all decay processes. Approximating the decay to be exponential, the initial decay rate γ^0_{coll} is given by

$$\gamma^0_{\mathrm{coll}} = -\left.\frac{\dot{R}_{\mathrm{Rb}_2^+}(r)}{R_{\mathrm{Rb}_2^+}(r)}\right|_{t=0} = \frac{4\pi\int_0^\infty \gamma_{\mathrm{AI}}(r)\left[\gamma(r)n^0_{\mathrm{Ry}}(r)+\beta n^0_{\mathrm{Ry}}(r)^2\right]r^2\,\mathrm{d}r}{4\pi\int_0^\infty \gamma_{\mathrm{AI}}(r)n^0_{\mathrm{Ry}}(r)r^2\,\mathrm{d}r}. \tag{4.2.10}$$

The involved time derivative is given by $\gamma_{\mathrm{AI}}(r)\dot{n}^0_{\mathrm{Ry}}(r)$ which can be taken directly from the differential equation (4.2.1). Splitting this expression into two integrals yields

$$\gamma^0_{\mathrm{coll}} = \frac{\int_0^\infty \gamma_{\mathrm{AI}}(r)\gamma(r)n^0_{\mathrm{Ry}}(r)r^2\,\mathrm{d}r}{\int_0^\infty \gamma_{\mathrm{AI}}(r)n^0_{\mathrm{Ry}}(r)r^2\,\mathrm{d}r} + \beta\frac{\int_0^\infty \gamma_{\mathrm{AI}}(r)n^0_{\mathrm{Ry}}(r)^2r^2\,\mathrm{d}r}{\int_0^\infty \gamma_{\mathrm{AI}}(r)n^0_{\mathrm{Ry}}(r)r^2\,\mathrm{d}r}. \tag{4.2.11}$$

Inserting the definition of $\gamma(r)$, the first integral can be transformed to

$$(\gamma_{\mathrm{n}}+\gamma_{\mathrm{PI}})\frac{\int_0^\infty \gamma_{\mathrm{AI}}(r)n^0_{\mathrm{Ry}}(r)r^2\,\mathrm{d}r}{\int_0^\infty \gamma_{\mathrm{AI}}(r)n^0_{\mathrm{Ry}}(r)r^2\,\mathrm{d}r} + \frac{\int_0^\infty \gamma_{\mathrm{AI}}(r)\gamma_{\mathrm{coll}}(r)n^0_{\mathrm{Ry}}(r)r^2\,\mathrm{d}r}{\int_0^\infty \gamma_{\mathrm{AI}}(r)n^0_{\mathrm{Ry}}(r)r^2\,\mathrm{d}r} \tag{4.2.12}$$

$$=(\gamma_{\mathrm{n}}+\gamma_{\mathrm{PI}}) + \frac{\int_0^\infty \gamma_{\mathrm{AI}}(r)\gamma_{\mathrm{coll}}(r)n^0_{\mathrm{Ry}}(r)r^2\,\mathrm{d}r}{\int_0^\infty \gamma_{\mathrm{AI}}(r)n^0_{\mathrm{Ry}}(r)r^2\,\mathrm{d}r}. \tag{4.2.13}$$

The remaining integrals can be solved analytically if we assume that the Rydberg density $n^0_{\mathrm{Ry}}(r) = an_0(r)$ is proportional to the ground state density. Then, this expression becomes

$$(\gamma_{\mathrm{n}}+\gamma_{\mathrm{PI}}) + \sqrt{\frac{8}{27}}\sigma_{\mathrm{inel}}\Phi. \tag{4.2.14}$$

The second appearing integral in eq. (4.2.13) can be solved analogously and the initial decay rate from eq. (4.2.10) becomes

$$\gamma^0_{\mathrm{coll}} = \sqrt{\frac{8}{27}}\left(\sigma_{\mathrm{inel}} + \frac{a\beta}{\bar{v}_{\mathrm{coll}}}\right)\Phi + (\gamma_{\mathrm{n}}+\gamma_{\mathrm{PI}}). \tag{4.2.15}$$

Under the assumption that the Rydberg–Rydberg collisions are small, it is thus possible to extract the inelastic scattering cross section σ_{inel} as the slope of the initial decay rate as a function of the atomic flux. Unfortunately, the Rydberg–Rydberg processes do not change the shape of the curve but only the slope and can thus lead to a wrong value for the inelastic cross section. However, the implicit dependence of the constant $a \equiv a(\Omega)$ on the driving strength allows to check its influence on the slope by varying Ω. If the variation of the driving strength does not change the observed slope, one can conclude that Rydberg–Rydberg losses are negligible.

4.2.3. Average collision velocity

So far, we did not specify the average collision velocity $\bar{v}_{\mathrm{coll}}$ between the Rydberg atom and the surrounding ground state atoms in the thermal ensemble. This problem is complicated by the fact that the Rydberg atom (r) as well as the ground state atoms (g) are moving.

For both particles with mass m, the average thermal velocity in equilibrium with a thermal gas of temperature T is given by [153]

$$\bar{v}_{\text{th}}^{(i)} = \sqrt{\frac{8k_B T}{\pi m}}, \tag{4.2.16}$$

where $i \in \{\text{r}, \text{g}\}$ denotes the considered particle. Even though the time-averaged velocity of the undirected thermal motion is zero, the particle i is moving with a randomly changing velocity $\vec{v}_{\text{th}}^{(i)}$ at every instance of time. In addition to this undirected thermal motion we also have to consider the directed motion of the Rydberg atom due to the recoil velocity

$$\vec{v}_{\text{rec}} = \frac{h}{m\lambda}\hat{z} \tag{4.2.17}$$

transferred during the excitation from a laser beam that is aligned in the z-direction. It is then easy to see that the momentary collision velocity $\vec{v}_{\text{coll}}$ is given by

$$\vec{v}_{\text{coll}} = \vec{v}_{\text{th}}^{(g)} - (\vec{v}_{\text{th}}^{(r)} + \vec{v}_{\text{rec}}). \tag{4.2.18}$$

In order to derive the average collision velocity $\bar{v}_{\text{coll}} = \sqrt{\langle \vec{v}_{\text{coll}}^2 \rangle}$, we need to calculate

$$\vec{v}_{\text{coll}}^2 = \left(v_{\text{th,x}}^{(\text{g})} - v_{\text{th,x}}^{(\text{r})}\right)^2 + \left(v_{\text{th,y}}^{(\text{g})} - v_{\text{th,y}}^{(\text{r})}\right)^2 + \left(v_{\text{th,z}}^{(\text{g})} - v_{\text{th,z}}^{(\text{r})} - v_{\text{rec}}\right)^2 \tag{4.2.19a}$$

$$\begin{aligned} &= v_{\text{th,x}}^{(\text{g})2} + v_{\text{th,x}}^{(\text{r})2} + v_{\text{th,y}}^{(\text{g})2} + v_{\text{th,y}}^{(\text{r})2} + v_{\text{th,z}}^{(\text{g})2} + v_{\text{th,z}}^{(\text{r})2} + v_{\text{rec}}^2 \\ &- 2\left(v_{\text{th,x}}^{(\text{g})}v_{\text{th,x}}^{(\text{r})} + v_{\text{th,y}}^{(\text{g})}v_{\text{th,y}}^{(\text{r})} + v_{\text{th,z}}^{(\text{g})}v_{\text{th,z}}^{(\text{r})} + v_{\text{th,z}}^{(\text{g})}v_{\text{rec}} - v_{\text{th,z}}^{(\text{r})}v_{\text{rec}}\right) \end{aligned} \tag{4.2.19b}$$

and average it to obtain $\langle \vec{v}_{\text{coll}}^2 \rangle$. Since the average is an additive quantity, the average of the sum equals the sum of the averages. Additionally, the random thermal motion of the Rydberg atom and the ground state atoms is completely uncorrelated and we see that $\langle v_{\text{th,j}}^{(\text{g})} v_{\text{th,j}}^{(\text{r})} \rangle = \langle v_{\text{th,j}}^{(\text{g})} \rangle \langle v_{\text{th,j}}^{(\text{r})} \rangle$ for $j \in \{x, y, z\}$. Furthermore, v_{rec} is a constant and thus $\langle v_{\text{th,j}}^{(i)} v_{\text{rec}} \rangle = v_{\text{rec}} \langle v_{\text{th,j}}^{(i)} \rangle$. As known from the Boltzmann distribution, the individual vector components of the thermal velocity average to zero $\langle v_{\text{th,j}}^{(i)} \rangle = 0$. Therefore, all mixed terms in eq. (4.2.19b) vanish. For the squared terms, we can apply the equipartition theorem $\langle v_{\text{th,j}}^{(i)2} \rangle = \frac{1}{3}\bar{v}_{\text{th}}^2$ [154]. We then obtain

$$\langle \vec{v}_{\text{coll}}^2 \rangle = 6\frac{1}{3}\bar{v}_{\text{th}}^2 + v_{\text{rec}}^2 \tag{4.2.20}$$

and the average collision velocity becomes

$$\bar{v}_{\text{coll}} = \sqrt{2 + \frac{v_{\text{rec}}^2}{\bar{v}_{\text{th}}^2}}\,\bar{v}_{\text{th}}. \tag{4.2.21}$$

We see that the average collision velocity is not identical but still proportional to the average thermal velocity. Even without the additional recoil that the Rydberg atom acquires, we see a factor of $\sqrt{2}$ that takes into account that both collision partners are moving with the thermal velocity distribution. If the recoil velocity is included, this changes the prefactor depending on the thermal velocity and thus on the temperature of the cloud. As the temperature range for the discussed experiments is rather small, we can extract an average numerical prefactor that is approximately valid in the studied temperature range. The average collision velocity in our experiment is then given by

$$\bar{v}_{\text{coll}} \approx 1.56\sqrt{2}\bar{v}_{\text{th}}. \tag{4.2.22}$$

4.3. Cross section measurement

In order to determine σ_{AI} and σ_{inel} from the experiment, we realised atomic samples at various atomic fluxes by changing the particle density. To achieve this, we prepared a thermal cloud of $N = 4 \times 10^5$ atoms in a trap with trapping frequencies of $\omega_{x,y,z} = 2\pi \times (77, 77, 94)\,\mathrm{Hz}$. For these parameters, we obtain a thermal cloud with a peak density of $n_0 = 3.1 \times 10^{14}\,\mathrm{cm}^{-3}$ and a temperature of 200 nK. In order to systematically change the atomic flux, we used a so-called release and recapture method, where the atom number is reduced by shortly ramping the trap depth below the point where the atoms can leave the trap in gravity direction. The trap depth is ramped down linearly in 2.5 ms and subsequently linearly back to the original configuration in the same time. By varying the lowest point of the ramp the number of atoms that remain in the trap is gradually reduced. Due to the centre of mass motion of the atomic cloud during the release and the inverse motion in the recapture phase, the energy of the system is increased. After the recapture, we thus usually wait 600 ms for the system to thermalise at a slightly higher temperature. With this method, it is possible to change the atom number at constant trap parameters by almost two orders of magnitude while the temperature of the sample increases at most by a factor of two.

In the final trap configuration, both low-power trapping beams had an intensity of $I = 3.6(2)\,{}^{\mathrm{kW}}/_{\mathrm{cm}^2}$ that was also present during the excitation of the Rydberg atoms. From the measured photoionisation cross sections (sec. A.11), we can therefore conclude that $\gamma_{\mathrm{PI}} = \sigma_{\mathrm{PI}} \frac{I}{h\nu}$ did not exceed 1.1 kHz for the principal quantum numbers addressed in our measurements. In particular the photoionisation is always much slower than the natural decay of the studied states, which makes it a weak probe for the dynamics that hardly changes the system.

The excitation into Rydberg states was achieved using the UV laser that was focused to a Gaussian beam waist of around $w_0 = 100\,\mu\mathrm{m}$ and aligned under an angle of roughly 48 ° with respect to the quantisation axis. For such configuration and a sample prepared in the $F = 1, m_F = 1$ hyperfine state, it is possible to couple all m_j states in the Rydberg level, irrespective of the laser polarisation. The coupling strength of the individual m_j states however does depend on the polarisation [112]. To still couple only to a single m_j state, we use the compensation coil above the atoms to create a magnetic field of approximately 35 G at the position of the atoms that is aligned along the direction of gravity. This gives rise to a Zeeman-splitting of 64 MHz between the m_j sublevels, which can then be addressed individually by choosing the appropriate laser detuning. For the measurements presented here, we always addressed the $m_j = +3/2$ state of the respective $nP_{3/2}$-state.

4.3.1. Partial cross section for associative ionisation

The measurements with varied atomic flux were performed for the principal quantum numbers $n = 25, 30, 35, 41, 51, 60$ and for different laser powers. For three exemplary measurements, all performed with an excitation laser power of roughly $P = 50\,\mu\mathrm{W}$, the scaling of the peak ratio with the atomic flux is shown in fig. 4.2a. As predicted by the theoretical model, we observe a linear dependence. The fact that we see no deviation from the linear scaling also indicates that Rydberg–Rydberg processes are still negligible for the chosen parameters. Even measurements with an increased excitation laser power of $P = 1\,\mathrm{mW}$ did not show any hint of Rydberg–Rydberg processes. Only for

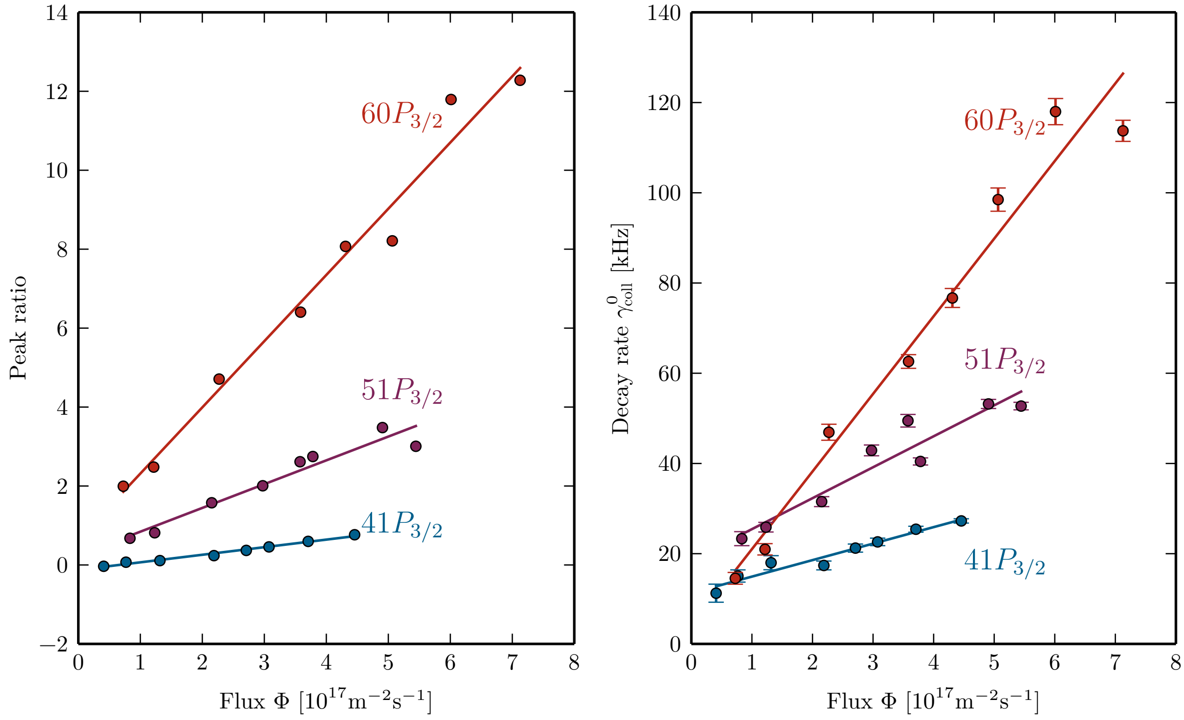

(a) **(b)**

Figure 4.2: As expected from the simple model presented in sec. 4.2, the peak ratio (a) and the initial decay rate (b) scale linearly with the atomic flux Φ. Measurements for $n = 41, 51, 60$ are shown, all taken with a laser power of 50 µW. A linear fit (solid lines) of the peak ratio reveals the cross section for associative ionisation σ_{AI}, while the linear fit of the initial decay rate gives the total inelastic scattering cross section σ_{inel}.

$P = 10\,\mathrm{mW}$, the peak ratio became approximately constant, as expected for dominant Rydberg–Rydberg collisions.

In the regime of small Rydberg–Rydberg collisions, according to eq. (4.2.9), it is possible to extract the cross section for associative ionisation σ_{AI} from the slope of a linear fit to the data if the photoionisation rate γ_{PI} is known. With the measured photoionisation cross sections (see sec. A.11), we can therefore extract the cross section for associative ionisation. For each principal quantum number, multiple measurements with laser powers between 50 µW and 1 mW were performed and the fit values were averaged. The obtained values are summarised in tab. 4.1 and depicted in fig. 4.3a. We see that the cross section is rather constant in the range between $n = 25$ and $n = 40$ and only rises significantly for $n = 51$ and $n = 60$. In contrast to measurements that were performed in the 1980s in hot atomic beam experiments and which obtained a cross section compatible with the size of the formed molecule [11–13], we see that in ultracold systems the measured cross section exceeds the geometrical cross section of the formed Rb_2^+ molecule by three orders of magnitude. This is particularly interesting as in the simple DRM model (sec. 2.3.3) the two nuclei need to approach each other up to the size of the formed molecule (less than 2 nm in our case) to undergo associative ionisation. Even though the ionisation process itself can only happen at such short distances, the measured values for σ_{AI} suggest that every perturber that enters the characteristic scattering radius $l = \sqrt{\sigma_{\mathrm{AI}}/\pi}$ of 35 nm to 80 nm will end up in an Rb_2^+ ion. Consequently, there must be a directed mass transport mechanism that efficiently moves the ground state atom towards the Rydberg core once it

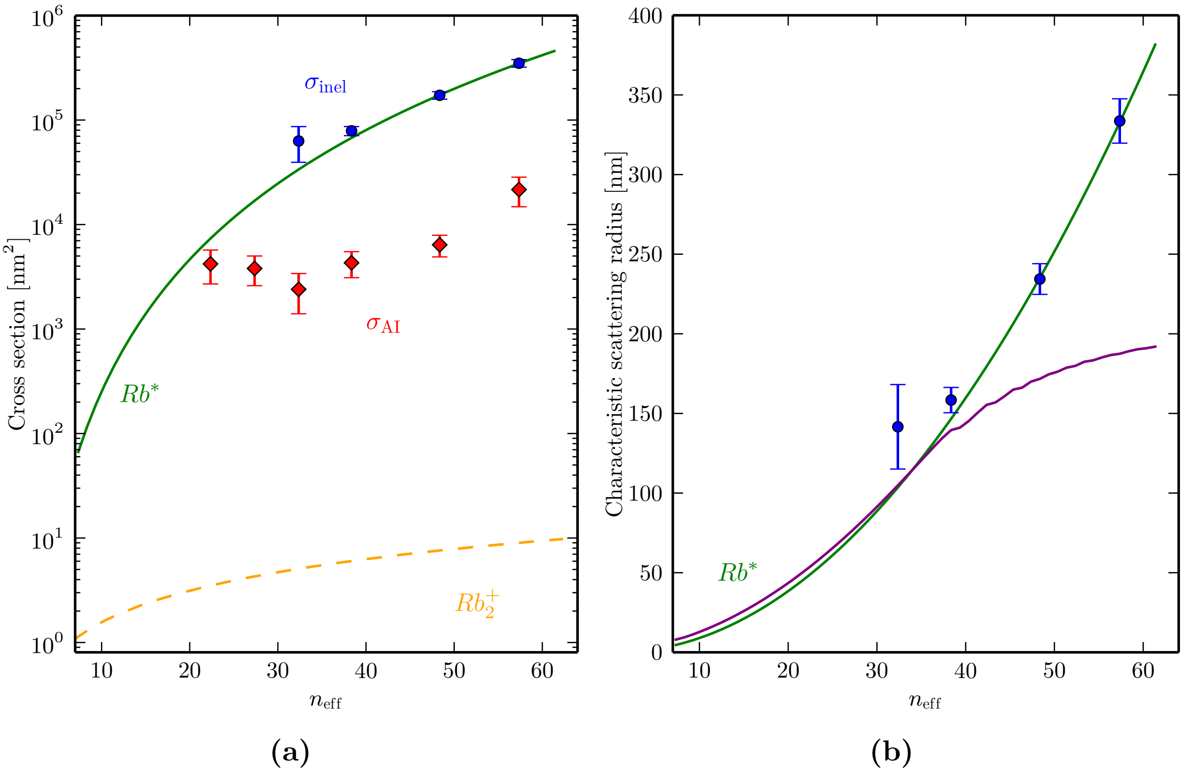

Figure 4.3: Extracted cross sections. (a) Comparison of the extracted partial cross section for associative ionisation σ_{AI} (red diamonds) and the total inelastic scattering cross section σ_{inel} (blue dots) with the geometrical cross section σ_{geo} of the Rydberg atom (solid green line) and an upper limit on the cross section of the formed Rb_2^+ molecule (dashed orange line) as a function of the effective principal quantum number n_{eff}. The error bars denote the standard deviation from the fit. (b) A detailed comparison of the characteristic scattering radius $l = \sqrt{\sigma_{\mathrm{inel}}/\pi}$ (blue dots) with the size of the Rydberg atom. Langevin capture through polarisation of the ground state atom by the screened Rydberg core (purple line) is not sufficient to explain the observed scattering radii.

trespasses the measured characteristic scattering radius up to the point where it can undergo associative ionisation. A detailed discussion of this mechanism and an explanation in terms of the Rydberg–ground state potentials is given in sec. 4.4.

4.3.2. Total inelastic scattering cross section

From the same measurements that allowed us to extract the cross section for associative ionisation, we can also extract the total inelastic scattering cross section by investigating the initial decay of the Rb_2^+ signal. As predicted by eq. (4.2.15), we see a linear scaling of the initial decay rate with the atomic flux as shown in fig. 4.2b. We have already seen in sec. 4.3.1 that Rydberg–Rydberg collisions are negligible for the analysed measurements. For the initial decay rates, this is once more confirmed by the fact that for varied excitation laser power up to 1 mW we always recover the same slope in a linear fit of the data. This indicates once more that in our parameter regime Rydberg–Rydberg collisions are not yet important. Hence, we can directly deduce the total inelastic scattering cross section σ_{inel} from the slope of the linear fit. The results are summarised in tab. 4.1 and depicted in fig. 4.3.

It is interesting to compare the characteristic scattering radius $l = \sqrt{\sigma_{\mathrm{inel}}/\pi}$ to the size

Table 4.1: Measured cross sections for photoionisation by the YAG trapping light $\sigma_{\mathrm{PI}}^{\mathrm{YAG}}$ (sec. A.11), for inelastic scattering between a Rydberg atom and a ground state atom σ_{inel}, and for associative ionisation σ_{AI}. For comparison the theoretical geometrical cross section $\sigma_{\mathrm{geo}}^{\mathrm{Rb}_2^+}$ of the formed Rb_2^+ molecules (sec. 2.3.3) is presented. σ_{inel} cannot be determined reliably for $n < 35$.

state	$\sigma_{\mathrm{PI}}^{\mathrm{YAG}}$ [nm^2]	σ_{inel} [nm^2]	σ_{AI} [nm^2]	$\sigma_{\mathrm{geo}}^{\mathrm{Rb}_2^+}$ [nm^2]
$25P_{3/2}$	$2.9(10) \times 10^{-6}$	-	$4(1) \times 10^3$	3.5
$30P_{3/2}$	$1.6(5) \times 10^{-6}$	-	$4(1) \times 10^3$	4.3
$35P_{3/2}$	$2.2(6) \times 10^{-6}$	$4.8(3) \times 10^4$	$2(1) \times 10^3$	5.1
$41P_{3/2}$	$1.4(4) \times 10^{-6}$	$7.3(4) \times 10^4$	$4(1) \times 10^3$	6.0
$51P_{3/2}$	$0.6(2) \times 10^{-6}$	$1.9(3) \times 10^5$	$6(1) \times 10^3$	7.6
$60P_{3/2}$	$0.8(3) \times 10^{-6}$	$3.7(4) \times 10^5$	$21(7) \times 10^3$	9.2

of the respective Rydberg atom. As a measure for the size, we consider the position of the outermost lobe of the radial wave function. Such comparison is shown in fig. 4.3b. It is striking that the measured scattering radii agree very well with the geometric size of the Rydberg atom. Only for the lowest Rydberg states, we see a deviation and a large error caused by the difficult determination of the initial decay rate due to the weak Rb_2^+ signal in this regime. For the states with $n < 35$, a reliable determination of the decay rate was not possible any more. The fact that the inelastic scattering cross section is identical to the geometrical cross section means that every collision between a Rydberg atom and a ground state atom leads to a decay of the Rydberg atom, which implies that there is essentially no elastic scattering in the studied parameter regime. We therefore conclude the presence of a dissipative interaction that becomes active as soon as the perturber atom enters the Rydberg wave function. The microscopic origin of this interaction is discussed in detail in the next section.

4.4. Directed mass transport

The observed giant increase in the cross section for associative ionisation can be attributed to a directed mass transport enabled by the potentials arising from the interaction between the Rydberg electron and the perturber. For the case of the pure triplet potential of the $51P_{3/2}; F = 2$ state, the relevant PEC (sec. 2.4.6) in combination with the C_4 polarisation potential (sec. 2.4) is shown in fig. 4.4a. In this potential, the interplay between the s- and p-wave terms creates an overall attractive shape, as discussed in sec. 2.4.5. Due to the shape of this potential, the incoming perturber already gains a lot of kinetic energy at the outermost parts of the wave function. Thus, in comparison to the pure C_4 interaction, the perturber needs much less time to arrive at small internuclear radii, where associative ionisation can occur through the DRM. Integrating the equation of motion of a classical particle in the potential shows that the transport can take place at a time scale of a few microseconds, which is much faster than the lifetime of the Rydberg atom. While a full quantum mechanical treatment of the problem is beyond the scope of this thesis, the experimental evidence for the mass transport is obvious through the giant increase of the measured cross section.

This mass transport mechanism is a unique effect that can only be observed in ultracold systems. In particular, previous atomic beam experiments [11–13] were not able to observe

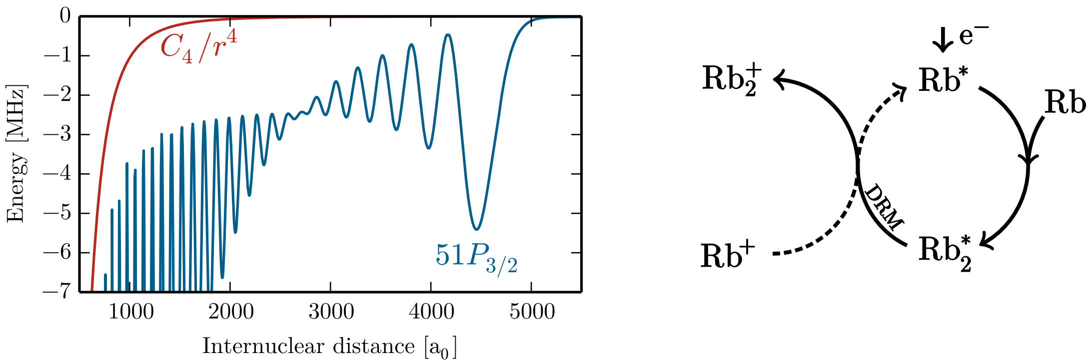

(a) **(b)**

Figure 4.4: Electron-mediated mass transport. (a) The potential acting on the perturber atom through the C_4 polarisation interaction alone (red line) and in combination with the scattering from the Rydberg electron in the $51P_{3/2}$ state (blue line). (b) The quasi-catalytic process enabled by the Rydberg electron (solid lines) vastly increases the probability of inelastic collisions with Rb ground state atoms, ultimately leading to metastable excited Rb_2^* molecules that subsequently ionise into Rb_2^+ through the DRM (sec. 2.3.3). In an ultracold plasma, the recombination of Rb^+ and e^- into Rydberg states (dashed line) could complete the catalytic cycle.

this effect since the beams had a temperature of roughly 500 K, corresponding to thermal energies on the order of 10 THz. This not only limits the highest addressable Rydberg state due to collisional ionisation but also makes the Rydberg–ground state interaction negligible compared to the thermal motion. Since only the C_4 interaction eventually becomes strong enough to dominate over the thermal energy, it is not surprising that those measurements found a cross section for associative ionisation that is in agreement with the geometrical size of the Rb_2^+ molecule.

A possible alternative microscopic explanation consists in the Langevin capture of the ground state atom in the C_4 potential created by the polarisation of the perturber through the Coulomb field of the Rydberg core. Extending the C_4 potential presented in sec. 2.3.3 to also include the partial screening by the charge of the Rydberg electron gives rise to the effective residual charge $q_{\text{eff}} = q\int_0^R \Psi(r)\,\mathrm{d}r$ and consequently to an effective $C_4^{\text{eff}}(R)$. For the Langevin capture, we are interested in the distance R_{L} at which the resulting $C_4^{\text{eff}}(R)/R^4$ potential equals the thermal energy as for deeper potentials the particle in the potential does not have sufficient energy to escape again. The comparison in fig. 4.3b reveals that for high principal quantum numbers the measured scattering radii exceed the Langevin radius R_{L} by far. The fact that the inelastic scattering cross section is given by the size of the Rydberg electron's wave function rather than the characteristic Langevin radius indicates that the interaction due to the electron's potential is dominant far from the core. In combination with the insights on l-changing collisions from ref. [57], it is therefore very likely that also the observed mass transport is not explained in terms of a simple Langevin capture and subsequent motion in the C_4 potential but the additional interaction between the Rydberg electron and the perturber plays a crucial role.

Despite the vast increase in the associative ionisation cross section by the mass transport mechanism, it still does not cover all inelastic collisions. By comparing σ_{AI} to σ_{inel}, we see that only roughly every 20th inelastic collision leads to the creation of a Rb_2^+ molecule. This means that the majority of collisions does not lead to the formation of a molecular ion and is thus not tracked in our system. Possible other decay mechanisms are listed in the following:

- The presence of the perturber changes the wave function of the Rydberg atom. Especially for small internuclear distances we see a significant admixture of surrounding states with different l quantum numbers. This repeals the dipole selection rules and thus opens further decay channels for the Rydberg atom. Ultimately, this process could lead to an accelerated spontaneous decay.
- After the collision partners already approached each other significantly, the Rydberg atom decays naturally into the ground state. For very small internuclear distances, the two ground state atoms also show a van-der-Waals interaction that gives rise to a molecular potential. Thus, it might be possible that the system decays into a neutral Rb_2 molecule.
- Inelastic collisions in which the partners separate again, leaving the Rydberg atom in a lower state [57]. The excess energy is converted to kinetic energy, which leads to a loss of the particles from the trap. The microscopic reason for such process might be the avoided crossing between the singlet trilobite PEC and the triplet butterfly PEC that is shown in fig. 2.12. Due to the high kinetic energy that the perturber acquired up to that point, diabatic crossings to the triplet trilobite PECs might also be considered as an escape channel. As both trilobite states adiabatically connect to the lower hydrogenic manifold, this process leads to a significant population of high-l states.

4.5. The electron as a catalyst

Like it was already observed for a single ion in an ultracold cloud [155], also here, a single charged particle—the Rydberg electron—vastly changes the reaction rate. The role of the Rydberg electron in the observed process shows a close analogy to a catalyst in a generic catalytic reaction. This can be seen by looking at the reaction dynamics that is readily described by the Arrhenius equation

$$k = n\sigma_{\mathrm{coll}}\bar{v}_{\mathrm{th}}e^{-E_A/(kT)}. \tag{4.5.1}$$

In conventional reactions, the role of the catalyst is to provide a transition state that is lower in energy and thus to reduce the activation barrier E_{A}. Due to the exponential dependence, this usually leads to a vast increase in the reaction rate. In our case, there is no activation barrier and the role of the Rydberg electron is rather to increase the collision frequency $n\sigma_{\mathrm{coll}}\bar{v}_{\mathrm{th}}$ by altering the cross section. Moreover, the final molecular ion formation process via the DRM relies on the presence of the electron. In this way, the production rate of Rb_2^+ molecules is increased by the presence of the Rydberg electron by several orders of magnitude, just like a catalyst would do. A second condition for catalysis is that the catalyst is not consumed by the reaction. This is obviously fulfilled in our case as well. This partial catalytic process can be part of a full catalytic cycle (fig. 4.4b), where free Rb^+ ions and free electrons recombine into high-lying Rydberg states [156] and therefore have a highly increased probability to react with surrounding ground state atoms, eventually releasing the electron again. In ultracold plasmas [70, 157, 158] for example, such catalytic cycles can take place and increase the production rate of molecular ions significantly.

4.6. Summary

By studying the decay dynamics of resonantly excited Rydberg atoms in dense thermal clouds, we were able to extract the scattering cross section for associative ionisation as well as the total inelastic scattering cross section for collisions with ground state atoms. The giant magnitude of the measured cross section for associative ionisation combined with the fact that the inelastic scattering cross section is as big as the geometric cross section strongly indicates the presence of a directed mass transport mechanism that accelerates the perturber atom towards the Rydberg core. As a simple Langevin capture model is not sufficient to explain the observed behaviour, we conclude that the potential created by the Rydberg electron is most likely the reason for the mass transport. In this picture, the electron takes the role of a catalyst that increases the production rate of Rb_2^+ ions by several orders of magnitude.

The existence of the Rydberg-mediated mass transport has a direct influence on ultracold Rydberg experiments. Without this process the expected cross section is on the order of $1\,\mathrm{nm}^2$ and for a typical cold sample with a peak density of $n_0 = 5 \times 10^{14}\,\mathrm{cm}^{-3}$ and a temperature of $T = 200\,\mathrm{nK}$ this amounts to an expected rate for associative ionisation of $\gamma_{\mathrm{AI}} = n_0 \sigma_{\mathrm{AI}} v_{\mathrm{th}}(T) \approx 10\,\mathrm{Hz}$. This is negligible compared to the natural decay rates of the studied states that range from 7 kHz to 50 kHz. Consequently, without the presented mass transport mechanism associative ionisation should be hardly visible in ultracold systems. However, the observed giant increase in the cross section renders associative ionisation an important process that even dominates the spontaneous decay for high Rydberg states. It is therefore necessary to consider associative ionisation as a decay channel in high-density ultracold Rydberg gases. Especially for coherent excitation schemes like Rydberg dressing or in the context of quantum information processing, it might thus be useful to stay in the regime of low ground state densities and small principal quantum numbers to minimise the rate of associative ionisation.

On the other hand, the increased cross section renders associative ionisation a useful probe that allows to continuously study the Rydberg excitations present in the sample. Especially in cases where the photoionisation cross section is small, e.g. for Rydberg S-states, or where photoionisation does not appear due to the absence of light fields, associative ionisation provides a well-suited probe for high-density samples. Due to its linear dependency on the ground state density, associative ionisation might also be used to probe the density distribution of a trapped atomic cloud by steering a tightly focused beam across the cloud and recording the created Rb_2^+ ions.

In addition to the decay by associative ionisation, also the excitation of Rydberg atoms in an ultracold cloud depends on the ground state density. The overall process, including excitation and decay into a molecular ion, therefore depends quadratically on the ground state density and is thus nonlinear. Hence, this process might also allow to study bistability and Zeno dynamics in nonlinear dissipative systems [159].

Furthermore, it should be noted that the interaction induced by the Rydberg electron and the resulting increase of the scattering cross section is quite universal and should also be present in other atomic species that show a negative scattering length for electron scattering. While the details of the underlying level scheme depend on the species of the Rydberg atom, the envelope of the arising Rydberg–ground state potential is just determined by the scattering properties between the electron and the perturber. Therefore, the overall shape of the potential depends on the perturber species. In the future it might be interesting to investigate the Rydberg–ground state scattering properties of different atomic species and in the combination of different species. Such systems and the comparison between them should be especially suited to study the role of the p-wave shape resonance in the observed mass transport mechanism.

5. Ultralong-range Rydberg molecules

After discussing the changes that the Rydberg–ground state interaction introduces in the scattering process of the collision partners, we will now turn to a static picture and discuss photoassociation of molecular bound states in the potential formed by the Rydberg electron. In this chapter, we will restrict the discussion to the outer regions of the potential that give rise to ultralong-range Rydberg molecules, as presented in sec. 2.4.6. In the following, we present the first extensive photoassociation spectroscopy for P-state Rydberg molecules in rubidium, spanning more than the full fine structure splitting of the $25P$-state. Due to the employed time-of-flight measurement, we are able to extract the lifetime of the studied molecules and, by applying an external electric field, we can determine the permanent electric dipole moment for some of the deepest bound states. Since the scattering of the Rydberg electron from the ground state perturber gives rise to states of mixed hyperfine character, we are able to observe spin-flip processes in the perturber atom upon photoassociation of the Rydberg molecule. Due to an incidental near-degeneracy of the Rydberg state's fine structure and the hyperfine structure of the perturber, we furthermore observe molecular states that strongly entangle the fine structure state of the Rydberg atom with the hyperfine state of the perturber.

5.1. Spectroscopy of P-state Rydberg molecules

To gain spectroscopic evidence for the ultralong-range Rydberg molecules predicted by the calculated PECs, we extended the TOF measurement scheme presented in sec. 4.1 by varying the detuning of the excitation laser. In contrast to a continuous excitation scheme, this allows us to still obtain the full information on the lifetime of the excited state while performing the spectroscopy. To increase the statistics, the TOF experiment is repeated multiple times for each laser detuning and the results are averaged. Since the excitation of a molecule requires two atoms to be much closer together than the average interatomic distance in the prepared samples, the small probability to find a suited atom pair suppresses the transition rate into molecular states. Due to this suppression, the sample is even less affected by the excitation pulse on a molecular line compared to the atomic transition. It is therefore possible to perform 1000 pulses of $1\,\mu$s length on the same sample, where each pulse is followed by $200\,\mu$s of free evolution during which we record the ion signal. In the presented experiments, the excitation laser had a power of roughly 40 mW and was focused to a beam waist of $40\,\mu$m. It entered the chamber in the horizontal plane with a linear polarisation oriented perpendicular to the quantisation axis. The spectrum obtained in a spin-polarised BEC of 10^5 atoms in the $F = 2$, $m_F = +2$ ground state at final trapping frequencies of $\omega_{x,y,z} = 2\pi \times (64, 64, 60)\,\mathrm{Hz}$ is shown in fig. 5.1. To our knowledge, this is the first extensive spectroscopy on P-state Rydberg molecules, spanning a range of more than 10 GHz with a frequency resolution of 1 MHz.

The most prominent features in the spectrum are surely the strong lines at 0 GHz and -7.7 GHz, corresponding to the atomic transition into the $25P_{3/2}; F = 2$ and $25P_{1/2}; F = 2$ state, respectively. As expected, we observe a plenitude of discrete molecular lines on the

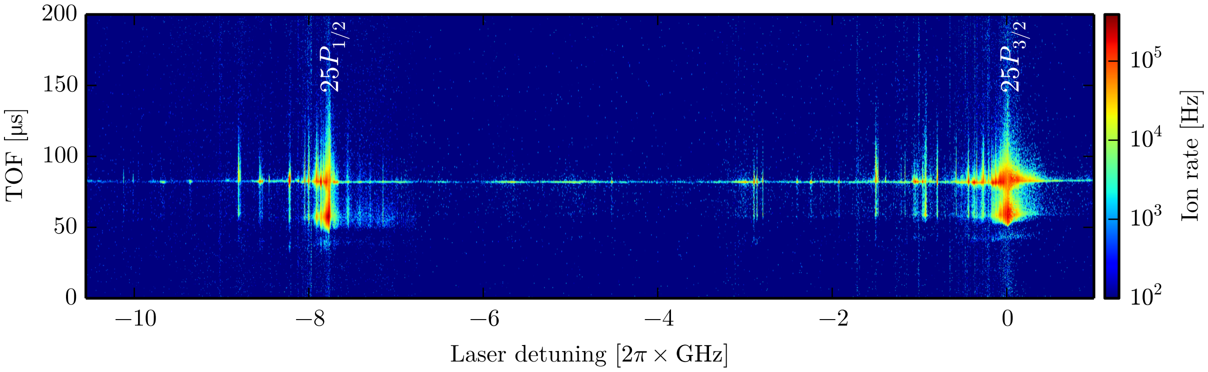

Figure 5.1: Measured spectrum around the $25P$-state from a BEC of 10^5 atoms in the $F = 2$, $m_F = +2$ ground state. The strong lines at 0 GHz and −7.7 GHz correspond to the atomic transition to the $25P_{3/2}$- and $25P_{1/2}$-state, respectively. The figure shows a combined spectrum from several measurements, each spanning roughly 1.5 GHz. The flight time is 82 µs for the Rb_2^+ ions and 58 µs for the Rb^+ ions. The spectrum was recorded with a resolution of 1 MHz.

red side (lower energy) of both atomic transitions that are visible as vertical lines of increased line intensity in fig. 5.1. A peculiar situation arises on the blue side (higher energy) of the $25P_{1/2}; F = 2$ atomic transition as the molecular lines appearing here are bound states in the $25P_{3/2}; F = 1$ potential. A detailed discussion on these hyperfine mixing molecular states is given in sec. 5.2.

A second, very interesting feature of the measured TOF spectrum is the omnipresent signal of Rb_2^+ ions giving rise to the almost continuous line at 82 µs. It is astonishing that even aside of the observed discrete molecular lines there always seems to be a small but finite probability to excite a molecular state that exclusively decays into molecular ions. This may possibly be caused by molecular states that have a non-vanishing probability density at small internuclear distances and can thus efficiently decay into molecular ions. As such an efficient decay implies a short lifetime of the molecular state the line broadens and individual short-lived states can overlap in the spectrum to an almost continuous signal. Possible candidates for such molecular states at small internuclear separations might be delocalised states in the complex potential landscape that arises beyond the crossing of the butterfly states with the P-state (fig. 2.12). A more detailed analysis of the bound states in this potential region and their overlap with the molecular ion state is beyond the scope of this work but might be interesting to study in the future.

5.1.1. Lifetimes

As a benefit of the TOF measurement technique, we obtain the full information on the lifetime of the observed molecular states in the spectroscopy. To quantify the lifetime, we can slice the spectrum from fig. 5.1 along the time axis and obtain the TOF decay signals for each of the observed molecular lines. Those can, in analogy to the evaluation presented in sec. 4.1, be fitted with exponential functions to extract the characteristic decay time τ_{Rb^+} of the Rb^+ peak and, after subtracting the Rb^+-decay, to extract the decay time $\tau_{Rb_2^+}$ of the Rb_2^+-signal.

In the following, we will give a very brief discussion of the measured lifetimes and refer to ref. [160] for a much more detailed study on the lifetimes of the individual molecular states, including a systematic study of the dependence on the atomic density.

Table 5.1: Lifetimes extracted by exponential fits to the decay signal of the Rb^+ peak (τ_{Rb^+}) and the Rb_2^+ peak ($\tau_{\mathrm{Rb}_2^+}$) on a subset of the observed molecular lines at a detuning ν_M from the $25P_{1/2}; F=2$ state and the $25P_{3/2}; F=2$ state. For the molecular lines with a fast decaying Rb_2^+ peak the signal of the Rb^+ peak is usually too small for a reliable fit and the values are omitted.

$25P_{1/2}$			$25P_{3/2}$		
ν_M [MHz]	τ_{Rb^+} [µs]	$\tau_{\mathrm{Rb}_2^+}$ [µs]	ν_M [MHz]	τ_{Rb^+} [µs]	$\tau_{\mathrm{Rb}_2^+}$ [µs]
−91	21.5(17)	3.0(1)	−110	18.3(11)	3.41(4)
−103	-	1.86(2)	−141	20.3(12)	4.05(2)
−125	17.6(8)	8.1(1)	−175	22.1(19)	3.92(3)
−245	21.7(8)	8.6(1)	−289	18.7(11)	8.7(1)
−454	19.1(21)	3.15(4)	−449	19.0(8)	6.4(1)
−691	-	1.74(5)	−807	20.6(8)	7.1(1)
−765	-	0.84(3)	−936	16.5(9)	7.0(3)
−778	18.0(15)	6.7(1)			
−793	20.2(15)	6.3(1)			
−1019	20.9(14)	8.4(1)			
−1035	22.5(12)	8.7(1)			
−1042	21.2(11)	7.7(1)			
−1592	-	0.90(2)			

A summary of the determined decay times τ_{Rb^+} and $\tau_{\mathrm{Rb}_2^+}$ is given in tab. 5.1. While the decay times of the Rb^+ peaks are all compatible with the lifetime $\tau_{25\mathrm{P}} = 18.6\,\mu\mathrm{s}$ of the atomic Rydberg excitation and show only small variations, the Rb_2^+ peaks generally decay faster and vary from roughly 1 µs[1] to almost 9 µs. For those states that show a fast decay of the Rb_2^+ signal, the decay into molecular ions is very efficient and accordingly only few Rydberg molecules decay into Rb^+ ions during their lifetime. Consequently, we observe only a very small Rb^+ signal that cannot be fitted reliably with an exponential function.

The lifetimes presented here were measured in the high density environment of a BEC with a peak particle density of $n_0 = 1.3 \times 10^{14}\,\mathrm{cm}^{-3}$. For such high densities, the collision of the photoassociated Rydberg molecules with the remaining ground state atoms becomes a limiting factor for the lifetime which is revealed by a systematic study of the lifetimes in thermal clouds of varying particle densities [160]. Interestingly, only the lifetime of the Rb_2^+ peak shows a dependency on the ground state density while the lifetime of the Rb^+ peak stays constant. This suggests that a collision of a Rydberg molecule with a ground state atom leads exclusively to a molecular ion or a loss of the particles. We thus observe different lifetimes for those Rydberg molecules that collided with a ground state atom and those that did not.

5.1.2. Dipole moments

Ultralong-range Rydberg molecules consist predominantly of one particular low-l state and thus the electron density is mostly given by the shape of the unperturbed Rydberg state $|\Psi_R\rangle \approx |n_1, l_1, j_1, m_{j1}\rangle \otimes |m_{s1}, m_{I2}\rangle$. Since a single, unperturbed atomic state is symmetric with respect to a reflection in the x-y-plane, the dipole matrix element $\langle\Psi|d\hat{z}|\Psi\rangle$

---

[1] Due to the excitation pulse length of 1 µs, we cannot detect lifetimes smaller than this.

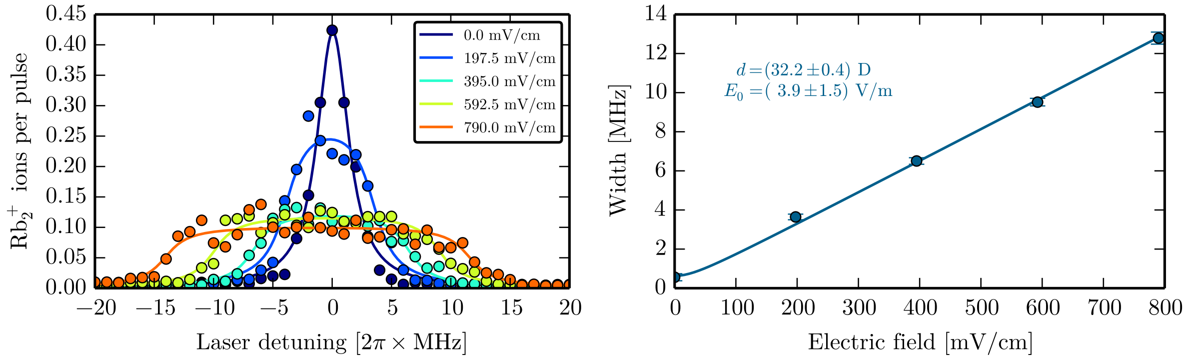

(a) **(b)**

Figure 5.2: Measurement of the dipole moment for bound states in the ultralong-range PECs. (a) Measured spectra (dots) for various applied electric field strengths with eq. (5.1.4) fitted to the data (lines). (b) Scaling of the measured field broadening (dots) as a function of the applied electric field. The values for the broadening are fitted with eq. (5.1.5) that allows to correct for a finite offset field E_0.

vanishes. In first order perturbation theory, i.e. neglecting the contribution of other states, ultralong-range Rydberg molecules do therefore not possess a permanent electric dipole moment. Going beyond perturbation theory, however, we see that in the increasingly deep wells of the ultralong-range PECs shown in fig. 2.14 we get an increasing admixture of other states, which in turn gives rise to a permanent electric dipole moment for the bound states in those wells. Especially in the vicinity of the avoided crossing with the butterfly PECs, we see a strong mixing with states from the hydrogenic manifolds and consequently expect high permanent electric dipole moments.

In order to experimentally study the dipole moment of the observed ultralong-range Rydberg molecules, we applied an electric field to the sample during photoassociation of the molecule. Field strengths up to $0.44\,\mathrm{V/cm}$ were applied through the main electrodes resulting in a field vector pointing in gravity direction. In this configuration, the generated ions are accelerated towards the ion optics and further guided to the ion detector. It is therefore possible to apply a finite electric field and still observe the generated ions in the detector. In the presence of the field, the same spectroscopy method that is described in sec. 5.1 was used. As an example, the obtained spectra for various field strengths at the molecular line at $-2802\,\mathrm{MHz}$ are shown in fig. 5.2a. While for vanishing field strength, we obtain a pure Lorentzian line shape

$$L(\nu) = A\frac{\gamma/2}{(\nu-\nu_0)^2+\gamma^2/4}, \tag{5.1.1}$$

with the amplitude A, the centre frequency ν_0, and the linewidth γ, the lines broaden as the field is increased.

From the simple theory of dipolar molecules in electric fields (sec. 2.6), we would expect to see discrete pendular states in the spectrum rather than the observed broadening. However, the rotational constant of ultralong-range molecules is rather small due to the high bond length, and the involved dipole moments are small as well. Therefore, the arising pendular states (see sec. 2.6) are closely spaced for the small fields used in this experiment. Due to the finite width of the molecular lines on the order of a few MHz, it is not possible to spectroscopically resolve them. Instead, they overlap to a continuous Stark fan [51] and the line shape is given by a convolution of the individual Lorentzian

Table 5.2: Measured dipole moments d and linewidths w of the molecular lines at frequency ν_M below the $25P_{1/2}$ and the $25P_{3/2}$ state. The molecular line at -240 MHz with respect to the $25P_{1/2}$ state was measured twice to check the reproducibility of the measurement.

$25P_{1/2}$			$25P_{3/2}$		
ν_M [MHz]	w [MHz]	d [D]	ν_M [MHz]	w [MHz]	d [D]
−240	4.7(3)	2.6(3)	−801	3.1(3)	11.8(7)
−240	3.0(1)	3.4(2)	−807	4.5(3)	13.1(5)
−694	2.4(3)	44.5(20)	−1931	3.5(1)	24.1(3)
−771	6.0(4)	59.9(16)	−2409	7.8(3)	53.0(11)
−803	12.5(12)	24.1(33)	−2802	3.0(1)	32.2(4)
−1019	3.2(2)	18.6(7)	−2869	2.7(1)	36.1(7)
−1035	3.2(2)	24.6(6)	−2904	2.7(1)	39.3(11)
−1592	24.1(22)	219.6(66)	−3002	5.3(7)	10.9(7)
−1902	25.8(29)	145.3(105)	−4530	6.0(3)	33.6(5)

lines with a step function of width $2dE$ [49]

$$S(\nu) = \frac{1}{2dE}\int_{-\infty}^{\infty}(1-\Theta(\tau-dE))\Theta(\tau+dE)L(\nu)\,\mathrm{d}\tau \tag{5.1.2}$$

$$= \frac{A\gamma}{4dE}\int_{-dE}^{dE}\frac{1}{(\nu-\nu_0-\tau)^2+\gamma^2/4}\,\mathrm{d}\tau. \tag{5.1.3}$$

This integral can be solved analytically and yields

$$S(\nu) = \frac{A}{2dE}\left[\arctan\left(\frac{\nu-\nu_0+dE}{\gamma/2}\right)-\arctan\left(\frac{\nu-\nu_0-dE}{\gamma/2}\right)\right]. \tag{5.1.4}$$

For each spectrum recorded in the presence of the field, this function could be fitted to the measured spectrum to obtain the dipole moment d and the Lorentzian linewidth γ of the molecular state under investigation, as shown in fig. 5.2a. While it was possible to insert the field strength E of the particular measurement into the model and extract the dipole moment as a fitting parameter, an additional advantage arises in taking the product $w = dE$ as a fitting parameter if measurements for different field strengths were performed. By definition, we expect a linear scaling for such set of measurements when plotting w as a function of the applied field E (fig. 5.2b). In this case, the slope is solely determined by the dipole moment. The advantage of extracting w from the individual measurements rather than d for a fixed E arises from its deviation from the linear scaling for small fields that allows to detect the presence of an offset field E_0 in the directions perpendicular to E. By applying the fit function

$$w(E) = d\sqrt{E_0^2+E^2}, \tag{5.1.5}$$

we can extract the dipole moment d even in the presence of a finite offset field. This kind of field-dependent measurement was performed for a set of molecular lines below the $25P_{1/2}$ and the $25P_{3/2}$ state. The results obtained on the permanent electric dipole moment d and the Lorentzian linewidth are summarised in tab. 5.2.

In general, the measured dipole moments show the trend that states that are further separated from the atomic resonance feature higher dipole moments. Furthermore, we

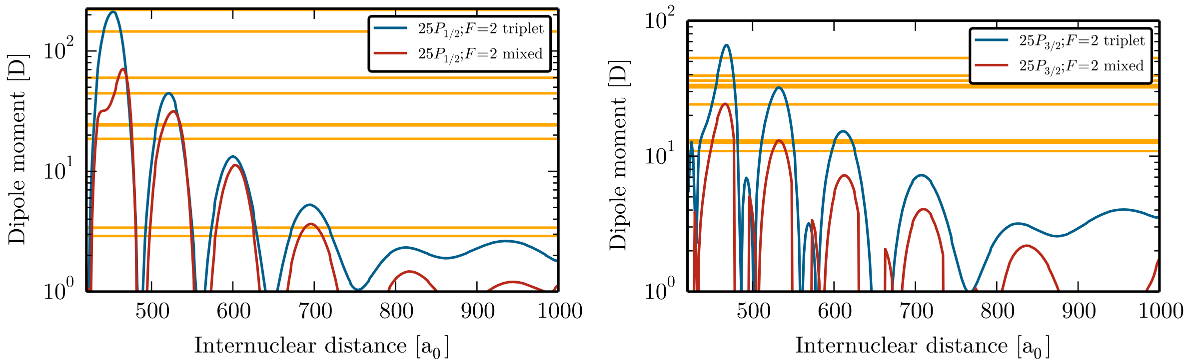

(a) **(b)**

Figure 5.3: Comparison of the measured dipole moments (orange lines) to theoretically calculated dipole moments for the pure triplet (blue) and mixed (red) potential curves. The comparison is shown separately for the observed lines (a) below the $25P_{1/2}; F = 2$ state and (b) below the $25P_{3/2}; F = 2$ state.

note that the measured values for the dipole moments show certain cluster points. In the case of the bound states below the $25P_{1/2}$ state (tab. 5.2), we find cluster points at around 3 D, 22 D, 52 D and 182 D. Since theory (sec. 2.4.9) predicts that the dipole moment of the molecular bound states mostly depends on the well in which the states are located, these cluster points give an indication to which well the individual lines correspond. This is demonstrated in fig. 5.3 where the measured dipole moments can be related to the theoretically expected dipole moments of each well. For example, in the case of the peak at −1592 MHz relative to the $25P_{1/2}$ atomic resonance, we observe an enormous dipole moment of roughly 220 D. In the theoretical model, such high dipole moments can only be realised by the well at 450 a_0 in the pure triplet potential (fig. 5.3a). Hence, it is likely that the studied line corresponds to an excited state in this well. Such states have only a small tunnel barrier to the inside and thus often show short lifetimes. Also in this case, we see from tab. 5.1 that the line at −1592 MHz indeed has a very short lifetime and accordingly is also quite broad even in the absence of an electric field.

To check the reproducibility of the measurement, we performed two independent measurements at the molecular line −240 MHz from the $25P_{1/2}$ state. Even though the revealed values for the dipole moment do not coincide within the error margin, the values are nevertheless quite close. The extracted linewidth γ however differs by almost a factor of two. This large discrepancy is mainly due to two reasons. For small applied fields, the effect of residual fields E_0 is large and is not compensated for in the fitting of γ, leading to an error in the determined value. For stronger fields, especially in combination with high dipole moments, a high uncertainty is introduced by the fact that only the steepness of the fit function's edges determines the value of γ (see highest field in fig. 5.2a). Hence, for most high-field measurements only very few data points determine the value of γ, giving rise to strong statistical fluctuations. The extracted γ-values can therefore only give information on the order of magnitude of the linewidth.

5.2. Spin-flips in Rydberg molecules

In this section, we take a closer look at the effect of the molecular bond on the internal states of the bound ground state atom. For the first time, we show experimentally that

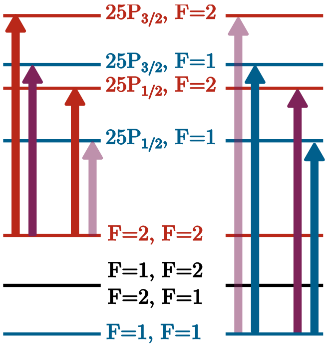

Figure 5.4: Two-particle level scheme and possible transitions. For a sample prepared in a certain F ground state, only transitions to Rydberg states with the same F quantum number are possible (blue arrows for $F = 1$ and red arrows for $F = 2$). Due to the admixture of opposite hyperfine character in the mixed type PECs, the bound states therein can be coupled from both hyperfine states. While these spin-changing transitions are usually very weak (faint purple arrows), the near-degeneracy of the $25P_{1/2}; F = 2$ state and the $25P_{3/2}; F = 1$ state leads to a much stronger coupling (strong purple arrows).

the Rydberg–ground state interaction can flip the internal state of the perturber atom (spin-flip) and can give rise to entangled states between the Rydberg fine structure state and the hyperfine state of the perturber atom.

If, at first, we consider an arbitrary pair of non-interacting atoms in a sample prepared in the hyperfine state $F \in \{1, 2\}$, we can write the quantum state in an abbreviated way[2] as $|F\rangle\, |F\rangle$. Using the single-photon transition realised by the UV laser, we can excite one of the atoms into a Rydberg state. If, as an example, we choose the $25P_{1/2}$-state, it is easy to see that the coupling strength is given by the dipole matrix element

$$d = \langle 25P_{1/2}|\, \langle F'|\hat{d}|F\rangle\, |F\rangle \tag{5.2.1}$$

$$= \langle 25P_{1/2}|\hat{d}|5S_{1/2}\rangle \otimes \langle F'|F\rangle\, . \tag{5.2.2}$$

Since $\langle F'|F\rangle = \delta_{F',F}$, the coupling to the opposite hyperfine state vanishes and the second ground state atom remains in the hyperfine state F when the first one is excited into the Rydberg state. This is not surprising as long as there is no interaction between the atoms that couples the hyperfine subspaces. As depicted in fig. 5.4, we can thus either probe the two $F = 1$ states $25P_{1/2}; F = 1$ and $25P_{3/2}; F = 1$ (blue arrows) or the two $F = 2$ states $25P_{1/2}; F = 2$ and $25P_{3/2}; F = 2$ (red arrows), depending on which hyperfine state the sample was prepared in. In particular, this means that it is not possible to observe all four $25P$-states in a single spectrum.

Due to the Rydberg–ground state interaction, this argument does no longer hold for the ultralong-range Rydberg molecules that appear on the red side of each of the four $25P$-states. As discussed in sec. 2.4.3, the Rydberg ground state interaction in conjunction with the hyperfine interaction leads to two qualitatively different ultralong-range PECs. While one is of pure triplet type and contains only one hyperfine state, the second type mixes the singlet and triplet subspace and also the hyperfine states. The electronic part of the molecular state in the mixed potential is thus of the form

$$|\Psi_{\text{mix}}\rangle = |25P\rangle\, (a\, |F = 1\rangle + b\, |F = 2\rangle)\, , \tag{5.2.3}$$

---

[2] When the state is just labelled by the hyperfine quantum number, we imply that the atom is in the ground state, i.e. in the $5S_{1/2}$ state, and the m_F state is not of importance.

with $a^2 + b^2 = 1$. A more detailed analysis of the emerging states is given in sec. 5.2.1 and sec. 5.2.2. The coupling to such a state from the initial state $|F\rangle\,|F\rangle$ is given by

$$
\begin{aligned}
d &= \langle \Psi_{\mathrm{mix}} | \hat{d} | F\rangle\,|F\rangle & (5.2.4)\\
&= \langle 25P_{1/2} | \hat{d} | 5S_{1/2}\rangle \otimes \left(a\,\langle F' = 1 | F\rangle + b\,\langle F' = 2|F\rangle\right). & (5.2.5)
\end{aligned}
$$

Since the mixed states have contributions of both hyperfine states, they can be coupled irrespective of the hyperfine state the sample was prepared in. It should therefore be possible to observe molecular states from the $F = 1$ potentials in the $F = 2$ spectrum and vice versa.

In addition to the extensive spectroscopy on a sample in the $F = 2$ state (fig. 5.1), we performed spectroscopy of the relevant frequency regions in an $F = 1$ sample. Furthermore, we calculated the relevant PECs for the four $25P$ states and quantified the amount of opposite hyperfine state admixture in each of the potential wells. A comparison of the two measured spectra with the calculated PECs on a common energy axis is shown in fig. 5.5. We see that, as expected from the above discussion, the bare atomic transitions are only visible for those states that match the hyperfine state of the prepared sample. Additionally, we see molecular lines from the mixed type PECs appearing in both spectra. This is demonstrated in detail in the following for the two distinct special cases of the *spin-flip regime* and the *entanglement regime* that differ by the degree of hyperfine mixing and the nature of the resulting molecular state.

5.2.1. Spin-flip regime

Due to the coupling of the hyperfine subspaces by the Rydberg–ground state interaction, we observe the very general effect that all mixed-type potentials obtain contributions of the opposite hyperfine state. Since in the two-atom basis all angular momentum states of the Rydberg atom split up according to the hyperfine states of the perturber, this mixing is a very generic effect that should not only affect all states in rubidium but should also hold for other alkali atoms that possess a non-vanishing nuclear spin. We observe such a situation for the $25P_{1/2}; F = 1$ state that is separated by 6.8 GHz from the $25P_{1/2}; F = 2$ state. Since the hyperfine splitting is large compared to the Rydberg–ground state interaction in the outermost wells of the ultralong-range PECs, we expect only a small mixing of the hyperfine states. Therefore, in our case, the resulting electronic part of the molecular state is of the form

$$
|\Psi\rangle = |25P_{1/2}\rangle \left(\alpha\,|F = 1\rangle + \epsilon\,|F = 2\rangle\right) + ..., \tag{5.2.6}
$$

with $\alpha \approx 1$ and $\epsilon \ll 1$. In such a state the small admixture $|\epsilon|^2$ of $|F = 2\rangle$ character allows for a weak coupling from a sample prepared in the $F = 2$ ground state. Still, the state has mostly $F = 1$ character and thus the created molecule will feature a ground state atom that is predominantly in the $F = 1$ state. The hyperfine state of the perturber is thus flipped upon excitation of the Rydberg molecule, which is why we denote this parameter range the spin-flip regime.

In the experimental $F = 2$ spectrum (fig. 5.5b), we see the spin-flip regime realised by the weak molecular line at an energy of −14.8 GHz (fig. 5.5e). Since this line is already 7 GHz detuned from the $25P_{1/2}; F = 2$ state and the calculated PECs do not predict any bound states so far from the resonance, this line cannot be attributed to the $F = 2$ PECs. Instead, the observed line is only 200 MHz below the $25P_{1/2}; F = 1$ state and

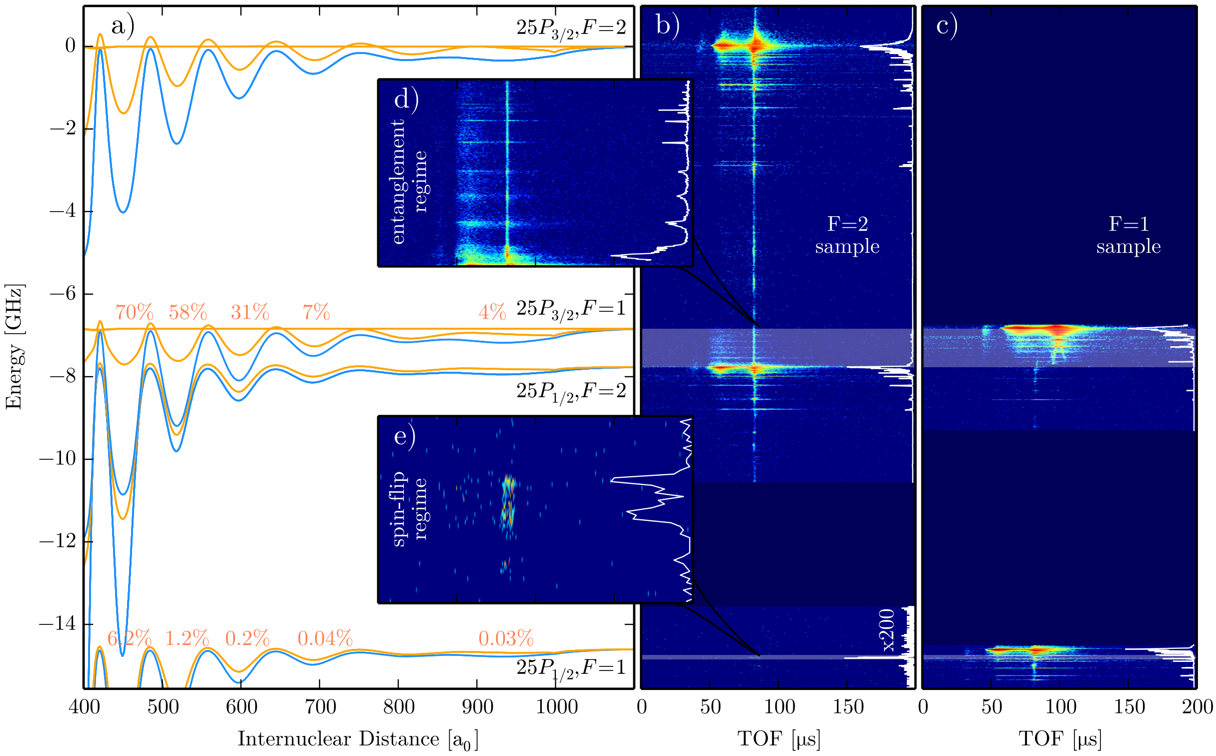

Figure 5.5: Photoassociation spectra around the $25P$-state for the two different initial hyperfine states. (a) Comparison of the calculated PECs of the four $25P$-states. The blue lines denote the pure triplet PECs that only consist of a single hyperfine state. The orange curves are of mixed singlet–triplet type and consist of both hyperfine states. The admixture of the opposite hyperfine state (red numbers) is given for each well of the mixed potentials. (b) and (c) show the measured spectra in a BEC prepared in the $F = 2$ state and the $F = 1$ state, respectively. The dark blue regions were not measured. The measured spectra share the energy axis of the calculated PECs. The white lines show the flight-time-integrated spectrum. Some states in the $F = 1$ mixed PECs appear also in the measured $F = 2$ spectrum due to a mixing of the spin states (sec. 2.4.3). The white shaded areas indicate where the effect of the spin mixing can be seen. The insets (d) and (e) show zoom-ins on the highlighted parts of the $F = 2$ spectrum and, respectively, illustrate the presence of resonances in the entanglement and the spin-flip regime (see text).

indeed the lowest bound state in the mixed potential well at $691\,a_0$ coincides with the measured energy up to 32 MHz. We thus conclude that here we observe a molecule that consists of roughly $\epsilon^2 = 0.04\%$ of $F = 2$ character (compare fig. 5.5a). Due to this small admixture of the $F = 2$ state, the coupling is very weak and the experimental detection is only possible with a very sensitive signal as it is provided by the observed ions. Since the admixture of the $F = 2$ state is so small, the perturber atom in the created molecules will be in the $F = 1$ state with a probability of 99.96%. Starting from an $F = 2$ sample, we thus couple to a molecule that is predominantly in the $F = 1$ state. The presence of the weak line in the experimental $F = 2$ spectrum therefore proves that it is possible to change the hyperfine state of the perturber atom upon photoassociation of the Rydberg molecule. This process can also be seen as a light-assisted spin-changing collision between the perturber atom and the Rydberg electron that requires the photon as a third particle to guarantee energy conservation. In this picture, the energy difference of 6.8 GHz that is bridged by the spin flip is provided or absorbed by the light field.

The fact that we observe only this one line even though the mixed potential of the $25P_{1/2}; F = 1$ state features many bound states can be explained by the admixture of the $F = 2$ and the distance distribution in the sample. While the former decreases for wells with higher internuclear separation, the latter decreases for smaller internuclear separation. The strongest coupling to the spin-flip molecule occurs therefore in a range where both contributions are still sufficiently large. We thus assume that only for the ground state in the well at $691\,a_0$ the signal is strong enough to not vanish in the noise floor of our measurement.

It should be noted that it is not possible to explain the observed line by a residual population of the $F = 1$ ground state in the prepared sample. As indicated in fig. 5.4, the transition from the $|F = 2\rangle\,|F = 2\rangle$ ground state to the $|25P_{1/2}\rangle\,|F = 1\rangle$ state is the lowest energy transition possible in the system. Consequently, a transition from $|F = 2\rangle\,|F = 1\rangle$ to $|25P_{1/2}\rangle\,|F = 1\rangle$ can be ruled out as it would require a 6.8 GHz higher photon energy.

5.2.2. Entanglement regime

In addition to the very general spin-flip regime, we see a second regime arising in the special case of the $25P$-state in rubidium. Here, the fine structure splitting $\Delta_{\text{FS}} = 7.7\,\text{GHz}$ of the Rydberg state is close to the hyperfine splitting $\Delta_{\text{HFS}} = 6.8\,\text{GHz}$ of the perturber atom and thus we see a separation of only 929 MHz between the $25P_{1/2}; F = 2$ state and the $25P_{3/2}; F = 1$ state (fig. 5.5a). Since the strength of the Rydberg–ground state interaction easily reaches the magnitude of this energy gap, we observe strong mixing between those states even for wells at high internuclear distances, as shown by the values for the opposite hyperfine state admixture in fig. 5.5a. Consequently, we are dealing with states of the form

$$|\Psi\rangle = a\,|25P_{1/2}\rangle\,|F = 2\rangle + b\,|25P_{3/2}\rangle\,|F = 1\rangle\,, \tag{5.2.7}$$

with $a \approx b$. Such a state highly entangles the fine structure of the Rydberg state with the hyperfine structure of the perturber atom, which is why we denote this the entanglement regime.

Experimental evidence for the strong mixing of states is given by the many molecular lines that appear in the energy region between $-7.7\,\text{GHz}$ and $-6.8\,\text{GHz}$ in the $F = 2$ spectrum (fig. 5.5d). In comparison to the calculated PECs (fig. 5.5a), these lines can only be attributed to the mixed type potential of the $25P_{3/2}; F = 1$ state. In contrast to the single line in the spin-flip regime, here we are able to see many distinct lines due to the higher coupling enabled by the strong mixing in the entanglement regime.

As the mixed state consists of both hyperfine states, the bound states therein should appear in the $F = 1$ spectrum as well as in the $F = 2$ spectrum. A comparison of the time-integrated signals in the relevant energy range for the $F = 1$ sample and the $F = 2$ sample is shown in fig. 5.6. Except for the line at $-189\,\text{MHz}$, every line in the $F = 2$ spectrum coincides with one line in the $F = 1$ spectrum within less than 3%. Furthermore, the positions of the observed lines in the $F = 2$ spectrum agree within 10% of the binding energy with the calculated energies of the deepest bound states in each well of the $25P_{3/2}; F = 1$ mixed potential (orange bars in fig. 5.6). The three highest energy states in the $F = 2$ spectrum are not matched by any calculated ground state and most likely correspond to higher vibrational states.

Apart from the matched lines, the $F = 1$ spectrum shows additional lines that do

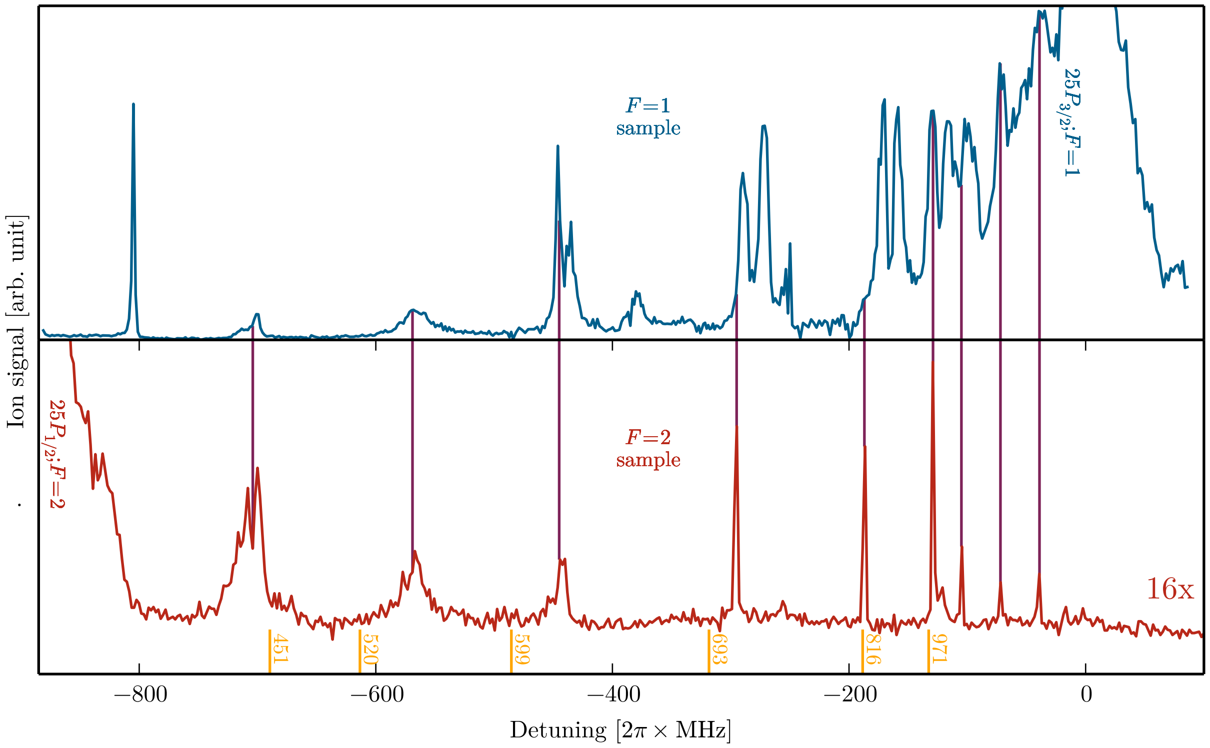

Figure 5.6: Comparison of the molecular spectra in the region between the $25P_{3/2}; F = 1$ state (0 MHz) and the $25P_{1/2}; F = 2$ state (−929 MHz) in a sample with all atoms in the $F = 1$ state (blue) and all atoms in the $F = 2$ state (red). Since in the $F = 2$ spectrum we only observe the mixed type PEC (see text) that also appears in the $F = 1$ spectrum, every line in the $F = 2$ spectrum has a corresponding line in the $F = 1$ spectrum (purple lines). The additional lines in the $F = 1$ spectrum originate from the pure triplet potential. The calculated energies of the lowest bound states in each well of the mixed type PEC (orange bars) agree with the observed resonances within 10%. The number beneath each orange bar gives the position of the corresponding potential well in units of a_0. Compared to the $F = 1$ spectrum the $F = 2$ spectrum is magnified by a factor of 16. Due to an uncertainty in the frequency calibration, the $F = 2$ measurement was stretched by 2% in accordance with the frequency mismatch observed in comparable measurements.

not appear in the $F = 2$ spectrum. Those lines correspond to bound states in the pure triplet PEC that only consists of the $F = 1$ state and can thus not appear in the $F = 2$ spectrum. The comparison between both spectra therefore not only indicates that the observed states are indeed of mixed hyperfine character but also allows to identify which states in the $F = 1$ spectrum belong to the mixed type potential and which, by exclusion, belong to the pure triplet potential.

The observed molecules are very peculiar in the sense that the Rydberg electron is stronger coupled to the nuclear spin of the perturber atom through the Rydberg–ground state interaction than it is coupled to nuclear spin of the Rydberg core. Hence, this is a state that couples the electron to the nuclear spin of a remote particle. Furthermore, the entanglement in this state is very interesting in conjunction with the long-range interaction of the involved Rydberg state. It might be possible to use the different Rydberg–Rydberg interaction of the two involved fine structure states to entangle the spin-states of the perturber in two separated Rydberg molecules. This could in principle allow for an effective long-range spin-interaction between the two ground state atoms.

The $25P$-state was chosen to prove the existence of hyperfine-mixed states in the entanglement regime because the residual spacing of 929 MHz between the involved states is still small enough to ensure a high mixing but also high enough to allow for a large spectral range in which the emerging lines can be observed without overlapping other lines. After knowing that the mechanism works, it might be beneficial to rather choose the $26P$ state, where the mismatch in fine structure splitting and hyperfine splitting is only 24 MHz. Since even the outermost well of the ultralong-range PECs exceeds this energy by far, all resulting states in the mixed potentials will be highly entangled, irrespective of the internuclear separation.

5.3. Summary

For the first time, we have carried out an extensive, high-resolution spectroscopy of P-state Rydberg molecules in a BEC of rubidium. The TOF measurement technique allowed us to observe molecular lines in the vicinity of the fine-structure-split $25P$-states and to extract their lifetimes. By studying the line broadening in an electric field, we could furthermore extract the permanent electric dipole moment that those states exhibit. In agreement with theoretical expectations, we saw that the dipole moment shows the trend to increase with the binding energy. A quantitative comparison of the measured dipole moments with the prediction from the ultralong-range PECs gave a rough indication on which potential well the studied state is bound in.

Extending our systematic study to the hyperfine state of the perturber atom, we were able to spectroscopically prove spin-flip processes in ultralong-range Rydberg molecules. Due to a near-degeneracy of the Rydberg atom's fine structure splitting and the perturber's hyperfine structure, we also observed strong transitions into states that entangle these fine structure and hyperfine structure states. By comparing the obtained spectra from different initial hyperfine states, we were able to attribute the molecular lines either to the mixed type potential or to the pure triplet potential. With these experiments, we open a completely new field of research by studying the effect of the molecular bond on the internal structure of the perturber.

By comparing the measured dipole moments to the theoretical expectations and attributing the individual lines to either the mixed or the triplet potential, we obtain additional information that allows us to characterise the studied molecules. Such information is important to reduce the complexity of the spectrum and to fully understand how the spectrum corresponds to the theoretical model. It is therefore likely that our results will provide a valuable input to more sophisticated models of the molecular interaction.

Apart from being of fundamental importance for the investigation of the molecular bond, the observed phenomena also bear great potential for application in many-body quantum systems. The long distance over which the molecular bond is active in Rydberg molecules makes them a promising candidate to implement optical Feshbach resonances [161]. Here, the coupling of a free two-particle scattering state to the molecular bound state allows to change the effective s-wave scattering length between the atoms and thus to modify the interaction among them. In such scheme, the observed spin-flip process might take a key role as it strongly reduces the off-resonant scattering to a bare atomic state which usually impedes such experiments. Moreover, long-range entanglement between the hyperfine states of multiple perturbers might be possible by combining the described spin-flip process with the Rydberg blockade arising from the interaction between a pair of Rydberg atoms (sec. A.12).

6. Butterfly Rydberg molecules

As a member of the high-l Rydberg molecules, the butterfly state is of particular interest. While theoretically predicted in 2002 [47], experimental evidence for the existence of this exotic type of molecule was so far missing. In the following, we present the first experimental proof for the existence of butterfly Rydberg molecules obtained by extensive photoassociation spectroscopy. By observing discrete pendular states inside an external electric field, we cannot only demonstrate experimentally that those states possess a giant permanent electric dipole moment in excess of 500 D but are also able to determine the bond length of the observed molecular states. This additional information allows us to attribute the measured molecular state to a certain well in the model potential, which in turn enables a much more detailed comparison to theory. Since the positions of the wells in the radial butterfly potential are determined by the nodes of the P-state wave function that is mixed in, the obtained bond lengths are also a direct measure for the nodes' positions. The comparison of the bond length and the dipole moment furthermore reveals a very peculiar situation where the centre of mass of the electron is located beyond the perturber atom, giving rise to a very unconventional molecule. At the end, the information obtained about the molecule enables us to photoassociate butterfly Rydberg molecules with controlled bond length, vibrational state, angular momentum state, and orientation in a small electric field. This tunability renders butterfly Rydberg molecules a very versatile tool and an interesting object of study.

6.1. Coupling to butterfly Rydberg molecules

The butterfly state arises due to the presence of a low-energy shape resonance in the triplet p-wave scattering between the Rydberg electron and the perturber. The resulting increase in the scattering length leads to very high interaction energies in the range of hundreds of Gigahertz in the case of the $n = 23$ hydrogenic manifold. Since the interaction energy is higher than the splitting between the hydrogenic manifold and the low-l states, we observe avoided crossings of the butterfly PECs with lower-lying S-, P-, and D-states (see fig. 2.12). Here, the crossing with the $25P$-state is of special interest as it lies close to the minimum of the butterfly PECs. The relevant butterfly PECs in the vicinity of the crossing are shown in fig. 6.1. To be able to couple to the bound states in this potential with a single photon transition, a substantial admixture of the P-state to the butterfly PECs is needed. As discussed in sec. 2.4.7, only the r-butterfly PECs preferably admix low-l states. Hence, we expect a substantial coupling only to the r-butterfly PECs but not to the θ-butterfly. In the following, we will therefore focus on the r-butterfly PECs.

In order to quantify the admixture and to estimate the coupling strength, the eigenvectors corresponding to the three r-butterfly PECs were analysed with respect to the contribution of the four possible $25P$-states. For the $\tilde{F} = 1/2$ and the $\tilde{F} = 3/2$ state, the results are shown in fig. 6.2a and fig. 6.2b, respectively. In both cases, we can observe the crossover from the ultralong-range potentials to the butterfly potentials by investigating the behaviour of the P-state contribution in the individual wells. For internuclear

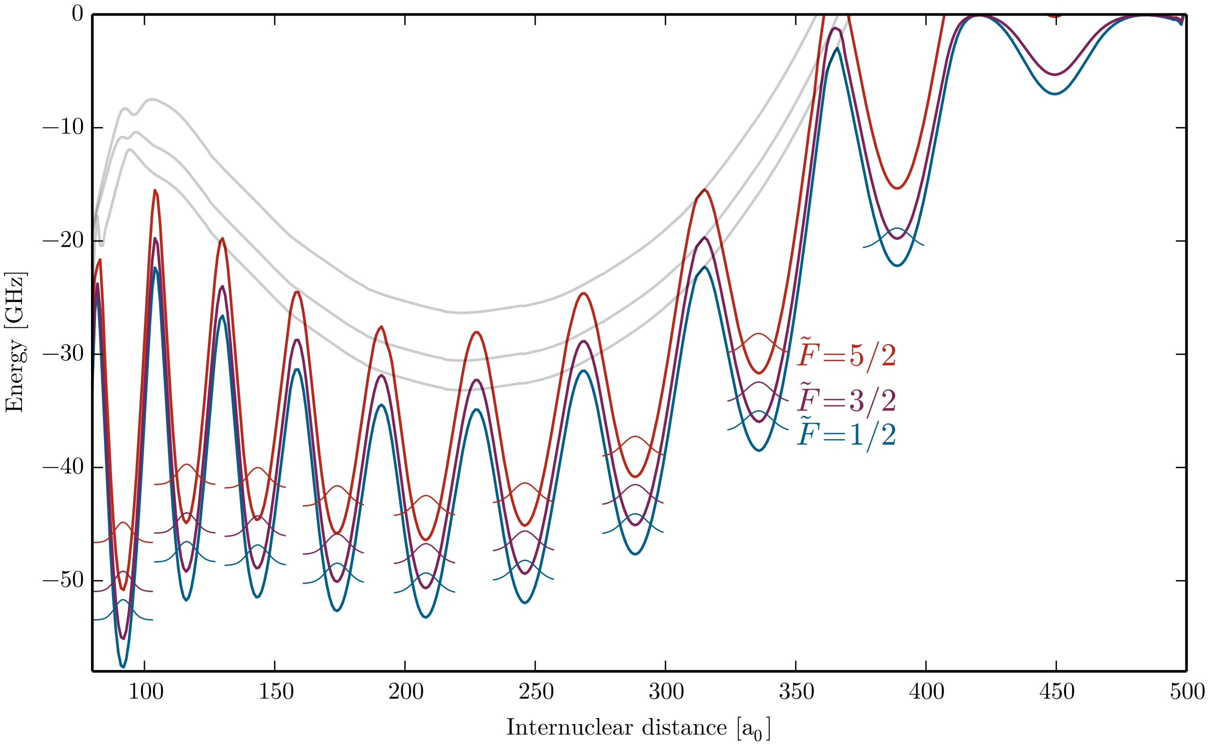

Figure 6.1: Potential energy curves for the ^3P-butterfly states. The θ-butterfly state (grey) and the r-butterfly state (coloured) are split by the spin–spin interaction into three lines each. While the θ-butterfly curves are smooth, the r-butterfly potential strongly oscillates since the high radial gradients of the P-state wave function get admixed (see text). For the r-butterfly potential curves the quantum numbers for the total angular momentum $\tilde{F}$ are given for each curve. Zero energy is set to the $25P_{1/2}; F = 1$ state.

separations higher than $370\,a_0$, we are still in the ultralong-range case where we observe 100% P-state character that only drops at the position of the potential wells due to the admixture of other states (see potential wells at $389\,a_0$ and $449\,a_0$). This situation is inverted for smaller internuclear separations where we see a P-state contribution close to zero that periodically rises at the position of the potential wells. This qualitative change in behaviour results from the adiabatic crossing into the butterfly state.

As mentioned above, the P-state gets periodically mixed into the radial butterfly state since the system can minimise its energy through the strong radial gradients of the P-state wave function. In fact, the deep oscillations of the radial butterfly PECs (fig. 6.1) are caused by the energy decrease that results from admixing the P-state wave function. It is thus no surprise that the position of the potential wells coincides with the position of the wave function nodes of the P-state. As will be shown in sec. 6.5, this relation can be used to indirectly measure the nodal positions of the P-state wave function.

To estimate the possible coupling to the bound states in the butterfly PECs, we have to properly define our initial state. Since the experiments presented in the following are performed in a BEC in the $F = 1$, $m_F = +1$ ground state, we are particularly interested in states that have a finite contribution of $F = 1$. As discussed in sec. 2.4.3, the $\tilde{F} = 5/2$ state consists only of $F = 2$ and the $\tilde{F} = 1/2$ is a pure $F = 1$ state. This is also revealed by the fact that in fig. 6.2a we see no admixture of the two $F = 2$ states to the $\tilde{F} = 1/2$ state. Only the $\tilde{F} = 3/2$ state admixes both hyperfine components, as depicted in fig. 6.2b. From an $F = 1$ initial state, it should thus be possible to couple to bound

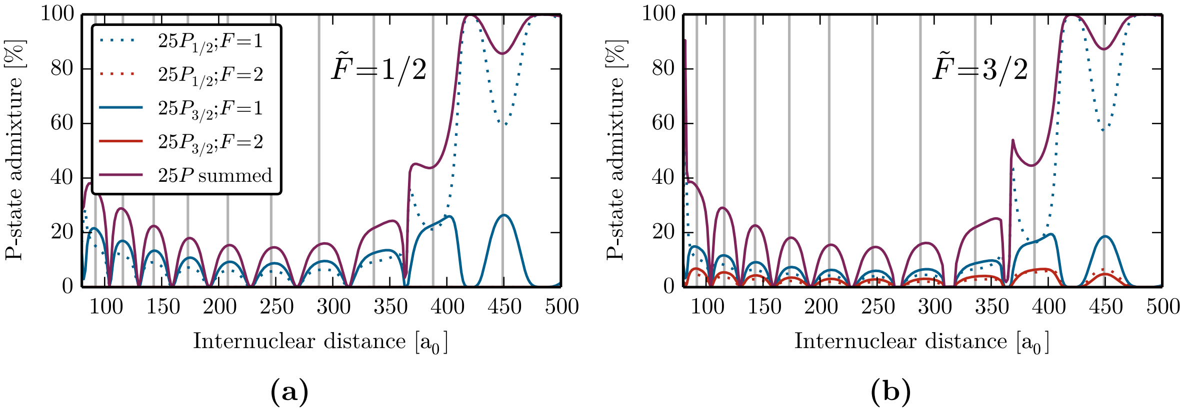

Figure 6.2: Admixture of the $25P$-states to the radial butterfly PECs. (a) Admixture to the $\tilde{F}=1/2$ r-butterfly PEC. (b) Admixture to the $\tilde{F}=3/2$ r-butterfly PEC. The figure legend in a) also holds for b). The vertical grey lines indicate the positions of the potential wells extracted from fig. 6.1.

states in the $\tilde{F}=1/2$ and $\tilde{F}=3/2$ PECs.

Since the molecule has a certain probability to be found at a certain internuclear distance, which is determined by the absolute square of the vibrational wave function $\Phi(R)$, we need to average the P-state admixture accordingly. Hence, the coupling strength to a particular bound state is given by the convolution between the P-state admixture to the electronic wave function and the absolute square of the molecule's vibrational wave function. Since the vibrational states in the deep r-butterfly wells are well-confined, the convolution reduces to considering approximately the maximum admixture in each well. As can be seen from fig. 6.2a, even for the deepest wells around $250\,a_0$, the summed contribution of all P-states still amounts to 15%. Also for the $\tilde{F}=3/2$ PECs, the sum of all P-state contributions amounts to 15%. However, only those states with $F=1$ character can be coupled and thus we get a summed contribution of only roughly 10%. Just considering the electronic part of the final state, we would therefore expect a coupling that is only one order of magnitude smaller than the coupling to the atomic Rydberg state. Additionally, however, the coupling is reduced by the distance distribution in the prepared sample. This can be understood in the picture of a classical gas. Since the potential wells of the butterfly PECs are in the range of 5 nm to 20 nm but the typical inter-particle distance in a BEC with a peak density of $n_0 = 10^{14}\,\mathrm{cm}^{-3}$ is around 200 nm, the probability to find two atoms in an appropriate distance is small. This tremendously reduces the number of available atom pairs that can be excited into the molecular state. Consequently, the overall number of excited molecules is strongly reduced, which can be taken into account by a reduced effective coupling to the molecular state. To minimise this reduction, it is therefore crucial to excite the butterfly molecules from high-density samples. Furthermore, the coupling to vibrational states of odd parity is suppressed since the initial state is approximately flat on the length scale of the vibrational wave function and due to the anti-symmetry of odd parity states the overlap integral will be small.

6.2. Spectroscopy of butterfly Rydberg molecules

Since it is in principle possible to couple to the wells of the radial butterfly PECs due to the strong P-state contribution, we performed a detailed spectroscopy using the single-photon

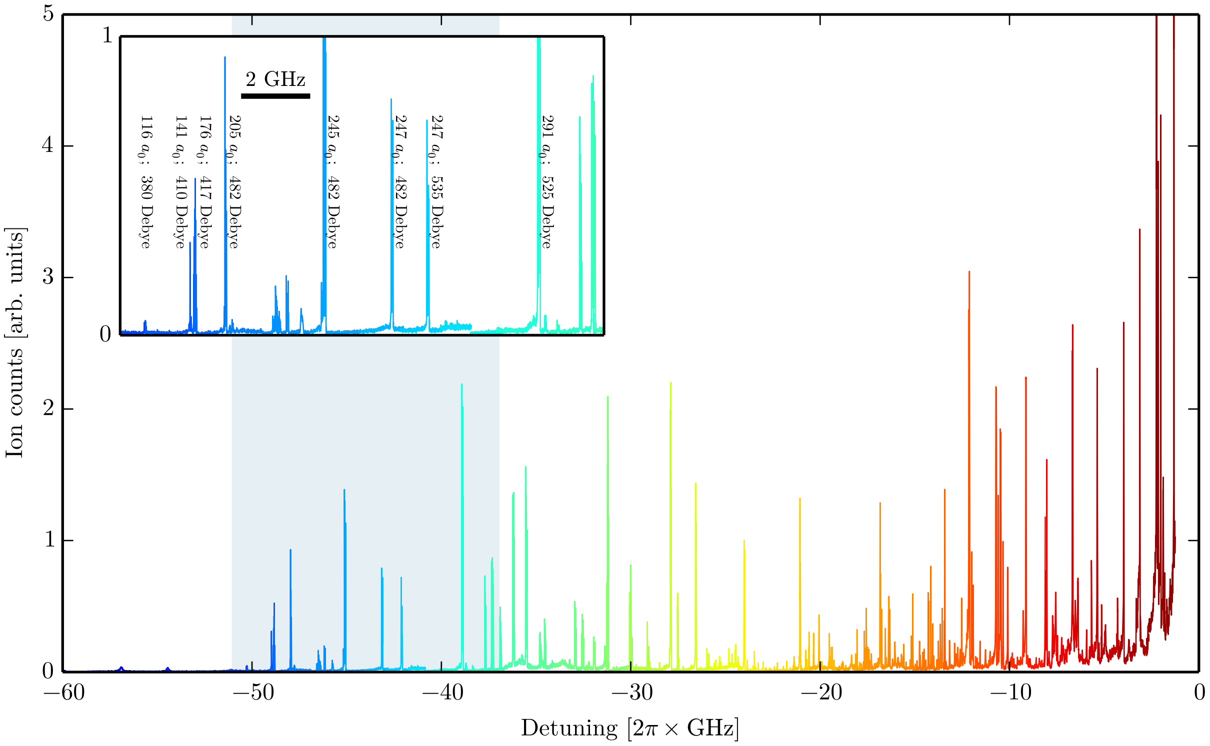

Figure 6.3: Measured photoassociation spectrum of butterfly Rydberg molecules from a BEC of 2.2×10^5 atoms in the $F = 1$, $m_F = +1$ ground state. Zero energy is set to the $25P_{1/2}; F = 1$ state. The inset shows a zoom-in on the region where we expect to see mostly vibrational ground states of the individual wells (blue shaded region). The information noted beneath the peaks in the inset are obtained from the electric field-dependent measurements discussed in sec. 6.3. The colour of the spectrum is a guide to the eye.

transition. Because the expected coupling is suppressed by the distance distribution of the sample, high number densities are crucial to increase the signal for such a spectroscopy. We therefore optimised the experimental sequence to prepare a maximum atom number in the BEC. Since the transfer of the BEC into the round trapping configuration (sec. 3.2) and the microwave transfer into the $F = 2$ hyperfine state (sec. 3.4) always imply atom loss, we omitted these steps in the preparation. After evaporative cooling to a sufficiently deep final trap, we create a quantum-degenerate sample that is spin-polarised in the $F = 1, m_F = +1$ state, as described in sec. 3.2. Typically, such a sample consists of 2.2×10^5 atoms at harmonic trapping frequencies of $\omega_{x,y,z} = 2\pi \times (168, 82, 161)\,\mathrm{Hz}$, which results in a peak particle number density of $n_0 = 4.3 \times 10^{14}\,\mathrm{cm}^{-3}$.

To further maximise the signal, we applied a long excitation pulse with a duration of 500 ms. Since the number of created ions through photoionisation and associative ionisation is proportional to the number of excited Rydberg molecules, we obtain a meaningful measurement signal by counting the ions during excitation. For a linear laser polarisation in the horizontal plane, a beam waist of 40 µm on the sample, and a laser power of roughly 20 mW, we obtained the spectrum shown in fig. 6.3. Due to the high spectral range of 60 GHz with an average resolution of 2 MHz, the total measurement time for the presented spectrum amounts to roughly one month. The spectrum thus consists of multiple individual measurements that were combined according to the frequency information from a wavemeter which in principle allows for a relative resolution of 1 MHz, as described in sec. 3.5. Since we are especially interested in the deepest bound states, as explained below, we sampled this region with a resolution of 1 MHz while for the states between 0 GHz and −20 GHz we measured only every 4 MHz to reduce the measurement time. Due to the average width of the observed resonances, it is unlikely to miss a molecular line even with the coarse detuning steps. Nevertheless, care has to be taken with respect to the observed line strength because it is possible that the measured data points were not recorded at the line centre of the appearing lines. Additionally, due to the long excitation time and the loss channels for the created molecules, the sample decays significantly when we hit one of the resonances. The analysis of the presented spectroscopy should therefore be restricted to the energy of the observed states and should not include the line strength.

Evaluating at the spectrum, we see a plenitude of resonances appearing in our measurement range. It is striking that, even though we measured down to −60 GHz, the observed molecular lines suddenly stop around −51 GHz. This is in very good agreement with the calculated PECs (fig. 6.1) that predict the deepest bound states to be in that region. A direct comparison between the PECs and the measured spectrum will be given in sec. 6.5. A second global feature of the measured spectrum is that around −37 GHz the density of states changes. This effect can also be understood on the basis of the calculated PECs as it happens at the energy where the second excited states for the lowest wells appear and start to overlap in the spectrum with the ground states of higher-lying wells[1]. To keep the discussion simple, it is useful to restrict the further analysis to the region of the lowest bound states in the butterfly potential wells, i.e. the energy region between −51 GHz and −37 GHz. For eight molecular lines in this region, we show in the following how their behaviour in the presence of an external electric field can be used to extract their bond length and their dipole moment.

6.3. Butterfly molecules in electric fields

In order to reveal the existence of a permanent electric dipole moment in the observed butterfly states, we performed a detailed spectroscopy of eight resonances in the selected energy region in the presence of an external electric field. The spectroscopy employed the same scheme as described in sec. 6.2 but additionally an electric field of up to 0.88 V/cm was applied across the sample through the main electrodes. The field was always applied such that the field vector was pointing in the direction of gravity. In this configuration, the created ions get still accelerated towards the ion optics located below the sample and can be detected by the ion detector. Therefore, we can, even in the presence of a finite field, observe the ions that are created by photoassociation of the molecule and subsequent ionisation.

The excitation laser was aligned to propagate in the horizontal plane and thus intersected the electric field axis at an angle of 90°. The light was linearly polarised and the polarisation vector could be rotated by a half-wave plate to align it to the field axis or perpendicular to it. The arising differences in the spectra, depending on the polarisation of the excitation light, are discussed in sec. 6.3.2.

As an example for the obtained field-dependent ion spectra, the measurement with the spectroscopic line at −47.9 GHz is shown in fig. 6.4. In contrast to the usual rotational spectroscopy of conventional molecules, the obtained photoassociation spectra have one defined initial state from which the molecular states are probed. Therefore, we do not

---

[1] We cannot observe the first excited state since its parity leads to a vanishing overlap with the initial BEC wave function

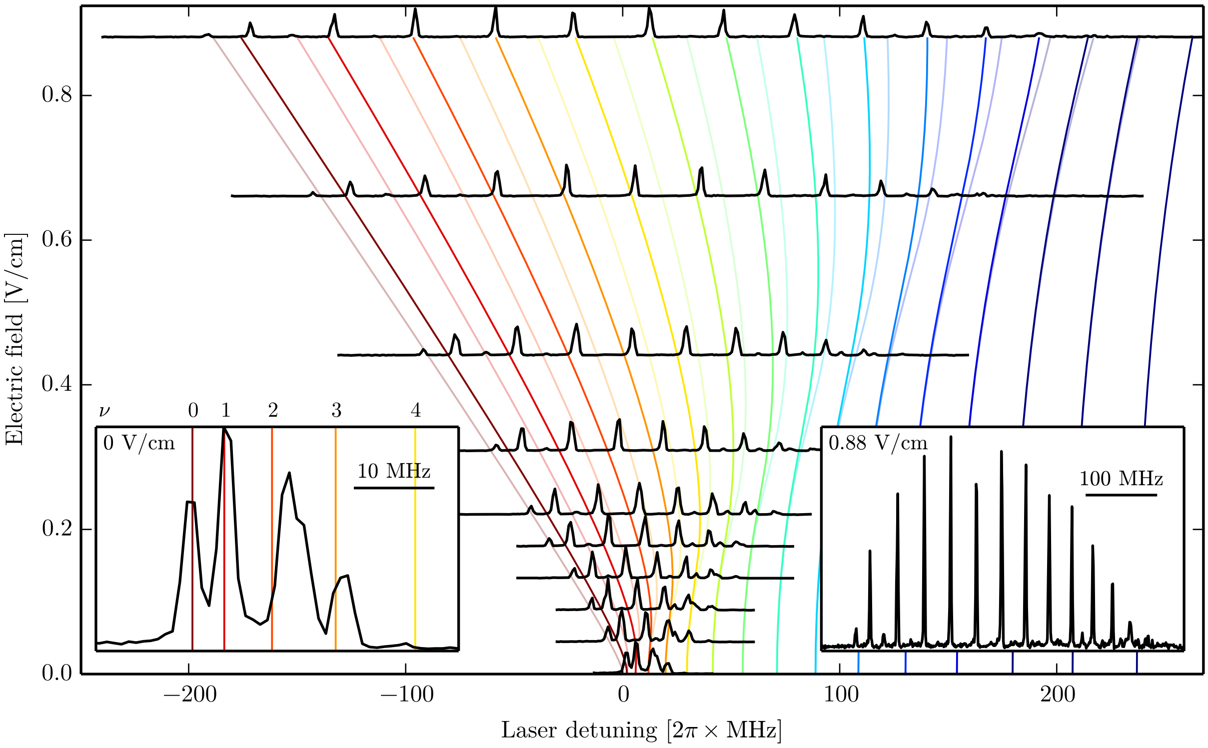

Figure 6.4: Electric field-dependent spectra for the butterfly state at an energy of −47.9 GHz. The measured spectra (black lines) are normalised with respect to their maximum and shifted on the y-axis according to the applied electric field. The measurements were taken in a BEC of 2.2×10^5 atoms in the $F = 1$, $m_F = +1$ ground state with the excitation laser polarisation parallel to the electric field. The coloured lines are the eigenenergies of the dipolar rigid rotor model (sec. 2.6) with the dipole moment and bond length adapted to fit the experimental spectra. The strong lines correspond to the $|M_N| = 1$ subspace, the faint lines to the $|M_N| = 0$ subspace. The insets show magnified views of the lowest (left) and the highest field measurement (right).

observe a complicated transition spectrum consisting of the usual P- and R-branch but see a direct spectrum of the molecular level structure, which enables a direct comparison to theory. In very good agreement with the model of the dipolar rigid rotor (sec. 2.6), we find that the molecular lines split into a number of pendular states that increases with the field strength. As shown in the left inset of fig. 6.4, we can observe a splitting of the molecular line even without an applied electric field. This is unexpected since under these circumstances we can only couple to the $N = 1$ state (see sec. 2.6.1 and sec. 6.3.2) and thus expect to see only a single line in the field-free case. However, the fact that we see several lines and that the splitting does not exactly match the theory indicates the presence of residual electric fields that could not be compensated. It is therefore no surprise that the theory does not perfectly cover the observed peak positions for small fields but becomes increasingly accurate for higher ones.

Since in this measurement the laser polarisation was set perpendicular to the electric field axis, we see a dominant $\sigma^{\pm}$-coupling and thus mainly observe the pendular states from the $|M_N| = 1$ subspace. However, we also find a weak signal of the $|M_N| = 0$ subspace in the spectrum, as can be seen at the right inset of fig. 6.4. This might be attributed to imperfections in the alignment of the polarisation or to the coupling between the external angular momentum $\vec{N}$ of the molecule with the electronic angular momentum $\vec{J}$ that is

Table 6.1: Summary of the extracted values for the bond length R_e and the dipole moment d of most of the observed butterfly states in the energy range from $-35\,\text{GHz}$ to $-50\,\text{GHz}$. The estimated error is $5\,a_0$ for the bond length and 20 D for the dipole moment. For each line, additionally, the type of spectrum (see text), the coupling due to the laser polarisation, the theoretically calculated dipole moment d_{theo} of the lowest bound state in the determined well, and the alignment $\langle \hat{z} \rangle_{\text{max}}$ for the the $\nu = 0$ state at the maximal field of $E = 0.88\,{}^{\text{V}}\!/\!_{\text{cm}}$ is given. The line at $-45.1\,\text{GHz}$ was measured twice to check the reproducibility.

	Experiment				Theory	
Energy [GHz]	type	coupling	R_e $[a_0]$	d [D]	d_{theo} [D]	$\langle \hat{z} \rangle_{\text{max}}$
−38.9	1	σ	291	525	695	0.97
−42.1	2	σ	247	535	653	0.97
−43.2	2	σ	247	477	653	0.97
−45.1	1	σ	245	482	653	0.97
−45.1	1	σ	245	490	653	0.97
−47.9	1	σ	205	482	597	0.96
−47.9	1	π	200	480	597	0.96
−48.8	1	σ	176	417	541	0.95
−48.9	1	σ	141	410	484	0.93
−50.3	1	σ	116	380	442	0.92

not considered in the simple theory of the rigid rotor.

Apart from the type of the field-dependent spectra shown in fig. 6.4 (type 1) that we observe for most of the lines, we also observe a second type of spectra for a minority of the lines (type 2). A comparison of both types of spectra is shown in fig. A.3. The second type differs from the first by splitting in twice as many lines in the presence of the electric field. Since the lines alternate in peak strength, they can be assigned to two groups. Despite of having a different total coupling strength, both groups show the same coupling envelope (see sec. 6.3.2). The additional peak group therefore looks like the original one but is scaled in height and shifted in energy. The absolute amount of the energy shift depends on the strength of the applied electric field. It is therefore reasonable to assume that this splitting in two groups originates from the splitting of the $\tilde{F} = 3/2$ PECs in the two components $|\tilde{m}_F| = 1/2$ and $|\tilde{m}_F| = 3/2$. In this case, it should be possible to attribute the observed states to the two possible PECs $\tilde{F} = 1/2$ and $\tilde{F} = 3/2$ according to the observed type of spectrum. However, the calculation of the PECs does not predict a splitting of the $\tilde{F} = 3/2$ line if the electric field term $\hat{d}_z E_z$ is added to the Hamiltonian (2.4.34). There might still be a field dependence in the scattering between the Rydberg electron and the perturber atom that leads to a splitting of the $\tilde{F} = 3/2$ state but is not included in the theoretical model. A more detailed model might therefore explain the observed second type of spectra and, by confirming the splitting, even allow to attribute the different measured lines to one of the two possible PECs. Since a more detailed model is beyond the scope of this thesis, we restrict the discussion to reporting the observed type of spectrum for each measured line in tab. 6.1.

6.3.1. Determination of dipole moment and bond length

Since the lowest harmonic oscillator states are tightly confined in the radial direction, we can approximate the butterfly molecule as a rigid rotor with an average bond length R_e and a dipole moment $\vec{d}$. It is therefore justified to apply the theory of the dipolar rigid

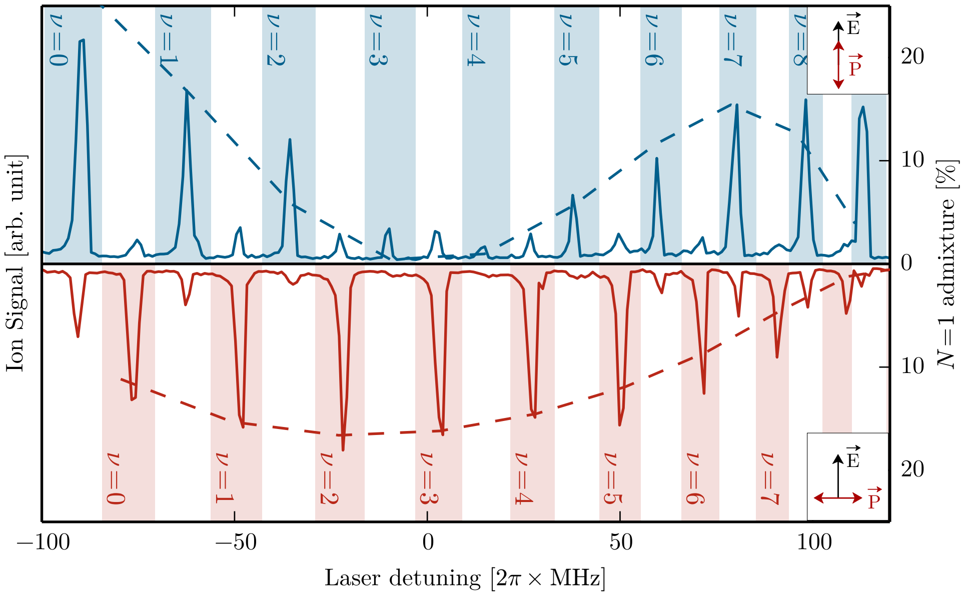

Figure 6.5: Laser polarisation dependence of the coupling to the pendular states for the molecular state at −47.9 GHz in a field of 0.88 V/cm in comparison to the theory discussed in sec. 2.6.1. The upper panel shows the spectrum obtained for the laser polarisation parallel to the electric field axis, giving rise to π-coupling. The lower panel shows the inverted spectrum for the laser polarisation perpendicular to the electric field axis, giving rise to $\sigma^{\pm}$-coupling. The blue shaded areas mark the lines corresponding to the $|M_N| = 0$ subspace, the red shaded areas the ones corresponding to the $|M_N| = 1$ subspace. The dashed lines represent the calculated admixture of the $N = 1$ state to the respective pendular state for coupling to $|M_N| = 0$ (blue) and $|M_N| = 1$ (red).

rotor (sec. 2.6) also quantitatively. We thus diagonalised the Hamiltonian from eq. (2.6.1) and adapted the dipole moment d and average bond length R_e such that the eigenenergies fit the measured spectra. At this point, it is helpful that in the model the energy of the $\nu = 0$ state is very sensitive to the chosen dipole moment but less sensitive to the bond length. We therefore pursued the strategy to adapt the dipole moment to fit the $\nu = 0$ state and then adapt the bond length to obtain the right energy spacing for the higher ν states. To diminish the effect of uncompensated residual fields, we focused the analysis on the measurements at higher field strength, where the relative error due to the residual fields becomes small. With this procedure it is possible to determine the bond length with an estimated precision of $5\,a_0$ and the dipole moment to a precision on the order of 20 D. In the case of the measurement at −47.9 GHz presented in fig. 6.4, we achieve a best fit for $R_e = 205\,\mathrm{a}_0$ and $d = 482\,\mathrm{D}$.

Repeating the field-dependent measurement and the above fitting procedure for all resonances in the energy region of interest, we obtain, for the lines that allow a reasonable evaluation, the values for the bond length and the dipole moments as they are denoted in the inset of fig. 6.3 and summarised in tab. 6.1. The obtained bond length in combination with the binding energy extracted from the spectroscopy allows for a precise comparison to the calculated PECs, as discussed in sec. 6.5. Furthermore, the extracted dipole moments are discussed in sec. 6.4

6.3.2. Polarisation dependence

As discussed in sec. 2.6.1, the coupling strength to the pendular states depends on the polarisation of the excitation laser. To verify the theoretical considerations experimentally, the molecular line at $-47.9\,\mathrm{GHz}$ was measured in a field of $0.88\,\mathrm{V/cm}$ for the laser polarisation being parallel to the electric field axis (upper panel of fig. 6.5) and perpendicular to it (lower panel of fig. 6.5). As the former configuration realises π-coupling, we find that in this case the lines of the $|M_N| = 0$ subspace dominate the spectrum. In the latter case, we drive $\sigma^{\pm}$ transitions and thus address mostly the $|M_N| = 1$ subspace. In both cases, we see a small residual coupling to the opposite subspace, which might be due to imperfections in the polarisation alignment or due to angular momentum couplings between the nuclear and the electronic motion.

With the employed dipole transition, we can only couple to the $N = 1$ contribution in the pendular states and thus we expect the coupling to be proportional to the $N = 1$ admixture to the final state. For the two coupling cases the expected behaviour is depicted in fig. 2.21. Here, we compare the line strength of the measured spectrum with the peak heights ($N = 1$ admixture) for the correspond slice at $0.88\,\mathrm{V/cm}$ through the theory spectrum. This comparison is shown in fig. 6.5 and reveals that, for both polarisation settings, the experiment nicely follows the qualitative behaviour of the theoretical model. In conjunction with the argument about the orientation of the dipole given in sec. 2.6.1, these measurements show that it is possible to orient the dipole of the molecule in the laboratory frame.

6.4. Dipole moments

Conventional homonuclear molecules cannot possess a permanent electric dipole moment due to the exchange symmetry of the involved electrons. Caused by the extreme bond lengths in Rydberg molecules, the probability for the perturber's valence electron to tunnel to the Rydberg core is negligible and the exchange energy vanishes. It is therefore possible that Rydberg molecules are excited asymmetrically and, despite of being homonuclear, possess a permanent electric dipole moment [51]. This is experimentally confirmed by the emergence of pendular states in the presence of an external electric field. The dipole moments extracted from the field-dependent measurements range from 380 D for the smallest molecule to 535 D for one of the largest molecules. These values are enormous compared to conventional diatomic molecules that are typically in the range of 0 D-10 D but they are compatible to the values that were reported for molecules with a high admixture of the trilobite state [49].

In order to compare the measured dipole moments to theory, it is necessary to determine the dipole moment for each point in the relevant PECs according to eq. (2.4.53). The result of this calculation for the $\tilde{F} = 1/2$ PEC is shown in fig. 6.6a. Interestingly, in the butterfly case, the well positions do not coincide with the extremal points of the dipole moments. Due to the high slope of the dipole moment as a function of the internuclear distance at the position of the well, it is not straight-forward to extract the dipole moment of a particular bound state. It is instead necessary to convolve the dipole moment with the vibrational wave function of that particular state according to eq. (2.4.54). For this purpose, we assigned each measured line to one of the potential wells in the relevant PECs according to the measured bond length (see sec. 6.5) and calculated the dipole moment for the harmonic ground state in that well. The results are given for the respective lines

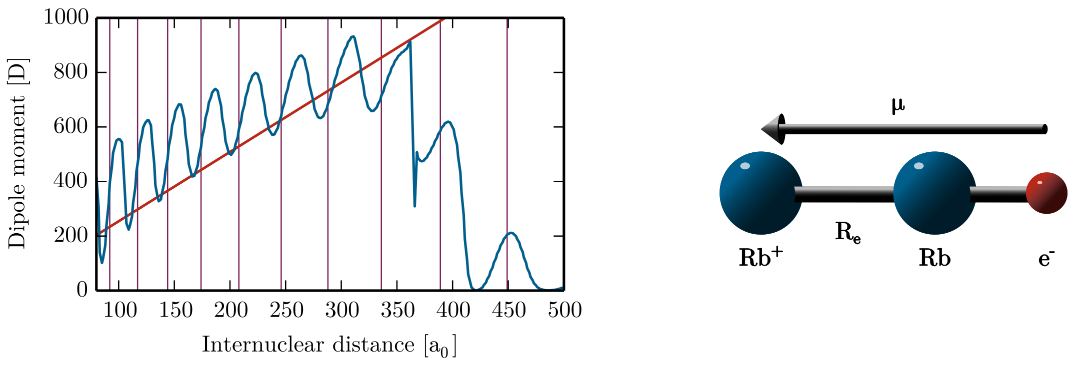

(a)

(b)

Figure 6.6: Dipole moments of butterfly molecules. (a) Calculated dipole moments of the $\tilde{F} = 1/2$ butterfly state as function of the internuclear distance (blue). In the region below $370\,a_0$, the system is in the butterfly state and shows higher dipole moments than a single electron separated from the positive charge by the respective distance (red). The minimum positions of the potential wells (purple lines) do not coincide with the extremal points of the calculated dipole moment. For internuclear distances higher than $370\,a_0$ the studied potential curve traverses into the P-state and with the butterfly character also the dipole moment is reduced. In this regime, the maximum dipole moment is observed close to the minimum position of the potential well. (b) Sketch of the unconventional situation that is realised in butterfly molecules where the electron is located beyond the perturber atom.

in tab. 6.1. It is striking that even though the measured values are in the right order of magnitude and also show the same scaling behaviour with respect to the bond length, they are systematically lower than the calculated values. This discrepancy could in principle arise from a miscalibration of the electric field. However, since the mismatch is on the order of 25% and a miscalibration of the electric field on that scale should be noticeable, it is more likely that the theoretical prediction is inaccurate. This assumption also agrees with the fact that a perfect matching of the observed molecular lines with the bound states in the calculated PECs is not possible (see sec. 6.5).

The giant dipole moment of Rydberg molecules arises partly because of the high bond length that in turn allows for a high charge separation. In the case of butterfly molecules, however, a further, very peculiar effect appears that can be seen in the calculation as well as in the experiment. From fig. 6.6a, we can see that the dipole moment of the butterfly state as a function of the internuclear separation is almost always higher than the dipole moment of two opposite charges separated by the same distance. This effect is also seen for the experimentally determined values of the bond lengths and the dipole moments. As an example, we consider the state at $-50.3\,\mathrm{GHz}$ from tab. 6.1, which was measured to have a bond length of $R_e = 116\,\mathrm{a}_0$ and a dipole moment of $d = 380\,\mathrm{D} = 150\,\mathrm{ea}_0$. For a molecule with a single charge to have this dipole moment, the positive and the negative charge have to be separated by $150\,a_0$. Since the measured bond length of this state amounts to only $116\,a_0$, we have to conclude that the centre of mass of the electron is located beyond the perturber atom. This leads to the very counter-intuitive picture of the Rydberg molecule that is sketched in fig. 6.6b. This is only possible because the size of the Rydberg wave function is much bigger than the extent of the nuclear part of the molecule and thus the electron can locate on the other side of the perturber. This is also visible from the electron density of the butterfly state depicted in fig. 2.13c where the maximum density peaks are already beyond the perturber.

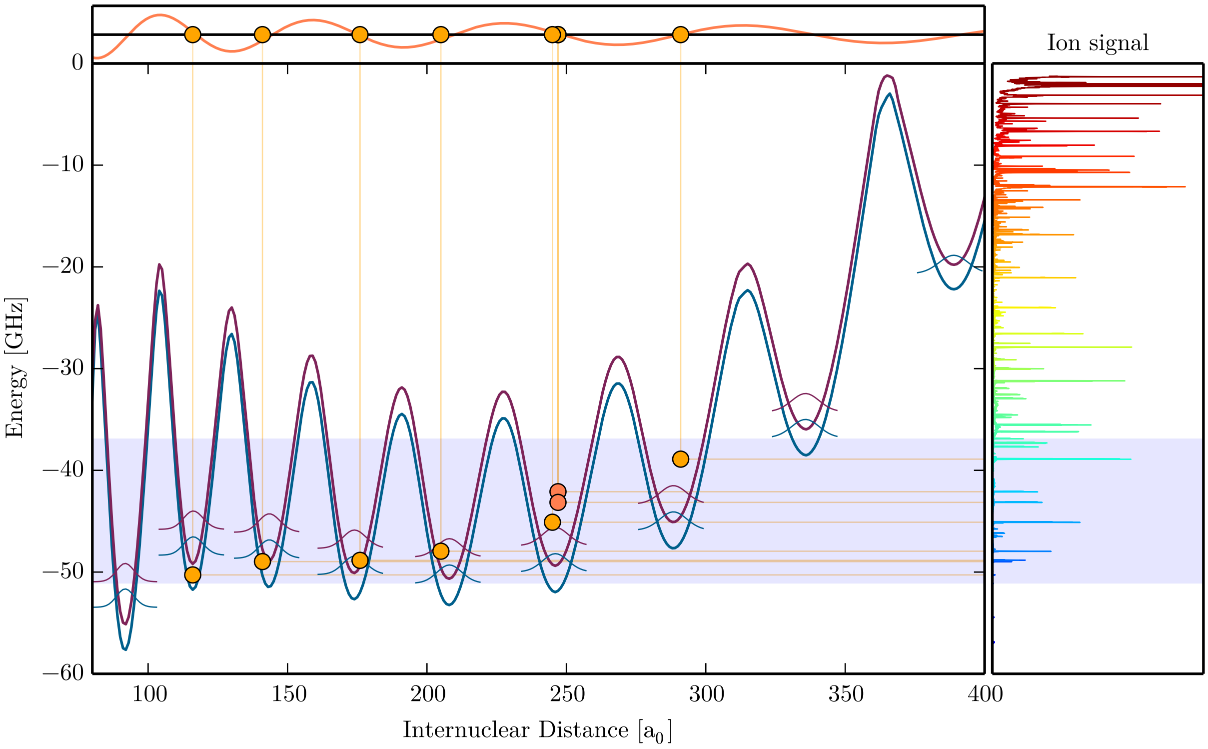

Figure 6.7: Comparison of the calculated PECs and the measured binding energies and the bond length for eight butterfly states in the energy range from −51 GHz to −37 GHz. The dots in the main panel combine the energy information from the spectroscopy and bond length information from the electric-field-dependent measurements. The size of the dots relates to the estimated error in the bond length. For the yellow dots type 1 spectra were observed, for the light red dots type 2 spectra were observed. The blue-shaded region marks the energy region of interest. The right panel shows the measured spectrum from fig. 6.3 on the same energy axis as the potential curves. The top panel demonstrates that the measured well positions (yellow dots) coincide with the nodes of the numerically integrated $25P_{1/2}$ wave function (light red).

In order to significantly orient a dipolar molecule in an external electric field, the interaction of the dipole with the field has to dominate the energy scale set by the rotation

$$\omega \equiv \frac{dE}{B} \gg 1. \tag{6.4.1}$$

Butterfly Rydberg molecules show a very strong interaction even with small electric fields due to their high dipole moment d that is two orders of magnitude bigger than that of conventional molecules. Furthermore, the separation between the nuclei in a butterfly Rydberg molecule is also two orders of magnitude higher than for conventional molecules and consequently the rotational constant B for these molecules is reduced by the same amount. Therefore, even small fields, on the order of 1 $^{\mathrm{V}}/_{\mathrm{cm}}$, are sufficient to highly orient the studied butterfly molecules. For conventional molecules to reach the same degree of orientation, a field strength on the order of 10 $^{\mathrm{kV}}/_{\mathrm{cm}}$ is needed, which is technically challenging.

6.5. Comparison to theory

We can now gather the information about the energy of the butterfly states that we obtain from the spectroscopy and combine it with the information about the bond length and dipole moment obtained from the field-dependent measurements. While the combination of the bond length with the dipole moment was already discussed in sec. 6.4, we will now turn to combining the information on the bond length with the binding energy. In contrast to previous studies [48,49,51,162,163], this allows us a more detailed comparison to theory because instead of attributing a molecular state to a line at constant energy in the PEC, we are able to narrow them down to a point. The comparison of these experimental points with the relevant PECs in fig. 6.7 reveals how valuable the additional information of the bond length is as it inevitably attributes each line to one of the potential wells. In general we see that for the wells at higher internuclear separations the calculated PECs are too low in energy while for smaller distances the observed lines agree well with the calculated bound states. The discrepancy at higher separations might be attributed to errors in the calculated scattering phase shifts that are fundamental to the calculated PECs. A small deviation in the exact energy at which the ^3P shape resonance appears might have strong influences on the exact energies of the PECs in the vicinity of the divergence.

It is interesting to note that in the well at $245\,a_0$ we find three lines while the calculated PECs support only one ground state for the $\tilde{F} = 1/2$ and the $\tilde{F} = 3/2$ potential. Since the energy spacing of the bound states in the calculated PECs is higher than the separation of the measured states, it is impossible to attribute them to higher excited states in this well. The presence of a third state in this well is therefore an indication for a splitting of the PECs that is not covered by the theoretical model. This might be due to spin–orbit effects in the scattering process between the Rydberg electron and the perturber, which gives rise to slightly different scattering lengths for the three individual triplet channels (see sec. 2.4.4). Insofar, the experimental data provides a very valuable benchmark for future theoretical models that also include the spin–orbit coupling in the scattering process.

While the energy of the states does not fit the calculated bound states in every case, the bond lengths coincide with the positions of the potential wells up to $3\,a_0$. This astonishing agreement is enabled by the high precision at which the bond length can be obtained from the pendular states. Since the positions of the wells are determined by the nodal positions of the close-by P-state's wave function (see sec. 6.1), the measurement can also be interpreted as a high precision measurement of the wave function nodes of the $25P$-state. That the measured positions indeed coincide with the wave function nodes of the $25P_{1/2}$-state is shown in the top panel of fig. 6.7. The fine structure splitting does not significantly change the position of the nodes and within the error of the measured well positions also coincides with the nodes of the $25P_{3/2}$-states. In this way, the perturber atom inside the butterfly molecule acts as a probe for the nodal positions.

6.6. Summary

We have shown the first clear experimental evidence for the existence of butterfly Rydberg molecules by performing an extensive photoassociation spectroscopy in the vicinity of the $25P$-state. Comparing the observed spectrum to the calculated butterfly PECs, we find that the sudden stop of the appearing resonances is nicely explained by the calculated potential depth. Studying the observed butterfly states in electric fields, we see the emergence of pendular states that, in comparison to the model of a dipolar rigid rotor, allows us to extract the dipole moment and the bond length of the butterfly molecules with high precision. This in turn allows us to go beyond the usual level of comparison to theory that is solely based on the binding energy. Instead, we are able to determine the energy and the bond length and thus to narrow the studied state down to a point in the calculated PECs. We find that the extracted bond lengths nicely agree with the well positions in the calculated PECs. By realising that the position of the wells is mainly determined by the nodes of the close-by $25P$-state radial wave function, we reveal the bond length of these molecules is also an indirect measure for those nodes. Through the additional information on the bond length and the dipole moment, we can furthermore identify a peculiar situation in which the average electron position is located beyond the perturber atom. This nicely demonstrates that the new type of chemical bond that Rydberg molecules rely on gives rise to peculiar molecular properties that are not possible in conventional molecules. Ultimately, the obtained knowledge on butterfly Rydberg molecules allows to gain a high degree of control on their internal and external degrees of freedom. Upon photoassociation inside an electric field, it is possible to choose the bond length, the vibrational state, the angular momentum and the alignment in the field by simply addressing the corresponding molecular line.

This high degree of control and their unique combination of an immense binding energy and giant dipole moment make butterfly Rydberg molecules a promising candidate to study strong dipolar interactions in a single species experiment. A detailed discussion on the prospects of studying dipolar physics with butterfly Rydberg molecules is given in the following chapter.

7. Conclusions and outlook

Within the framework of this thesis, we presented a detailed study of the peculiar interaction that arises between Rydberg and ground state atoms in ultracold gases. We demonstrated that this interaction strongly affects the physics in such combined systems by altering the scattering properties and causing a previously unknown type of chemical bond in Rydberg molecules. Since a detailed discussion of the obtained results has already been given in the corresponding chapters, we will restrict this chapter to a concise review of the three presented experiments and possible applications and future extensions.

Rydberg-electron mediated mass transport

The interaction of the Rydberg electron with the perturber significantly alters the scattering process between Rydberg and ground state atoms. We successfully studied this effect for resonantly excited Rydberg atoms embedded in the ground state atoms of a dense ultracold gas. By performing a time-of-flight spectroscopy, we could distinguish atomic Rb^+ ions created through photoionisation and molecular Rb_2^+ ions created by associative ionisation. Extracting the typical decay times of these two ion signals as a function of the atomic flux allowed us to indirectly measure the partial cross section for associative ionisation σ_{AI} as well as the total inelastic scattering cross section σ_{inel} for principal quantum numbers ranging from $n = 30$ to $n = 60$. We found that σ_{inel} equals the geometric cross section of the Rydberg atom and thus conclude that in the studied range of principal quantum numbers almost every scattering process between a Rydberg atom and a ground state atom is inelastic. Consequently, elastic collisions seem to be rather unlikely. This is not really surprising because the intruding ground state atom probes the molecular potential and thus causes an admixing of many surrounding Rydberg states. Especially for internuclear separations below the crossing between the butterfly state and the studied P-state many high-l states are admixed to the eigenstates. This strong mixing provides an inelastic scattering channel in terms of l-changing collisions [57], where the Rydberg atom leaves the collision in a lower energy state of different l and the excess energy is converted into kinetic energy of the collision partners.

We were further able to show that the partial cross section for associative ionisation in ultracold clouds is increased by three orders of magnitude compared to previous experiments preformed in atomic beams. While those early experiments obtained cross sections on the order of the formed molecules' geometric size, our results exceed this size by far. Since the formation of the Rb_2^+ ion through the DRM can only take place at the length scale of the formed molecule's size, we deduce the existence of an efficient mass transport mechanism that accelerates the ground state atom towards the Rydberg core. Microscopically, this transport is driven by the overall attractive shape of the molecular interaction potential. This transport mechanism can only be seen in ultracold systems as it becomes relevant only if the molecular interaction energy is larger than the kinetic energy of the collision partners. On the other hand, it is solely this mass transport mechanism that renders associative ionisation a relevant process in ultracold Rydberg systems. The mass transport and the accompanied acceleration of the molecular ion's production show close analogies to a catalytic process where the Rydberg electron acts as the catalyst. While we could not observe a full catalytic cycle, we anticipate that in ultracold plasmas the recombination of ions and free electrons into Rydberg states might complete the cycle and thus enable an efficient reaction from Rb^+ to Rb_2^+.

Spin-flips and entanglement in Rydberg molecules

Due to the highly oscillatory shape of the pseudopotential that is created by the Rydberg electron–perturber scattering, the resulting interaction not only alters the scattering properties but also gives rise to molecular bound states. This previously unknown type of bound state comes along with very peculiar properties of the formed molecules, including giant bond lengths, permanent electric dipole moments, and a complex vibrational state structure. To study this fascinating facet of the Rydberg–ground state interaction, we performed the first extensive high-resolution spectroscopy on P-state ultralong-range Rydberg molecules in ultracold clouds of $^{87}\mathrm{Rb}$, spanning more than the fine structure splitting of the $25P$-state. Due to the employed TOF measurement scheme, the information on the lifetime of the observed molecular resonances is contained in the spectrum and could be evaluated for selected resonances [160]. Furthermore, the broadening of the observed resonances in an applied external electric field revealed that, due to the mixing with high-l states, bound states in the inner wells possess permanent electric dipole moments up to 220 D.

While most previous studies on ultralong-range Rydberg molecules focused on the perturbation of the Rydberg state by the presence of the perturber, we instead focused on the perturber and showed that also the hyperfine state of the perturber atom is affected by the molecular interaction. By analysing the mixing of the hyperfine states by the system Hamiltonian from eq. (2.4.34) we anticipated the possibility that this interaction can be used to trigger a spin-flip of the perturber atom upon photoassociation of the molecule. By the comparison of spectra for samples prepared in the $F = 1$ and $F = 2$ hyperfine states, we found strong experimental evidence for such spin-flip processes. We further saw that a peculiar situation arises for the studied $25P$-state since the fine structure splitting of the Rydberg state is close to the hyperfine splitting of the perturber atom, thus leading to a close energetic vicinity of the $25P_{1/2}; F = 2$ and the $25P_{3/2}; F = 1$ state. Since the energy gap between those states can be overcome by the molecular interaction, we observed a strong mixing of those two states, giving rise to a strong entanglement between the fine structure state of the Rydberg atom and the hyperfine structure of the perturber.

Butterfly Rydberg molecules

A very special molecular state arises in rubidium due to the presence of a shape resonance in the p-wave electron–perturber scattering. Caused by the strong scattering interaction, these butterfly states show enormous binding energies compared to ultralong-range or trilobite Rydberg molecules. While butterfly states were already predicted in 2002 [47], clear experimental evidence for their existence was so far missing. In this thesis, we presented the first experimental proof for the existence of butterfly Rydberg molecules by performing photoassociation spectroscopy in a BEC. We found excellent agreement between the depth of the calculated r-butterfly PECs and the lowest energy lines in the measured spectrum. Also, the changing density of states in the measured spectrum could be well explained by the bound states in the modelled potential. These strong indications were complemented by a detailed study of the behaviour of the observed lines inside a small external electric field. The appearing line splitting could be nicely explained by the simple model of a dipolar molecule in an electric field. The applicability of this theory not only proved that the observed states possess a permanent electric dipole moment of up to 500 D but also allowed us to extract the exact size of the dipole moment and the bond length of the molecule with an unprecedented precision. By means of the field-dependent measurements, we were, for the first time, able to resolve and study the rotational structure of a Rydberg molecule. Due to the high dipole moment of the investigated butterfly Rydberg molecules, the rotational states turn into highly oriented pendular states, even for small electric fields below $1\,\mathrm{V/cm}$. The information on the bond length of the molecule extracted from the splitting of the pendular states allowed for a detailed comparison to theory and permitted a definite assignment of the measured spectroscopic lines to one of the wells in the calculated PECs. As it is clear from the theory that the deep potential wells in the radial butterfly PECs are caused by the admixing of the strong gradients created by the P-state wave function nodes, the high-precision measurement of the molecule's bond length is an indirect measurement for the position of the P-state's radial wave function nodes. The fact that the measured bond lengths coincide with the nodes of the numerically integrated radial wave functions can thus also be seen as an indirect experimental confirmation of the Schrödinger equation.

The performed study of butterfly molecules revealed several peculiar properties that cannot be observed with conventional molecules. While in conventional molecules there exists one defined vibrational ground state that shows an almost Gaussian wave function, the highly oscillatory shape of the r-butterfly potentials gives rise to many individual wells, each hosting the lowest few harmonic oscillator states. It is therefore possible to photoassociate butterfly molecules in the vibrational ground state with a selectable discrete bond length between $100\,\mathrm{a}_0$ and $400\,\mathrm{a}_0$. Once all states are identified in the spectrum, it is possible, in the presence of a small electric field, to create a molecule with a controlled bond length, vibrational state, angular momentum state, and orientation in the lab frame. To our knowledge, there is no other molecular system that allows such high degree of control over the molecular parameters. In particular, it is even possible to excite butterfly molecules that show a very peculiar combination of bond length and dipole moment. While in conventional molecules the maximum dipole moment is achieved in an ionic bond, where the electron localises completely at the binding partner, we observed a situation in butterfly molecules where this limit is exceeded and the average position of the Rydberg electron is located beyond the perturber atom.

Outlook and future developments

Since the interaction of the Rydberg electron with the perturber is only relevant for sufficiently low thermal energies, the studied Rydberg–ground state interaction is a unique effect that arises only at ultracold temperatures. Hence, this interaction is located at the interface between ultracold many-body systems and quantum chemistry with Rydberg atoms. It is therefore not surprising that the obtained knowledge on this peculiar interaction will in turn also have influence on both of these research fields. In the following, we will show how the Rydberg–ground state interaction, and in particular the studied effects arising from it, might affect these fields.

In the context of quantum chemistry in Rydberg systems, the reaction dynamics and the molecular bond are surely interesting in their own right. To develop more sophisticated future models and to plan more detailed studies on the nature of the molecular bond, our systematic spectroscopy that also considered the hyperfine degree of freedom might provide valuable input. While we have already achieved a very good overall agreement for the butterfly states, there is still space for improvement in the matching between the calculated energies of the bound states and the measured spectrum. A refined theoretical model including the spin–orbit coupling in the scattering processes will affect the energetic positions of the butterfly wells and might thus be a promising candidate to improve the theoretical model. Since also the scattering phase shifts have not been measured so far, our data might even provide a possibility to determine these quantities by adapting the calculated PECs to the measured spectra.

Moreover, the systematic study of the hyperfine state's influence on the molecular resonances of ultralong-range Rydberg molecules provides valuable spectroscopic information and allows to attribute each line either to the mixed type potential or the corresponding triplet potential. This additional information allows for an even better interpretation of the spectrum and can serve as a benchmark for refined theoretical models. In the future, it might also be interesting to extend the study on hyperfine mixing to trilobite and butterfly states since the molecular interaction in those states vastly exceeds the hyperfine interaction. Consequently, the $\tilde{F} = 3/2$ state contains both hyperfine states and the bound states therein appear in both, the $F = 1$ and the $F = 2$ spectrum. By comparing the spectra, it should thus be possible to identify coincident lines belonging to the $\tilde{F} = 3/2$ PEC. Since the $\tilde{F} = 1/2$ and the $\tilde{F} = 5/2$ are pure $F = 1$ and $F = 2$ states, respectively, the remaining lines in each spectrum can also be attributed to the corresponding PEC. This additional information will further ease the interpretation of the spectrum and will provide even more valuable input for benchmarking theoretical models.

A particularly good example of how the Rydberg–ground state interaction simultaneously touches the field of quantum chemistry and ultracold systems is the observed mass transport mechanism. While the increased reaction kinetics itself surely falls in the realm of quantum chemistry, it has also direct consequences for many-body dynamics in ultracold quantum gases since the mass transport renders associative ionisation an important dissipative process in high-density clouds. For the studied $60P$-state with a natural decay rate of 7 kHz, the measured cross section indicates that in a cloud with a temperature of 100 nK and atomic densities above $6 \times 10^{13}\,\mathrm{cm}^{-3}$ associative ionisation even becomes the dominant decay mechanism. For future experiments on Rydberg dressing and studies of dissipative quantum phases of Rydberg gases beyond the frozen gas approximation, it is therefore crucial to take these processes into account.

Furthermore, the peculiar properties of Rydberg molecules might find application in ultracold gases to alter the many-body dynamics. As an example, one could use the giant interaction length of hundred manometers to micrometres (for very high principal quantum numbers) to employ Rydberg molecules to implement tunable short-range interactions by an optical Feshbach resonance [161]. Here, the laser-induced coupling of a free two-particle scattering state to the molecular bound state allows to change the effective s-wave scattering length between the atoms and thus to modify the interaction among them. This scheme, however, suffers from intrinsic losses and decoherence due the coupling laser. Molecular states with a long lifetime and minimal off-resonant scattering from the bare atomic resonance are therefore beneficial. Due to the absence of a bare atomic resonance in the vicinity of the spin-flip molecular line, photoassociation of spin-flip molecules might be well suited to implement an optical Feshbach resonance. Due to the suppression of the spin-flip excitation by the small admixture of the opposite hyperfine state, such scheme would however require high laser intensities to achieve a decent coupling strength. Moreover, the lifetime of the molecular state $\gamma/2\pi = 10$ - $30\,\mathrm{kHz}$ is compatible to that of molecular states in ytterbium and strontium that were already successfully employed in optical Feshbach resonances [161].

While the spin-flip process opens up promising new perspectives to tailor the short-range physics in cold gases, also long-range interactions could be induced through the enormous dipole moment of butterfly Rydberg molecules. Compared to ultralong-range molecules or trilobite molecules, the interaction enhancement caused by the shape resonance increases the binding energy of butterfly Rydberg molecules by several orders of magnitude. The calculated depth of the butterfly PECs of several hundred GHz is even stronger than the typical Rydberg–Rydberg interaction strength in cold gases. While other Rydberg molecules might be broken apart by the Rydberg–Rydberg interaction, the stronger binding in butterfly molecules might enable the observation of direct dipole–dipole interaction. Photoassociating butterfly molecules with a dipole moment of 500 D from an $n = 2$ Mott insulator would allow for a nearest neighbour dipole–dipole interaction of 250 MHz in an optical lattice with a lattice constant of 532 nm. In lower dimensional systems, the possibility to orient the nuclear dipole in external electric fields in terms of pendular states opens the possibility to tune the dipole–dipole interaction. In such case, the perturber atom can be seen as a handle to break the symmetry of the Rydberg atom and to orient it in the lab frame. However, the unbeneficial distance distribution in cold samples strongly reduces the coupling to the butterfly state. To still obtain a significant amount of molecules in the system, either high laser intensities or pre-associated, weakly bound Feshbach molecules [164, 165] as initial state can be employed. For sufficient coupling strength, it might also be possible to use an off-resonant excitation to butterfly molecules to create a dressed state that combines the long-range interaction of the dipolar molecules with the long lifetimes of the ground state. Therefore, butterfly Rydberg molecules are well-suited to explore dipolar many-body systems with tunable interactions in single-species ultracold gases.

In summary, we have demonstrated that the interaction of the Rydberg electron with a perturber atom has many important consequences for the physics of ultracold Rydberg gases but also bears potential applications in quantum chemistry and quantum many-body systems. It will thus be interesting to see in which future direction this very vital and steadily growing research field develops.

A. Appendix

A.1. Spherical Bessel functions

Asymptotic behaviour for $kr \to \infty$

When the argument of the spherical Bessel functions tend to infinity ($kr \gg l(l+1)$), they can be replaced by the asymptotic expressions [**?**, eq. B.51]

$$j_l(kr) \underset{kr\to\infty}{\to} \frac{1}{kr}\sin\left(kr - \frac{1}{2}l\pi\right) = \frac{i^{-l}}{(2ikr)}\left[e^{ikr} + (-1)^{l+1}e^{-ikr}\right], \tag{A.1.1a}$$

$$y_l(kr) \underset{kr\to\infty}{\to} \frac{1}{kr}\cos\left(kr - \frac{1}{2}l\pi\right) = \frac{i^{-l}}{(2kr)}\left[e^{ikr} - (-1)^{l+1}e^{-ikr}\right]. \tag{A.1.1b}$$

Asymptotic behaviour for $kr \to 0$

If the argument of the Bessel functions is small, one can use the expansion [**?**, eq. B.52]

$$j_l(kr) \underset{kr\to 0}{\to} \frac{(kr)^l}{(2l+1)!!}\left[1 - \frac{(kr)^2}{2(2l+3)} + ...\right] \tag{A.1.2a}$$

$$y_l(kr) \underset{kr\to 0}{\to} -\frac{(2l+1)!!}{(2l+1)}\frac{1}{(kr)^{l+1}}\left[1 + \frac{(kr)^2}{2(2l+3)} + ...\right] \tag{A.1.2b}$$

A.2. Angular momentum coupling with ladder operators

In angular momentum coupling, the scalar product $\hat{\vec{J_1}} \cdot \hat{\vec{J_2}}$ of two angular momentum operators often appears. In order to find a matrix representation for this operator, it is useful to express it using angular momentum ladder operators. Their use becomes obvious by splitting the scalar product into its components

$$\hat{\vec{J_1}} \cdot \hat{\vec{J_2}} = \hat{J}_{1,x}\hat{J}_{2,x} + \hat{J}_{1,y}\hat{J}_{2,y} + \hat{J}_{1,z}\hat{J}_{2,z}. \tag{A.2.1}$$

While most of the time the basis of the system is chosen such, that $\hat{J}_z$ are diagonal, the off-diagonal terms for the other angular momentum projections can be found using the angular momentum projection operators

$$\hat{J}_{i,x} = \frac{1}{2}\left(\hat{J}_{i,+} + \hat{J}_{i,-}\right), \tag{A.2.2}$$

$$\hat{J}_{i,y} = \frac{1}{2i}\left(\hat{J}_{i,+} - \hat{J}_{i,-}\right). \tag{A.2.3}$$

Applying this individually to the two angular momenta $\hat{\vec{J_1}}$ and $\hat{\vec{J_2}}$, we obtain

$$\hat{\vec{J_1}} \cdot \hat{\vec{J_2}} = \frac{1}{2}(\hat{J}_{1,+}\hat{J}_{2,-} + \hat{J}_{1,-}\hat{J}_{2,+} + 2\hat{J}_{1,z}\hat{J}_{2,z}). \tag{A.2.4}$$

While the z-terms create diagonal elements, the ladder operators create off-diagonal elements according to

$$\langle j', m_j' | \hat{J}_{i,+} | j, m_j \rangle = \hbar \sqrt{(j - m_j)(j + m_j + 1)} \delta_{m_j'+1, m_j} \delta_{j',j}, \tag{A.2.5}$$

$$\langle j', m_j' | \hat{J}_{i,-} | j, m_j \rangle = \hbar \sqrt{(j + m_j)(j - m_j + 1)} \delta_{m_j'-1, m_j} \delta_{j',j}. \tag{A.2.6}$$

A.3. Clebsch–Gordan coefficients

If two angular momenta $\vec{L}$ and $\vec{S}$ couple to the total angular momentum

$$\vec{J} = \vec{L} + \vec{S} \tag{A.3.1}$$

and the system Hamiltonian contains a coupling term of the form

$$\hat{H}_{\text{couple}} = \alpha \hat{\vec{L}} \cdot \hat{\vec{S}}, \tag{A.3.2}$$

one can find a basis of coupled angular momenta states that diagonalises the system Hamiltonian. The transformation between the uncoupled basis $|L, m_l, S, m_s\rangle$ and the coupled basis can be obtained by inserting unity in terms of the subspace of one of the uncoupled angular momenta. If we choose to insert unity in terms of the Hilbert space of S, we get the coupled state

$$|J, m_j\rangle = \sum_{m_s} |L, m_l, S, m_s\rangle \langle L, m_l, S, m_s | J, m_j\rangle . \tag{A.3.3}$$

The appearing scalar product is called *Clebsch–Gordan coefficient* and can be calculated as [65, eq. C.12]

$$\langle L, m_l, S, m_s | J, m_j \rangle = (-1)^{L-S+m_j} \sqrt{2J+1} \begin{pmatrix} L & S & J \\ m_l & m_s & m_j \end{pmatrix}, \tag{A.3.4}$$

where the expression in parentheses is the Wigner-3j symbol [**?**].

A.4. Gradients of single particle wave functions

For the p-wave interaction of a Rydberg electron with a ground state perturber, we need to evaluate the gradient of the Rydberg wave function at the perturber's position. Here, we show how the gradient is calculated and especially how an analytic expression for the angular directions can be obtained.

We assume to have a wave function $\Psi(r, \theta, \phi)$ that is separable and can thus be written as

$$\Psi_{nlm}(r, \theta, \phi) = R(r)_{nl} Y_l^m(\theta, \phi). \tag{A.4.1}$$

In spherical coordinates the gradient of such a wave function is given as

$$\vec{\nabla}\Psi(r, \theta, \phi) = \begin{pmatrix} \frac{\partial R_{nl}(r)}{\partial r} Y_l^m(\theta, \phi) \\ \frac{1}{r} R_{nl}(r) \frac{\partial Y_l^m(\theta,\phi)}{\partial \theta} \\ \frac{R_{nl}(r)}{r \sin(\theta)} \frac{\partial Y_l^m(\theta,\phi)}{\partial \phi} \end{pmatrix}. \tag{A.4.2}$$

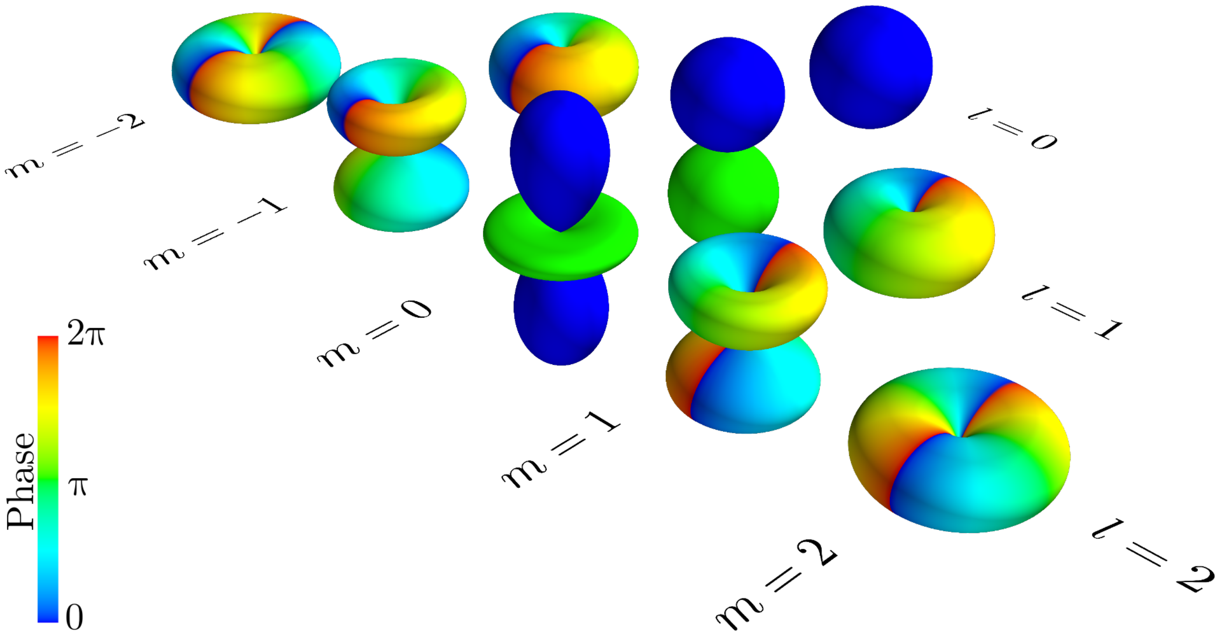

Figure A.1: 3D representation of the spherical harmonics $Y_l^m(\theta,\phi)$ up to $l = 2$ in spherical coordinates. For each object, the distance from the origin gives the absolute value $|Y_l^m(\theta,\phi)|$ and the colour denotes the complex phase.

Since the radial wave function $R_{nl}(r)$ is calculated numerically, we have to determine the derivative for $\partial_r R_{nl}(r)$ also numerically. The angular derivatives on the other hand can be obtained analytically from the analytic expression for the spherical harmonics as shown in the following.

Derivatives of the spherical Harmonics

The angular modulation of the Rydberg wave functions is fully determined by the spherical harmonics (see fig. A.1). The derivatives of the spherical harmonics can be calculated analytically. Starting from the analytical expression

$$Y_l^m(\theta,\phi) = \frac{1}{\sqrt{2\pi}}\sqrt{\frac{2l+1}{2}\frac{(l-m)!}{(l+m)!}}P_l^m(\cos(\theta))e^{im\phi} \tag{A.4.3}$$

for the spherical harmonics, we calculate the derivative separately for the polar (θ)- and the azimuthal (ϕ)-direction.

Polar direction

The partial derivative in θ-direction is given by

$$\frac{\partial Y_l^m(\theta,\phi)}{\partial\theta} = \frac{1}{\sqrt{2\pi}}\sqrt{\frac{2l+1}{2}\frac{(l-m)!}{(l+m)!}}(-\sin(\theta))\frac{\partial P_l^m(\cos(\theta))}{\partial(cos(\theta))}e^{im\phi}, \tag{A.4.4}$$

where the derivative of the associated Legendre polynomial is given by

$$\frac{\partial P_l^m(cos(\theta))}{\partial(\cos(\theta))} = -\frac{m\cos(\theta)}{\sin^2(\theta)}P_l^m(\cos(\theta)) - \frac{1}{\sin(\theta)}P_l^{m+1}(\cos(\theta)). \tag{A.4.5}$$

Thus, we obtain

$$\frac{\partial Y_l^m(\theta,\phi)}{\partial\theta} = \frac{1}{\sqrt{2\pi}}\sqrt{\frac{2l+1}{2}\frac{(l-m)!}{(l+m)!}}\left[\frac{\cos(\theta)m}{\sin(\theta)}P_l^m(\cos(\theta)) + P_l^{m+1}(\cos(\theta))\right]e^{im\phi}. \tag{A.4.6}$$

Despite the $\sin(\theta)^{-1}$ term, the expression does not diverge since the denominator approaches zero as fast as P_l^m. However, it is problematic to calculate the expression for $\theta = 0$ numerically since one has to calculate $P_l^m(0)$ and $1/\sin(0)$ separately, where the latter one makes the result useless. Therefore, it is useful to apply the recurrence formula of the associated Legendre polynomials [166]

$$mxP_l^m(x) = -\frac{1}{2}\sqrt{1-x^2}\left[P_l^{m+1}(x) + (l+m)(l-m+1)P_l^{m-1}(x)\right]. \tag{A.4.7}$$

Setting $x = \cos(\theta)$ and applying it to the "diverging term" of the derivative, one obtains

$$\frac{\partial Y_l^m(\theta,\phi)}{\partial\theta} = \sqrt{\frac{2l+1}{16\pi}\frac{(l-m)!}{(l+m)!}}\left[P_l^{m+1}(\cos(\theta)) - (l+m)(l-m+1)P_l^{m-1}(\cos(\theta))\right]e^{im\phi}, \tag{A.4.8}$$

which is regular for all values of θ. However, care must be taken that the Legendre polynomials vanish if $m+1 \geq l$ or $m-1 \leq -l$. Expressing the associated Legendre polynomials in terms of $Y_l^{m+1}(\theta,\phi)$ and $Y_l^{m-1}(\theta,\phi)$, we can furthermore identify

$$\frac{\partial Y_l^m(\theta,\phi)}{\partial\theta} = \frac{1}{2}\sqrt{l^2-m^2}\left[Y_l^{m+1}(\theta,\phi)e^{-i\phi} - (l+m+1)Y_l^{m-1}(\theta,\phi)e^{i\phi}\right]. \tag{A.4.9}$$

Azimuthal direction

The partial derivative in ϕ-direction is given by

$$\frac{\partial Y_l^m(\theta,\phi)}{\partial\phi} = \frac{1}{\sqrt{2\pi}}\sqrt{\frac{2l+1}{2}\frac{(l-m)!}{(l+m)!}}P_l^m(\cos(\theta))ime^{im\phi} = imY_l^m(\theta,\phi). \tag{A.4.10}$$

While this expression itself is regular for all θ and ϕ, a numerical problem arises from the volume element in eq. A.4.2 when the ϕ-component of the gradient is calculated for $\theta = 0$. To treat the appearing $\sin(\theta)^{-1}$, the same properties of the associated Legendre polynomials can be used as for the θ direction. Expanding the expression with $1 = \frac{\cos(\theta)}{\cos(\theta)}$ and applying the recurrence formula [166], one obtains

$$\begin{aligned}\frac{\partial Y_l^m(\theta,\phi)}{\partial\phi} &= \frac{i}{\sqrt{2\pi}}\sqrt{\frac{2l+1}{2}\frac{(l-m)!}{(l+m)!}}\\ &\quad\times(-\sin(\theta))\frac{P_l^{m+1}(\cos(\theta)) + (l+m)(l-m+1)P_l^{m-1}(\cos(\theta))}{2\cos\theta}e^{im\phi}.\end{aligned} \tag{A.4.11}$$

Unfortunately, this expression is hard to evaluate at $\theta = \pi/2$ but it can be evaluated at $\theta = 0$. Hence, by combining both expressions, the ϕ gradient can be calculated for all θ. In summary, the gradient of the wave function thus reads

$$\vec{\nabla}\Psi(r,\theta,\phi) = \begin{pmatrix} \frac{\partial R_{nl}(r)}{\partial r} Y_l^m(\theta,\phi) \\ \frac{1}{r} R_{nl}(r) \frac{1}{2}\sqrt{l^2 - m^2}\left[Y_l^{m+1}(\theta,\phi)e^{-i\phi} - (l+m+1)Y_l^{m-1}(\theta,\phi)e^{i\phi}\right] \\ \frac{\Psi(r,\theta,\phi)}{r\sin(\theta)} im \end{pmatrix}. \tag{A.4.12}$$

A.5. Decoupling of states and angular dependence in the diagonalisation

Decoupling of degenerate interacting states in a delta potential

In the diagonalisation of the Rydberg–ground state interaction, we often see that from a set of degenerate states some detach and others stay uncoupled. This is a direct consequence of the structure of the Hamiltonian that is obtained if the states interact with each other and do not differ in additional degrees of freedom, e.g. the spin. To illustrate this, it is useful to make a simple example that can be calculated analytically. To this end, we want to diagonalise the Rydberg–ground state interaction operator restricted to s-wave scattering using a basis that only consists of a $nP_{1/2}$ Rydberg state with its two degenerate Zeeman states $m_j = \pm 1/2$. Calculating the Clebsch–Gordan coefficients for the spin–orbit coupling, the spatial wave functions of these Zeeman states may be defined as

$$X_+(r,\theta,\phi) = R_{nl}(r)\left[\sqrt{\frac{2}{3}}Y_1^1(\theta,\phi)\chi_- - \sqrt{\frac{1}{3}}Y_1^0(\theta,\phi)\chi_+\right] \tag{A.5.1}$$

$$X_-(r,\theta,\phi) = R_{nl}(r)\left[-\sqrt{\frac{2}{3}}Y_1^{-1}(\theta,\phi)\chi_+ + \sqrt{\frac{1}{3}}Y_1^0(\theta,\phi)\chi_-\right], \tag{A.5.2}$$

with the radial wave function $R_{nl}(r)$, the spherical harmonics $Y_l^m(\theta,\phi)$, and the spin wave function $\chi_\pm$. Since the interaction potential from eq. (2.4.27) is a delta-type potential, we have to evaluate the spatial wave function at $\vec{R} = (R,\Theta,\Phi)$. For the sake of brevity, we omit the explicit notation of the (R,Θ,Φ)-dependence but keep in mind that $X_\pm$ is always evaluated at that point. With this definition the interaction Hamiltonian reads:

$$\hat{H}_{\text{int}} = 2\pi A_0(k_R)\begin{pmatrix} |X_+|^2 & X_+^* X_- \\ X_-^* X_+ & |X_-|^2 \end{pmatrix}. \tag{A.5.3}$$

With the definition $a \equiv 2\pi A_0(k_R)$, we get the characteristic polynomial

$$(a|X_+|^2 - \lambda)(a|X_-|^2 - \lambda) - a^2 X_-^* X_+ X_+^* X_- = 0, \tag{A.5.4}$$

which reduces to

$$\lambda^2 + a(|X_+|^2 + |X_-|^2)\lambda = 0. \tag{A.5.5}$$

From this we obtain the eigenvalues

$$\lambda_1 = 0; \qquad \lambda_2 = a(|X_+|^2 + |X_-|^2). \tag{A.5.6}$$

We thus see that the first eigenstate decouples completely and is equivalent to zero for all angles and distances. It is important to note here that this result also holds for more basis states. In the case of three basis states, one can formally do the same diagonalisation and obtains $\lambda_1 = \lambda_2 = 0$ and $\lambda_3 = |X_1|^2 + |X_2|^2 + |X_3|^2$. In general, this structure of eigenvalues is always obtained when for every 2×2 submatrix the product of the diagonal terms equals the product of the off-diagonal terms. In our case, this unique structure of the interaction Hamiltonian is caused by the δ-operator and thus the decoupling follows from the zero-range nature of the potential. If we had correctly considered the singlet and triplet projectors as introduced in sec. 2.4.3, we would have obtained one coupled singlet and one coupled triplet state, all other states would remain uncoupled. Since our basis has only two states, we would end up with no decoupled state. This can also be observed in fig. 2.12 where there is no uncoupled state remaining for the $25P_{1/2}$-state. In the case of the $25P_{3/2}$-state however, there is a set of uncoupled states remaining. The decoupling of states becomes even more obvious in the high-l manifolds where a few trilobite and butterfly PECs detach but the majority of states remains uncoupled.

Angular dependence

At first glance, one could expect the Rydberg–ground state interaction to be angular dependent due to the angular dependence of the wave functions $X_\pm$. However, the dependence vanishes when diagonalising the Hamiltonian and taking into account all m_j states for a given J. To observe this in the remaining eigenvalue λ_2, we have to calculate the absolute square of the two states

$$|X_+|^2 = R_{nl}^* \sqrt{\frac{1}{3}} \left(\sqrt{2} Y_1^{1*} \chi_-^* - Y_1^{0*} \chi_+^* \right) R_{nl} \sqrt{\frac{1}{3}} \left(\sqrt{2} Y_1^1 \chi_- - Y_1^0 \chi_+ \right) \tag{A.5.7}$$

$$= \frac{|R_{nl}|^2}{3} \left[2|Y_1^1|^2 + |Y_1^0|^2 \right] \tag{A.5.8}$$

$$|X_-|^2 = R_{nl}^* \sqrt{\frac{1}{3}} \left(-\sqrt{2} Y_1^{-1*} \chi_+^* + Y_1^{0*} \chi_-^* \right) R_{nl} \sqrt{\frac{1}{3}} \left(-\sqrt{2} Y_1^{-1} \chi_+ + Y_1^0 \chi_- \right) \tag{A.5.9}$$

$$= \frac{|R_{nl}|^2}{3} \left[2|Y_1^{-1}|^2 + |Y_1^0|^2 \right]. \tag{A.5.10}$$

Inserting this into the eigenvalue λ_2 of eq. (A.5.6), we obtain:

$$\lambda_2 = \frac{a|R_{nl}|^2}{3} \left[2|Y_1^1|^2 + 2|Y_1^0|^2 + 2|Y_1^{-1}|^2 \right]. \tag{A.5.11}$$

Here, we can apply Unsöld's theorem [?]

$$\sum_{m=-l}^{l} |Y_l^m|^2 = \frac{2l+1}{4\pi} \tag{A.5.12}$$

and finally obtain

$$\lambda_2 = \frac{2a|R_{nl}|^2}{3} \frac{2l+1}{4\pi} = A_0(k_R)|R_{nl}|^2, \tag{A.5.13}$$

where in the last step we set $l = 1$ for the P-state and used the definition of a. This eigenvalue carries also no angular dependence any more but in contrast to λ_1 the radial dependence still persists. Note that even though one obtains the same eigenvalues for all angles, the eigenvectors are still angular dependent. In principle this is the same result that should be obtained from degenerate perturbation theory.

Even though we considered the case of only two Zeeman substates, this result similarly applies to all levels with degenerate Zeeman substates. The physical interpretation for this is that, as long as the interaction between the wave function and the perturber is stronger than the interaction that is setting the quantisation axis prior to the excitation, the system has no distinct axis and will orient itself to minimise energy. If, on the other hand, the quantisation axis is strong so the Zeeman states are split further in energy than the interaction energy, the angular dependence reappears. In this regime, the alignment of Rydberg states can be studied [104, 167].

A.6. Regularised pseudopotentials

A word of caution is needed for the simple pseudopotentials given by eq. (2.4.27) and (2.4.28). As pointed out in ref. [168], the eigenenergies of the Hamiltonian in eq. (2.4.15) obtained in a full diagonalisation (sec. 2.4.5) do not converge when the number of basis states is increased. Moreover, the results obtained by a diagonalisation do not coincide with the eigenenergies from a quantum defect theory approach using Green's function and Dirichlet boundary conditions [47, 102]. This is due to the fact that in contrast to the Green's function approach, the delta-type pseudopotentials do not exactly fulfil the scattering boundary condition from eq. (2.2.21) outside but in the vicinity of the scattering potential. In the s-wave case this boundary condition for the wave function reads

$$\Psi(\vec{r}) = \frac{\sin(|\vec{r}-\vec{R}| - \delta(k))}{k|\vec{r}-\vec{R}|}. \tag{A.6.1}$$

The pseudopotential approach can also fulfil this boundary condition when a regularised delta function potential [168, 169] of the form

$$\begin{aligned}
\hat{V}_s^{\mathrm{reg}} &= 2\pi A_0(k)\delta^{(3)}(\vec{r}-\vec{R})\frac{\partial}{\partial\rho}\rho && \text{(A.6.2a)}\\
&= 2\pi A_0(k)\delta^{(3)}(\vec{r}-\vec{R})\left[1+\rho\frac{\partial}{\partial\rho}\right] && \text{(A.6.2b)}\\
&= \hat{V}_s + \hat{V}_s\rho\frac{\partial}{\partial\rho} && \text{(A.6.2c)}
\end{aligned}$$

is employed. Here, the relative distance $\rho = |\vec{r}-\vec{R}|$ between the electron and the perturber is introduced. Eq. (A.6.2b) was obtained by applying the regularisation operator $\frac{\partial}{\partial\rho}\rho$ to a test function. Obviously, the regularised potential recovers the expression for the unregularised potential $\hat{V}_0$ but adds a second term that includes the ρ-derivative of the ket-wave function. This additional term, however, is only non-vanishing, if the ρ-derivative of the ket-wave function is infinite at $\vec{R}$ since $\lim_{\vec{r}\to\vec{R}}\rho = 0$. Hence, if we choose a basis set that only includes eigenfunctions regular in $\vec{R}$, the unregularised pseudopotential will not cover the full problem. In that sense the regularisation of the delta function potential fixes the handling of irregular wave functions at the perturber's position, which are needed to exactly fulfil the boundary condition given by eq. (A.6.1).

Similarly, the divergence can be handled for the p-wave interaction by using the regularised potential [170]

$$\hat{V}_p^{\text{reg}} = 6\pi A_1(k)\delta^{(3)}(\vec{r}-\vec{R})\frac{1}{k^2}\overleftarrow{\nabla}\cdot\vec{\nabla}\frac{1}{2}\frac{\partial^2}{\partial\rho^2}\rho^2 \tag{A.6.3a}$$

$$= \hat{V}_p + 2\hat{V}_p\rho\frac{\partial}{\partial\rho} + \frac{1}{2}\hat{V}_p\rho^2\frac{\partial^2}{\partial\rho^2}. \tag{A.6.3b}$$

Also in this case, the ρ-derviative can be expanded and one finds that a ρ-independent term appears, that is identical to the unregularised p-wave potential. Thus, the same result is obtained for the regularised and the unregularised potential when performing first-order perturbation theory. Even beyond first order perturbation, the unregularised potential can be a good approximation for the regularised potential if the set of basis states is not chosen too big. This is particularly advantageous since, as shown above, the regularised potential cannot be employed in a standard diagonalisation scheme that relies on eigenfunctions that are regular in $\vec{R}$ [168]. By this means, a valid approximation to the system's eigenenergies can be obtained even without including irregular wave functions.

A.7. Calculation of the electronic density

It is often useful to calculate the electronic density in position space of a superposition state $|\Psi\rangle = \sum_i c_i |i\rangle$ that is obtained from the diagonalisation of a certain Hamiltonian. If the representation of the basis vectors $|i\rangle$ in position space $\Psi_i(R,\theta,\phi)$ is known, the electronic density D at position $\vec{x} = (R,\theta,\phi)$ is simply given by

$$D(\vec{x}) = |\langle\vec{x}|\Psi\rangle|^2 = |\sum_i c_i\Psi_i(R,\theta,\phi)|^2. \tag{A.7.1}$$

However, care has to be taken if the basis consists of product states, e.g a spatial and a spin state, as interferences will only occur for states that are non-orthogonal in the additional Hilbert space.

As a simple example, let us consider an electron that is described in the basis $|\Psi_i\rangle\otimes|\chi_j\rangle$ with the spatial states $|\Psi_i\rangle$ and the spin states $|\chi_j\rangle$. The Hamiltonian we are interested in can now mix states depending on the spatial part and the spin part. Thus, the resulting state from the diagonalisation has the form $|\Psi\rangle = \sum_{i,j} c_{i,j}|i\rangle\otimes|\chi_j\rangle$. Since states with different spins cannot interfere in space, we have to generalise eq. (A.7.1) to

$$D(\vec{x}) = \sum_{j'} |\langle\chi_{j'}|\otimes\langle\vec{x}|\Psi\rangle|^2, \tag{A.7.2}$$

where we trace over the spin states. With the definition of the state $|\Psi\rangle$, we obtain

$$D(\vec{x}) = \sum_{j'} |\sum_j \langle\chi_{j'}|\chi_j\rangle \otimes \sum_i c_{i,j}\Psi(R,\theta,\phi)|^2. \tag{A.7.3}$$

Since the spin states are orthogonal, we have $\langle\chi_{j'}|\chi_j\rangle = \delta_{j,j'}$ and thus the expression simplifies to

$$D(\vec{x}) = \sum_j |\sum_i c_{i,j}\Psi_i(R,\theta,\phi)|^2. \tag{A.7.4}$$

A.8. Numerical calculation of bound states by the shooting method

As discussed in sec. 2.4.8, the non-trivial shape of the electronic PECs makes it difficult to determine the vibrational bound states therein. Here, we present a numerical method to find bound state energies and wave functions in an arbitrary 1D potential that is able to confine a bound state. This method relies on the fact that in the classically forbidden region of a potential ($E < V(R)$) the k-vector becomes imaginary and thus two solutions of the Schrödinger equation (2.4.51) with energy $E = \hbar^2 k^2/(2M)$ of the type

$$\Phi_E^{\mathrm{reg}}(R) \propto e^{-ikR} = e^{-|k|R} \tag{A.8.1}$$

$$\Phi_E^{\mathrm{irreg}}(R) \propto e^{ikR} = e^{|k|R} \tag{A.8.2}$$

exist. In general, any superposition of those functions is a valid solution to the differential equation. However, physically meaningful wave functions need to be square-integrable in order to be normalisable. Since the irregular solution $\Phi_E^{\mathrm{irreg}}(R)$ tends to infinity as $R \to \infty$, it cannot be normalised and thus a physical wave function can only contain the regular solution. Bound states are thus characterised by the exponential decay of their wave function in the classically forbidden regions. We can employ this fact to numerically find the bound states for almost arbitrary real, one-dimensional potentials $E_{\mathrm{pot}}(R)$ that vanish for $R \to \infty$.

For an arbitrary energy E_{g} we can use Numerov's algorithm (compare sec. 2.3.1) to numerically integrate the spatial wave function $\Phi_{E_g}(R)$ on the interval $[R_1, R_2]$. We choose R_2 to always be in the classically forbidden region of the potential and start the integration at that point, as a valid solution decays exponentially here and thus we can guess the initial value of the integration to be zero. If the arbitrarily chosen energy E_{g} does not match the energy of one of the bound states, the obtained wave function will have no physical meaning. However, we can make use of the fact that only for the right energy E the integration result will have a vanishing contribution of the irregular solution. Studying the value of the integrated wave function at an arbitrary, fixed value of R that is sufficiently deep in or behind a potential barrier, we realise that it usually varies slowly with the guessed energy E_{g}. However, when passing a bound state the wave function undergoes a phase jump of $\Delta\varphi = \pi$ and the integrated wave function consequently changes its sign [55]. This is demonstrated in fig. A.2a, where eq. (2.4.51) is integrated in a simple box-type potential for 11 different energies around the bound states' energy. Starting at $400\,\mathrm{a}_0$, all curves follow the same trajectory until they enter the classically forbidden region at $175\,\mathrm{a}_0$ and start to differ significantly. As discussed above, only the curve with the right energy will decay exponentially, all other curves start to diverge at some point. Due to the phase jump, the sign of the divergence depends on whether the energy was chosen too small or too big. We can use this fact to find the bound state energies in the potential by integrating equation (2.4.51) for an equally spaced set of energies $\{E_{\mathrm{g}}^{(n)}\}$ from R_2 to R_1 and look for changes in the sign of $\Phi_{E_{\mathrm{g}}}(R_1)$ for adjacent energies $E_{\mathrm{g}}^{(n)}$ and $E_{\mathrm{g}}^{(n+1)}$. For every sign-changing energy interval $[E_{\mathrm{g}}^{(n)}, E_{\mathrm{g}}^{(n+1)}]$, we repeat the above procedure until a certain energy precision is reached and we end up with a set of bound state energies and corresponding wave functions. Due to the analogy of approaching a target by changing the angle of a cannon until it hits, this procedure is called *shooting method*. The reliability of the results however depends on whether the analysis point R_1 is chosen sufficiently deep inside (or behind) the potential barrier that

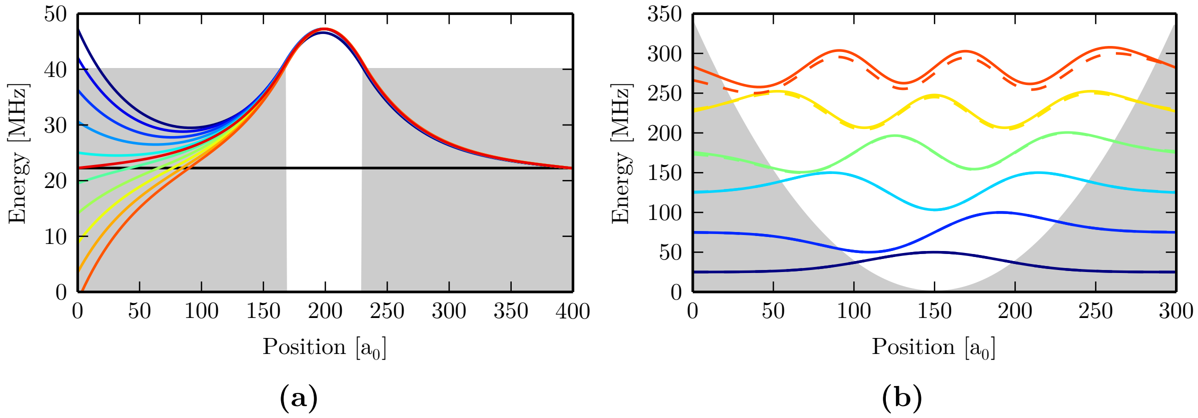

Figure A.2: Numerical calculation of bound states in one-dimensional potentials. The wave functions are shifted on the y-axis according to their energy. (a) Numerical solution of the Schrödinger equation in a box-potential for different energies ($\Delta E = \pm 0.5\,\mathrm{MHz}$) around the energy of the bound state. Only if the energy matches that of a valid bound state (red line), the solution approaches zero in the classically forbidden region. Depending on the sign of the energy mismatch the numerical solution diverges to $+\infty$ or $-\infty$, what allows to find the bound state energy by bisection. (b) Comparison of the numerically determined wave functions (solid lines) to the analytic solution (dashed lines) for the harmonic oscillator potential. All wave functions are normalised to their maximum absolute value in the plotted range. The colour is a guide to the eye. The low-lying states match perfectly and thus the numerical and the analytic solution lie on top of each other.

confines the bound state.

In order to test the method, we apply it to the quantum harmonic oscillator that is characterised by the potential

$$E^{\mathrm{HO}}_{\mathrm{pot}}(x) = \frac{1}{2} m\omega^2 x^2 \tag{A.8.3}$$

for a particle of mass m and a harmonic oscillation frequency ω. The solution of the Schrödinger equation for this potential can be obtained analytically and is given by [77]

$$\Phi^{\mathrm{HO}}(x) = \frac{1}{\sqrt{2^n n!}} \left(\frac{m\omega}{\pi\hbar}\right)^{1/4} e^{-\frac{m\omega x^2}{2\hbar}} H_n\left(\sqrt{\frac{m\omega}{\hbar}}x\right), \tag{A.8.4}$$

with the well-known eigenenergies

$$E^{\mathrm{HO}}_n = \hbar\omega\left(n + \frac{1}{2}\right). \tag{A.8.5}$$

The comparison of the wave functions and the eigenenergies is shown in fig. A.2b. The phase change of the wave function is always determined at the leftmost point that is plotted. We see an overall excellent agreement between the numerical result and the analytic solution, especially for the deeply bound states. The deviations for the higher energy states are caused by the fact that the analysis point R_1 for finding the bound state energy is not sufficiently deep inside the classically forbidden region and thus the determined energy is inaccurate.

Table A.1: Fit values of the harmonic frequency ω and the energy offset E_0 for the harmonic fit to the potential wells in the three r-butterfly PECs with the quantum numbers $\tilde{F} = 1/2$, $\tilde{F} = 3/2$, and $\tilde{F} = 5/2$.

	$\tilde{F} = 1/2$		$\tilde{F} = 3/2$		$\tilde{F} = 5/2$	
x_0 [a$_0$]	$\omega/2\pi$ [GHz]	E_0 [GHz]	$\omega/2\pi$ [GHz]	E_0 [GHz]	$\omega/2\pi$ [GHz]	E_0 [GHz]
91.9	8.248	−57.5	8.232	−55	8.233	−50.7
116.5	6.565	−51.6	6.562	−49	6.565	−44.7
143.8	5.449	−51.3	5.449	−48.8	5.449	−44.5
174.2	4.641	−52.5	4.642	−49.9	4.641	−45.7
208.2	4.119	−53.1	4.119	−50.5	4.119	−46.3
246.1	3.705	−51.8	3.705	−49.2	3.705	−44.9
288.4	3.356	−47.5	3.356	−44.9	3.356	−40.6
335.7	3.297	−38.4	3.295	−35.9	3.297	−31.6
388.8	2.952	−22.1	2.931	−19.7	2.952	−15.3
449.4	1.925	−7	1.79	−5.3	1.925	-0.2

A.9. Harmonic approximation to the r-butterfly potential

In order to be able to calculate approximate bound states in the deep wells of the r-butterfly PECs, each of the wells was fitted individually with the harmonic potential from eq. (A.8.3) with an additional energy offset E_0 and a free position of the minimum x_0. With the resulting fit parameters, the energy of the lowest two bound states ($\nu = 0, 1$) can be determined up to a precision of three significant digits. Due the anharmonicity of the real potential, the approximation becomes worse for higher states. For the next two higher bound states ($\nu = 2, 3$), the approximation is thus only precise up to two significant digits. With the fit parameters summarised in tab. A.1 the bound state energies can by calculated by

$$E = \hbar\omega(\nu + \frac{1}{2}) + E_0. \tag{A.9.1}$$

A.10. Butterfly spectra in electric fields

As discussed in sec. 6.3, we observe two qualitatively different types of spectra if we study butterfly states in an external electric field. While we observe type 1 spectra for the majority of the studied butterfly states, we found two states that showed type 2 spectra (compare tab. 6.1). A comparison of both types is shown in fig. A.3 for the molecular states at −45.1 GHz and −43.2 GHz. These states are localised in the same well and show very similar dipole moments (compare tab. 6.1) but still differ in the type of the observed spectrum. In general, the second type differs from the first by splitting in twice as many lines. The leftmost peaks in the type 2 spectrum in fig. A.3b seem to alternate in line strength. It might thus be reasonable to identify two almost identical spectra that lie on top of each other and are shifted relative to each other. Such behaviour might be explained by a splitting of the $\tilde{F} = 3/2$ state in the electric field, as discussed in sec. 6.3.

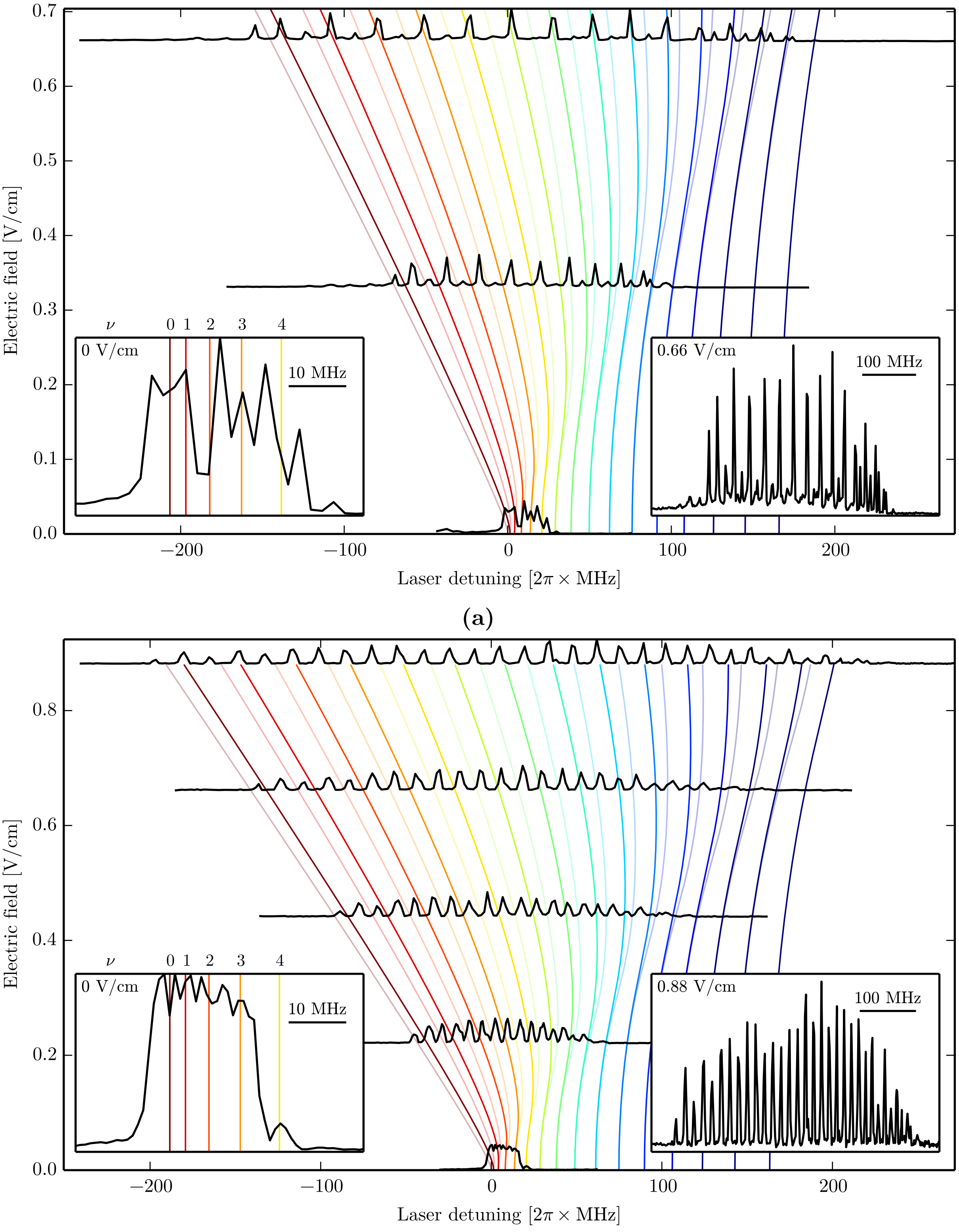

(a)

(b)

Figure A.3: The two types of field-dependent spectra. (a) The type 1 spectrum was observed for the majority of the studied butterfly states. Here, the measurement for the state at −45.1 GHz is shown. (b) The butterfly state at −43.2 GHz shows a type 2 spectrum that splits in twice as many lines compared to the type 1 spectra. For an explanation of the figure, please refer to fig. 6.4.

A.11. Photoionisation cross sections

Since the trapped Rydberg atoms are subject to the focussed YAG trapping lasers at a wavelength of $\lambda_{\mathrm{YAG}} = 1064\,\mathrm{nm}$, it is useful to know the photoionisation cross section $\sigma_{\mathrm{PI}}^{\mathrm{YAG}}$ for the studied Rydberg state. In general, the photoionisation-induced decay rate R_{ion} is given by

$$R_{\mathrm{ion}} = \sigma_{\mathrm{PI}} \frac{\text{photons}}{\text{Area} \times \text{time}} = \sigma_{\mathrm{PI}} \frac{I}{h\nu}, \tag{A.11.1}$$

where σ_{PI} is the photoionisation cross section for the specific incident photons and the Rydberg state under study, I is the intensity of the YAG laser, and ν the frequency of the photon. The cross section is thus given by

$$\sigma_{\mathrm{PI}} = \frac{R_{\mathrm{ion}}}{I} h\nu. \tag{A.11.2}$$

The quantity $\frac{R_{\mathrm{ion}}}{I}$ denotes the change of the Rydberg state's decay rate with the YAG intensity. We can thus determine the cross section by monitoring the total decay rate of the excited Rydberg state as a function of the incident YAG laser intensity. Since all other YAG-power-independent decay channels just add as an offset, we can even determine the cross section from the slope if photoionisation is not the dominant decay channel. We thus prepare a BEC in the high power YAG trapping configuration and recompress it by ramping the high power beam to 320 mW to obtain a radially small, axially elongated cloud. This way, we prepare a sample that is radially much smaller than the Gaussian beam waist of the high-power beam and thus minimise the error by intensity variation of the trapping beam along the cloud. We then switch off both trapping lasers completely and after a free expansion of 50 µs we apply a Rydberg excitation pulse for 1 µs. After another 1 µs waiting time, we abruptly switch on the high power YAG laser at a specific power. The laser is kept on for 200 µs during which the Rydberg atoms decay under the effect of the incident YAG photons. With the Rydberg excitation pulse, we also start the continuous ion detection that lasts until the end of the experiment. The obtained ion signals for various YAG laser powers are shown in fig. A.4a. In order to obtain the decay rate for the individual measurements, we fit an exponential decay to the obtained signals. Plotting the fitted decay rate against the YAG laser power (fig. A.4b), we see a linear dependency as expected from eq. (A.11.1).

In order to obtain the photoionisation cross section from the slope of such fit $\frac{R_{\mathrm{ion}}}{P}$, the power P of the laser must be translated to the intensity I and, thus, the slope $\frac{R_{\mathrm{ion}}}{I}$. For this purpose, $\frac{R_{\mathrm{ion}}}{P}$ must be divided by the intensity of the laser at 1 W (if R_{ion}/P is given in Hz/W). In our case, we obtain an intensity of $7.84 \times 10^{8}\,\mathrm{W/m^2}$ at a power of 1 W for a waist $w = 28.5\,\mu\mathrm{m}$ of the high-power YAG beam.

The measured cross section of 5.8(17) kb for the $51P_{3/2}$ state is in good agreement with ref. [86, p. 18], which gives a value on the order of $\sigma_{\mathrm{lit}} \approx 10\,\mathrm{kb}$. It should be further noted that in fig. A.4b the intersection with the y-axis at 11.1(8) kHz agrees with the natural decay rate $\gamma_{\mathrm{nat}}^{51P} = 10.3\,\mathrm{kHz}$ of the $51P_{3/2}$ state. This kind of measurement was performed for different Rydberg states. A summary of the measured photoionisation cross section values is given in tab. A.2.

Extracting the number of Rydberg excitations

Under the assumption, that photoionisation by the trapping lasers is the only decay path leading to the creation of an ion, we can use the known photoionisation cross section to

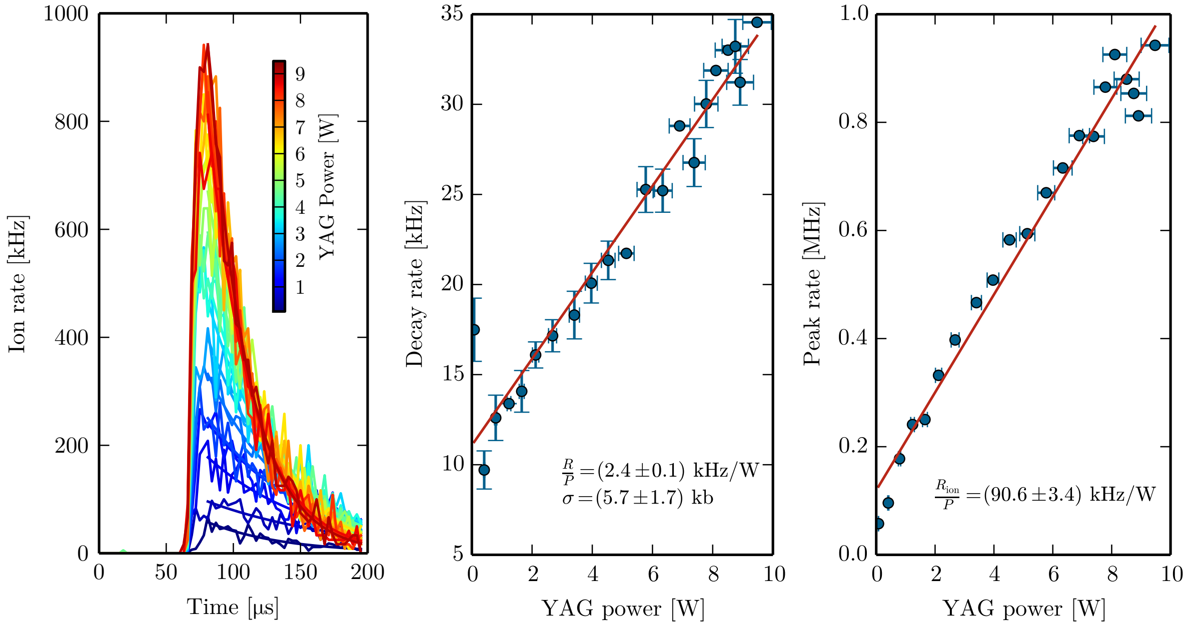

(a) **(b)** **(c)**

Figure A.4: Measurement of the photoionisation cross section $\sigma_{\text{PI}}^{\text{YAG}}$ for the YAG laser light on the $51P_{3/2}$ Rydberg state. (a) TOF signals obtained for different powers of the YAG laser with an exponential fit to the decay (solid lines). (b) Decay rate extracted from the exponential fits as a function of the YAG laser power. The slope of the linear fit is used to obtain $\sigma_{\text{PI}}^{\text{YAG}}$ according to eq. (A.11.1). (c) Maximum value of the exponential fit as a function of the YAG laser power.

extract the number of excited Rydberg atoms from the measured ion rate. At any time, the ion rate that we observe is given by

$$R_{\text{ion}} = N_{\text{Ry}} \eta R_{\text{ionise}}^{(1)} = N_{\text{Ry}} \eta \sigma \frac{I}{h\nu}, \tag{A.11.3}$$

where N_{Ry} is the number of excited Rydberg atoms, η is the detection efficiency for an ion, and $R_{\text{ionise}}^{(1)}$ is the single particle ionisation rate. If we now also use the information about the peak count rate from the TOF measurement (fig. A.4c), we can obtain the rate R_{ion}. To reduce the error in the determination of the Rydberg atom number, we can calculate it without any assumptions on the actual intensity of the YAG laser. By

Table A.2: Measured cross sections for photoionisation in the YAG trap for various Rydberg states. Here $\frac{R_{\text{ion}}}{P}$ gives the fitted slope, $\sigma_{\text{PI}}^{\text{YAG}}$ denotes the photoionisation cross section under YAG light, and γ_0 is the decay rate without the influence of the trapping laser.

state	$\frac{R_{\text{ion}}}{P}$ [kHz/W]	$\sigma_{\text{PI}}^{\text{YAG}}$ [kb]	γ_0 [kHz]
$30P_{3/2}$	6.8(3)	16.2(48)	27.2(15)
$35P_{3/2}$	9.2(3)	21.9(62)	27.2(14)
$41P_{3/2}$	5.8(2)	13.8(39)	16.1(15)
$51P_{3/2}$	2.4(1)	5.8(17)	11.1(8)
$60P_{3/2}$	3.2(3)	7.7(27)	11.0(15)

dividing eq. (A.11.3) by the power P of the YAG laser, we get

$$\frac{R_{\text{ion}}}{P} = N_{\text{Ry}}\eta\frac{R^{(1)}_{\text{ionise}}}{P}, \tag{A.11.4}$$

so we obtain

$$N_{\text{Ry}} = \frac{\frac{R_{\text{ion}}}{P}}{\eta\frac{R^{(1)}_{\text{ionise}}}{P}}. \tag{A.11.5}$$

We identify $\frac{R_{\text{ion}}}{P}$ to be the slope of the peak count rate (fig. A.4c) and $\frac{R^{(1)}_{\text{ionise}}}{P}$ to be the slope of the decay rate fit (fig. A.4b). Knowing the detection efficiency η to be 43%, we can calculate the number of Rydberg excitations in the measurement shown above to be

$$N_{\text{Ry}} = \frac{1}{0.43}\frac{90.6\,{}^{\text{kHz}}\!/\!_{\text{W}}}{2.4\,{}^{\text{kHz}}\!/\!_{\text{W}}} = 87.8. \tag{A.11.6}$$

A.12. Long-range entanglement of ground state atoms

A very interesting application of the presented spin-flip states arises in conjunction with the Rydberg blockade (sec. 2.5.1) that enables long-distance entanglement between the hyperfine-states of remote atoms. This can be illustrated if we consider a system of two potential wells A and B that are separated by less than the Rydberg blockade radius and are each filled with two atoms that can be photoassociated to a Rydberg molecule. While the following derivation also holds in the case of identical atoms, we will assume here that the two atoms in each well are distinguishable, i.e. different species or different isotopes of the same species. In this case, we can choose which of the two atoms we promote into the Rydberg state , denoted helper atom, and which atom will take the role of the perturber. If excited to a spin-flip molecule, the resulting state in well A/B is given by

$$|M\rangle_{A/B} = |r,1\rangle + \epsilon\,|r,2\rangle\,, \tag{A.12.1}$$

where we use the notation $|R,F\rangle$ for the two-particle state where R gives the quantum state of the helper atom that can be in the ground state g or in the Rydberg state r and F denotes the hyperfine state of the perturber atom. Even though in the molecule the Rydberg state is slightly changed by the interaction with the ground state atom, it still interacts with other Rydberg atoms in its surrounding. For a strong Rydberg–Rydberg interaction, we recover the blockade mechanism described in sec. 2.5.1. Since the two considered potential wells are closer together than the blockade radius, the atoms therein cannot simultaneously be excited to the Rydberg molecular state. Instead, we obtain an entangled state of the form

$$|\Psi\rangle = \frac{1}{\sqrt{2}}\left(|M\rangle_A\,|g,2\rangle_B + |g,2\rangle_A\,|M\rangle_B\right), \tag{A.12.2}$$

where we assume that the pertuber atoms were prepared in the $F = 2$ state. Inserting eq. (A.12.1), we obtain

$$|\Psi\rangle = \frac{1}{\sqrt{2}}\left(|r,1\rangle_A\,|g,2\rangle_B + |g,2\rangle_A\,|r,1\rangle_B\right) \tag{A.12.3}$$

$$+\frac{\epsilon}{\sqrt{2}}\left(|r,2\rangle_A\,|g,2\rangle_B + |g,2\rangle_A\,|r,2\rangle_B\right). \tag{A.12.4}$$

Since $\epsilon \ll 1$, we can neglect the latter term. If, furthermore, we trace out the state of the Rydberg atom, we obtain

$$|\Psi\rangle \approx \frac{1}{\sqrt{2}} \left(|1\rangle_A |2\rangle_B + |2\rangle_A |1\rangle_B \right), \tag{A.12.5}$$

which is a maximally entangled state of the two involved perturber atoms. We thus employed the hyperfine-mixing in the spin-flip molecules to transfer the entanglement that arises due to the Rydberg blockade to the spin states of the perturber atom. What is derived here in the two-particle picture should also hold in the many-particle regime. For N ground state atoms within the blockade radius, it should thus be possible to create a state where one spin excitation is shared among all N atoms to give the state

$$|\Psi\rangle_N = \frac{1}{\sqrt{N}} \left(|2\rangle_A |1\rangle_B |1\rangle_C ... + |1\rangle_A |2\rangle_B |1\rangle_C ... + |1\rangle_A |1\rangle_B |2\rangle_C ... + ... \right). \tag{A.12.6}$$

Bibliography

[1] J. J. Balmer. “Notiz über die Spectrallinien des Wasserstoff”. *Wiedemann’s Annalen der Physik und Chemie* 25, 80 (1885).

[2] J. R. Rydberg. “Recherces sur la constitution des spectres d‘emission des elements chimique”. *Den Kungliga Svenska Vetenskapsakademiens Handlingar* 23 (1889).

[3] I. Martinson and L. Curtis. “Janne Rydberg – his life and work”. *Nuclear Instruments and Methods in Physics Research Section B: Beam Interactions with Materials and Atoms* 235, 17 (2005).

[4] N. Bohr. “On the constitution of atoms and molecules”. *Philosophical Magazine Series 6* 26, 1 (1913).

[5] E. Amaldi and E. Segrè. “Effect of Pressure on High Terms of Alkaline Spectra”. *Nature* 133, 141 (1934).

[6] E. Fermi. “Sopra lo spostamento per pressione delle righe elevate delle serie spettrali”. *Nuovo Cimento* 11, 157 (1934).

[7] K. W. Meissner. “Application of Atomic Beams in Spectroscopy”. *Rev. Mod. Phys.* 14, 68 (1942).

[8] J. E. Mack and E. C. Barkofsky. “Atomic Beam Apparatus for Studying the Atomic Spectra of Gases, Especially Hydrogen”. *Rev. Mod. Phys.* 14, 82 (1942).

[9] I. Beigman and V. Lebedev. “Collision theory of Rydberg atoms with neutral and charged particles”. *Physics Reports* 250, 95 (1995).

[10] M. Hugon, F. Gounand, P. R. Fournier, and J. Berlande. “Collisional properties of highly excited rubidium atoms”. *Journal of Physics B: Atomic and Molecular Physics* 12, 2707 (1979).

[11] A. N. Klucharev, A. V. Lazarenko, and V. Vujnovic. “The ionisation rate coefficients of radiatively excited rubidium atoms Rb(n^2P) +Rb(5^2S)”. *Journal of Physics B: Atomic and Molecular Physics* 13, 1143 (1980).

[12] L. Barbier and M. Cheret. “Experimental study of Penning and Hornbeck-Molnar ionisation of rubidium atoms excited in a high s or d level (5d$\leq$nl$\leq$11s)”. *Journal of Physics B: Atomic and Molecular Physics* 20, 1229 (1987).

[13] M. Cheret, L. Barbier, W. Lindinger, and R. Deloche. “Penning and associative ionisation of highly excited rubidium atoms”. *Journal of Physics B: Atomic and Molecular Physics* 15, 3463 (1982).

[14] M. Gross, P. Goy, C. Fabre, S. Haroche, and J. M. Raimond. “Maser Oscillation

and Microwave Superradiance in Small Systems of Rydberg Atoms". *Phys. Rev. Lett.* 43, 343 (1979).

[15] P. Goy, J. M. Raimond, M. Gross, and S. Haroche. "Observation of Cavity-Enhanced Single-Atom Spontaneous Emission". *Phys. Rev. Lett.* 50, 1903 (1983).

[16] R. M. Flannery and E. Oks. "Plasma screening within Rydberg atoms in circular states". *The European Physical Journal D* 47, 27 (2008).

[17] M. Hagström, J. Davidsson, and L. Holmlid. "Transport of charge and atomic particles in Rydberg state-rich plasmas". *Journal of Physics D: Applied Physics* 31, 434 (1998).

[18] T. R. Geballe and T. Oka. "Detection of H_3^+ in interstellar space". *Nature* 384, 334 (1996).

[19] A. Dalgarno. "Molecular processes in the early Universe". *Journal of Physics: Conference Series* 4, 10 (2005).

[20] J. E. Bjorkholm, R. R. Freeman, A. Ashkin, and D. B. Pearson. "Observation of Focusing of Neutral Atoms by the Dipole Forces of Resonance-Radiation Pressure". *Phys. Rev. Lett.* 41, 1361 (1978).

[21] E. L. Raab, M. Prentiss, A. Cable, S. Chu, and D. E. Pritchard. "Trapping of Neutral Sodium Atoms with Radiation Pressure". *Phys. Rev. Lett.* 59, 2631 (1987).

[22] M. H. Anderson, J. R. Ensher, M. R. Matthews, C. E. Wieman, and E. A. Cornell. "Observation of Bose-Einstein Condensation in a Dilute Atomic Vapor". *Science* 269, 198 (1995).

[23] C. C. Bradley, C. A. Sackett, J. J. Tollett, and R. G. Hulet. "Evidence of Bose-Einstein Condensation in an Atomic Gas with Attractive Interactions". *Phys. Rev. Lett.* 75, 1687 (1995).

[24] K. B. Davis, M. O. Mewes, M. R. Andrews, N. J. van Druten, D. S. Durfee, D. M. Kurn, and W. Ketterle. "Bose-Einstein Condensation in a Gas of Sodium Atoms". *Phys. Rev. Lett.* 75, 3969 (1995).

[25] B. DeMarco and D. S. Jin. "Onset of Fermi Degeneracy in a Trapped Atomic Gas". *Science* 285, 1703 (1999).

[26] R. Grimm, M. Weidemüller, and Y. B. Ovchinnikov. "Optical dipole traps for neutral atoms". *Advances in Atomic, Molecular and Optical Physics* 42, 95 (2000).

[27] M. Greiner, O. Mandel, T. Esslinger, T. W. Hänsch, and I. Bloch. "Quantum phase transition from a superfluid to a Mott insulator in a gas of ultracold atoms". *Nature* 415, 39 (2002).

[28] M. Greiner, C. A. Regal, and D. S. Jin. "Emergence of a molecular Bose-Einstein condensate from a Fermi gas". *Nature* 426, 537 (2003).

[29] Z. Hadzibabic, P. Krüger, M. Cheneau, B. Battelier, and J. Dalibard. "Berezinskii-Kosterlitz-Thouless crossover in a trapped atomic gas". *Nature* 441, 1118 (2006).

[30] T. Lahaye, T. Koch, B. Fröhlich, M. Fattori, J. Metz, A. Griesmaier, S. Giovanazzi, and T. Pfau. “Strong dipolar effects in a quantum ferrofluid”. *Nature* 448, 672 (2007).

[31] L. Santos, G. V. Shlyapnikov, P. Zoller, and M. Lewenstein. “Bose-Einstein Condensation in Trapped Dipolar Gases”. *Phys. Rev. Lett.* 85, 1791 (2000).

[32] S. A. Moses, J. P. Covey, M. T. Miecnikowski, B. Yan, B. Gadway, J. Ye, and D. S. Jin. “Creation of a low-entropy quantum gas of polar molecules in an optical lattice”. *Science* 350, 659 (2015).

[33] S. Fölling, S. Trotzky, P. Cheinet, M. Feld, R. Saers, A. Widera, T. Müller, and I. Bloch. “Direct observation of second-order atom tunnelling”. *Nature* 448, 1029 (2007).

[34] D. Jaksch, J. I. Cirac, P. Zoller, S. L. Rolston, R. Côté, and M. D. Lukin. “Fast Quantum Gates for Neutral Atoms”. *Phys. Rev. Lett.* 85, 2208 (2000).

[35] M. D. Lukin, M. Fleischhauer, R. Cote, L. M. Duan, D. Jaksch, J. I. Cirac, and P. Zoller. “Dipole Blockade and Quantum Information Processing in Mesoscopic Atomic Ensembles”. *Phys. Rev. Lett.* 87, 037901 (2001).

[36] K. Singer, M. Reetz-Lamour, T. Amthor, L. G. Marcassa, and M. Weidemüller. “Suppression of Excitation and Spectral Broadening Induced by Interactions in a Cold Gas of Rydberg Atoms”. *Phys. Rev. Lett.* 93, 163001 (2004).

[37] D. Tong, S. M. Farooqi, J. Stanojevic, S. Krishnan, Y. P. Zhang, R. Côté, E. E. Eyler, and P. L. Gould. “Local Blockade of Rydberg Excitation in an Ultracold Gas”. *Phys. Rev. Lett.* 93, 063001 (2004).

[38] T. C. Liebisch, A. Reinhard, P. R. Berman, and G. Raithel. “Atom Counting Statistics in Ensembles of Interacting Rydberg Atoms”. *Phys. Rev. Lett.* 95, 253002 (2005).

[39] C. Ates, T. Pohl, T. Pattard, and J. M. Rost. “Antiblockade in Rydberg Excitation of an Ultracold Lattice Gas”. *Phys. Rev. Lett.* 98, 023002 (2007).

[40] T. Amthor, C. Giese, C. S. Hofmann, and M. Weidemüller. “Evidence of Antiblockade in an Ultracold Rydberg Gas”. *Phys. Rev. Lett.* 104, 013001 (2010).

[41] J. Honer, R. Löw, H. Weimer, T. Pfau, and H. P. Büchler. “Artificial Atoms Can Do More Than Atoms: Deterministic Single Photon Subtraction from Arbitrary Light Fields”. *Phys. Rev. Lett.* 107, 093601 (2011).

[42] T. M. Weber, M. Höning, T. Niederprüm, T. Manthey, O. Thomas, V. Guarrera, M. Fleischhauer, G. Barontini, and H. Ott. “Mesoscopic Rydberg-blockaded ensembles in the superatom regime and beyond”. *Nat Phys* 11, 157 (2015).

[43] J. Zeiher, P. Schauß, S. Hild, T. Macrì, I. Bloch, and C. Gross. “Microscopic Characterization of Scalable Coherent Rydberg Superatoms”. *Phys. Rev. X* 5, 031015 (2015).

[44] N. Malossi, M. M. Valado, S. Scotto, P. Huillery, P. Pillet, D. Ciampini, E. Arimondo, and O. Morsch. “Full Counting Statistics and Phase Diagram of a Dissipative Rydberg Gas”. *Phys. Rev. Lett.* 113, 023006 (2014).

[45] H. Schempp, G. Günter, M. Robert-de Saint-Vincent, C. S. Hofmann, D. Breyel, A. Komnik, D. W. Schönleber, M. Gärttner, J. Evers, S. Whitlock, and M. Weidemüller. “Full Counting Statistics of Laser Excited Rydberg Aggregates in a One-Dimensional Geometry”. *Phys. Rev. Lett.* 112, 013002 (2014).

[46] C. H. Greene, A. S. Dickinson, and H. R. Sadeghpour. “Creation of Polar and Nonpolar Ultra-Long-Range Rydberg Molecules”. *Phys. Rev. Lett.* 85, 2458 (2000).

[47] E. L. Hamilton, C. H. Greene, and H. R. Sadeghpour. “Shape-resonance-induced long-range molecular Rydberg states”. *Journal of Physics B: Atomic, Molecular and Optical Physics* 35, L199 (2002).

[48] V. Bendkowsky, B. Butscher, J. Nipper, J. P. Shaffer, R. Löw, and T. Pfau. “Observation of ultralong-range Rydberg molecules”. *Nature* 458, 1005 (2009).

[49] D. Booth, S. T. Rittenhouse, J. Yang, H. R. Sadeghpour, and J. P. Shaffer. “Production of trilobite Rydberg molecule dimers with kilo-Debye permanent electric dipole moments”. *Science* 348, 99 (2015).

[50] T. Niederprüm, O. Thomas, T. Eichert, C. Lippe, J. Pérez-Ríos, C. H. Greene, and H. Ott. “Observation of pendular butterfly Rydberg molecules” (2016). arXiv:1602.08400.

[51] W. Li, T. Pohl, J. M. Rost, S. T. Rittenhouse, H. R. Sadeghpour, J. Nipper, B. Butscher, J. B. Balewski, V. Bendkowsky, R. Löw, and T. Pfau. “A Homonuclear Molecule with a Permanent Electric Dipole Moment”. *Science* 334, 1110 (2011).

[52] F. Böttcher, A. Gaj, K. M. Westphal, M. Schlagmüller, K. S. Kleinbach, R. Löw, T. C. Liebisch, T. Pfau, and S. Hofferberth. “Observation of mixed singlet-triplet Rb_2 Rydberg molecules”. *Phys. Rev. A* 93, 032512 (2016).

[53] H. Saßmannshausen, F. Merkt, and J. Deiglmayr. “Experimental Characterization of Singlet Scattering Channels in Long-Range Rydberg Molecules”. *Phys. Rev. Lett.* 114, 133201 (2015).

[54] M. Schlagmüller, T. C. Liebisch, H. Nguyen, G. Lochead, F. Engel, F. Böttcher, K. M. Westphal, K. S. Kleinbach, R. Löw, S. Hofferberth, T. Pfau, J. Pérez-Ríos, and C. H. Greene. “Probing an Electron Scattering Resonance using Rydberg Molecules within a Dense and Ultracold Gas”. *Phys. Rev. Lett.* 116, 053001 (2016).

[55] D. A. Anderson, S. A. Miller, and G. Raithel. “Angular-momentum couplings in long-range Rb_2 Rydberg molecules”. *Phys. Rev. A* 90, 062518 (2014).

[56] T. Niederprüm, O. Thomas, T. Manthey, T. M. Weber, and H. Ott. “Giant Cross Section for Molecular Ion Formation in Ultracold Rydberg Gases”. *Phys. Rev. Lett.* 115, 013003 (2015).

[57] M. Schlagmüller, T. C. Liebisch, F. Engel, K. S. Kleinbach, F. Böttcher, K. M.

Westphal, A. Gaj, R. Löw, S. Hofferberth, T. Pfau, J. Pérez-Ríos, and C. H. Greene. "Ultracold chemical reactions of a single Rydberg atom in a dense gas" (2016). arXiv:1605.04883.

[58] G. Pupillo, A. Micheli, M. Boninsegni, I. Lesanovsky, and P. Zoller. "Strongly Correlated Gases of Rydberg-Dressed Atoms: Quantum and Classical Dynamics". *Phys. Rev. Lett.* 104, 223002 (2010).

[59] J. B. Balewski, A. T. Krupp, A. Gaj, S. Hofferberth, R. Löw, and T. Pfau. "Rydberg dressing: understanding of collective many-body effects and implications for experiments". *New Journal of Physics* 16, 063012 (2014).

[60] T. Macrì and T. Pohl. "Rydberg dressing of atoms in optical lattices". *Phys. Rev. A* 89, 011402 (2014).

[61] S. Ray, S. Sinha, and K. Sengupta. "Phases, collective modes, and nonequilibrium dynamics of dissipative Rydberg atoms". *Phys. Rev. A* 93, 033627 (2016).

[62] B. B. Blinov, D. Leibfried, C. Monroe, and D. J. Wineland. "Quantum Computing with Trapped Ion Hyperfine Qubits". *Quantum Information Processing* 3, 45 (2004).

[63] C. Gerry and P. Knight. *Introductory Quantum Optics*. Cambridge University Press (2005).

[64] C. Cohen-Tannoudji, J. Dupont-Roc, and G. Grynberg. *Atom-photon interactions: basic processes and applications*. Wiley (2004).

[65] A. Messiah. *Quantum Mechanics*, volume 2 of *Quantum Mechanics*. North-Holland (1981).

[66] H. Friedrich. *Scattering Theory*. Lecture Notes in Physics. Springer Berlin Heidelberg (2013).

[67] E. Urban, T. A. Johnson, T. Henage, L. Isenhower, D. D. Yavuz, T. G. Walker, and M. Saffman. "Observation of Rydberg blockade between two atoms". *Nat Phys* 5, 110 (2009).

[68] J. B. Balewski, A. T. Krupp, A. Gaj, D. Peter, H. P. Büchler, R. Löw, S. Hofferberth, and T. Pfau. "Coupling a single electron to a Bose-Einstein condensate". *Nature* 502, 664 (2013).

[69] J. Wang, J. N. Byrd, I. Simbotin, and R. Côté. "Tuning Ultracold Chemical Reactions via Rydberg-Dressed Interactions". *Phys. Rev. Lett.* 113, 025302 (2014).

[70] T. C. Killian, S. Kulin, S. D. Bergeson, L. A. Orozco, C. Orzel, and S. L. Rolston. "Creation of an Ultracold Neutral Plasma". *Phys. Rev. Lett.* 83, 4776 (1999).

[71] G. Bannasch, T. C. Killian, and T. Pohl. "Strongly Coupled Plasmas via Rydberg Blockade of Cold Atoms". *Phys. Rev. Lett.* 110, 253003 (2013).

[72] T. M. Weber, T. Niederprüm, T. Manthey, P. Langer, V. Guarrera, G. Barontini, and H. Ott. "Continuous coupling of ultracold atoms to an ionic plasma via Rydberg excitation". *Phys. Rev. A* 86, 020702 (2012).

[73] M. Saffman, T. G. Walker, and K. Mølmer. "Quantum information with Rydberg atoms". *Rev. Mod. Phys.* 82, 2313 (2010).

[74] H. Weimer, M. Müller, I. Lesanovsky, P. Zoller, and H. P. Büchler. "A Rydberg quantum simulator". *Nat Phys* 6, 382 (2010).

[75] R. Stebbings and F. Dunning. *Rydberg States of Atoms and Molecules.* Essays in nuclear astrophysics. Cambridge University Press (1983).

[76] T. F. Gallagher. *Rydberg Atoms.* Cambridge Monographs on Atomic, Molecular and Chemical Physics. Cambridge University Press (2005).

[77] W. Demtröder. *Experimentalphysik 3: Atome, Moleküle und Festkörper.* Experimentalphysik / Wolfgang Demtröder. Springer (2005).

[78] C.-J. Lorenzen and K. Niemax. "Quantum Defects of the $n^2P_{1/2,3/2}$ Levels in ^{39}K I and ^{85}Rb I". *Physica Scripta* 27, 300 (1983).

[79] L. A. M. Johnson, H. O. Majeed, B. Sanguinetti, T. Becker, and B. T. H. Varcoe. "Absolute frequency measurements of ^{85}Rb $nF_{7/2}$ Rydberg states using purely optical detection". *New Journal of Physics* 12, 063028 (2010).

[80] P. Goy, J. M. Raimond, G. Vitrant, and S. Haroche. "Millimeter-wave spectroscopy in cesium Rydberg states. Quantum defects, fine- and hyperfine-structure measurements". *Phys. Rev. A* 26, 2733 (1982).

[81] K.-H. Weber and C. J. Sansonetti. "Accurate energies of nS , nP , nD , nF , and nG levels of neutral cesium". *Phys. Rev. A* 35, 4650 (1987).

[82] C. E. Theodosiou. "Lifetimes of alkali-metal atom Rydberg states". *Phys. Rev. A* 30, 2881 (1984).

[83] I. Hertel and C. Schulz. *Atome, Moleküle und optische Physik 1: Atomphysik und Grundlagen der Spektroskopie.* Springer-Lehrbuch. Springer Berlin Heidelberg (2015).

[84] T. Niederprüm. *Aufbau eines Lasersystems zur Anregung von Rydbergzuständen in ultrakalten Quantengasen.* Diplomarbeit, TU Kaiserslautern (2011).

[85] G. Arfken, H. Weber, and F. Harris. *Mathematical Methods for Physicists: A Comprehensive Guide.* Elsevier (2012).

[86] M. Saffman and T. G. Walker. "Analysis of a quantum logic device based on dipole-dipole interactions of optically trapped Rydberg atoms". *Phys. Rev. A* 72, 022347 (2005).

[87] I. I. Beterov, D. B. Tretyakov, I. I. Ryabtsev, V. M. Entin, A. Ekers, and N. N. Bezuglov. "Ionization of Rydberg atoms by blackbody radiation". *New Journal of Physics* 11, 013052 (2009).

[88] F. Robicheaux. "Ionization due to the interaction between two Rydberg atoms". *Journal of Physics B: Atomic, Molecular and Optical Physics* 38, S333 (2005).

[89] W. Li, P. J. Tanner, and T. F. Gallagher. "Dipole-Dipole Excitation and Ionization in an Ultracold Gas of Rydberg Atoms". *Phys. Rev. Lett.* 94, 173001 (2005).

[90] P. O'Keeffe, P. Bolognesi, L. Avaldi, A. Moise, R. Richter, A. A. Mihajlov, V. A. Srećković, and L. M. Ignjatović. "Experimental and theoretical study of the chemi-ionization in thermal collisions of Ne Rydberg atoms". *Phys. Rev. A* 85, 052705 (2012).

[91] A. Mihajlov, V. A. Srećković, L. M. Ignjatović, and A. Klyucharev. "The Chemi-Ionization Processes in Slow Collisions of Rydberg Atoms with Ground State Atoms: Mechanism and Applications". *Journal of Cluster Science* 23, 47 (2012).

[92] A. Steck. "Rubidium 87 D Line Data" (2010).

[93] J. Boulmer, R. Bonanno, and J. Weiner. "Crossed-beam measurements of absolute rate coefficients in associative ionisation collisions between Na*(np) and Na(3s) for $5 \leq n \leq 15$". *Journal of Physics B: Atomic and Molecular Physics* 16, 3015 (1983).

[94] R. Johnson. *Introduction to Atomic and Molecular Collisions.* Springer US (2012).

[95] C. Bahrim, U. Thumm, and I. I. Fabrikant. "Negative-ion resonances in cross sections for slow-electron–heavy-alkali-metal-atom scattering". *Phys. Rev. A* 63, 042710 (2001).

[96] Omont, A. "On the theory of collisions of atoms in Rydberg states with neutral particles". *J. Phys. France* 38, 1343 (1977).

[97] A. A. Khuskivadze, M. I. Chibisov, and I. I. Fabrikant. "Adiabatic energy levels and electric dipole moments of Rydberg states of Rb_2 and Cs_2 dimers". *Phys. Rev. A* 66, 042709 (2002).

[98] R. Shankar. *Principles of quantum mechanics.* Springer Science & Business Media (2012).

[99] G. Grawert. *Quantenmechanik.* Akademische Verlagsgesellschaft Frankfurt (1977).

[100] D. A. Anderson. *Rydberg molecules and circular Rydberg states in cold atom clouds.* Ph.D. thesis, University of Michigan (2015).

[101] F. S. Levin. *An introduction to quantum theory.* Cambridge University Press (2002).

[102] E. L. Hamilton. *Photoionization, Photodissociation, and Long-Range Bond Formation in Molecular Rydberg States.* Ph.D. thesis, University of Colorado (2003).

[103] D. A. Anderson, S. A. Miller, and G. Raithel. "Photoassociation of Long-Range nD Rydberg Molecules". *Phys. Rev. Lett.* 112, 163201 (2014).

[104] A. T. Krupp, A. Gaj, J. B. Balewski, P. Ilzhöfer, S. Hofferberth, R. Löw, T. Pfau, M. Kurz, and P. Schmelcher. "Alignment of D-State Rydberg Molecules". *Phys. Rev. Lett.* 112, 143008 (2014).

[105] J. Deiglmayr, H. Saßmannshausen, P. Pillet, and F. Merkt. "Observation of Dipole-Quadrupole Interaction in an Ultracold Gas of Rydberg Atoms". *Phys. Rev. Lett.* 113, 193001 (2014).

[106] B. Bransden and C. Joachain. *Physics of Atoms and Molecules.* Pearson Education. Prentice Hall (2003).

[107] P. L. Garrido, S. Goldstein, J. Lukkarinen, and R. Tumulka. "Paradoxical reflection in quantum mechanics". *American Journal of Physics* 79, 1218 (2011).

[108] A. Reinhard, T. C. Liebisch, B. Knuffman, and G. Raithel. "Level shifts of rubidium Rydberg states due to binary interactions". *Phys. Rev. A* 75, 032712 (2007).

[109] W. P. Wolf and R. J. Birgeneau. "Electric Multipole Interactions between Rare-Earth Ions". *Phys. Rev.* 166, 376 (1968).

[110] P. Schauß, M. Cheneau, M. Endres, T. Fukuhara, S. Hild, A. Omran, T. Pohl, C. Gross, S. Kuhr, and I. Bloch. "Observation of spatially ordered structures in a two-dimensional Rydberg gas". *Nature* 491, 87 (2012).

[111] O. Thomas. *Langzeitanregung von rydbergblockierten ultrakalten Quantengasen.* Diplomarbeit, TU Kaiserslautern (2014).

[112] T. Weber. *Rydberg-excited Mesoscopic Atomic Ensambles: Spectroscopy of a Super-atom.* Ph.D. thesis, TU Kaiserslautern (2014).

[113] J. M. Rost, J. C. Griffin, B. Friedrich, and D. R. Herschbach. "Pendular states and spectra of oriented linear molecules". *Phys. Rev. Lett.* 68, 1299 (1992).

[114] P. A. Block, E. J. Bohac, and R. E. Miller. "Spectroscopy of pendular states: The use of molecular complexes in achieving orientation". *Phys. Rev. Lett.* 68, 1303 (1992).

[115] T. Gericke. *A scanning electron microscope for ultracold quantum gases.* Ph.D. thesis, Universität Mainz (2010).

[116] T. Gericke, P. Würtz, D. Reitz, T. Langen, and H. Ott. "High-resolution scanning electron microscopy of an ultracold quantum gas". *Nat Phys* 4, 949 (2008).

[117] P. Würtz, T. Gericke, A. Vogler, F. Etzold, and H. Ott. "Image formation in scanning electron microscopy of ultracold atoms". *Applied Physics B* 98, 641 (2010).

[118] P. Langer. *Aufbau eines Lasersystems bei 297 nm zur Einphotonenanregung von Rydbergzuständen in Rubidium.* Diplomarbeit, Technische Universität Kaiserslautern (2012).

[119] T. Manthey. *Probing of ultracold samples with Rydberg excitation.* Ph.D. thesis, Technische Universität Kaiserslautern (2016).

[120] T. Manthey, T. M. Weber, T. Niederprüm, P. Langer, V. Guarrera, G. Barontini, and H. Ott. "Scanning electron microscopy of Rydberg-excited Bose–Einstein condensates". *New Journal of Physics* 16, 083034 (2014).

[121] T. Manthey, T. Niederprüm, O. Thomas, and H. Ott. "Dynamically probing ultracold lattice gases via Rydberg molecules". *New Journal of Physics* 17, 103024 (2015).

[122] H. Metcalf and P. van der Straten. *Laser Cooling and Trapping.* Graduate Texts in Contemporary Physics. Springer New York (2001).

[123] J. Dalibard and C. Cohen-Tannoudji. "Laser cooling below the Doppler limit by polarization gradients: simple theoretical models". *J. Opt. Soc. Am. B* 6, 2023 (1989).

[124] L. Ricci, M. Weidemüller, T. Esslinger, A. Hemmerich, C. Zimmermann, V. Vuletic, W. König, and T. Hänsch. "A compact grating-stabilized diode laser system for atomic physics". *Optics Communications* 117, 541 (1995).

[125] T. Manthey. *Aufbau einer Apparatur zur Erzeugung eines Bose-Einstein-Kondensates.* Diplomarbeit, Technische Universität Kaiserslautern (2011).

[126] G. C. Bjorklund, M. D. Levenson, W. Lenth, and C. Ortiz. "Frequency modulation (FM) spectroscopy". *Applied Physics B* 32, 145 (1983).

[127] T. W. Hänsch, M. D. Levenson, and A. L. Schawlow. "Complete Hyperfine Structure of a Molecular Iodine Line". *Phys. Rev. Lett.* 26, 946 (1971).

[128] M. J. Padgett, N. Bett, and R. J. Butcher. "A simple frequency discriminator circuit for offset locking of lasers". *Journal of Physics E: Scientific Instruments* 21, 554 (1988).

[129] E. I. Gordon. "A Review of Acoustooptical Deflection and Modulation Devices". *Appl. Opt.* 5, 1629 (1966).

[130] C. Utfeld. *Aufbau einer Hochleistungsquelle für ultrakalte Atome.* Diplomarbeit, Johannes Gutenberg-Universität Mainz (2006).

[131] K. Dieckmann, R. J. C. Spreeuw, M. Weidemüller, and J. T. M. Walraven. "Two-dimensional magneto-optical trap as a source of slow atoms". *Phys. Rev. A* 58, 3891 (1998).

[132] A. Zach. *Entwicklung und Aufbau eines frequenzstabilen, schmalbandigen Trapez-Diodenlaser-Verstärker-Systems mit hoher Ausgangsleistung.* Diplomarbeit, Fachhochschule Ulm (1998).

[133] W. Ketterle, K. B. Davis, M. A. Joffe, A. Martin, and D. E. Pritchard. "High densities of cold atoms in a *dark* spontaneous-force optical trap". *Phys. Rev. Lett.* 70, 2253 (1993).

[134] R. C. Hilborn. "Einstein coefficients, cross sections, f values, dipole moments, and all that". *Am. J. Phys.* 50, 982 (1982).

[135] R. Loudon. *The Quantum Theory of Light.* OUP Oxford (2000).

[136] M. Reicherter, T. Haist, E. U. Wagemann, and H. J. Tiziani. "Optical particle trapping with computer-generated holograms written on a liquid-crystal display". *Opt. Lett.* 24, 608 (1999).

[137] D. G. Grier. "A revolution in optical manipulation". *Nature* 424, 810 (2003).

[138] D. Meschede. *Optics, Light and Lasers: The Practical Approach to Modern Aspects of Photonics and Laser Physics*. Physics textbook. Wiley (2008).

[139] W. Ketterle, D. S. Durfee, and D. M. Stamper-Kurn. "Making, probing and understanding Bose-Einstein condensates" (1999). arXiv:cond-mat/9904034.

[140] P. Würtz. *Detection of Ultracold Atoms Using Electron-Impact-Ionization*. Diplomarbeit, Johannes Gutenberg-Universität Mainz (2007).

[141] A. G. Martin, K. Helmerson, V. S. Bagnato, G. P. Lafyatis, and D. E. Pritchard. "rf Spectroscopy of Trapped Neutral Atoms". *Phys. Rev. Lett.* 61, 2431 (1988).

[142] D. W. Sesko and C. E. Wieman. "Observation of the cesium clock transition in laser-cooled atoms". *Opt. Lett.* 14, 269 (1989).

[143] J. R. Rubbmark, M. M. Kash, M. G. Littman, and D. Kleppner. "Dynamical effects at avoided level crossings: A study of the Landau-Zener effect using Rydberg atoms". *Phys. Rev. A* 23, 3107 (1981).

[144] R. Löw, H. Weimer, J. Nipper, J. B. Balewski, B. Butscher, H. P. Büchler, and T. Pfau. "An experimental and theoretical guide to strongly interacting Rydberg gases". *Journal of Physics B: Atomic, Molecular and Optical Physics* 45, 113001 (2012).

[145] M. Viteau, J. Radogostowicz, M. G. Bason, N. Malossi, D. Ciampini, O. Morsch, and E. Arimondo. "Rydberg spectroscopy of a Rb MOT in the presence of applied or ion created electric fields". *Opt. Express* 19, 6007 (2011).

[146] P. Geppert. *Aufbau und Charakterisierung eines EIT-stabilisierten Lasersystems zur Zwei-Photonen-Rydberganregung ultrakalter* ^{87}Rb-*Quantengase über den* $6P_{3/2}$-*Zustand*. Diplomarbeit, Technische Universität Kaiserslautern (2016).

[147] B. G. Lindsay, K. A. Smith, and F. B. Dunning. "Control of long-term output frequency drift in commercial dye lasers". *Review of Scientific Instruments* 62, 1656 (1991).

[148] R. W. P. Drever, J. L. Hall, F. V. Kowalski, J. Hough, G. M. Ford, A. J. Munley, and H. Ward. "Laser phase and frequency stabilization using an optical resonator". *Applied Physics B* 31, 97 (1983).

[149] H. Liebl. *Applied Charged Particle Optics*. Springer Berlin Heidelberg (2008).

[150] B. Butscher, V. Bendkowsky, J. Nipper, J. B. Balewski, L. Kukota, R. Löw, T. Pfau, W. Li, T. Pohl, and J. M. Rost. "Lifetimes of ultralong-range Rydberg molecules in vibrational ground and excited states". *Journal of Physics B: Atomic, Molecular and Optical Physics* 44, 184004 (2011).

[151] V. Bendkowsky, B. Butscher, J. Nipper, J. B. Balewski, J. P. Shaffer, R. Löw, T. Pfau, W. Li, J. Stanojevic, T. Pohl, and J. M. Rost. "Rydberg Trimers and Excited Dimers Bound by Internal Quantum Reflection". *Phys. Rev. Lett.* 105, 163201 (2010).

[152] A. Studer and D. P. Curran. "The electron is a catalyst". *Nat Chem* 6, 765 (2014).

[153] W. Demtröder. “Experimentalphysik 1”. *Springer-Lehrbuch* (2001).

[154] L. Landau and E. Lifshitz. *Statistical Physics*. Bd. 5. Elsevier Science (2013).

[155] A. Härter, A. Krükow, A. Brunner, W. Schnitzler, S. Schmid, and J. H. Denschlag. “Single Ion as a Three-Body Reaction Center in an Ultracold Atomic Gas”. *Phys. Rev. Lett.* 109, 123201 (2012).

[156] D. Vrinceanu, H. R. Sadeghpour, and T. Pohl. “Rydberg atom formation in ultracold plasmas: Non-equilibrium dynamics of recombination”. *Journal of Physics: Conference Series* 194, 012067 (2009).

[157] T. C. Killian. “Ultracold Neutral Plasmas”. *Science* 316, 705 (2007).

[158] M. P. Robinson, B. L. Tolra, M. W. Noel, T. F. Gallagher, and P. Pillet. “Spontaneous Evolution of Rydberg Atoms into an Ultracold Plasma”. *Phys. Rev. Lett.* 85, 4466 (2000).

[159] R. Labouvie, B. Santra, S. Heun, and H. Ott. “Bistability in a Driven-Dissipative Superfluid”. *Phys. Rev. Lett.* 116, 235302 (2016).

[160] T. Eichert. *Anregung und Lebensdauerbestimmung von Rydbergmolekülen in einem ultrakalten Quantengas*. Diplomarbeit, TU Kaiserslautern (2016).

[161] T. L. Nicholson, S. Blatt, B. J. Bloom, J. R. William, J. W. Thomsen, J. Ye, and P. S. Julienne. “Optical Feshbach resonances: Field-dressed theory and comparison with experiments”. *Phys. Rev. A* 92, 022709 (2015).

[162] M. A. Bellos, R. Carollo, J. Banerjee, E. E. Eyler, P. L. Gould, and W. C. Stwalley. “Excitation of Weakly Bound Molecules to Trilobitelike Rydberg States”. *Phys. Rev. Lett.* 111, 053001 (2013).

[163] C. H. Greene, E. L. Hamilton, H. Crowell, C. Vadla, and K. Niemax. “Experimental Verification of Minima in Excited Long-Range Rydberg States of Rb_2”. *Phys. Rev. Lett.* 97, 233002 (2006).

[164] T. Köhler, K. Góral, and P. S. Julienne. “Production of cold molecules via magnetically tunable Feshbach resonances”. *Rev. Mod. Phys.* 78, 1311 (2006).

[165] F. Ferlaino, S. Knoop, and R. Grimm. “Ultracold Feshbach Molecules” (2008). arXiv:0809.3920.

[166] Wikipedia. “Associated Legendre polynomials — Wikipedia, The Free Encyclopedia” (2016). [Online; accessed 16-March-2016].

[167] S. Ravets, H. Labuhn, D. Barredo, T. Lahaye, and A. Browaeys. “Measurement of the angular dependence of the dipole-dipole interaction between two individual Rydberg atoms at a Förster resonance”. *Phys. Rev. A* 92, 020701 (2015).

[168] C. Fey, M. Kurz, P. Schmelcher, S. T. Rittenhouse, and H. R. Sadeghpour. “A comparative analysis of binding in ultralong-range Rydberg molecules”. *New Journal of Physics* 17, 055010 (2015).

[169] K. Kanjilal and D. Blume. “Nondivergent pseudopotential treatment of spin-polarized fermions under one- and three-dimensional harmonic confinement”. *Phys. Rev. A* 70, 042709 (2004).

[170] Z. Idziaszek and T. Calarco. “Pseudopotential Method for Higher Partial Wave Scattering”. *Phys. Rev. Lett.* 96, 013201 (2006).

Danksagung

Diese Dissertationsschrift steht am Ende eines langen Weges, der zuweilen viel Geduld und Frustrationstoleranz verlangte, aber in weitaus höherem Maß geprägt war von der Lust Neues zu entdecken, der Faszination für die Physik und der Freude über die großen und kleinen Durchbrüche im Labor und hinter dem Schreibtisch. Glücklicherweise musste ich diesen Weg nicht alleine gehen, sondern konnte Freude und Leid, Enttäuschung und Motivation mit vielen großartigen Menschen teilen. In dem Bewusstsein, dass die vielen großen und kleinen Hilfestellungen im Alltag maßgeblich waren, um mich ans Ziel zu bringen, möchte ich an dieser Stelle allen herzlich danken, die diesen Weg mit mir gegangen sind. Besonderer Dank geht dabei an

- Prof. Herwig Ott, für die Möglichkeit meine Doktorarbeit in deiner Gruppe und mit deiner Hilfe anfertigen zu können sowie für die Freiheiten, die ich dabei stets hatte. Deine Art wissenschaftlich zu arbeiten hat mich stets inspiriert und immer wieder angespornt, mich zu verbessern. Deine ausgewogene Art die Gruppe zu führen und dein enger Kontakt zum Experiment und zu uns waren mit Sicherheit grundlegend für den Erfolg der letzten Jahre.

- Tobias Weber, Torsten Manthey und Giovanni Barontini für die vielen gemeinsamen Stunden im Labor, für die gemeinsam erlebten Höhen und Tiefen und für so manches Gespräch über Gott und die Welt. Ich bin stolz auf das, was wir gemeinsam aufgebaut haben! Das Geräusch der umschaltenden Relais wird mich sicher noch viele Jahre im Traum begleiten und mich immer an die tolle gemeinsame Zeit erinnern.

- Oliver Thomas, der mit seiner investigativen Art vom ersten Tag an frischen Wind in unser Labor gebracht hat; ohne ihn wäre die Ionenoptik sicher heute noch falsch beschaltet. Es war unglaublich, wie schnell Du vom "Lehrling" zum wertvollen Diskussionspartner und wichtigen Kollegen herangewachsen bist. Es ist ein beruhigender Gedanke, das gemeinsam Aufgebaute in so fähige Hände übergeben zu können.

- Ralf Labouvie für die tolle gemeinsame Zeit und die unzähligen Diskussionen über physikalische - und manchmal auch banale - Fragestellungen, bei denen du meine Probleme immer wie selbstverständlich zu Deinen gemacht hast. Das Büro mit Dir zu teilen war von Anfang an eine Freude und eine Bereicherung für meinen Arbeitstag.

- Philipp Langer, Philipp Geppert und Tanita Eichert dafür, dass ihr Euch auf Anhieb in unser Team eingefügt und immer mit Begeisterung und Herzblut für unsere gemeinsamen Ziele gearbeitet habt. Es war immer eine Freude mit Euch zu arbeiten und Euch mit Rat und Tat zur Seite zu stehen.

- Gabriele Koschmann, Richard Walther und Peter Bohnert dafür, dass sie uns an so vielen Stellen die Last von den Schultern nehmen und den Laden hinter den Kulissen am laufen halten.

- die gesamte Arbeitsgruppe. Ihr alle habt großen Anteil daran, dass ich mit Freude auf unseren gemeinsamen Weg zurückschaue!
- meine Studienfreunde, die immer Anteil nehmen an Freude und an Leid, die immer da sind, wenn man Probleme hat oder einfach nur Ablenkung braucht. Über die Jahre sind wir zu einer einzigartigen Truppe herangewachsen.
- meine Eltern und meine Schwester, die jederzeit zu 100% hinter mir stehen und mich in Wort und Tat immer unterstützen. Ohne Euch wäre ich niemals so weit gekommen!
- meine Frau Katharina, die der Fixpunkt meines Universums ist und ohne die für mich alles seinen Sinn verliert. Mit Deiner unvergleichlich liebevollen Art und deinem Interesse an meiner Arbeit hast du nie einen Zweifel daran gelassen, dass ich auf dem richtigen Weg bin.

Curriculum Vitae

Persönliche Angaben

Vorname: Thomas
Name: Niederprüm

Ausbildung

seit 01.11.2011	**TU Kaiserslautern** Doktorand am Fachbereich Physik
28.10.2011	**Diplom** in Physik an der TU Kaiserslautern mit der Note 1,1
10.2010 – 10.2011	**Diplomarbeit** in der Gruppe von Prof. Dr. Herwig Ott, Fachbereich Physik, TU Kaiserslautern Thema: Aufbau eines Lasersystems zur Anregung von Rydbergzuständen in ultrakalten Quantengasen
01.2010 – 06.2010	**Universität Uppsala** (Uppsala Universitet) Auslandsaufenthalt am Fachbereich Physik, gefördert durch ein ERASMUS-Stipendium der Europäischen Union
25.08.2008	**Vordiplom** in Physik mit der Note 1,7
10.2006 – 10.2011	**TU Kaiserslautern** Studium der Physik mit der Vertiefungsrichtung Experimentalphysik.
31.03.2006	**Abitur** mit der Note 1,4
09.1997 – 03.2006	**Thomas-Morus-Gymnasium, Daun** mit naturwissenschaftlich-technischem Schwerpunkt